THÈSE DE DOCTORAT
de l'Université de recherche
Paris Sciences Lettres –
PSL Research University

préparée à
l'École normale supérieure

The Two-Dimensional Bose Gas in Box Potentials

École doctorale n°564
Spécialité: Physique
Soutenue le 02.06.2016

par Laura Corman

Composition du Jury :

M Tilman Esslinger
ETH Zürich
Rapporteur

Mme Hélène Perrin
Université Paris XIII
Rapporteur

M Zoran Hadzibabic
Cambridge University
Membre du Jury

M Gilles Montambaux
Université Paris XI
Membre du Jury

M Jean Dalibard
Collège de France
Directeur de thèse

M Jérôme Beugnon
Université Paris VI
Membre invité

ENS
PSL RESEARCH UNIVERSITY PARIS

ABSTRACT

Degenerate atomic gases are a versatile tool to study many-body physics. They offer the possibility to explore low-dimension physics, which strongly differs from the three dimensional (3D) case due to the enhanced role of fluctuations. In this work, we study degenerate 2D Bose gases whose original in-plane confinement is uniform and of arbitrary shape. These 2D uniform traps, which we first developed on an existing set-up, were subsequently implemented on a new set-up using versatile optical potentials.

We present a series of experiments that take advantage of this flexible geometry. First, we study the static and dynamic behaviours of a uniform gas at the transition between a 3D normal and a 2D superfluid state. We observe the establishement of extended phase coherence, followed, as the gas is quench cooled, by the apparition of topological defects whose scaling is compared to the Kibble-Zurek prediction. Second, we present the first results of the new set-up : we investigate collective effects in light-matter interactions, where the resonance properties of a dense ensemble of atoms are strongly modified with respect to the single atom ones.

Last, we develop two experimental proposals for the new set-up. The first one studies how a 2D gas can be uniformly evaporated using the tilted lattice providing the 2D confinement. In the second one, we propose to produce supercurrents in a deterministic way in ring-shaped traps either by condensing in an artificial gauge field or by implementing a topological vortex pump.

RÉSUMÉ

Les gaz quantiques atomiques constituent un outil de choix pour étudier la physique à N corps grâce à leurs nombreux paramètres de contrôle. Ils offrent la possibilité d'explorer la physique en basse dimension, modifiée par rapport au cas à trois dimensions (3D) à cause du rôle accru des fluctuations. Dans ce travail, nous étudions le gaz de Bose à deux dimensions (2D) avec un confinement original dans le plan atomique, uniforme et de motif arbitraire. Ces gaz 2D et uniformes, développés sur un montage existant, ont été installés sur un nouveau montage grâce à des potentiels optiques polyvalents.

Nous présentons une série d'expériences exploitant cette géométrie flexible. D'abord, nous étudions le comportement statique et dynamique d'un gaz uniforme lors de la transition d'un état 3D normal vers un état 2D superfluide. Nous observons l'établissement de la cohérence de phase dans un gaz à l'équilibre puis nous montrons l'apparition après une trempe de défauts topologiques dont le nombre est comparé à la prédiction de Kibble-Zurek. Ensuite, nous étudions grâce au nouveau montage les effets collectifs dans l'interaction lumière-matière, où les propriétés de résonance d'un nuage d'atomes dense sont fortement modifiées par rapport à celles d'un atome unique.

Enfin, nous proposons deux protocoles pour le nouveau montage. Le premier permet d'évaporer de manière uniforme un gaz 2D grâce au réseau incliné du confinement à 2D. Le second propose de produire des supercourants de manière déterministe dans des pièges en anneaux, soit par condensation dans un champ de jauge, soit en réalisant une pompe à vortex topologique.

REMERCIEMENTS

Les performances individuelles, ce
n'est pas le plus important. On gagne
et on perd en équipe.

Zinedine Zidane

L'examen du doctorat semble une épreuve solitaire tant pour la rédaction du manuscrit que pour la présentation orale ; ce n'est qu'une apparence, et les résultats présentés ici sont fortement le produit — direct ou indirect — d'une équipe, d'interactions fructueuses avec collègues, amis et famille que j'aimerais remercier ici.

Tout d'abord, je tiens à remercier Jean Dalibard qui a accepté que je rejoigne l'expérience rubidium en tant que doctorante. Cela réalisait ainsi une ancienne aspiration de ma part suite à un bref échange que j'avais eu avec lui à la suite d'une conférence de vulgarisation à l'Observatoire de Paris, et qui s'était peu à peu concrétisée grâce à des stages dans son équipe. Ses capacités scientifiques internationalement reconnues sont associées à un souci pédagogique remarquable qui m'a permis de comprendre énormément d'aspects de la physique, depuis les cours de l'École polytechnique jusqu'aux discussions impromptues le matin autour d'un tableau et d'un café. Sa modestie et sa bienveillance ont contribué grandement à construire une atmosphère de travail où chacun peut apprendre et proposer ses idées (et je le remercie également d'avoir écouté mes propositions plus ou moins fantaisistes au cours de ces quatre années !).

Je tiens également à remercier Jérôme Beugnon qui travaillait sur l'ancienne expérience (dite "rubidium 2") et qui a pris en main la gestion de l'équipe de la nouvelle expérience "rubidium 3". Sa franchise, son humour et son pragmatisme ont permis la construction rapide de l'expérience. La thèse étant rarement un long fleuve tranquille d'un point de vue personnel, je lui suis également très reconnaissante de m'avoir écoutée et aidée lorsque je rencontrais des problèmes pas nécessairement scientifiques qui pouvaient influencer mon travail.

Je tiens tout particulièrement à remercier Jean et Jérôme pour leur suivi infaillible lors du feuilleton des travaux à l'ENS qui ont conduit à l'arrêt prématuré de l'expérience "rubidium 2", afin de trouver la meilleure solution pour la fin de ma thèse. Rétrospectivement, construire la nouvelle expérience jusqu'à l'obtention de premiers résultats a été un choix très satisfaisant pour moi, et je les remercie à la fois de m'avoir proposé plusieurs options et de m'avoir intégrée dans la nouvelle équipe. Je remercie également l'école doctorale et Jean-Marc Berroir pour avoir été compréhensifs au vu de la situation des travaux.

Mes remerciements vont également à Sylvain Nascimbène, "observateur" sur les expériences rubidium (en particulier avec le début de la construction de l'expérience dysprosium). Il était toujours possible de passer dans son bureau pour discuter d'un sujet de physique de manière décontractée. Je resterai particulièrement impressionnée par sa capacité de concentration en réunion où

certains points de physique étaient tranchés dans la minute — quand j'espèrai secrètement profiter de quelques minutes de calme en sortant pour réfléchir au problème !

Lors des présentations du métier de chercheur que j'ai eu l'occasion de faire dans des classes de lycée, on n'échappe pas à la traditionnelle "journée-type" du doctorant. Pour moi une certitude : elle a lieu dans la salle de manip, entourée de collègues et amis avec qui la discussion permet d'avancer. Je tiens ainsi à remercier toutes les personnes avec lesquelles j'ai travaillé directement au cours de ces quatre années. Tout d'abord, je remercie Rémi pour m'avoir initiée au fonctionnement de l'expérience "rubidium 2", des boîtiers électroniques cachés sous la chambre à vide au fonctionnement des mystérieuses switch boxes. Sa capacité à s'attaquer à un problème nouveau pour l'expérience (comme ce fut le cas pour le premier défrichage des possibilités ouvertes par la production de gaz dans des boîtes) a été un exemple pour moi. Je remercie également chaleureusement Christof, dont la bonne humeur inattaquable et l'enthousiasme pour les projets m'ont beaucoup aidé lors des moments incertains de ma première année de thèse. Je garde également un excellent souvenir de nos convergences musicales, littéraires, etc. Merci également à Lauriane pour son engagement dans l'expérience, en particulier pour la prise et l'interprétation des données qui ont conduit à la compréhension de la condensation transverse. La lente agonie de l'expérience, éprouvée par les marteaux-piqueurs, m'a été moins pénible grâce à Andrea, en stage long, grâce à sa bonne humeur et son autonomie.

Je voudrais aussi remercier Tom, avec qui j'ai eu l'occasion de travailler sur les deux expériences. Je garderai en mémoire le comptage de vortex lorsque nous les avons vu apparaître pour la première fois dans les carrés, ainsi que la joie de voir le premier BEC sur "rubidium 3". Son esprit d'équipe, son dévouement et sa volonté d'en savoir toujours plus ont largement contribué à l'atmosphère très agréable de cette nouvelle expérience. Impossible d'utiliser l'expression "très agréable" sans remercier Jean-Loup pour sa contribution à la nouvelle expérience, pour son calme et sa rigueur, ainsi que Raphaël, très impliqué sur l'expérience dès les premières semaines de sa thèse. Avec eux, ainsi qu'avec Monika, je n'ai aucun doute que l'expérience soit entre d'excellentes mains pour la suite ! Merci également à David, Katharina et Junyi, contributeurs de la première heure sur rubidium 3, ainsi qu'à Victor et Lorenzo, en stage sur l'expérience.

L'atmosphère exceptionnelle du groupe ne repose pas exclusivement sur l'équipe rubidium, mais aussi sur tous ses autres membres avec qui il est toujours possible d'échanger, de discuter. Merci notamment à Fabrice, toujours prêt à discuter d'un point de physique. Je remercie l'équipe sodium, Vincent, Camille, Tilman, Karina, pour les relations de bons voisins qu'ils ont toujours su maintenir, l'équipe dysprosium avec Davide, Wilfried, Chayma, Leonid, Tian, qui compensent leur éloignement au premier étage par une attitude chaleureuse (et un volume sonore important) et l'équipe ytterbium avec Alexandre, Matthias, Daniel, Quentin, Manel, Raphaël, qui représente la force tranquille de cet étage. J'ai beaucoup interagi de manière très positive avec les membres des autres groupes, comme le groupe de Christophe Salomon,

en particulier Marion, Daniel, Benno, Sébastien, Andrew, Igor, le groupe de Jakob Reichel, en particulier Cyril, Claire et Konstantin, le groupe de Serge Haroche, en particulier Mariane et Eva-Katharina, mon parrain Félix et la jeune équipe voisine d'Alexeï, avec Kilian, Quentin et Nicolas. Merci à tous d'avoir accepté d'instaurer successivement une "réunion de progrès technique", puis des journal club dont j'ai tenté le lancement à plusieurs reprises et qui, repris très sérieusement par l'ensemble des thésards et post-docs de l'étage, semble désormais installé pour durer !

Bien que j'aie passé beaucoup de temps dans la salle de manip, la réussite de ma thèse a grandement bénéficié de l'environement exceptionnel que constitue le LKB, dirigé par Antoine Heidmann à l'humour et à la gentillesse remarquable. Cela a été une grande chance de participer et de m'impliquer dans la vie du laboratoire, de la participation aux séminaires au rôle de déléguée au conseil de laboratoire en passant par l'organisation des journées prospectives et la fête de la science : merci à toutes les personnes que j'ai pu côtoyer lors de ces événements. Je remercie également tous les services techniques qui permettent chaque jour que les travaux de recherche se déroulent dans les meilleures conditions possibles : le service informatique, toujours disponible malgré son sous-effectif, l'atelier de mécanique du LKB, de l'ENS et du Collège de France, sans qui la construction d'une expérience serait simplement impossible, José Palomo de la salle blanche de l'ENS qui a produit les masques à l'origine d'une grande partie des résultats de cette thèse, le service électronique, les différents service logistique de l'ENS (Didier Courtiade et son équipe) et du Collège de France. Un remerciement particulier va également aux services administratifs du LKB (Thierry, Audrey, Delphine, Monique, Christophe, Dominique, Romain, Nora) et de l'Institut de Physique, Françoise et surtout Carmen pour leur patience à m'expliquer certaines procédures que j'avais trop souvent tendance à oublier. Je remercie également les personnes que j'ai cotoyées lors de mes missions doctorales, en particulier Arnaud Boissière du bureau ETT à Jussieu, ainsi que Max Marangolo, Yves Berthaud et Philippe Jacquier pour ma mission d'enseignement. Je tiens à souligner l'importance de la DGA qui a financé ma thèse pendant trois ans, en s'intéressant très régulièrement à mes travaux, ainsi qu'au Collège de France qui m'a financé pour ma dernière année de thèse. Je remercie également la Fondation l'Oréal pour leur reconnaissance de mes travaux, et pour les opportunités de communication qu'elle ouvre aux boursières.

Je remercie également tous les membres de mon jury, Tilman Esslinger, Hélène Perrin, Zoran Hadzibabic et Gilles Montambaux pour leur apport et leurs questions lors de la soutenance. Je remercie en particulier la lecture très attentive de mon manuscrit (malgré la longueur) par Hélène Perrin et Tilman Esslinger, ainsi que par Jean et Jérôme.

Enfin, je tiens à remercier tous les amis avec qui j'ai partagé des discussions enflammées, des sorties culturelles ou photo, et parfois — il faut bien l'avouer — à qui j'ai pu me confier sur les difficultés liées à la thèse. Un grand merci à Alexandre, qui restera le colocataire parfait (au point qu'on parte en vacances ensemble), entre expérimentations culinaires, échange de lectures et organisation du ménage aux Wallons selon un planning qui nous mettait tous les deux d'accord. Merci aussi à Thomas et Géraldine, Yue et Michel pour tous les

moments passés ensembles, Xavier pour avoir ressucité l'idée des salons, Buu-Minh pour la découvertes des restaurants asiatiques et sichuanais de la capitale, Guillaume pour m'avoir fait passer pour une récitante lors d'un concert dans le Jura, Claire, Audrey-Marine pour tous les spectacles partagés.

Un immense merci va naturellement à ma famille, présente au grand complet lors de ma soutenance, qui m'a toujours soutenue et encouragée. Merci à Antoine, de savoir me faire découvrir de nouveaux horizons, musicaux ou autres. Merci à mes parents, qui ne reculent devant rien pour être avec moi et m'aider, lors d'un aller-retour dans la journée à Nancy pour assister à "ma thèse en 180s", pour la préparation de la soutenance et du pot, pour partager des spectacles à Paris ou à Lille. Enfin, merci Wilfried, depuis les cafés matinaux avec la vue sur les toits de Paris jusqu'à la logistique infaillible pendant la rédaction et la préparation du pot, pour tous les moments passés ensemble à des concerts improbables à la Philharmonie ou ailleurs, et qui se multiplieront à Zurich je l'espère.

CONTENTS

ACRONYMS

2D two-dimensional

2D MOT Two-dimensional Magneto-Optical Trap

AOM acousto-optical modulator

BEC Bose-Einstein Condensate

BKT Berezinskii-Kosterlitz-Thouless

DMD Digital Micromirror Device

MOT Magneto-Optical Trap

OD optical density

ToF Time-of-Flight

INTRODUCTION

The first experimental demonstration of Bose-Einstein condensation in weakly interacting, dilute gases of alkali atoms [1–3] has represented an important milestone, confirming a seventy-year old theoretical prediction [4, 5]. It is achieved by cooling down atoms to the quantum degenerate regime, where the interparticle distance is on the order of the extent of the wavepacket of each atom. Liquid helium has enabled the first studies of Bose-Einstein condensation [6–8]; yet, the strength of the interactions in liquid helium is very large, which does not correspond to the description of the phenomenon by Bose and Einstein, based solely on the quantum statistics of the particles. However, far from only implementing a long-standing theoretical proposal, the ability to cool down atomic species to the quantum degenerate regime, combined with the tools to manipulate the degenerate gases (optically, magnetically, etc.) has provided the atomic physics community with a platform to study macroscopic quantum objects and many-body problems.

The first reason that makes Bose-Einstein condensates interesting objects to study is linked to their intrisic properties — this state of matter has also been obtained in a variety of other physical systems like cavity photons [9], polaritons [10–12] and magnons [13]. They are produced in clean and controlled environment, such that their behaviour can be accurately compared to theoretical predictions. For example, in an atomic Bose-Einstein Condensate (BEC), interactions are usually small and the behaviour of the gas can be predicted using the mean-field Gross-Pitaevskii [14, 15] equation. Precise measurements also allow to verify beyond mean-field predictions [16]. The properties of degenerate gases were therefore extensively studied, revealing phase coherence through the interference of independent condensates [17] or of atoms from different part of the same condensate [18], the apparition of vortices organized in an Abrikosov lattice in a rotating cloud [19–21] as well as superfluid behaviour [22, 23].

The strong interest in studying BEC and degenerate Fermi gases, which were produced shortly after the first atomic BEC [24–26], mainly comes from the variety of parameters that can be tuned and controlled — quantum statistics, interactions, confining potential, etc. — which allows to produce clean systems where the measurements can be compared to theoretical predictions [27]. These systems therefore realize Feynman's idea of the "quantum simulator" [28].

Choosing the atomic species and isotope enables to pick a quantum statistics, boson or fermions, as well as a type of interaction: while alkali atoms interact via contact interactions [29], species such as chromium [30], dysprosium [31] or erbium [32] have a large magnetic moment leading to strong dipole interactions. Some "infinite range" interactions have also been realized using light-induced interaction between the atoms of a BEC in an optical resonator [33]. Some species also allow to tune the strength of the contact interactions when varying a magnetic field, using a so-called Feshbach resonance [34, 35]. This prop-

erty has been especially important to the study of fermions, where different regimes exist: the weakly repulsive regime, where a BEC of molecules forms at low temperatures, the weakly attractive regime, described by the Bardeen-Cooper-Schrieffer theory of superconductivity where weakly bound pairs form a superfluid, and the unitarity regime where the particles interact strongly [24, 36]. The choice of the atomic species also fixes the availability of different internal states for the atoms. This is important in the study of spinor physics [37, 38] or in exploring geometrical and topological properties of atoms whose internal states have been astutely coupled [39].

Magnetic and radio-frequency fields or light are commonly used to confine the atoms [1, 40, 41]. The most common trap is harmonic, since the atoms are usually trapped in a local extremum of the potential landscape; increasing the trapping strength in one or two directions has enable the study of low-dimensional systems by freezing one to two motional degrees of freedom. These systems of reduced dimensionality are especially interesting for the study of quantum and thermal beyond mean-field models since in one [42, 43] or two dimensions [44, 45], the fluctuations are very important and destroy long-range order [46–48].

Further engineering of light beams interacting with degenerate quantum gases have given access to new phenomena. The interaction between light and matter can be studied in two different regimes: (i) when the light is far from any atomic resonances, which allows to produce potential landscapes for the atoms and (ii) when the light is close to an atomic resonance.

Far-detuned beams create attractive or repulsive potentials for the atoms; they can be easily shaped to investigate different geometries. The paradigmatic example of this type of study is the realization of optical lattices, where interfering light beams create a periodic potential on the atoms analogue to the periodic potential of ions in solids. Ultracold atoms allow to implement the Hubbard model, which is a simple model believed to contain many features of complex materials. This was demonstrated by revealing experimentally the transition from a superfluid to a Mott insulator state in a cloud of atoms [49, 50]. Using optical potentials has also allowed to produce many other rich geometries: rings of atoms in which the decay of a supercurrent was studied [51–53], the textbook box potential for quantum particles [54, 55], or disordered potentials leading for example to the demonstration of Anderson localization [56].

Close to resonance beams can be used to manipulate the internal state of the atoms, for example create artificial magnetic fields on the atoms thanks to laser-assisted internal state transfer [39], as was recently demonstrated [57]. Their interaction with dense samples of atoms coupled by dipole-dipole interactions also reveals interesting many-body effects, as was recently demonstrated in small dense clouds [58, 59].

In addition to having a large number of tunable parameters, degenerate quantum gases are very appropriate systems to study dynamical effects. All their energy scales are low, meaning that their evolution is slow, on the order of milliseconds to seconds, which is easily tractable in an experiment. Furthermore, they are well isolated from perturbations from the environment and

the quantum macroscopic states that are created have long life times (up to tens seconds). Dynamical phenomena which were observed in ultracold atoms include the study of prethermalization of elongated condensates [60], of supercurrents in rings in the presence of a defect [52], transport experiments both with fermions [61–63] and bosons [64, 65], the study of turbulences [66] as well as critical dynamics when quench cooling a gas through a phase transition point [67, 68].

In many respects, degenerate quantum gases provide a great degree of control over all experimental parameters. The same level of control is difficult to achieve in condensed matter, whose most pristine system, the two-dimensional electron gas, has led to the observation of many novel phenomena [69] such as the quantum Hall effect (QHE) [70], the fractional quantum Hall effect (FQHE) [71, 72] and the quantized conductance through a quantum point contact [73]. On the one hand, the QHE and the FHQE analogues in atomic physics still remain a challenge for the community, since they require large artificial magnetic fields to be produced on the atoms, which has not been realized so far in experiments. On the other hand, the observation of quantized conductance only requires the ability to shape the two-dimensional electron gas (using gate potentials for instance), which is an available technique for cold atoms using for instance light potentials. This has led to the development of a new set of experiments studying the evolution of atoms in tailored optical potential, called "atomtronics".

In this work, I describe the experimental techniques used on an existing set-up to produce bosonic gases which are two-dimensional (2D) and where an in-plane flexible and uniform confinement was developped, in contrast to the previous studies of 2D atomic gases. Building a new quantum gas experiment where an improved version of the 2D box potentials was implemented has been part of my thesis work. I also present a series of results taking advantage of this geometry: I will first study experimentally the static and dynamical properties of phase transitions in a uniform system. I will then explore the scattering of light in a complex medium, last describing two possible experiments for the new set-up, taking advantage of the confinement techniques that were developed during my thesis.

DETAILED OUTLINE

Chapter 1 gives an overview of the ins and outs of producing 2D gases whose motion is frozen in one direction using a tightly confining harmonic trap. In particular, starting from a three dimensional gas, we show that bosonic amplification tends to accelerate the accumulation of atoms in the ground state of the tight harmonic trap, which corresponds to transverse condensation. Last, the rich physics of 2D systems is briefly described.

In chapter 2, we present the main theoretical concepts necessary to describe the static and dynamic properties of systems close to a phase transition, such as scaling and universality. The main results relevant for Bose gases close to degeneracy are recalled. These concepts are then used to explain the Kibble-Zurek mechanism, which predicts the formation of topological defects in a

system which is quenched cooled through a phase transition point. The density of defects can be related to a characteristic length deduced from the universality class of the transition.

The experimental observations of the theoretical predictions of chapter 1 and chapter 2 are presented in chapter 3. After describing the first generation of the experimental set-up used to produce 2D uniform gases, we explain the appearance of coherence in the samples through the transverse condensation mechanism. Then, we study the dynamical aspect of this phase transition by quench cooling a non-degenerate gas to the deeply degenerate regime and compare the production of topological defects to the prediction by Kibble and Zurek. In these experiments, having a uniform confinement helps us reveal the physical phenomena because the in-plane trap does not introduce a length scale (or only a large one, on the order of the size of the trap).

In chapter 4, we describe the characteristics of the new experimental set-up aimed at studying 2D physics in tailored optical potentials built as part of my thesis work. After presenting the technical choices made in order to obtain a quantum degenerate gas of rubidium 87, we give a more detailed explanation of the apparatus used to produce uniform traps, using a digital micromirror device, and to confine them to 2D, using an "accordion lattice" (originally proposed in [74]) whose spacing can be dynamically changed.

The first results obtained with this new set-up are presented in chapter 5. Using our ability to produce a uniform slab of atoms of controlled thickness and density, we show that the collective response to the atoms to a near resonant probe is different from that of a single atom: the resonance frequency is shifted to higher frequencies and the response of the atoms is broadened with respect to the natural linewidth of the transition.

The last two chapters are dedicated to the description of two experiment proposals which are easily accessible on the new experimental set-up.

In chapter 6, we study how the accordion lattice can be used in combination with a tilted potential to evaporate a 2D cloud in a uniform manner, without relying on the fact that the most energetic particles reach the edges of the uniform trap. After applying the calculations of [75] to our case, we perform molecular dynamic simulations on a thermal gas and show that some collision-assisted processes lead to cooling and increased degeneracy of the atoms.

Last, in chapter 7, we study the possibility of creating topologically non-trivial states by combining a 2D ring-shaped gas with the magnetic field generated by a quadrupole trap. We show that it is possible (i) to demonstrate condensation in the presence of an artificial magnetic field, where the lowest energy state has a non zero permanent current (ii) to create a "vortex pump" equivalent to the Thouless pump [76, 77] that produces large supercurrents in an atomic ring.

1

THE BOSE GAS FROM THREE TO TWO DIMENSIONS

This chapter aims at introducing some relevant concepts concerning Bose gases, which are necessary to understand the context of the experiments and calculations of the following chapters. The main results on Bose gases can be found in textbooks and reviews [27, 29, 78] and the specificities of 2D atomic systems have been detailed in [79].

First, the basics of Bose-Einstein statistics will be used in order to explain why, in some configurations, a macroscopic occupation of the lowest energy state available, called a BEC, can appear thanks to bosonic amplification at the thermodynamic limit. Then, the aim of both experimental set-ups described in this thesis is to produce 2D Bose gases; the meaning of which will be detailed in the chapter. These gases are usually produced using a combination of a strong harmonic confinement in one direction and a weak in-plane confinement. In order to macroscopically populate the ground state of the former confinement, there are two possibilities:

1. All the relevant energy scales of the gas (temperature, chemical potential) are small compared to the energy spacing between the ground state and the first excited state of the harmonic oscillator.

2. Thanks to Bose enhancement, the atoms macroscopically occupate the ground state of the harmonic oscillator even though the energy scale given by the temperature is larger than the level spacing.

Several experimental studies have been carried out as close as possible to the first regime [45, 80, 81]. In the case of the experiments described in [82], we explore a range of parameters that additionally covers the second regime, also called transverse condensation [83]. The study of the transverse condensation transition will be done in section 1.2. In particular, the variation of the correlation length across the transverse condensation transition will be evaluated. Last, having a plane of atoms realized by either one of the two methods (usually with some additional, in-plane confinement), we will briefly recall the behaviour of a non-interacting and interacting gas in 2D. In particular, we will detail the experimental range in which the two possible transitions that lead to a superfluid can be observed, namely the Bose-Einstein condensation and the Berezinskii-Kosterlitz-Thouless (BKT) transition [79, 84, 85]. We will focus on the case where the in-plane confinement is a box potential, whose flatness is particularly suited for the study of critical phenomena.

1.1 STATISTICS AND BOSE GASES

1.1.1 *Non-interacting bosons in the grand-canonical ensemble*

Let us consider a system of bosonic particles of mass M whose dynamics is given by the single-particle Hamiltonian $\hat{H}$. If the bosons are spin-less particles in a d-dimension space, the eigenfunctions solutions of $\hat{H}$ are going to be characterized by a set of d good quantum numbers $\boldsymbol{m}$. If the Hamiltonian of the system can be written as a sum of Hamiltonian for each quantum number, the energy of one particle with quantum numbers $\boldsymbol{m}$ is

$$\varepsilon_{\boldsymbol{m}} = \sum_{i=1}^{d} \varepsilon_{m_i} \tag{1.1}$$

Let us now consider an ensemble of such quantum particles in contact with a heat reservoir characterized by a temperature $T = 1/(k_B\beta)$ and a particle reservoir of chemical potential μ, whose fugacity is defined as $z = e^{\beta\mu}$. The partition function in the grand-canonical description is

$$\begin{aligned} \mathcal{Z} &= \mathrm{Tr}\left(e^{-\beta\left(\hat{H}-\mu\hat{N}\right)}\right) && (1.2)\\ &= \prod_{\boldsymbol{m}}\sum_{n_{\boldsymbol{m}}}\left(ze^{-\beta\varepsilon_{\boldsymbol{m}}}\right)^{n_{\boldsymbol{m}}} && (1.3)\\ &= \prod_{\boldsymbol{m}}\frac{1}{1-ze^{-\beta\varepsilon_{\boldsymbol{m}}}} && (1.4) \end{aligned}$$

with $n_{\boldsymbol{m}}$ the number of particles with quantum numbers $\boldsymbol{m}$. The second line uses the fact that the quantum particles are indistinguishable and the third line uses the fact that for bosons, $n_{\boldsymbol{m}}$ is an integer. The value of the chemical potential has to stay below the ground state energy of the system to avoid any divergence of the partition function in the non-interacting case. We will always redefine the energy scale by adding a constant such that the energy of the ground state is 0. In that case, $\mu < 0$ and $z < 1$.

From the partition function, the total atom number N can be computed

$$N = \sum_{\boldsymbol{m}} \bar{n}_{\boldsymbol{m}} = \sum_{\boldsymbol{m}} \frac{1}{z^{-1}e^{\beta\varepsilon_{\boldsymbol{m}}} - 1} \tag{1.5}$$

where $\bar{n}_{\boldsymbol{m}}$ is the mean occupation number of the state with quantum number $\bar{n}$. The average value of any one-body observable $\hat{A}$ for the ideal gas can also be calculated:

$$\left\langle \hat{A} \right\rangle = \frac{1}{N}\sum_{\boldsymbol{m}} \bar{n}_{\boldsymbol{m}} \left\langle \psi_{\boldsymbol{m}} \left| \hat{A} \right| \psi_{\boldsymbol{m}} \right\rangle \tag{1.6}$$

where $|\psi_{\boldsymbol{m}}\rangle$ is the wavefunction of an atom with quantum numbers $\boldsymbol{m}$.

From equation 1.5, the atom number can be approximated by an integral:

$$N = \int \frac{1}{z^{-1}\exp\left(\beta\sum_{i=1}^{d}\varepsilon_{m_i}\right) - 1} \prod_{i=1}^{d} \frac{\mathrm{d}m_i}{\alpha_i} \tag{1.7}$$

where $1/\alpha_i$ denotes the number of states per unit of m_i, also called the density of states. The condition for the approximation of the sum by an integral to

be valid depends on the specific form of the energy ε_{m_i}. It requires that the thermodynamic limit can be taken simultaneously for all quantum numbers, i. e. the parameters are such that $\beta\left(\varepsilon_{m_i+1} - \varepsilon_{m_i}\right) \to 0$.

In the following, the fugacity expansion of N will be important to us

$$N = \sum_{n=1}^{\infty} z^n \int \exp\left(-n\beta \sum_{j=1}^{d} \varepsilon_{m_j}\right) \prod_{i=1}^{d} \frac{\mathrm{d}m_i}{\alpha_i} \tag{1.8}$$

$$= \sum_{n=1}^{\infty} z^n \prod_{i=1}^{d} \left[\int \exp\left(-n\beta\varepsilon_{m_i}\right) \frac{\mathrm{d}m_i}{\alpha_i}\right] \tag{1.9}$$

$$= \sum_{n=1}^{\infty} z^n \prod_{i=1}^{d} \mathcal{I}(m_i, n) \tag{1.10}$$

Let us now treat two forms of interest for the energy ε_i: the case of a free gas and the case of a harmonic oscillator.

1.1.1.1 *Free gas*

In this case, we consider that the bosons can move freely in a one-dimensional box of size L, where the coordinate x is such that $0 \leqslant x \leqslant L$. We consider hard wall boundary conditions for this calculation. The single-particle Hamiltonian only contains a kinetic term

$$\hat{H} = \frac{\hat{p}^2}{2M} \tag{1.11}$$

where M is the mass of one particle and $\hat{p}$ its momentum along the direction of interest. The eigenfunctions are plane waves labelled by an integer $j_1 \in \mathbb{Z}$ such that we can define a wave vector $k_1 = \pi j_1 / L$:

$$\psi_{j_1}(x_1) = \frac{\sin\left(k_1 \cdot x_1\right)}{\sqrt{L/2}} \tag{1.12}$$

with an energy $\varepsilon_{j_1} = \frac{\hbar^2 k_1^2}{2M}$.

We compute the integral $\mathcal{I}(j_1, n)$:

$$\mathcal{I}(j_1, n) = \frac{L}{2\pi} \int \exp\left(-n\beta \frac{\hbar^2 k_1^2}{2M}\right) \mathrm{d}k_1 = \frac{L}{\lambda_{\mathrm{dB}}} n^{-1/2} \tag{1.13}$$

with $\lambda_{\mathrm{dB}} = h/\sqrt{2\pi M k_{\mathrm{B}} T}$ the thermal wavelength. In this case, the condition for the discrete sum of equation 1.5 to be approximated by an integral reads

$$\beta\left(\varepsilon_{j_1+1} - \varepsilon_{j_1}\right) = \frac{\pi}{2} \frac{\lambda_{\mathrm{dB}}^2}{L^2} \left(j + \frac{1}{2}\right) \to 0 \tag{1.14}$$

which is fulfilled for $L/\lambda_{\mathrm{dB}} \to \infty$.

1.1.1.2 *Harmonic oscillator*

In this case, we consider a one-dimensional harmonic oscillator characterized by the angular frequency ω such that the single-particle Hamiltonian reads

$$\hat{H} = \frac{\hat{p}^2}{2M} + \frac{1}{2} M\omega^2 \hat{x}_1^2 \tag{1.15}$$

The eigenstates are characterized by a non-negative integer j_1 and are the product of a Gaussian and the j_1th Hermite polynomial H_{j_1}. They can be expressed using the length scale associated to the problem $a_{\mathrm{ho}} = \sqrt{\hbar/(M\omega)}$

$$\chi_{j_1}(x_1) = \frac{1}{\sqrt{2^{j_1}\, j_1!\, a_{\mathrm{ho}}}\pi^{1/4}} H_{j_1}\left(\frac{x_1}{a_{\mathrm{ho}}}\right) e^{-x_1^2/(2a_{\mathrm{ho}}^2)} \tag{1.16}$$

with an energy $\varepsilon_{j_1} = \hbar\omega j_1$ (here we redefine the zero of energy at $\hbar\omega/2$).

We compute the integral $\mathcal{I}(j_1, n)$:

$$\mathcal{I}(j_1, n) = \int \exp\left(-n\beta\hbar\omega j_1\right) \mathrm{d}j_1 = \zeta n^{-1} \tag{1.17}$$

with

$$\zeta = \frac{k_{\mathrm{B}}T}{\hbar\omega} = 2\pi\frac{a_{\mathrm{ho}}^2}{\lambda_{\mathrm{dB}}^2}$$

In this case, the condition for the discrete sum of equation 1.5 to be approximated by an integral reads

$$\beta\left(\varepsilon_{j_1+1} - \varepsilon_{j_1}\right) = \frac{1}{\zeta} \to 0 \tag{1.18}$$

which is fulfilled for $\zeta \to \infty$, i. e. $a_{\mathrm{ho}}/\lambda_{\mathrm{dB}} \to \infty$.

1.1.2 *Bose-Einstein condensation*

Assuming that the gas of bosons is confined in the first d_1 dimensions in harmonic oscillators of angular frequency ω_i and in the remaining $d - d_1$ dimensions in boxes of size L_i, the total atom number at the thermodynamic limit is

$$N = \left(\prod_{i=1}^{d_1}\zeta_i \prod_{j=d_1+1}^{d}\frac{L_j}{\lambda_{\mathrm{dB}}}\right)\sum_{n=1}^{\infty}\frac{z^n}{n^{d/2+d_1/2}} \tag{1.19}$$

$$= \left(\prod_{i=1}^{d_1}\zeta_i \prod_{j=d_1+1}^{d}\frac{L_j}{\lambda_{\mathrm{dB}}}\right) g_{d/2+d_1/2}(z) \tag{1.20}$$

where $g_\alpha(z) = \sum_{i=1}^{\infty} z^n/n^\alpha$ which is defined for all allowed values of $z < 1$.

Here we distinguish two cases:

- If $\alpha \leqslant 1$, $g_\alpha(z) \to \infty$ as $z \to 1$. Hence for a given atom number and temperature, it is always possible to find a chemical potential $\mu < 0$ such that equation 1.20 is fulfilled.
- If $\alpha > 1$, g_α converges as $z \to 1$. For a given temperature, the atom number cannot exceed

$$N_{\mathrm{c}} = \left(\prod_{i=1}^{d_1}\zeta_i \prod_{j=d_1+1}^{d}\frac{L_j}{\lambda_{\mathrm{dB}}}\right) g_\alpha(1) \tag{1.21}$$

  This apparently paradoxical result actually comes from the substitution of the discrete sum by an integral in equation 1.7. The population of the

ground state is not correctly accounted for and the total atom number should be written

$$N = N_0 + \left(\prod_{i=1}^{d_1} \zeta_i \prod_{i=d_1+1}^{d} \frac{L_i}{\lambda_{\mathrm{dB}}} \right) g_\alpha(z) \tag{1.22}$$

The second case corresponds to the well-known Bose-Einstein condensation [4, 5]. For example, for a three-dimension Bose gas in a box, $d = 3$ and $d_1 = 0$ so $\alpha = 3/2$. There is a Bose-Einstein condensation and for a given temperature, the chemical potential and population of the ground state are chosen to fulfil the following equations:

$$N = \begin{cases} \frac{L^3}{\lambda_{\mathrm{dB}}^3} g_{3/2}(z) & \text{if } N < N_{\mathrm{c}} = \frac{L^3}{\lambda_{\mathrm{dB}}^3} g_{3/2}(1) \\ N_{\mathrm{c}} + N_0 & \text{if } N > N_{\mathrm{c}} \end{cases} \tag{1.23}$$

For a three-dimension Bose gas trapped in a harmonic potential with frequencies $(\omega_x, \omega_y, \omega_z)$, $d = 3$ and $d_1 = 3$ so $\alpha = 3$: there is a Bose-Einstein condensation .

A 2D Bose gas with harmonic confinement will also undergo a Bose-Eintein condensation ($\alpha = 2$), while a 2D Bose gas in a box of size L yields $d = 2$ and $d_1 = 0$ so $\alpha = 1$: the function g_1 diverges in 1 so there is no accumulation of atoms in the ground state. Calling the 2D atomic density $n^{(2\mathrm{D})} = N/L^2$, it is always possible to find a fugacity z such that

$$\mathcal{D} = n^{(2\mathrm{D})} \lambda_{\mathrm{dB}}^2 = g_1(z) = -\ln(1 - z) \tag{1.24}$$

where $\mathcal{D}$ is the phase-space density, a dimensionless quantity that quantifies the degeneracy of the gas. The fact that a uniform 2D Bose gas cannot undergo Bose-Einstein condensation is actually a special case of the Mermin-Wagner-Hohenberg theorem [46–48] that states that in a 2D system with contact interaction, it is not possible to have long-range order provided by the breaking of a continuous symmetry with a second-order phase transition at the thermodynamic limit. However, the case $\alpha = 1$ is only weakly, logarithmically divergent, which can lead to interesting behaviours as will be studied later.

1.1.3 *Validity of the derivation of Bose-Einstein condensation*

The previous subsection has showed that, under the assumption that the sum over all possible states can be replaced by an integral using the density of states in equations 1.5 and 1.7 and with some conditions on the degrees of freedom the atoms have, there can be a Bose-Einstein condensation, that is a saturation of the excited states of the gas that leads to an accumulation of atoms in the ground state. However, if the the atoms have d degrees of freedom, going from equation 1.5 to equation 1.7 requires making the density of state approximation d times successively. It turns out that depending on the order in which the sums are turned into integrals, the physical interpretation of the situation can be different.

This phenomena was first pointed out in the case of a highly elongated harmonic trap [83]. In this situation, a three-dimensional harmonic oscillator is characterized by three quantum numbers (j_x, j_y, j_z) and frequencies $(\omega_x, \omega_y, \omega_z)$ such that $\omega_x \ll \omega_y = \omega_z$; this corresponds to the case of a cigar-shaped gas. For a given temperature, $\zeta_x \gg \zeta_y = \zeta_z$ so it is justified to first carry out the approximation on the discrete sum first for the x direction then for the y and z directions. The outcome of this calculation is that for a given atom number, as the temperature is lowered, the population of the $j_y = 0$, $j_z = 0$ becomes first macroscopically occupied (independent of the quantum number j_z); then the population of the true ground state $j_x = 0$, $j_y = 0$, $j_z = 0$ becomes macroscopically occupied, which is a two-step condensation.

In the following we will focus on the case of a tight vertical harmonic confinement and a box-like in-plane confinement. In this case, the in-plane sums are first replaced by integrals, because the thermodynamic condition $\beta\left(\varepsilon_{j_1+1} - \varepsilon_{j_1}\right) \to 0$ is more easily respected. Then, as the remaining sum is turned into an integral, we will see that there will be an accumulation of particle in the ground state of the harmonic oscillator, though not in the overall ground state of the gas: this is the phenomenon called transverse condensation.

1.2 DIMENSIONAL CROSSOVER FROM TWO TO THREE DIMENSIONS

1.2.1 *Experimental realization of a 2D Bose gas*

In the previous subsection, we stressed the difference of behaviour between 2D and 3D Bose gases with respect to Bose-Einstein condensation. Experimental investigation of the specificities of the 2D regime has attracted a lot of interest after the production of Bose-Einstein condensates in dilute atomic gases [44, 45, 80, 86–89]. In order to perform these experiments, a gas of bosonic atoms is trapped with a strong confinement in one direction and with a weak confinement in the two other directions of space. The state of an atom in the weak confinement is characterized by the two quantum numbers j_x and j_y. Weak harmonic confinement has traditionally been used for early studies of the properties of 2D Bose gases. One of the realizations of this thesis work has been to implement box-like confinement for this weak confinement [82, 90]. The strong confinement is usually provided by a harmonic trap of frequency ω_z; the state of an atom is then characterized by an integer j_z. With these two confinements, the gas is said to be motionally 2D if

- the motion along the tightly confined direction is frozen, allowing only for $j_z = 0$; for a harmonic confinement of frequency ω_z, this means that the relevant energy scales of the gas are small compared to the typical energy spacing between two levels of the harmonic oscillator. In the case of a thermal, non-interacting gas, this reads $k_B T \ll \hbar\omega_z$, i. e. $\zeta \ll 1$.
- the two remaining weakly confined directions are allowing many significant values for j_x and j_y.

The first condition ensures that the number of atoms in the $j_z = 0$ states $N_{j_z=0}$ is much higher than those in the $j_z > 0$ states, i. e. that $N_{j_z=0}/N \gg 1$. However,

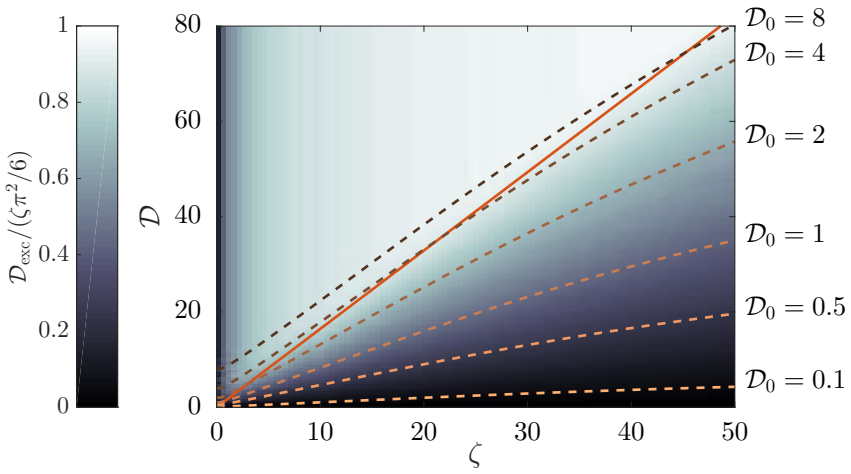

Figure 1.1: Phase-space density of the excited states $\mathcal{D}_{\rm exc}$ renormalized by its maximum value $\mathcal{D}_{\rm c} = \frac{\pi^2}{6}\zeta$ as a function of total phase-space density $\mathcal{D}$ and of the ratio $\zeta = k_{\rm B}T/(\hbar\omega_z)$. The computation is the sum of the 500 first terms in equation 1.28. The red solid line represents the $\mathcal{D} = \mathcal{D}_{\rm c}$ line. For total phase-space densities higher than $\mathcal{D}_{\rm c}$, the population of the excited states saturates. The dotted lines represent values of $(\zeta, \mathcal{D})$ such that $\mathcal{D}_0 =$ constant.

the condition $\zeta \ll 1$ is not necessary as we will see in subsection 1.2.2. We will focus on the case where the confinement in the xy plane is provided by a box potential of characteristic size L and show that a macroscopic occupation of the $j_z = 0$ states can appear even if $\zeta > 1$.

1.2.2 *Transverse condensation*

According to the previous subsection, having a box potential in two directions and a harmonic confinement for the last direction yields $d = 3$ and $d_1 = 1$ so $\alpha = 2$: the gas should undergo a Bose-Einstein condensation transition. However, as stressed in the case of a three-dimensional harmonic oscillator in [83], this line of reasoning is not always valid since the approximations of the d sums by integrals have to be performed successively. In our case, we have $L \gg a_{\rm ho}$ such that the continuum limit for the sum has to be taken first for the x and y directions, then in the z direction according to the conditions which were derived in section 1.1.1.1 and 1.1.1.2 for a given temperature. Thus the atom number reads:

$$N = \sum_{\boldsymbol{j}} \frac{1}{z^{-1}e^{\beta\varepsilon_{\boldsymbol{j}}} - 1} \tag{1.25}$$

$$= \sum_{j_z} \sum_{j_x, j_y} \frac{1}{z^{-1}e^{\beta\varepsilon_{\boldsymbol{j}}} - 1} \tag{1.26}$$

$$= -\sum_{j_z} \frac{L^2}{\lambda_{\rm dB}^2} \ln\left(1 - ze^{-j_z/\zeta}\right) \tag{1.27}$$

and the 2D phase-space density reads:

$$\mathcal{D} = -\sum_{j_z} \ln\left(1 - ze^{-j_z/\zeta}\right) = \sum_{j_z} \mathcal{D}_{j_z} \tag{1.28}$$

where $\mathcal{D}_{j_z}$ is the 2D phase-space density associated with the atoms in the j_zth state of the harmonic oscillator:

$$\mathcal{D}_{j_z} = \frac{\lambda_{\mathrm{dB}}^2}{L^2} \sum_{j_x, j_y} \frac{1}{z^{-1}e^{\beta\varepsilon_j} - 1} \tag{1.29}$$

As explained in the previous section, even if only the $j_z = 0$ states are considered and for a given atom density and temperature, a value of $z < 1$ such that

$$n^{(2\mathrm{D})}\lambda_{\mathrm{dB}}^2 = \ln(1 - z) \tag{1.30}$$

always exists. When trying to compute the total phase-space density for a given fugacity, we turn the discrete sum of equation 1.29 into an integral

$$\mathcal{D} \simeq -\int \ln\left(1 - ze^{-j/\zeta}\right) \mathrm{d}j = \zeta g_2(z) \tag{1.31}$$

As in the derivation of Bose-Einstein condensation, the value of the phase-space density is apparently bounded due to the convergence $g_2(z) \to \pi^2/6$ as $z \to 1$. This is due to the fact that the phase-space density in the $j_z = 0$ states, $\mathcal{D}_0$, is not well accounted for. Hence we define a critical phase-space density

$$\mathcal{D}_{\mathrm{c}} = \frac{\pi^2}{6}\zeta \tag{1.32}$$

and write the total phase-space density as

$$\mathcal{D} = \mathcal{D}_0 + \mathcal{D}_{\mathrm{exc}} \tag{1.33}$$

The value of $\mathcal{D}_0$, $\mathcal{D}_{\mathrm{exc}}$ and z are determined from the value of $\mathcal{D}$ according to:

$$\mathcal{D}_{\mathrm{exc}} = \sum_{j_z \geqslant 1} \mathcal{D}_{j_z} \simeq \begin{cases} \zeta g_2(z) & \text{and } \mathcal{D}_0 = 0 \text{ if } \mathcal{D} < \mathcal{D}_{\mathrm{c}} \\ \mathcal{D}_{\mathrm{c}} & \text{and } z = 1 \text{ if } \mathcal{D} > \mathcal{D}_{\mathrm{c}} \end{cases} \tag{1.34}$$

The occupation of the $j_z = 0$ state thus becomes macroscopic as soon as $\mathcal{D} > \mathcal{D}_{\mathrm{c}}$, which does not require $\zeta \ll 1$. This can be considered as a phase transition: if we call $x = \mathcal{D}/\mathcal{D}_{\mathrm{c}}$ and $x_0 = \mathcal{D}_0/\mathcal{D}_{\mathrm{c}}$, we have

$$x_0 = 0 \text{ if } x < 1, \quad x_0 = x - 1 \text{ if } x \geqslant 1 \tag{1.35}$$

We call this accumulation of atoms in the lowest energy state of the vertical degree of freedom transverse condensation. It is physically relevant for our experimental situation because it describes the fact that, owing bosonic amplification, the occupation of the ground state of the z axis harmonic oscillator becomes dominant even if the vertical degree of freedom is not frozen in the sense that $\zeta \ll 1$. This can be seen in figure 1.1 and 1.2. In figure 1.1 and 1.2(a) we see that $\mathcal{D}_{\mathrm{exc}}$ saturates as $\mathcal{D}$ approaches $\mathcal{D}_{\mathrm{c}}$. Actually, the expression 1.32 is

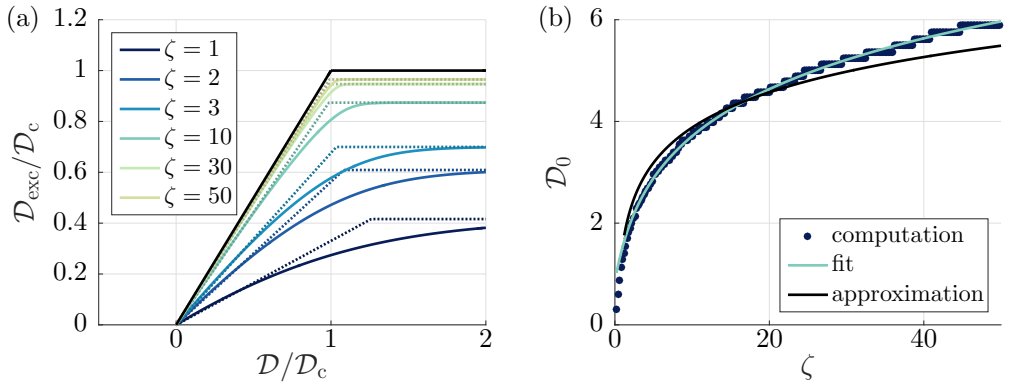

Figure 1.2: (a) Renormalized phase-space density in the excited states as a function of the renormalized total phase-space density. Solid colour lines represent different values of ζ; the saturation of $\mathcal{D}_{\mathrm{exc}}$ is seen for all curves. The solid black curve represents the thermodynamic limit with $\zeta \to \infty$. The dotted lines represent the concatenation of two linear fits, one fitting the initial slope and the other fitting the final asymptote. The intersection of the two fits gives the critical phase-space density for a given ζ, with $\mathcal{D}_{\mathrm{c}}(\zeta)/\zeta \to \pi^2/6$ as $\zeta \to \infty$. (b) Phase-space density in the $j_z = 0$ states computed at $\mathcal{D}_{\mathrm{c}}(\zeta)$ (dark blue dots, see text for the derivation). The light blue solid line is a fit of the data with $\zeta \mapsto \ln(1+\zeta)^p + c$. The values of the fitted parameters are (with a 95% confidence bound) $p = 1.093 \pm 0.003$ and $c = 1.00 \pm 0.01$. The black solid line represents the estimate of equation 1.39.

only valid when replacing a discrete sum by an integral, that is when $\zeta \to \infty$. More accurate values of $\mathcal{D}_{\mathrm{c}}(\zeta)$ are computed in figure 1.2(a).

Note that the line of reasoning of section 1.1.2 would give $\alpha = 2$, meaning that a gas in a 2D box and a one dimensional harmonic oscillator in the remaining direction can undergo Bose-Einstein condensation if the thermodynamic limit can be taken for all directions. Here, the fact that the integrals were first taken for the box directions leads to an accumulation of the atoms in the $j_z = 0$ states and not in the overall ground state of the system.

In order to study the properties of the 2D Bose gas, we want to know what is the value of $\mathcal{D}_0$ at the critical point. Indeed, when $\zeta \to \infty$, $\mathcal{D}_0/\mathcal{D} = 0$ for $\mathcal{D} < \mathcal{D}_{\mathrm{c}}$ but at finite ζ, the value of $\mathcal{D}_0$ at $\mathcal{D}_{\mathrm{c}}$ is not necessarily 0. The value of $\mathcal{D}_0$ at the critical total phase-space densities $\mathcal{D}_{\mathrm{c}}(\zeta)$ is shown on figure 1.2(b). For a given value of ζ, the fugacity z is varied until the correponding total phase-space density $\mathcal{D}$ reaches its critical value $\mathcal{D}_{\mathrm{c}}(\zeta) = \zeta\pi^2/6$ for $z = z_{\mathrm{c}}$. The phase-space density corresponding to the atoms in the $j_z = 0$ states is then recorded as $\mathcal{D}_{0,\mathrm{c}}$. It is well approximated by the following formula:

$$\mathcal{D}_{0,\mathrm{c}} \simeq \ln(1+\zeta)^{1.1} + 1.0 \tag{1.36}$$

This value can also be evaluated analytically. From equation 1.28, we obtain

$$\mathcal{D} = \sum_{n=1}^{\infty} \frac{z^n}{n} \frac{1}{1-e^{-n/\zeta}} = \sum_{n=1}^{\infty} \alpha_n z^n \tag{1.37}$$

If $n \ll \zeta$, then $\alpha_n \simeq \zeta/n^2$. If $n \gg \zeta$, then $\alpha_n \simeq 1/n$. Thus we can approximately write

$$\mathcal{D} \simeq \zeta \sum_{n=1}^{\zeta} \frac{z^n}{n^2} + \sum_{n=\zeta+1}^{\infty} \frac{z^n}{n} = \zeta \sum_{n=1}^{\zeta} \frac{z^n}{n^2} + \mathcal{D}_0 - \sum_{n=1}^{\zeta} \frac{z^n}{n} \tag{1.38}$$

If $z \to 1$ and $\mathcal{D}$ takes the critical value $\mathcal{D}_c = \zeta\pi^2/6$

$$\mathcal{D}_0 \simeq \zeta \sum_{n=\zeta+1}^{\infty} \frac{z^n}{n^2} + \sum_{n=1}^{\zeta} \frac{z^n}{n} \simeq \ln\zeta + 1 + \gamma \tag{1.39}$$

where $\gamma \simeq 0.577$ is the Euler-Mascheroni constant. This approximated value of the phase-space density at the transition point is shown in black solid line in figure 1.2(b). This means that close to the transition point, the phase-space density associated to the atoms in the $j_z = 0$ states is logarithmically large at large values of ζ.

1.2.3 *Coherence length at the transverse condensation point*

In order to characterize the behaviour of a gas of atoms, it is interesting to look into its coherence length. Let us consider the value of the wavefunction of one atom at two points with a distance r. This lengthscale, ℓ_c, distinguishes the distances for which the values of the wavefunction are correlated ($r < \ell_c$) and the distances for which the values of the wavefunction are uncorrelated ($r > \ell_c$). This length scale is computed by finding the typical length scale over which the one-body correlation G_1 decreases. This correlation function is defined as [91]

$$G_1(\boldsymbol{r}) = \left\langle \hat{\psi}^\dagger(\boldsymbol{r})\hat{\psi}(\boldsymbol{0}) \right\rangle \tag{1.40}$$

where $\hat{\psi}^\dagger(\boldsymbol{r})$ is the operator that creates a particle at the position $\boldsymbol{r}$. It can equivalently be defined as the Fourier transform of the occupation in reciprocal space (that is for the momentum distribution)

$$G_1(\boldsymbol{r}) = \sum_{\boldsymbol{k}} \left\langle \hat{\psi}^\dagger(\boldsymbol{k})\hat{\psi}(\boldsymbol{k}) \right\rangle e^{i\boldsymbol{k}\cdot\boldsymbol{r}} \tag{1.41}$$

In the case of transverse condensation, we will be interested in the first-order correlation function at $z = 0$, where z is the direction of the harmonic confinement. This function is the sum of all the correlation functions corresponding to each state of the strongly confining harmonic oscillator j_z

$$\begin{aligned} G_1(\boldsymbol{r}) &= \sum_{j_z} G_{1,j_z}(\boldsymbol{r}) && (1.42)\\ &= \frac{1}{4\pi^2 a_{\mathrm{ho}}} \sum_{j_z} \left|\chi_{j_z}(0)\right|^2 \int n_{\boldsymbol{k},j_z} e^{i\boldsymbol{k}\cdot\boldsymbol{r}} \mathrm{d}^2k && (1.43)\\ &= \frac{1}{4\pi^2 a_{\mathrm{ho}}} \sum_{j_z} \left|\chi_{j_z}(0)\right|^2 \int \frac{e^{i\boldsymbol{k}\cdot\boldsymbol{r}}}{z^{-1}e^{j_z/\zeta} e^{\lambda_{\mathrm{dB}}^2 k^2/4\pi} - 1} \mathrm{d}^2k && (1.44) \end{aligned}$$

using the solutions of the harmonic oscillator of equation 1.16.

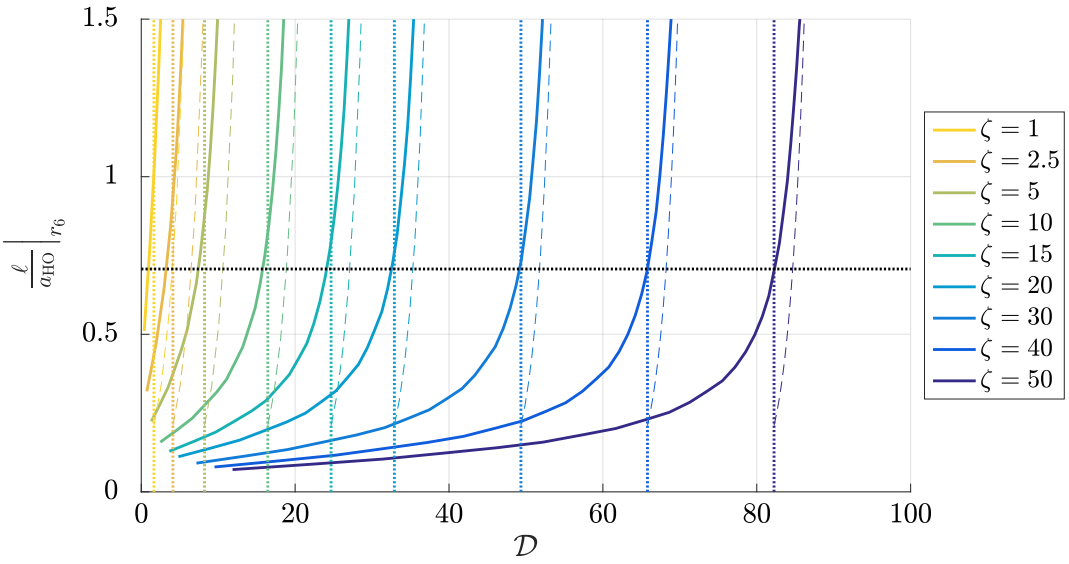

Figure 1.3: Coherence length in units of the harmonic oscillator length computed from equation 1.50 for $\zeta = 1$, 2.5, 5, 10, 15, 20, 30, 40, 50 (from yellow to dark blue) as the total phase-space density is increased. The horizontal black dotted line represents the value of ℓ at the transition point according to equation 1.48. The vertical dotted lines represent the phase-space density at which the transverse condensation should appear. The equality of equation 1.48 is fulfilled at large ζ. The dashed lines represent the limit of equation 1.49.

In the case of a weakly degenerated gas ($z \ll 1$):

$$G_1(\boldsymbol{r}) = \frac{1}{4\pi^2 a_{\mathrm{ho}}} \left(\sum_{j_z} \left|\chi_{j_z}(0)\right|^2 z\, e^{-j_z/\zeta} \right) e^{-\pi r^2/\lambda_{\mathrm{dB}}^2} \tag{1.45}$$

The first order correlation function is thus a Gaussian with a typical length scale of $\lambda_{\mathrm{dB}}/\sqrt{\pi}$, giving the value of $\ell_c \simeq \lambda_{\mathrm{dB}}/\sqrt{\pi}$ in the weakly degenerate regime (using the length at which the correlation function has been decreased by a factor $1/e$). Note that due to the rotational symmetry of the system G_1 depends only on r.

In the case of a strongly degenerated gas, i. e. $z \simeq 1$, the first order correlation function at large r function will be a sum of exponentials [79]

$$G_{1,j_z}(r) \propto \exp\left(-r/\ell_{j_z}\right), \qquad \text{with} \quad \ell_{j_z} = \frac{\lambda_{\mathrm{dB}}}{\sqrt{4\pi}} \exp\left(\mathcal{D}_{j_z}/2\right) \tag{1.46}$$

The dominant contribution of the sum is that of the $j_z = 0$ state, such that

$$\ell_c \simeq \ell_0 = \frac{\lambda_{\mathrm{dB}}}{\sqrt{4\pi}} \exp\left(\mathcal{D}_0/2\right) = \frac{\lambda_{\mathrm{dB}}}{\sqrt{4\pi(1-z)}} \tag{1.47}$$

derived in the $z \simeq 1$ case, but which is also a good approximation in the weakly degenerate regime $z \ll 1$.

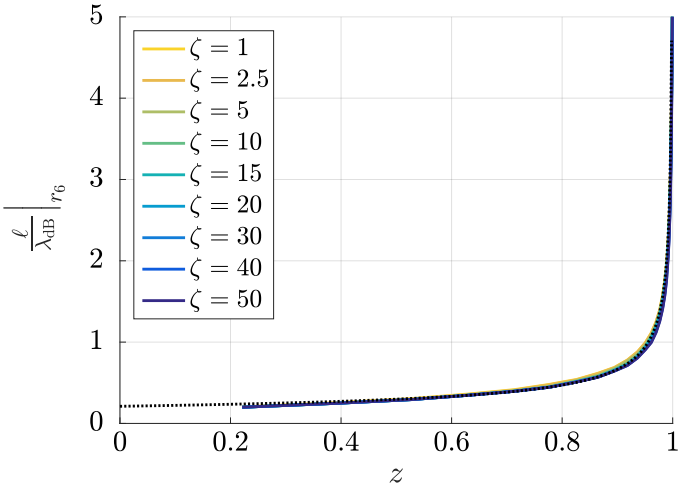

Figure 1.4: Coherence length in units of the thermal wave length computed from equation 1.50 for $\zeta = 1$, 2.5, 5, 10, 15, 20, 30, 40, 50 (from yellow to dark blue) as the fugacity $z = e^{\beta\mu}$ is varied. The dotted black line represent the estimate of equation 1.47 renormalized by $1/\sqrt{\ln 6}$ to account for the fact that ℓ was computed at r_6. All the data collapses onto the same curve, showing the validity of equation 1.47 over a broad range of fugacities.

At the transverse condensation point, $\mathcal{D}_0 \sim \ln \zeta$ such that

$$\ell_{\mathrm{c}} \simeq \frac{a_{\mathrm{ho}}}{\sqrt{2}} \tag{1.48}$$

In the regime where $\mathcal{D} > \mathcal{D}_{\mathrm{c}}$,

$$\ell_c \simeq \frac{\lambda_{\mathrm{dB}}}{\sqrt{4\pi}} \exp\left[\left(\mathcal{D} - \mathcal{D}_{\mathrm{c}}\right)/2\right] \tag{1.49}$$

We numerically check these equations by computing an estimate of the correlation length. We determine the distance r_6 such that the value of G_1 is divided by 6 with respect to its value at $r = 0$ (there is no strong constraint on the choice of the factor of 6, which can be picked according to the ease of its computation). We define the length ℓ as

$$\frac{1}{\ell} = -\left.\frac{\mathrm{d}\ln\left[G_1(r)\right]}{\mathrm{d}r}\right|_{r=r_6} \tag{1.50}$$

and compare it to the previous formulas in figures 1.3 and 1.4.

As shown both by the numerical simulation and by the calculation, the in-plane coherence length increases as the degeneracy increases, but it does not diverge at the transverse condensation point. Rather, its value is bounded by the natural length scale of the vertical harmonic oscillator. It is remarkable that the in-plane coherence properties are controlled by the typical length scale in the vertical direction. This is a consequence of the dimensional crossover that happens at the transverse condensation point. The fact that the atoms in the $j_z = 0$ states become dominant indicates that the chemical potential is on the order of $-\hbar\omega_z$, which is also the quantity that determines the in-plane coherence properties.

1.3 BEHAVIOUR OF A 2D PLANE OF ATOMS

In section 1.2, we have seen that in order to have macroscopic occupation of the ground state of the harmonic oscillator in the vertical direction, we can either rely on having the chemical potential and temperature smaller than the typical energy scale set by the harmonic oscillator μ, $k_B T < \hbar\omega_z$ or, if $\zeta = k_B T/\hbar\omega_z > 1$, on having a total phase-space density which is high enough such that the phenomenon of transverse condensation takes place, leading to a macroscopic occupation of the ground state of the harmonic oscillator as soon as $\mathcal{D} > \mathcal{D}_c = \zeta\pi^2/6$. In the former case, the phase-space density associated to the atoms in the ground state of the harmonic oscillator $\mathcal{D}_0$ can take any value. In the latter case, as soon as $\mathcal{D} > \mathcal{D}_c$, i.e. $\mathcal{D}_0/\mathcal{D} > 0$, the phase-space density associated to the atoms in the ground state of the harmonic oscillator takes a non zero value

$$\mathcal{D}_0 \simeq \mathcal{D}_{0,c} + (\mathcal{D} - \mathcal{D}_c) \tag{1.51}$$

where $\mathcal{D}_{0,c}$ is given by equation 1.36 or 1.39. In the experiments described in [82], we will investigate the coherence properties of the atoms confined in the $j_z = 0$ states. These coherence properties depend on the degree of degeneracy of the atoms with that quantum number: they depend on the phase-space density $\mathcal{D}_0$. This section is therefore dedicated to describing the properties of a 2D Bose gas as its phase-space density $\mathcal{D}_0$ is varied, in the interacting and non-interacting case.

1.3.1 *Non-interacting Bose gas*

The behaviour of a non-interacting Bose gas in 2D can be deduced from the calculation of the previous section by restricting the sums to the $j_z = 0$ states.

Using the expression of the one-body correlation function defined in section 1.2.3, we find that for a non-degenerate gas with $z \ll 1$, the correlations are Gaussian with a characteristic length scale $\lambda_{dB}/\sqrt{2\pi}$, which corresponds to low phase-space densities.

Then, the behaviour of the one-body correlation function changes as the value of the fugacity is increased; while it remains Gaussian at short distances, it becomes exponential at large distances (compared to λ_{dB}) with a correlation length given by

$$\ell_c \simeq \frac{\lambda_{dB}}{\sqrt{4\pi}} e^{\mathcal{D}_0/2} \tag{1.52}$$

This regime becomes relevant when $\ell_c \gtrsim \lambda_{dB}$, that is for a phase-space density $\mathcal{D}_0 \gtrsim 1$. According to the Mermin-Wagner theorem, here in a case with no interactions, there is no long-range order in the 2D Bose gas since $G_1(r) \to 0$ as $r \to \infty$. However, as the phase-space density is increased, the typical length over which the correlations decay increases exponentially.

This exponential increase of the coherence length is important in the experimental situations which deal with finite systems. There, the gas is constrained to a box of size L. As soon as the correlation length reaches the size of the

sample, the one body correlation function takes a finite value for all available distances in the cloud

$$\forall r \leqslant \sqrt{2}L, \quad G_1(r) \geqslant C > 0 \tag{1.53}$$

which corresponds to the appearance of a Bose-Einstein condensate [92] at a phase-space density of

$$\mathcal{D}_{0,\mathrm{BEC}} \propto \ln\left(4\pi\frac{L^2}{\lambda_{\mathrm{dB}}^2}\right) \tag{1.54}$$

A detailed calculation for the phase-space density at which a Bose-Einstein condensate appears for a square and disk box is found in [93]. For the range of values that can be taken by L/λ_{dB} in the relevant experimental range that will be presented in [82], the phase-space density at which full Bose-Einstein condensation is reached is on the order of $\mathcal{D}_{0,\mathrm{BEC}} = 8$ to 10.

In the case of a gas trapped in a 2D box and in a harmonic potential along the third direction, transverse condensation will happen before Bose-Einstein condensation if

$$\mathcal{D}_{0,\mathrm{c}} \sim \ln\zeta < \mathcal{D}_{0,\mathrm{BEC}} \approx \ln\left(4\pi\frac{L^2}{\lambda_{\mathrm{dB}}^2}\right) \tag{1.55}$$

i. e. if

$$\frac{2L^2}{a_{\mathrm{ho}}^2} > 1 \tag{1.56}$$

meaning that the box containing the gas has to be flat.

1.3.2 *The interacting 2D Bose gas*

So far, we have only considered Bose gases without interactions, where the phase transitions are driven by the bosonic statistics. However, degenerate gases of ultra cold atoms do interact. At low enough temperatures, the interactions can be characterized by a contact potential in three dimensions [94]:

$$V(\boldsymbol{r}_i - \boldsymbol{r}_j) = \frac{4\pi\hbar^2}{M} a_{\mathrm{sc}} \delta(\boldsymbol{r}_i - \boldsymbol{r}_j) \tag{1.57}$$

where M is the mass of the particles and a_{sc} is the scattering length which is the only parameter needed to describe low-energy collisions. For rubidium 87, $a_{\mathrm{sc}} = 5.3\,\mathrm{nm}$ [95]. The simplicity of the expression of the interactions in three dimensions comes from the fact that the scattering amplitude $f_{3\mathrm{D}}(\boldsymbol{k})$ characterizing the scattering state for two particles with relative wave vector $\boldsymbol{k}$ tends towards a constant for low-energy collisions

$$f_{3\mathrm{D}}(k) \xrightarrow[k\to 0]{} a_{\mathrm{sc}} \tag{1.58}$$

When treating the scattering problem in a 2D geometry, this last equation does not hold anymore in the general case [96, 97]; the scattering amplitude $f_{2\mathrm{D}}$ keeps a dependence in k at small wave vectors. However, the experiments that were achieved so far with ultra cold atoms never entered the collisional 2D

regime for which $a_{\mathrm{ho}} \ll R_s$, where R_s is the range of the scattering potential, on the order of a_{sc} for rubidium 87. They were done in the regime where $a_{\mathrm{ho}} \gg R_s$, meaning that although the motion along the vertical direction is frozen, the collisions can still be treated as almost three-dimensional. In fact, in that case, the momentum-dependence of the scattering amplitude is logarithmically weak, and for the range of momenta relevant to the experiment, the scattering amplitude can be approximated by a dimensionless number:

$$f_{\mathrm{2D}}(k) \simeq \sqrt{8\pi}\frac{a_{\mathrm{sc}}}{a_{\mathrm{ho}}} = \tilde{g} \tag{1.59}$$

Degenerate, quasi-2D Bose gases have been realized experimentally with values of $\tilde{g}$ ranging from 0.01 to 3 [44, 45, 80, 86–89].

If we consider the 2D density of the gas $n^{(\mathrm{2D})}(\boldsymbol{r})$ as a classical function, the interaction energy of the gas can then be written as

$$E_{\mathrm{int}} = \frac{\hbar^2}{2M}\tilde{g}\int \left[n^{(\mathrm{2D})}(\boldsymbol{r})\right]^2 \mathrm{d}^2 r \tag{1.60}$$

We will now briefly describe the behaviour of the equilibrium interacting 2D gas; this is most conveniently done by finding the equation of state of the system — that is the relation between $\mathcal{D}_0$ and $\mu/k_{\mathrm{B}}T$. Beyond the two limits that are discussed below, both numerical calculations and experimental studies have been performed [80, 88, 98, 99]. Building on density measurements performed in a 2D harmonic trap, an experimental, fit-free determination of the equation of state of the 2D Bose gas has been realized as can be seen in Appendix A.

Weakly degenerate regime

In the non-interacting regime, the equation of state is given by the relation

$$\mathcal{D}_0 = -\ln\left(1 - e^{\mu/k_{\mathrm{B}}T}\right) \tag{1.61}$$

In order to know the modification of this equation of state with interactions, the mean-field Hartree-Fock approximation is used [29, 78]. If the gas is weakly degenerate, a trial many-body wave function where all single-particle states factorize can be used to minimize the total energy of the system. The result of this minimization is that the chemical potential is replaced by $\mu - 2\tilde{g}\hbar^2 n^{(\mathrm{2D})}/M$ (where $n^{(\mathrm{2D})}$ is the 2D atomic density) in the previous equation:

$$\mathcal{D}_0 = -\ln\left(1 - e^{\mu/k_{\mathrm{B}}T - \tilde{g}\mathcal{D}_0/\pi}\right) \tag{1.62}$$

This self-consistent equation can be solved for any value of μ.

Strongly degenerate regime

As the phase-space density of the gas is increased, it is possible to show by a Bogoliubov analysis that the density fluctuations are reduced. The mean-field value for the interaction energy of N atoms then yields:

$$E_{\mathrm{int}}^{\mathrm{MF}} = \frac{\hbar^2}{2M}\tilde{g}\frac{N^2}{L^2} \tag{1.63}$$

and the gas can be described locally by a complex field obeying the Gross-Pitaevskii equation. In this regime, the Thomas-Fermi approximation will be used, which neglects the kinetic energy to get

$$\mathcal{D}_0 \simeq \frac{2\pi}{\tilde{g}} \frac{\mu}{k_B T} \tag{1.64}$$

1.3.3 *Superfluid regime: Berezinskii-Kosterlitz-Thouless transition versus Bose-Einstein condensation*

In a finite-size 2D system, according to equation 1.54, a Bose-Einstein condensate appears for high enough phase-space densities. In an interacting, Bose-Einstein condensed system, the analysis of the excitations using Bogoliubov techniques leads to the conclusion that there exist sound waves with a linear dispersion relation $\omega = c_s k$ (c_s is the sound velocity). According to Landau's criterion, this means that the gas is superfluid, that is that a point-like impurity can move in the gas without creating any excitations in a frictionless manner [29, 78]. This "flow without friction" exists as long as the speed of the impurity is below a critical value given by c_s.

For an infinite 2D gas with local interactions, the Mermin-Wagner theorem states that there cannot be any long-range order: Bose-Einstein condensation is not allowed for an infinite system. However, this does not necessarily prevent a superfluid behaviour to exist. Some local coherence exists in a 2D gas: it can thus be described by a complex field. As mentioned in the previous paragraph, the amplitude fluctuations of this field are reduced because of repulsive interaction, while the phase fluctuations still exist. The question which arises then is whether this system exhibits phase rigidity or, equivalently, a superfluid behaviour.

The answer was provided in the case of zero amplitude fluctuations by Berezinskii, Kosterlitz and Thouless [84, 85]: at high temperature, the existence of free vortices, that is of phase defects where the phase winds around a point by an integer multiple of 2π, prevents phase rigidity to appear and leads to vanishingly small correlation lengths. At low temperatures, those vortices only exist in tightly bound pairs, and they have little influence on the coherence properties of the gas. The coherence in this cold regime is only determined by phonons, which leads to an algebraic decay of the correlations and to the appearance of superfluidity. This change represent an infinite-order phase transition (all thermodynamic quantities and derivatives are smooth), the BKT transition.

This reasoning has been adapted to the case of quasi-2D ultra cold atoms [79] and numerical simulations have been performed by Prokof'ev and Svistunov [98, 99]. For weakly interacting gases, this transition happens at the critical point

$$\mathcal{D}_{0,\mathrm{BKT}} = \ln\left(\frac{380(3)}{\tilde{g}}\right) \tag{1.65}$$

$$(\mu/k_B T)_{\mathrm{BKT}} = \frac{\tilde{g}}{\pi} \ln\left(\frac{13.2(4)}{\tilde{g}}\right) \tag{1.66}$$

The superfluid behaviour of a 2D gas has been demonstrated experimentally and the critical parameters were shown to be consistent with the simulated values [89, 100]. With a value for $\tilde{g}$ ranging from 0.01 to 0.1, the critical phase-space density at which the BKT transition happens ranges from 8 to 10.

In finite-size, interacting gases, Bose-Einstein condensation and the BKT transition can take place. For experimental parameters which will be relevant for the following chapters, the phase-space densities at which they happen are approximately the same, meaning that it is difficult to distinguish between the two.

1.4 CONCLUSION

As the temperature of a Bose gas is decreased, depending on its dimension and trapping geometry, it can undergo a Bose-Einstein condensation at the thermodynamic limit where a macroscopic fraction of the atoms occupies the overall ground state of the system. This is the case for a three-dimension harmonically trapped or free gas or for a two-dimensional harmonically trapped gas, but not for a two-dimension free gas.

However, if the thermodynamic limit cannot be taken at the same time for all degrees of freedom, a mixed situation can appear. This is the case for a gas which is free in two directions and harmonically confined in the third direction. There, as the degeneracy of the gas is increased, the lowest state of the harmonic oscillator becomes macroscopically occupied (while excitations in the two other directions still exist): this phenomenon is called transverse condensation.

At the thermodynamic limit (i. e. as $\zeta = k_B T/\hbar\omega_z \to \infty$), as the transition point, given for a total 2D phase-space density $\mathcal{D}$ of $\pi^2\zeta/6$, is approached, the correlation length increases to reach its critical value of $a_{ho}/\sqrt{2}$ and the phase-space density associated to the atoms in the ground state of the harmonic oscillator becomes on the order of $\ln\zeta + 1.6$. Beyond the transition point, a large fraction of the atoms accumulate in the ground state of the harmonic oscillator, allowing to study the properties of a motionaly 2D Bose gas. This technique is complementary to the regime one usually tends to reach to obtain quasi-2D Bose gases, which consists in ensuring that the energy spacing between two levels of the harmonic oscillator is much larger than all the other energy scales, i. e. $\zeta \to 0$.

As soon as the gas can be considered in the quasi-2D regime, the specificities of low dimensional physics can be studied. In two dimensions, three regimes can be distinguished: (i) at low degeneracies, i. e. $\mathcal{D}_0 \ll 1$ the gas is in the normal phase with correlations decaying exponentially fast on length scales $\ell \sim \lambda_{dB}$; (ii) at phase-space densities on the order of 1, the gas enters the presuperfluid regime where the length scale over which the correlations exponentially decay becomes larger $\ell \gg \lambda_{dB}$, that is the decay is slower than in the normal phase. With the presence of interactions, in this regime, density fluctuations start to be reduced. (iii) Last, in the presence of interactions, the gas undergoes a normal-to-superfluid transition. If finite-size effects are important, this transition will be the Bose-Einstein condensation. If the box in which the 2D gas is constrained is arbitrarily large, the transition leading to a superfluid behaviour will be the Berezinskii-Kosterlitz-Thouless transition, where

phase fluctuations, though large enough to destroy long-range order, are sufficiently small to allow for local phase rigidity, that is a superfluid behaviour. For typical experimental parameters, these two transitions will appear when the phase-space density is on the order of 8 to 10.

2 THE KIBBLE-ZUREK MECHANISM

Thanks to the development of many theoretical and experimental tools, the physics of phase transitions is now well understood [101]. It is very interesting in many aspects:

- A continuous change of parameters leads to a discontinuous or non-analytic change in the state of the system. In a second order phase transition, the system goes from a disordered phase where its states respect the symmetries of the underlying Hamiltonian to an ordered phase which breaks one of the symmetries of the Hamiltonian as a parameter — for instance temperature — is varied. The ordered phase is characterized by an order parameter which becomes non-zero as the transition point is crossed.
- The ordered phase can exhibit interesting properties (such as magnetization or superconductivity).
- The behaviour of the properties of a system close to the phase transition point (correlation length, amplitude of the order parameter, etc.) falls into a small number of well-identified universality classes, depending only on general parameters. The properties of the system close to the transition point are therefore independent of its microscopic details.

These aspects have been extensively studied, in particular using the scaling assumption and the renormalization group technique for second-order phase transitions [102, 103]. The variation of many quantities close to the transition point can often be described by power laws, and the set of critical exponents that characterizes those variations defines the universality class of a system.

Dynamic properties, i. e. the properties of excitations, have also been studied close to transition points [104]. There, some dynamical processes become slower and slower: this is called critical slowing down, and has also received a lot of attention in the frame of the theory of dynamical critical phenomena [101, 105]. Critical slowing down is characterized by the dynamic critical exponent z.

The experimental determination of critical exponents has been a long-standing effort in a variety of systems [102] and usually requires that the system is at equilibrium.

In this context, a mechanism brought forward by Kibble first in the cosmological context [106] and then extended by Zurek to condensed matter systems [107] can help measuring some critical exponents by studying a non-equilibrium situation. The Kibble-Zurek mechanism describes a quench cooling of the system through a phase transition point; this represents an out-of-equilibrium situation. Due to the critical slowing down of the dynamics,

the system cannot follow adiabatically the thermal equilibrium state associated with the time-varying temperature. As a result, defects appear, whose scaling with the temperature quench slope is predicted to depend only on equilibrium critical exponents.

In this chapter, I will first describe the relevant critical exponents which are used for the derivation of the Kibble-Zurek scaling, looking into static and dynamics of phase transitions. Some systems will be particularly relevant to the experimental study of chapter 3:

- The mean-field model, which helps to illustrate the concepts of critical and dynamical scaling.
- The ideal Bose gas close to the BEC transition.
- The ideal Bose gas close to the transverse condensation as described in chapter 1.
- The 3D-XY model, which describes the properties of interacting Bose gases.

Then, I will briefly state Zurek's argument for the scaling law that governs the density of defects as a function of the temperature quench duration. Last, typical limitations preventing the observation of the Kibble-Zurek scaling will be discussed.

2.1 PHASE TRANSITIONS AND CRITICAL SLOWING DOWN

The aim of this section is to recall the main outcomes of the studies of static and dynamical aspects of second-order phase transitions.

2.1.1 *Static critical exponents*

2.1.1.1 *Definitions*

Let us define the most important static critical exponents. In the following, we will call ε the distance to the transition point. If the temperature T is varied close to the critical value T_c, we define

$$\varepsilon = \frac{T - T_c}{T_c} \tag{2.1}$$

Let $\psi(\boldsymbol{r})$ be the function that characterizes the physical system; it can be a complex field in the case of Bose-Einstein condensation, the complex gap for a superconductor, magnetization, etc.; it can be either a scalar or a vectorial function. We assume that the system is described by its free energy $F[\psi]$[1]. The order parameter is defined as the average value over the thermal fluctuations

1 Actually we need a thermodynamic potential that describes the system and that can be chosen according to the situation (canonical, grand-canonical ensemble, etc.).

(see equation 2.3) of $\psi(\boldsymbol{r})$. At a phase transition, it will increase from zero to finite values. The exponent that characterizes this evolution is β:

$$\langle \psi(\boldsymbol{r}) \rangle = \begin{cases} 0 & \text{if } \varepsilon > 0 \\ A\,|\varepsilon|^{\beta} & \text{if } \varepsilon < 0 \end{cases} \tag{2.2}$$

where A is a proportionality constant and where the average is:

$$\langle \psi(\boldsymbol{r}) \rangle = \frac{\int \mathcal{D}\psi\, \psi(\boldsymbol{r}) \exp\left(-F[\psi]/k_{\mathrm{B}}T\right)}{\int \mathcal{D}\psi\, \exp\left(-F[\psi]/k_{\mathrm{B}}T\right)} \tag{2.3}$$

$$= Z^{-1} \int \mathcal{D}\psi\, \psi(\boldsymbol{r}) \exp\left(-F[\psi]/k_{\mathrm{B}}T\right) \tag{2.4}$$

Here the notation $\int \mathcal{D}\psi$ represents the sum over all possible configurations of ψ and Z is the partition function of the system.

A quantity of interest for us is the correlation function G_1 which describes how much the change of the order parameter in $\boldsymbol{r}$ from its mean value affects its value at position $\boldsymbol{r}'$:

$$G_1(\boldsymbol{r}, \boldsymbol{r}') = \left\langle \psi(\boldsymbol{r})\psi(\boldsymbol{r}') \right\rangle - \langle \psi(\boldsymbol{r}) \rangle^2 \tag{2.5}$$

Note that the definition differs from the one provided in chapter 1 (where the mean squared is not removed). With this definition, $G_1(\boldsymbol{r}, \boldsymbol{r}')$ measures the correlation length of perturbations with respect to the value of the order parameter, rather than correlations in the value of the order parameter. According to the theory of scaling of phase transition, at the transition point (i. e. $\varepsilon = 0$), the correlation function decays algebraically

$$G_1(\boldsymbol{r}, \boldsymbol{r}') \sim \left|\boldsymbol{r} - \boldsymbol{r}'\right|^{-d+2-\eta} \tag{2.6}$$

where d is the dimension of $\boldsymbol{r}$ and η is an exponent called "anomalous dimension". Away from the transition (i. e. $\varepsilon \neq 0$), the correlation function has an exponential cut-off at a length ξ

$$G_1(\boldsymbol{r}, \boldsymbol{r}') \sim f(\boldsymbol{r}, \boldsymbol{r}') \exp\left(-\left|\boldsymbol{r} - \boldsymbol{r}'\right| / \xi\right) \tag{2.7}$$

with f an algebraic function.

The length scale ξ is called the correlation length and also depends on ε with a power-law

$$\xi \propto \begin{cases} |\varepsilon|^{-\nu} & \text{if } \varepsilon > 0 \\ |\varepsilon|^{-\nu'} & \text{if } \varepsilon < 0 \end{cases} \tag{2.8}$$

The various exponents which have been defined so far are summed up in Table 2.1.

Many other exponents can be defined [101–103] — though they are not independent. However, they are not relevant for the discussion of the Kibble-Zurek mechanism that will follow.

Quantity	Behaviour	Exponent
$\langle\psi(\boldsymbol{r})\rangle$	$= 0 \quad \text{if } \varepsilon > 0$ $\propto \lvert\varepsilon\rvert^{\beta} \quad \text{if } \varepsilon < 0$	β
$G_1(\boldsymbol{r}, \boldsymbol{r}')$	$\sim \lvert\boldsymbol{r} - \boldsymbol{r}'\rvert^{-d+2-\eta}$ at $\varepsilon = 0$	η
ξ	$\lvert\varepsilon\rvert^{\nu} \quad \text{if } \varepsilon > 0$	$\nu > 0$
	$\lvert\varepsilon\rvert^{\nu'} \quad \text{if } \varepsilon < 0$	$\nu' > 0$

Table 2.1: Definition of the critical exponents

2.1.1.2 *Mean-field approximation*

In this section, we will briefly comment on the mean-field approximation, since it illustrates the concept of scaling. This approximation consists in neglecting the fluctuations.

Though the mean-field description can describe some properties of the thermal or of the ordered phase, its validity breaks down close to the critical point; it is not quantitatively correct very close to a phase transition point in $d = 2$ or $d = 3$, for which more refined analyses based on the renormalization group approach are needed.

Neglecting fluctuations of the order parameter means taking the saddle point approximation in equation 2.3. This consist in approximating the weight function by a Dirac function in ψ_0 such that $F[\psi]$ is minimum for $\psi = \psi_0$ or, since F is a functional in ψ, such that

$$\left.\frac{\delta F}{\delta \psi}\right|_{\psi_0} = 0 \tag{2.9}$$

Thus, $\langle\psi\rangle = \psi_0$.

In order to compute the exponent β in the mean-field picture, one considers the Ginzburg-Landau functional for the free energy:

$$F[\psi] = a\varepsilon\psi^2 + c\psi^4 \tag{2.10}$$

where a and c are posotive constants. It is a free energy for a space-independent field. The first term has an ε dependence which causes a phase transition to happen at $\varepsilon = 0$ (ψ acquires a finite value for $\varepsilon < 0$). The second term, with $c > 0$, ensures that an arbitrarily large value of ψ always has a large energy cost. This gives (see for example [101])

$$\beta = 1/2 \tag{2.11}$$

In order to compute ν the mean-field exponent for the correlation length ξ, let us take the simplest form of free energy that allows for a phase transition and for spatial fluctuations of the order parameter

$$F[\psi] = \int \left[a\varepsilon\,|\psi(\boldsymbol{r})|^2 + b\,|\boldsymbol{\nabla}\psi(\boldsymbol{r})|^2\right] \mathrm{d}^d r \tag{2.12}$$

with a and b two constants. The first term is similar to that of the Ginzburg-Landau free energy 2.10. The second term represents an energy cost for having

large spatial fluctuations. The last term of the Ginzburg-Landau functional is not included. This can be understood by the fact that, close to the transition point, the order parameter is small such that $\psi(\boldsymbol{r})^2 \gg \psi(\boldsymbol{r})^4$. Neglecting this term means that only configurations where $\varepsilon > 0$ (i.e. $T > T_c$) will be considered. For this simple functional, also called the Gaussian model, the critical exponents can be calculated (see for example [101]) and yield

$$\nu = 1/2 \tag{2.13}$$
$$\eta = 0 \tag{2.14}$$

In order to compute the critical exponent ν' which corresponds to the ordered phase, one needs to allow for some spatial fluctuations in equation 2.3 beyond the mean-field approximation. This gives $\nu = \nu' = 1/2$ [103, 108].

2.1.1.3 *Ideal Bose gas*

For the ideal Bose gas approaching the Bose-Einstein condensation transition point [109], the correlation length can be computed (with a method similar to that of Chapter 1, subsection 1.2.3):

$$\xi_{\mathrm{BEC}} = \frac{\lambda_{\mathrm{dB}}}{\sqrt{2\pi\left[-\mu/\left(k_{\mathrm{B}}T\right)\right]}} = \frac{\lambda_{\mathrm{dB}}}{\sqrt{2\pi\alpha}} \tag{2.15}$$

where $\alpha = -\mu\beta$. From the expression of the phase-space density for the ideal Bose gas in three dimensions

$$\mathcal{D}_{\mathrm{BEC}} = g_{3/2}(z) \tag{2.16}$$

one can compute $\mathcal{D}_{\mathrm{BEC}} - \mathcal{D}_{\mathrm{BEC}}^{\mathrm{critical}}$ in two different ways, one using the approximation [109]

$$g_{3/2}\left(e^{-\alpha}\right) \approx g_{3/2}(1) - \left|\Gamma\left(-\frac{1}{2}\right)\right| \alpha^{1/2} \tag{2.17}$$

and the other computing (at fixed density) $n\lambda_{\mathrm{dB}}^3 - n\lambda_{\mathrm{dB,\,critical}}^3$ which yields

$$\alpha \propto \varepsilon^2 \tag{2.18}$$

Hence for the ideal Bose gas

$$\nu = 1 \tag{2.19}$$

2.1.1.4 *Transverse condensation*

In the case of the ideal gas phase transition described in chapter 1, the correlation length does not diverge as the system approaches the transverse condensation transition point; still, its variation depends on the chemical potential of the gas and diverges as $\mu \to 0$. The behaviour of the various quantities (correlation length, susceptibility, etc.) can be expressed using μ rather than $T - T_c$. Starting from Equation 1.47, the correlation length reads:

$$\xi = \ell_c \simeq \frac{\lambda_{\mathrm{dB}}}{\sqrt{4\pi(1-z)}} \tag{2.20}$$

For a gas with increasing degeneracy, $z \to 1$ so $z = \exp(\beta\mu) \simeq 1 + \beta\mu$, such that

$$\xi \simeq \frac{\lambda_{\mathrm{dB}}}{\sqrt{4\pi\alpha}} \simeq \frac{\hbar}{\sqrt{2M(-\mu)}} \propto |\mu|^{-1/2} \tag{2.21}$$

where $\alpha = -\mu\beta$. The exponent ν for the ideal gas close to the transverse condensation transition point is the same as the mean-field exponent.

If one wants to know the critical exponent associated to the temperature, one can use the same line of reasoning as in subsection 2.1.1.3 to link the variation of μ with that of T; knowing that $\mathcal{D} = \zeta g_2(z) \leqslant \mathcal{D}_{\mathrm{c}} = \zeta g_2(1)$, one gets (for a fixed 2D density):

$$\mathcal{D}_{\mathrm{c}} - \mathcal{D} = n\left[\left(\lambda_{\mathrm{dB}}^{\mathrm{crit}}\right)^2 - \lambda_{\mathrm{dB}}^2\right] \approx 2\mathcal{D}_{\mathrm{c}}\varepsilon \approx \zeta\varepsilon\frac{\pi^2}{3} \tag{2.22}$$

and using[109]

$$g_2(e^{-\alpha}) \approx g_2(1) - (\ln(1/\alpha) + 1)\,\alpha \tag{2.23}$$

we find

$$\mathcal{D}_{\mathrm{c}} - \mathcal{D} \approx \zeta\left[\ln\left(\frac{1}{\alpha}\right) + 1\right]\alpha \tag{2.24}$$

such that

$$\varepsilon \propto \left[\ln\left(\frac{1}{\alpha}\right) + 1\right]\alpha \tag{2.25}$$

Neglecting the logarithmic divergence (dans la limite $\alpha \to 0$), we therefore find

$$\nu = 1/2 \tag{2.26}$$

(as in the mean-field model). However, the correlation length does not grow indefinitely. At the transition point (see Chapter 1 subsection 1.2.3):

$$\xi_c = \frac{a_{\mathrm{ho}}}{\sqrt{2}} \tag{2.27}$$

where a_{ho} is the harmonic oscillator length associated with the frequency ω_z.

2.1.1.5 *Interacting Bose gas*

For our study, there is a universality class which is of particular interest, which is that of the interacting Bose gas. This class describes a phase transition of a three-dimensional system (i. e. $\boldsymbol{r} \in \mathbb{R}^3$) with a two-dimensional order parameter, i. e. ψ is a two-component vector, at some critical temperature T_{c}. For an interacting Bose-Einstein condensate, the order parameter is a complex number (representing the eigenvalue of the particle annihilation operator [29, 78]). This is also the universality class of liquid helium and may be relevant to transitions in liquid crystals [110]. It is usually named 3D-XY model, reflecting the dimensionality of the space ($\boldsymbol{r} \in \mathbb{R}^3$) and of the order parameter ($\psi \in \mathbb{R}^2$).

This transition is characterized by the appearance of a superfluid density ρ_s below the transition point (also called phase stiffness in the context of magnets). Josephson showed [103, 111] that the superfluid density has a power-law behaviour close to the phase transition. Using some measurements on helium, he states that

$$\rho_s \propto |\varepsilon|^{2/3} \tag{2.28}$$

The correlation length close to the transition point is related to ρ_s (see [105] section IV.A):

$$\xi \propto \rho_s^{-1} \tag{2.29}$$

Hence

$$\xi \propto |\varepsilon|^{-2/3} \tag{2.30}$$

and

$$\nu' = \frac{2}{3} \tag{2.31}$$

For the behaviour at $\varepsilon > 0$, it was measured in ultracold atomic gases [112] and calculated by Monte-Carlo simulations [110, 113–115] and is found to be on the order of

$$\nu \approx \frac{2}{3} \tag{2.32}$$

For a review on the various estimates of ν, see for example [110].

2.1.2 *Dynamical exponent*

2.1.2.1 *Definition*

In the previous subsection, we have seen how static properties behave close to the transition point. Experimental studies have shown that dynamic phenomena — for example response to small perturbations — also exhibit a general behaviour that does not depend on the microscopic details of the system close to a transition point.

If the system departs from equilibrium, its equilibrium state will be restored on a certain time-scale τ. The typical time for an excitation with wavevector $\boldsymbol{k}$ to relax is assumed to follow the general form [101, 105]

$$\tau_{\boldsymbol{k}} \propto k^{-z} A(k\xi) = \xi^z A'(k\xi) \tag{2.33}$$

which is called the scaling hypothesis. Here, ξ is the (static) correlation length defined in equation 2.7, and A and A' are functions such that $A(x) = x^z A'(x)$. This form postulates that the only relevant length scale is the correlation length. From equation 2.33, one can define a characteristic dissipative frequency $\omega(\boldsymbol{k})$ [105]

$$\omega(\boldsymbol{k}) \propto k^z \Omega(k\xi) \propto \xi^{-z} \Omega'(k\xi) \tag{2.34}$$

with $\Omega(k\xi) = 1/A(k\xi)$. This characteristic dissipative frequency has a behaviour similar to the dispersion relation of the excitations of the system $\varpi(\boldsymbol{k})$ (if such a relation exists) in the case where the dynamics has the following form:

$$Ci\frac{\partial \psi(\boldsymbol{r}, t)}{\partial t} = -\frac{\delta F}{\delta \psi(\boldsymbol{r}, t)} \tag{2.35}$$

as in the Schrödinger equation (C is a constant, $\hbar$ in the case of the Schrödinger equation).

The equation 2.34 does not mean that the dissipative frequency or dispersion relation is of the form $\omega(\boldsymbol{k}) \propto k^z$ (with no k dependence in the proportionality coefficient). It means that, in addition to the natural expectation that $\omega(\boldsymbol{k})$ has

to be expressed in terms of the dimensionless quantity $k\xi$, there is an extra dependence on the correlation length.

The value of z depends on two issues:

- the universality class to which the underlying model belongs, and the value of its parameters close to the transition point.
- the assumptions made on how a perturbation will relax toward equilibrium, as will be illustrated in the following paragraph.

Therefore, the universality classes described in the static case are split up in several behaviours according to the relaxation mechanism. The various behaviours have been gathered in the review by Hohenberg and Halperin [105].

In the following, we will discuss the mean-field case as an illustration of the previous definitions. We will compute the value of z for the F model, corresponding to the behaviour of interacting Bose gas. Finally, we will propose a possible mechanism for transverse condensation.

2.1.2.2 *Illustration: mean-field theory*

The mean-field solution ψ_0 for a free energy F is such that

$$\left.\frac{\delta F}{\delta \psi}\right|_{\psi_0} = 0 \tag{2.36}$$

Now if the state of the system is $\psi \neq \psi_0$, we have to postulate a relaxation mechanism towards equilibrium. We will consider two cases: (i) a non-conserved order parameter and (ii) a conserved order parameter.

In the first case, neglecting all fluctuations, we can assume that the state will relax to the initial state according to the following equation:

$$\frac{\partial \psi(\boldsymbol{r}, t)}{\partial t} = -\Gamma \frac{\delta F}{\delta \psi(\boldsymbol{r}, t)} \tag{2.37}$$

The coefficient Γ is a transport — or kinetic — coefficient which we assume to be constant. The integral of ψ over space is not conserved by this relaxation mechanism.

We use the free energy of the Gaussian model (equation 2.12):

$$\frac{\delta F}{\delta \psi(\boldsymbol{r}, t)} = 2a\varepsilon\psi(\boldsymbol{r}, t) - b\boldsymbol{\nabla}^2\psi(\boldsymbol{r}, t) \tag{2.38}$$

Replacing in the Fourier-transformed equation 2.37:

$$\frac{\partial \psi(\boldsymbol{k}, t)}{\partial t} = \Gamma\left(2a\varepsilon + b\boldsymbol{k}^2\right)\psi(\boldsymbol{k}, t) \tag{2.39}$$

A perturbation with wavevector $\boldsymbol{k}$ will thus decay exponentially fast as $\exp\left(-t/\tau_{\boldsymbol{k}}\right)$ with

$$\tau_{\boldsymbol{k}} = \frac{1}{\Gamma\left(2a\varepsilon + b\boldsymbol{k}^2\right)} \tag{2.40}$$

In the small wavelength limit $\boldsymbol{k} \to \boldsymbol{0}$, we get

$$\tau_{\boldsymbol{k}} \sim \frac{1}{2\Gamma a\varepsilon} \propto \varepsilon^{-1} \propto \xi^2 \tag{2.41}$$

since $\xi \propto \varepsilon^{-1/2}$ in the mean-field model. Comparing this to the scaling law of equation 2.33, we find

$$z = 2 \tag{2.42}$$

for the mean-field model with this type of relaxation.

Let us now consider the "conserved order parameter" case. If ψ represents a particle density, relaxation toward equilibrium cannot happen as in equation 2.37 because this would imply destroying particles. The coefficient Γ is replaced by a coefficient λ times the laplacian operator, such as in a diffusion equation:

$$\frac{\partial\psi(\boldsymbol{r},t)}{\partial t} = -\lambda\,\boldsymbol{\nabla}^2\frac{\delta F}{\delta\psi(\boldsymbol{r},t)}$$

The same reasoning can be applied to this case and yields

$$\tau_{\boldsymbol{k}} = \frac{1}{\lambda\boldsymbol{k}^2\left(2a\varepsilon + b\boldsymbol{k}^2\right)} = \frac{\xi^4}{\lambda\left[a'\left(k\xi\right)^2 + b\left(k\xi\right)^4\right]} = \xi^4 A(k\xi) \tag{2.43}$$

(using the fact that $\varepsilon \propto \xi^{-2}$) thus giving $z = 4$. Here, the characteristic frequency (equivalent of the dispersion relation obtained for equations of motion such as equation 2.35) at small k is *not* $\omega(\boldsymbol{k}) \propto k^z$, but $\omega(\boldsymbol{k}) \propto \xi^{-z}\left(\xi k\right)^2$.

2.1.2.3 *Interacting Bose gas*

The dynamic behaviour of the weakly interacting Bose gas follows that of model F [105]. This takes into account the fact that the order parameter, the eigenvalue of the annihilation operator, is not conserved. However, the order parameter is coupled to a conserved quantity, the atom number, via the chemical potential.

In order to discuss the value of the dynamic critical exponent z for the model F, we consider the excitations of a superfluid below its critical temperature. These excitations are sound waves, as can be shown by a Bogoliubov analysis [29, 78]

$$\varpi(\boldsymbol{k}) = \tilde{c}_s k \tag{2.44}$$

where c_s is the speed of sound. As explained in 2.1.2.1, the behaviour of the characteristic dissipative frequency ω is similar to that of the dispersion relation ϖ. This comes from the similarity between the equation used to derive the dispersion relation 2.35 and the equation used for the relaxation of a non-conserved order parameter 2.37. Hence:

$$\omega(\boldsymbol{k}) = c_s k \tag{2.45}$$

The velocity c_s has actually a very general form, being the square root of a ratio between a stiffness term and a susceptibility

$$c_s \propto \sqrt{\frac{\rho_s}{\chi}} \tag{2.46}$$

In the case of a superfluid, ρ_s is the superfluid density, which has been showed to behave as $\rho_s \propto \xi^{-1}$ close to the transition point (see equation 2.29), and χ corresponds to the specific heat, which has been measured to vary weakly close to the transition point in liquid helium. This yields the following variation for the speed of sound close to the critical point:

$$c_s \propto \xi^{-1/2} \tag{2.47}$$

giving for the dispersion relation

$$\omega(\boldsymbol{k}) \propto \xi^{-1/2} k \propto k^{3/2} \left(k\xi\right)^{-1/2} \tag{2.48}$$

Hence

$$z = \frac{3}{2} \tag{2.49}$$

for the model F. This derivation, using properties of the $\varepsilon < 0$ phase, can be extended to the $\varepsilon > 0$ phase since the dynamical critical exponent z does not depend on which side of the transition the system is [105].

2.1.2.4 *Ideal gas and transverse condensation*

In the case of an ideal gas being cooled, in 3D or in a mixed geometry (transverse condensation), we will make the simple assumption — similar to what was described in the mean-field case — that a perturbation with wavevector $\boldsymbol{k}$ will decay with a characteristic time

$$\tau_{\boldsymbol{k}} = \frac{1}{K\left(-\mu + \frac{\hbar^2 k^2}{2M}\right)} \tag{2.50}$$

This is the non-conserved order parameter case. In the non-degenerate phase, large fluctuations exists for $k \ll \xi^{-1}$ since the value of the order parameter is not correlated between two points with distance $r \gg \xi$; hence this equation is only interesting for $k > \xi^{-1}$:

$$\tau_{\boldsymbol{k}} < \tau_{\xi^{-1}} = \frac{1}{K\left(-\mu + k_{\mathrm{B}} T\right)} \tag{2.51}$$

Since we are close to degeneracy, $\beta\left(-\mu\right) \ll 1$ such that for all relevant $\boldsymbol{k}$ ($k > \xi^{-1}$)

$$\tau_{\boldsymbol{k}} \simeq \frac{1}{K\left(\frac{\hbar^2 k^2}{2M}\right)} = \xi^2 \frac{2M}{K\hbar^2 \left(k\xi\right)^2} \tag{2.52}$$

which yields

$$z = 2 \tag{2.53}$$

The dynamical exponent z for the ideal gas close to the transverse condensation transition point or close to the 3D Bose-Einstein condensation transition is the same as the mean-field exponent, under this approximation for the relaxation mechanism.

To summarize, from the static and dynamic analysis of critical phenomena, the behaviour of various quantities close to a phase transition point can be

Quantity	Exponent	Mean-Field	Model F	Tranverse condensation	Ideal BEC
ξ	ν	$1/2$	$\approx 2/3$	$1/2$	1
$\tau_{\boldsymbol{k}}$	z	2	$3/2$	2	2

Table 2.2: Critical exponent relevant to the Kibble-Zurek prediction for the mean-field model, for the model F, for the transverse condensation and for BEC in an ideal gas. In the case of transverse condensation, the quantities ξ and $\tau_{\boldsymbol{k}}$ follow a power-law but they do not diverge at the transition point.

described by critical exponents. The two exponents which are going to be important in the derivation of the Kibble-Zurek scaling are ν, which characterizes the divergence of the correlation length, and z, which characterizes the critical slowing down of dynamics close to the transition point, that is, the slowing down of information propagation. The values of these exponents are summed up in table 2.2.

2.2 THE KIBBLE-ZUREK PREDICTION

2.2.1 *Correlation length and thermalization time*

Suppose that we have a system undergoing a second-order phase transition. At a temperature T close to the transition temperature T_c, we have defined $\varepsilon = (T - T_c)/T_c$; the correlation length grows as

$$\boxed{\xi = \xi_0 |\varepsilon|^{-\nu}} \tag{2.54}$$

where ξ_0 depends on the short length scale details of the system; the relaxation time for a perturbation of wavevector $\boldsymbol{k}$ varies as

$$\tau_{\boldsymbol{k}} = \xi^z A'(k\xi) \tag{2.55}$$

We will consider now the case where the temperature — or equivalently ε — is varied, and look at the condition under which the system can adiabatically follow the change in temperature. In order for the system to follow the change of temperature, any excitation that has been created due to the temperature variation must have the time to decay. In a rough approximation, the order parameter will stay constant over a distance of ξ, forming "patches" of size ξ with constant value. The main wave vectors contributing to excitations that have to relax in order to follow the dynamics of the quench are those such that

$$|\boldsymbol{k}| \sim \xi^{-1} \tag{2.56}$$

Indeed, as the temperature is decreased, the equilibrium correlation length increases from ξ to ξ'. In order to consider that the state follows adiabatically the varying temperature, the correlations have to change such that the correlation length goes from ξ to ξ'. Initially, all fluctuations with $k < \xi^{-1}$ were

already damped out. The only fluctuations which have to relax to allow adiabatic following are thus those such that $k < \xi'^{-1}$. We can therefore define the thermalization time τ as the relaxation time for an excitation with a wave vector of modulus ξ^{-1}:

$$\tau = \tau_{\xi^{-1}} = \xi^z A'(1) \propto \xi^z \tag{2.57}$$

We get a temperature variation for the thermalization time which is

$$\boxed{\tau = \tau_0 \left|\varepsilon\right|^{-\nu z}} \tag{2.58}$$

The exact value of τ_0 depends on the details of the system.

2.2.2 *Freezing out of the system*

The Kibble-Zurek scaling prediction assumes that the size of the "order parameter patches" will stop growing as soon as there is not enough time for the system to thermalize before it reaches the critical temperature. At this time, the value of the order parameter — for example, the phase of the complex number describing the order parameter for a weakly interacting condensate — will be frozen within one "patch". We assume that ε goes from a positive to a negative value with $\varepsilon = 0$ at $t = 0$ and we call $\hat{t}$ the time at which the dynamics will be frozen. According to the previous description:

$$\tau\left(\varepsilon\left(-\hat{t}\right)\right) \simeq \hat{t} \tag{2.59}$$

For a given temperature ramp, this equation along with equation 2.58 allows to find the value of $\hat{t}$. The typical size over which the order parameter is constant, that is the typical size of the "patches", is then $\hat{\xi} = \xi(\hat{t})$.

If we consider the case of a linear temperature ramp

$$\varepsilon = -\frac{t}{\tau_Q} \tag{2.60}$$

and use the scaling of equation 2.58, the freezing out time is given by

$$\hat{t} = \left(\tau_0 \tau_Q^{\nu z}\right)^{\frac{1}{1+\nu z}} \tag{2.61}$$

and the size of the "patches" at the freezing out time is

$$\boxed{\hat{\xi} = \xi_0 \left(\frac{\tau_Q}{\tau_0}\right)^{\frac{\nu}{1+\nu z}}} \tag{2.62}$$

The size of the phase domains in a quench cooled Bose gas will therefore depend with a power-law scaling on the quench duration.

Some phase transitions are not second-order phase transitions: this is the case for example of the BKT transition which explains the appearance of a superfluid behaviour for a 2D system. Close to the transition point, the correlation length and the thermalization time can still be defined, but their variation as the system approaches the transition does not have a power-law behaviour. For the BKT transition, the coherence length has an exponential divergence close to the transition point [116]. The value of the coherence length at the time where the dynamic is frozen will then still depend on τ_Q, though not with a power-law scaling [117].

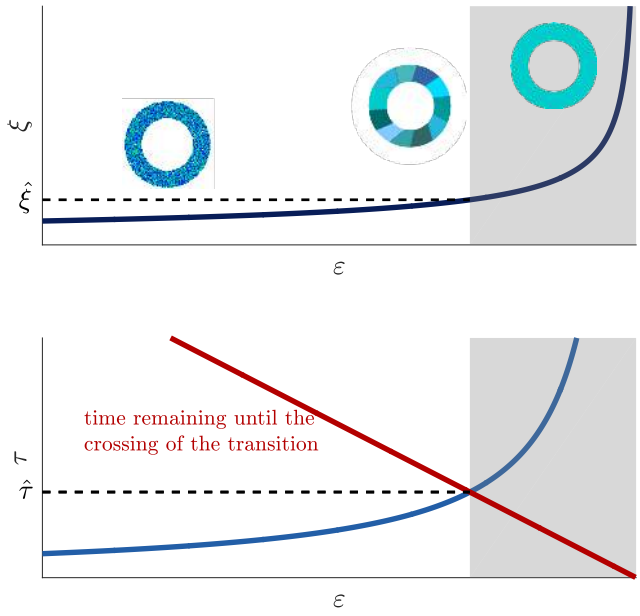

Figure 2.1: Illustration of the Kibble-Zurek mechanism. Top: Divergence of the correlation length $\hat{\xi}$ as a function of the distance to the phase transition point ε. Bottom: Divergence of the thermalization time $\hat{\tau}$ as a function of the distance to the phase transition point ε (blue) and time remaining until the phase transition point is crossed t assuming a linear temperature ramp (red). As $\hat{\tau} = t$, the system is assumed to be frozen at the correlation length $\hat{\xi}$. The distribution of "phase patches" in a ring is illustrated in the top picture, the grey shaded area represents the correlation lengths that are inaccessible due to the freezing out of the dynamics.

2.2.3 *Detection of the order parameter variation: topological defects*

In this section, we will focus on the case of the order parameter of a Bose-Einstein condensate; in particular, since this order parameter is a complex number, we will be interested in its phase, which is the symmetry-breaking parameter.

After a temperature quench, the distribution of the phase of the condensate is not uniform as it would be after an infinitely slow cooling procedure: it consists of areas of typical size $\hat{\xi}$ where the phase of two points is correlated, while the phase of points whose distance is larger than $\hat{\xi}$ is uncorrelated. In a simplified picture, we can picture the phase distribution consisting of "patches" of size $\hat{\xi}$.

If we can measure directly the phase of the system, we can access the freezing-out size $\hat{\xi}$. A recent experiment using ultracold atoms has been probing directly the first-order correlation function after a quench cooling [68]. However, this is usually difficult to do, which is why the Kibble-Zurek prediction was originally based on the observation of topological defects in the phase. A topological defect is a perturbation of the phase from the uniform distribution that cannot be transformed continuously back into a uniform phase distribution. A typical example of a topological phase defect is a vortex, that is a phase winding of 2π around a point in a 2D system. Other examples of topological defects include vortex lines in 3D systems or solitons, i. e. a phase change of π between two parts of the system. One advantage of topological defects is that they can have stronger signatures than phase domains. For example, in a 2D degenerate gas, a vortex can be detected in Time-of-Flight (ToF) experiment as an expanding density hole. Another advantage is that topological defects do not disappear easily, so they might live for a long time after the quench has been performed.

Zurek used the prediction on the typical domain size $\hat{\xi}$ to predict the density of topological defects [107, 118]. In the naive phase patch picture for a system in d dimensions, a patch has a volume $V \propto \hat{\xi}^d$. Depending on the dimension D of the defect (a point vortex has $D = 0$, a vortex line $D = 1$, a soliton $D = d - 1$), the scaling of the density of defects can be computed. We will consider two cases: the case of a vortex in a ring (1D system) and the case of a vortex in a 2D system.

2.2.3.1 *Phase winding in a ring*

In this section, we are interested in a narrow ring undergoing a quench cooling. This is the original situation considered by Zurek [107]. The ring has a circumference of $\mathcal{C}$, and assuming that its width $\Delta r \ll \hat{\xi}$, the number of "patches" is

$$N \propto \frac{\mathcal{C}}{\hat{\xi}} \tag{2.63}$$

We will first consider the case where $N \gg 1$. In this case, the phase along the ring is a random walk with N steps such that the average phase between the first and the last patch while going around the ring is on average

$$\langle |\Delta\varphi| \rangle \propto \sqrt{N} \tag{2.64}$$

The ring will exhibit a phase winding of $\mathcal{W}$ such that the closest multiple of 2π to $\Delta\varphi$ is $2\pi\mathcal{W}$. Thus the mean average phase winding in the ring is

$$\langle|\mathcal{W}|\rangle \propto \sqrt{N} \propto \hat{\xi}^{-1/2} \tag{2.65}$$

that is

$$\boxed{\langle|\mathcal{W}|\rangle \propto \tau_Q^{-\frac{\nu}{2(1+\nu z)}}} \tag{2.66}$$

In the opposite case $N_d \ll 1$, the scaling can be shown to become [118, 119]:

$$\langle|\mathcal{W}|\rangle \propto \hat{\xi}^{-2} \propto \tau_Q^{-\frac{2\nu}{1+\nu z}} \tag{2.67}$$

2.2.3.2 *Vortices in a plane*

We are now interested in the density of (point-like) vortices that appear in a plane of area $\mathcal{A}$ undergoing a quench cooling. In this case, the number of defect is proportional to the number of phase patches [118]:

$$N_v \propto \frac{\mathcal{A}}{\hat{\xi}^2} \tag{2.68}$$

To justify this form, let us imagine that the "phase patches" are small squares of typical length $\hat{\xi}$ tiling a large square of area $\mathcal{A} = L^2$. Calling $N = L/\hat{\xi}$, there are $(N-1)^2$ intersections of four patches. At a given vertex, considering the phases of the patches as uncorrelated, the probability to have a phase winding is on the order of 0.33. Thus, the number of vortices should be

$$N_v^{\text{patches}} = 0.33\left(\frac{L}{\hat{\xi}} - 1\right)^2 \sim 0.33\left(\frac{L}{\hat{\xi}}\right)^2 \tag{2.69}$$

for $\hat{\xi} \ll L$. The scaling of this equation is in agreement with equation 2.68. Of course, even in the phase patch picture, the approximation of having a large square tiled with small squares of size $\hat{\xi}$ is very crude; with arbitrary patch shapes, it is more likely to have intersections with three patches (where the probability of having a phase winding is 0.25), though this does not modify the $(L/\hat{\xi})^2$ scaling.

It turns out that this kind of very rough approximate overestimates the number of vortices with respect to the values which are obtained via numerical simulations (for example solving the stochastic Gross-Pitaevskii equation). This is accounted for by using a so-called "fudge factor" f, usually on the order of 10 [118, 120]:

$$N_v \sim \frac{N_v^{\text{patches}}}{f} \tag{2.70}$$

This factor can come from the fact that the decay of the correlation function is not abrupt but has an exponential form. Hence, some phase rigidity persists even for $r > \hat{\xi}$, making the effective size of the "patches" larger. When performing a quench, it also is possible that some of the created topological defects disappear during the end of the quench (for example, annihilation of vortices of opposite charge), leading to a smaller number of defects than expected in the "patch" picture.

Using the scaling of $\hat{\xi}$, this yields that the number of vortices follows the scaling law:

$$\boxed{N_v \propto \tau_Q^{-\frac{2\nu}{1+\nu z}}} \tag{2.71}$$

2.3 LIMITATIONS TO THE OBSERVATION OF THE KIBBLE-ZUREK PREDICTION

Let us now state some of the obstacles that must be overcome when trying to verify experimentally the Kibble-Zurek scaling.

First, experimental verification of a power-law scaling requires in principle to probe several orders of magnitude in the different parameters, that is in the topological defect density and in the quench duration, which is a challenging experimental task. In the case of the BKT transition, the orders of magnitude that have to be spanned for an accurate determination of the scaling behaviour are for the moment far out of reach of atomic physics experiments [117]. In addition, in the case of a power-law behaviour, the values of the exponents to be measured are small: $1/8$ or $1/6$ for the phase winding in the ring, depending on the model (mean-field or model F), and $1/2$ to $2/3$ in the case of vortices in a plane, also depending on the model; this makes their accurate determination more difficult.

Second, the finite size L of the experimental systems can also limit the range of quench durations to be tested. The scaling behaviour is indeed valid only in the limits $L \gg \hat{\xi}$ or $L \ll \hat{\xi}$: the intermediate regime $L \sim \hat{\xi}$ does not follow such simple laws [118].

Last, the picture of two extremely well separated regimes $t < \hat{t}$ where the system follows adiabatically the parameter ε and $t > \hat{t}$ where the order parameter is completely frozen is not completely valid [120–122]. Even if the dynamic is slow below the transition point $\varepsilon > 0$, the system can still evolve. This was important in the demonstration of Kibble-Zurek scaling in the experiments performed in [68]. Even the density of topological defects, which cannot easily decay and whose lifetime is therefore long, can evolve during the quench, for example in the case of annihilation of vortices with opposite charge in a 2D system [90].

2.4 CONCLUSION

In this chapter, we have recalled the result that, close to phase transition points, quantities such as the correlation length have a universal behaviour that only depends on some very general parameters of the system (dimensionality, number of degrees of freedom). In the case of second-order phase transitions, this behaviour follows a power-law characterized by critical exponents. For example, the correlation length ξ diverges a $|\varepsilon|^{-\nu}$ (where ε is the distance to the transition point in dimensionless units). Dynamic quantities, such as the time for a perturbation to relax, also follow a scaling form close to the phase transition, characterized by the critical exponent z. In particular, a thermalization time τ can be defined, which varies as $|\varepsilon|^{-\nu z}$ close to the transition.

Since the thermalization time diverges close to the transition, a system which is cooled at a finite speed through the transition point cannot stay at equilibrium during the whole cooling procedure. Rather, at some point, the system will be frozen because its dynamics will have become too slow, showing correlations of the order parameter on length scales up to $\hat{\xi}$. The Kibble-Zurek scaling [106, 107, 118] predicts the variation of $\hat{\xi}$ with the duration of the quench using the exponents ν and z.

This freezing out of the system is most "easily" seen with the formation of topological defects, which are robust features of the order parameter distribution. As a consequence of the power-law variation of $\hat{\xi}$, the density of topological defects can also be shown to vary with a power-law of the quench duration. This exponent depends on ν, z, the dimension of the system and the type of the defect.

As a consequence, by varying the quench duration of a system undergoing a phase transition and measuring the resulting density of topological defects, one can access the equilibrium critical exponents ν and z that characterize the transition — although measuring a power-law scaling can be challenging experimentally.

3

QUENCHING THE BOSE GAS BETWEEN THREE AND TWO DIMENSIONS

In this chapter, I present the experiments on the crossover between three and two dimensions due to transverse condensation presented in chapter 1 as well as quench-cooling experiments whose results were compared to the Kibble-Zurek mechanism described in chapter 2. These experiments were performed on an experimental setup stopped in 2014.

First, the main features of the experimental setup (already described in previous thesis [90, 93, 123, 124]) as well as the preparation of 2D Bose gases in uniform traps are presented. Then, the appearance of phase coherence in the cloud is studied by analyzing (i) bimodality in ToF profiles and (ii) interference fringes when two atomic clouds overlap after expansion. The results are compared to the predictions for transverse condensation. Last, we observe topological defects when quench-cooling the gas in two different geometries: first, point vortices are observed in square clouds; second, supercurrents coming from a phase winding of the wavefunction of the atomic gas in a ring are detected interferometrically.

3.1 EXPERIMENTAL SET-UP

The experimental set-up used to perform the experiments of sections 3.2 and 3.3 has been extensively described by the previous students working on the experiment [90, 93, 123, 124]. Therefore, this section will be devoted to recalling and justifying the main technical choices which led to the production of uniform Bose gases in a tightly confined vertical trap.

3.1.1 *Laser set-up*

3.1.1.1 *Cooling lasers*

In order to improve the stability of the laser part of the experiment, I designed and built a renovated laser table in order to provide nearly resonant light for the laser-cooling stages, for imaging the atomic cloud as well as for the single-atom imaging scheme which was planned to be installed on the experiment [93]. The red-detuned light with respect to the cycling transition of rubidium 87 was provided by a 2.5 W Toptica TA pro laser. The repumping light was provided by a Radiant Dyes interference filter stabilized external cavity laser diode (providing 40 mW of light) combined with a Sacher Lasertechnik tapered amplifier. Laser light of the Toptica TA pro laser was used for

- locking the laser

- producing the Magneto-Optical Trap (MOT) and optical molasses beams
- optical pumping of the cloud to the right magnetic state for loading a quadrupole trap
- imaging the cloud at the end of the experimental sequence

The light shaping for each of these functionalities was done on different, fiber-coupled breadboards. In this configuration, the laser set-up can be easily upgraded, at the cost of a slight power loss due to extra fiber coupling.

3.1.1.2 *Dipole trap laser*

The far red-detuned light producing the conservative potential for atom trapping and evaporation to degeneracy was provided by a fiber 8.4 W laser at 1064 nm from Azurlight technologies. This laser integrates an analog input that controls its power. The bandwidth of this analog modulation input was tested to be 1 kHz. It allows to tune the power of the laser between it maximum power (8.4 W) to the power of the seed laser (40 mW), providing an extinction ratio of 200. The lowest powers are nevertheless not perfectly suited to trapping of ultracold atoms due to the important intensity noise.

3.1.1.3 *Blue-detuned laser for 2D and box confinement*

2D vertical confinement as well as in-plane, horizontal, uniform trapping is provided by a 10 W laser at 532 nm, a Verdi V10. The light is brought to the experiment via optical fibers with length up to 4 m, which limits the maximum power available due to Brillouin scattering. The maximum power of 1 W at the output of the fibers is obtained using the laser at a restrained operating point of 4 W and coupling the light into end-capped fibers from Schäfter-Kirchhoff.

3.1.2 *Production of degenerate gases*

The production of a three dimensional BEC requires an experimental sequence of 46 s:

Laser cooling and magnetic trap

For 8.5 s, a MOT of several 10^{10} rubidium 87 atoms is loaded from the background pressure of a vacuum chamber, then, the atomic cloud is further compressed and cooled during an optical molasses stage. After optical pumping to the $|F = 2, m_F = 2\rangle$ state, a first magnetic trap with a vertical gradient of $b'_z = 140\,\mathrm{G/cm}$ is switched on, trapping $5 \cdot 10^9$ atoms with a temperature of 450 μK.

Magnetic transport

During 6 s, the atoms are transported from the vacuum chamber to a glass cell through a differential pumping stage by continuous displacement of a quadrupole trap with a vertical gradient of 90 G/cm [125]. Back and forth transport of

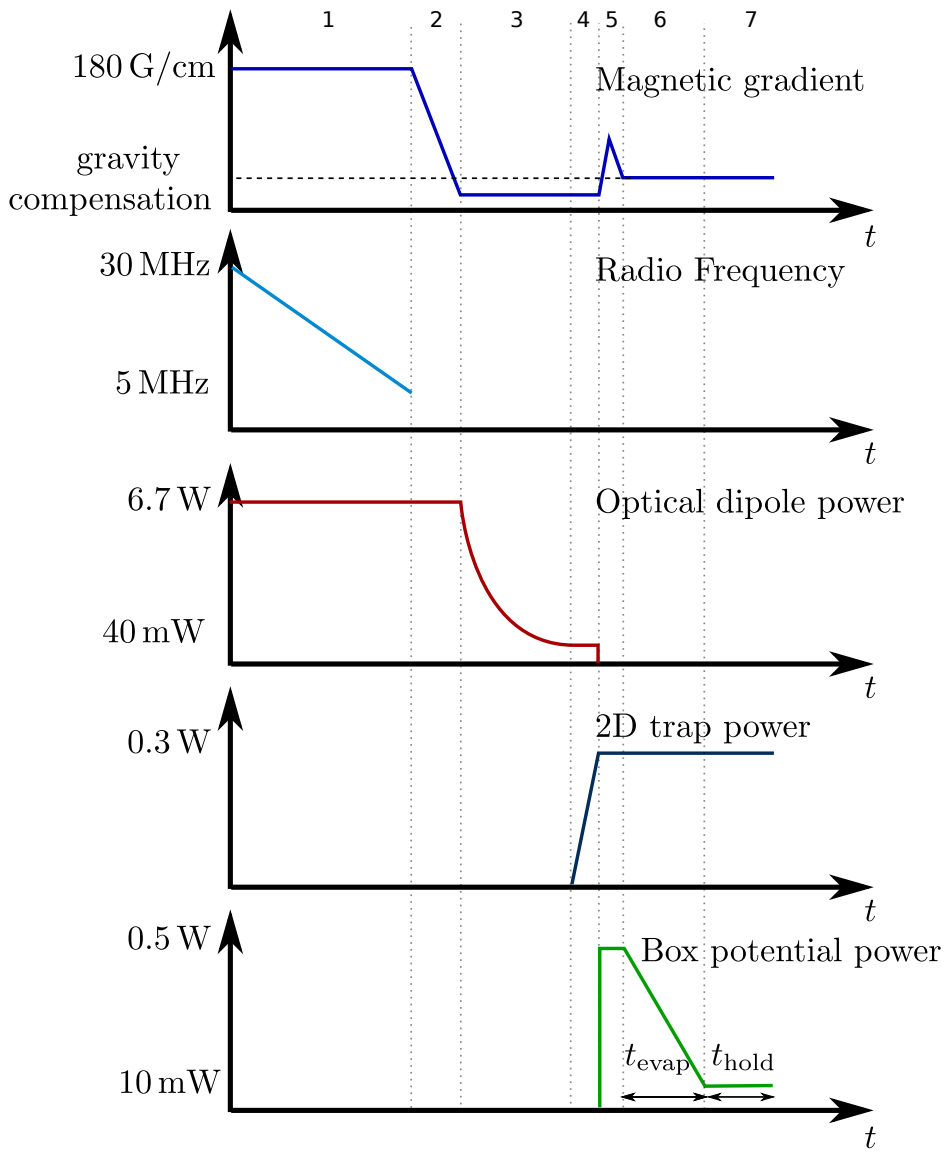

Figure 3.1: Main experimental steps for creating a 2D uniform Bose gas after the atoms have been transported to the glass cell. The various steps are (1) radio frequency evaporation, (2) loading of the optical dipole trap, (3) evaporation in the dipole trap, (4) loading of the 2D plane and of the box potential, (5) removal of the atoms not in the central plane, (6) evaporation in the box potential during a time t_{evap}, (7) hold time during t_{hold}.

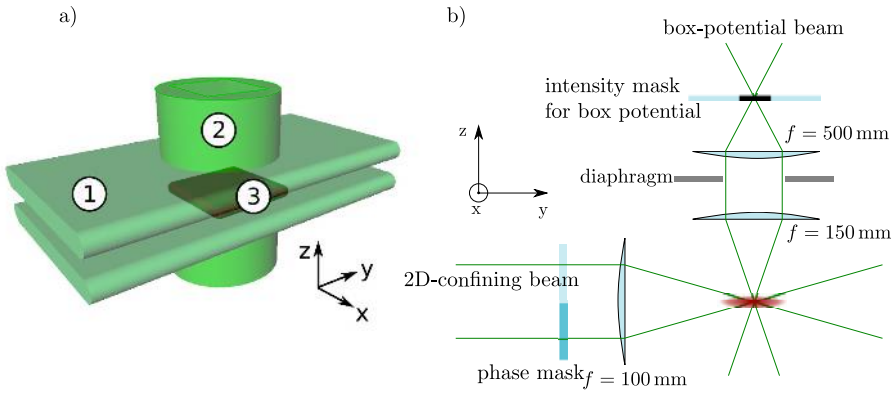

Figure 3.2: Schematic view of the two blue-detuned traps providing the 2D box potential for the atoms. In (a) (1) is the Hermite-Gauss beam providing the 2D, vertical confinement; (2) is the box potential whose production is explained in 3.1.3; the atoms are located in (3). The optical system used to produce the 2D confinement and the box potential is shown in (b).

the cloud leads to the estimation of a one-way loss percentage on the order of 50 %.

Radio-frequency evaporation

After the atoms have been transported in the science cell, the quadrupole trap is compressed to $b'_z = 180\,\mathrm{G/cm}$. During 16 s, the atoms are evaporated using a swept radio-frequency pulse from 30 MHz to 5 MHz that selectively transfers the most energetic atoms from a trapped to an untrapped state (see step 1 of figure 3.1). For a detailed analysis of this evaporation procedure and of the collisional properties of the gas, see [126]. At the end of this stage, there are $\sim 2 \cdot 10^8$ atoms at a temperature of 30 μK.

Loading and evaporation in the hybrid trap

In 2.5 s, the cold cloud of atoms is then transferred in into a far-red detuned optical dipole trap (step 4 of figure 3.1). The laser beam focus with waists of 50 μm is located 100 μm below the zero of the quadrupole field and has an initial power on the atoms of 6.7 W. Loading the cloud in the optical dipole trap is done by reducing the magnetic field gradient to $b'_z = 12.5\,\mathrm{G/cm}$ (this slightly under compensates gravity). This trap configuration, also called hybrid trap, was first proposed in [127] and its implementation on our experimental setup was described in [90, 93]. After decreasing the power of the optical dipole trap from 6.7 W on the atoms to 40 mW in 13 s, we obtain an almost pure Bose-Einstein condensate of 10^5 atoms (step 3 of figure 3.1). The degeneracy of the atomic cloud is controlled by the end power of the optical dipole trap.

Preparation of a flat atomic gas in a box potential

First, the 2D-confining beam is ramped up (see figure 3.2 and step 4 of figure 3.1); it is a laser beam at 532 nm with a power of 300 mW, shaped into a first

order Hermite-Gauss mode. This is obtained by inserting in the beam path a phase plate that imprints a π phase shift to its upper half. The intensity profile of the blue-detuned light vanishes along the y axis, so that it creates a repulsive dipole potential on the atoms with a minimum in the $z = 0$ plane around which the atoms are confined (see figure 3.2 for a definition of the axes). The waists on the atoms (without phase plate) are $w_z = 11\,\mu$m and $w_y = 50\,\mu$m. The frequency of the harmonic potential along the vertical direction z ranges from $\omega_z/2\pi = 370\,$Hz to $1500\,$Hz. This is achieved either by changing the power of the laser beam or by changing the position of the Hermite-Gauss focal point with respect to the atoms. Putting the atoms closer to the focal point increases the confinement frequency at the expense of an increased potential roughness; the 2D confinement beam has some defects which are stronger close to its focal point. The difference of laser power between the center and the outer part of the Hermite-Gauss beam leads to some anticonfinement in the y direction (orthogonal to the propagation axis); it is equivalent to an inverted harmonic potential with frequency $\omega_{\text{anti}}/2\pi = 4.2\,$Hz for the largest trapping frequency considered in the following of $\omega_z/2\pi = 1.5\,$kHz.

We then ramp up the box-potential beam (step 5 of figure 3.1, see 3.1.3 for more details about its production) in $0.1\,$s to its maximal power ($500\,$mW) as shown on figure 3.2.

Most of the atoms are loaded in the box potential and into the $z = 0$ plane. To remove the atoms which were not trapped in the correct plane or which are outside the box potential, the magnetic field gradient is quickly varied to let them escape the trap (step 5 of figure 3.1). After this procedure, the magnetic field gradient is tuned to a value of $15\,$G/cm in order to levitate the atoms.

The power of the box-potential beam is then lowered within a time t_{evap} to its final value (step 6 of figure 3.1) corresponding to a typical barrier height of $45\,$nK, and kept constant for a time t_{hold} (step 7 of figure 3.1). The production of 3D uniform gases in similar "optical box potentials" has recently been reported in [55].

With the available vertical confinement, the size of the ground state of the vertical confining potential a_{ho} ranges from 0.3 to $0.6\,\mu$m. This is small compared to the typical size of the box potentials we imprint in the horizontal plane, from 15 to $30\,\mu$m. The atoms number in this type of traps ranges from 1000 to 100 000, and the temperatures T from 10 to $250\,$nK. We are able to study the transverse condensation (see chapter 1) because the parameter $\zeta = k_{\text{B}}T/\hbar\omega_z$ can span a large range of values (from 0.2 to 15). Examples of in situ images of 2D gases with various areas $\mathcal{A}$ are shown in figure 3.3.

Expansion and imaging of the atoms

After the preparation of the cloud in a 2D uniform trap, the atoms can be imaged:

1. in-situ
2. after ToF: all traps are turned off and the atoms are let to fall for durations up to $12\,$ms.

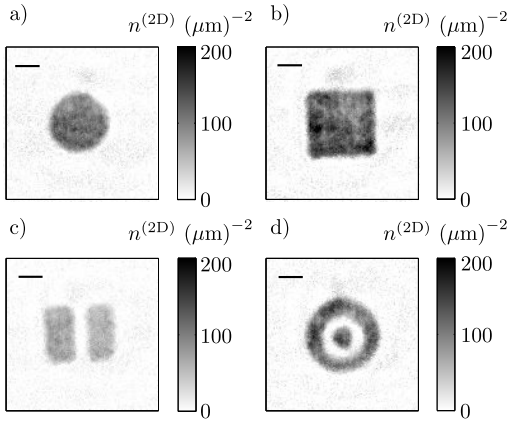

Figure 3.3: (a-d) Examples of in-situ density distributions of uniform gases for different intensity masks. (a) is a disk of radius 12 μm, (b) a square of length 30 μm, (c) two rectangular boxes of size 24 μm $\times$ 12 μm separated by 4.5 μm, (d) the so-called "target" potential consisting in a disk of radius 4.5 μm surrounded by a ring of inner radius 9 μm and of external radius of 15 μm. The scale bars indicate a length of 10 μm.

3. after a hydrodynamic expansion, also called 2D time-of-flight. In that case, the box-potential trap is switched off for durations up to 10 ms while maintaining the vertical confinement. The atoms expand in the horizontal plane, the density stays important and so do the interactions.

The resolution of the imaging system is on the order of 1 μm. It is provided by a custom-made microscope objective from Nachet with a focal length of 10 mm, optimized for a numerical aperture of 0.45 at a wavelength of 780 nm while imaging through a glass slab of 5 mm.

We measure the atomic density distribution in the xy plane using resonant absorption imaging along z. We use two complementary values for the probe beam intensity I. First we use a conventional low intensity technique with $I/I_{\text{sat}} \approx 0.7$, where I_{sat} is the saturation intensity of the Rb resonance line, with a probe pulse duration of 20 μs. This procedure enables a reliable detection of low density atomic clouds, but it is unfaithful for high density ones, especially in the 2D geometry due to multiple scattering effects between neighboring atoms [128]. We thus complement it by a high intensity technique inspired from [129], in which we apply a short pulse of 4 μs of an intense probe beam with $I/I_{\text{sat}} \approx 40$[1].

In ToF measurements (case 2), the cloud is essentially three-dimensional at the moment of the detection, hence they are performed using the low-intensity procedure. For in-situ or after hydrodynamic expansion measurements, the high-intensity procedure is preferable.

1 This paragraph was originally published in [82]

3.1.3 *Parameter estimation of Bose gases in box potentials*

3.1.3.1 *Method for producing a hollow beam*

Some tests to produce a hollow beam were performed using a phase-plate producing a Laguerre-Gauss beam of order six [90, 123]. The quality of the potential was not sufficient for our applications, since the light potential has defects whose peak intensity can reach 40 % of the maximum intensity. We therefore turned to direct imaging of a mask onto the atoms to produced dark regions in the blue-detuned box potential beam with sufficient quality. However, note that a Laguerre-Gauss beam has been successfully used to produced three-dimensional box potentials for ultracold atoms [55, 130].

We create the box-like potential in the xy plane using a laser beam that is blue-detuned with respect to the ^{87}Rb resonance. At the position of the atomic sample, we image a dark mask placed on the path of the laser beam. This mask is realized by a metallic deposit on a wedged, anti-reflective coated glass plate[2]. The xy confinement of the atoms is provided by a hollow, blue-detuned beam trapping the atoms in its dark regions. We characterize the box-like character of the resulting trap in two ways. (i) The flatness of the domain where the atoms are confined is characterized by the root mean square intensity fluctuations of the inner dark region of the beam profile. The resulting variations of the dipolar potential are $\delta U/U_{\mathrm{box}} \sim 3\%$, where U_{box} is the potential height on the edges of the box. The ratio $\delta U/k_{\mathrm{B}}T$ varies from $\sim 40\,\%$ at the loading temperature to $\sim 10\,\%$ at the end of the evaporative cooling. In particular, it is of $\sim 20\,\%$ at the transverse condensation point for the largest square pattern. (ii) The sharp spatial variation of the potential at the edges of the box-like trapping region is characterized by the exponent α of a power-law fit $U(r) \propto r^{\alpha}$ along a radial cut. We restrict the fitting domain to the central region where $U(r) < U_{\mathrm{box}}/4$ and find $\alpha \sim 10$–15, depending on the size and the shape of the box.[1]

3.1.3.2 *Temperature measurement in the box potentials*

Due to the spatial extension of the condensate in a box potential, it is necessary to perform long ToF in order to separate the thermal from the degenerate part in very cold samples. Therefore another method for thermometry has been developed.

All temperatures indicated in this chapter are deduced from the value of the box potential, assuming that the evaporation barrier provided by U_{box} sets the thermal equilibrium state of the gas. This hypothesis was tested, and the relation between T and U_{box} calibrated, using atomic assemblies with a negligible interaction energy. For these assemblies, we compared the variance of their velocity distribution Δv^2 obtained from a ToF measurement to the prediction for the ideal gas description of trapped atomic samples as in Equation 1.6.

The calibration obtained from this set of measurements can be empirically written as

$$T(U_{\mathrm{box}}) = T_0 \left(1 - \mathrm{e}^{-U_{\mathrm{box}}/(\eta\, k_{\mathrm{B}} T_0)}\right), \tag{3.1}$$

2 We thank José Palomo of the ENS clean room for fabricating the masks.

where the values of the dimensionless parameter η and of the reference temperature T_0 slightly depend on the precise shape of the trap. For the square trap of side $24\,\mu$m we obtain $T_0 = 191\,(6)\,$nK and $\eta = 3.5\,(3)$. The reason for which T saturates when the box potential increases to infinity is due to the residual evaporation along the vertical direction, above the barrier created by the horizontal Hermite–Gauss beam.[1]

3.1.3.3 *Estimation of the interaction energy for weakly interacting gases*

We estimate the local value of the interaction energy per particle

$$\epsilon_{\text{int}} = (2\pi\hbar^2 a_{\text{sc}}/m) n^{(3\text{D})}(\boldsymbol{r}) \tag{3.2}$$

where $a_{\text{sc}} = 5.1\,$nm is the 3D scattering length or ^{87}Rb and $n^{(3\text{D})}(\boldsymbol{r})$ the spatial 3D density estimated using the ideal gas description. It is maximal at trap center $\boldsymbol{r} = 0$ (i. e. $z = 0$). For example, using a typical experimental condition with $N = 40\,000$ atoms in a square box of size $L = 24\,\mu$m at $T = 200\,$nK, we find a maximal 3D density of $n^{(3D)}(0) = 13.8\,\mu\text{m}^{-3}$.

The mean-field interaction energy for an atom localized at the center of cloud is then $\epsilon_{\text{int}} = k_{\text{B}} \times 2.1\,$nK. We note that ϵ_{int} is negligible compared to $k_{\text{B}}T$ and $\hbar\omega_z$ for all atomic configurations corresponding to the onset of an extended phase coherence. In this case the interactions play a negligible role in the 2D ToF expansion that we use to reveal matter-wave interferences.[1]

3.1.3.4 *Chemical potential in the degenerate interacting regime*

To compute the chemical potential μ of highly degenerate interacting gases, we perform a $T = 0$ mean-field analysis. We solve numerically the 3D Gross–Pitaevskii equation in imaginary time using a split–step method, and we obtain the macroscopic ground state wave-function $\psi(\boldsymbol{r})$. Then we calculate the different energy contributions at $T = 0$ for N atoms with mass M – namely the potential energy E_{pot}, the kinetic energy E_{kin} and interaction energy E_{int} – by integrating over space:

$$E_{\text{pot}} = \frac{N}{2} M\omega_z^2 \int z^2 \left|\psi\left(\boldsymbol{r}\right)\right|^2 \mathrm{d}^3 r \tag{3.3}$$

$$E_{\text{kin}} = \frac{N\hbar^2}{2M} \int \left|\boldsymbol{\nabla}\psi\left(\boldsymbol{r}\right)\right|^2 \mathrm{d}^3 r \tag{3.4}$$

$$E_{\text{int}} = N^2 \frac{2\pi\hbar^2 a_{\text{sc}}}{M} \int \left|\psi\left(\boldsymbol{r}\right)\right|^4 \mathrm{d}^3 r \tag{3.5}$$

We obtain the value of the chemical potential μ by taking the derivative of the total energy with respect to N and subtracting the single-particle ground state energy:

$$\mu = \frac{1}{N}\left(E_{\text{pot}} + E_{\text{kin}} + 2E_{\text{int}}\right) - \frac{h^2}{4mL^2} - \frac{1}{2}h\nu_z. \tag{3.6}$$

In the numerical calculation, we typically use time steps of $10^{-4}\,$ms and compute the evolution for 10 ms. The 3D grid contains $152 \times 152 \times 32$ voxels[3], with a voxel size $0.52 \times 0.52 \times 0.26\,\mu\text{m}^3$.

3 Elementary volume cell.

3.2 EXPERIMENTAL EVIDENCE FOR THE DIMENSIONAL CROSSOVER

In this section, we use the combination of vertical harmonic and in-plane uniform trapping to study the tranverse condensation phenomenon described in chapter 1. We use two tools to measure the appearance of coherence in the cloud: (i) the appearance of a bimodal distribution in ToF measurements, indicating an important population of the low in-plane momentum states; (ii) the study of matter-wave interference fringes. These two methods enable us to find a critical phase-space density for which, at a given ζ, extended phase coherence appears in the gas. This critical value is then compared to the predicted values for the expected transitions in a uniform gas between three and two dimensions: the BEC transition, the BKT transition [44, 45, 86, 100, 131–133] and the transverse condensation [83, 134, 135]. The results show that the appearance of in-plane coherence is consistent with the latter mechanism. When the atoms starts accumulating in the ground state of the vertical harmonic oscillator, they already have a non-negligible in-plane coherence length (on the order of the harmonic oscillator length of the vertical confinement, i. e. from 0.28 to 0.55 μm for the available vertical confinement frequencies).

The rest of the text of this section was originally published in [82].

3.2.1 *Phase coherence revealed by velocity distribution measurements*

3.2.1.1 *Time-of-flight measurements of gases in a box potential*

To characterize the coherence of the gas, we study the velocity distribution, i. e., the Fourier transform of the $G_1(r)$ function. We approach this velocity distribution in the xy plane by performing a 3D ToF: we suddenly switch off the trapping potentials along the three directions of space, let the gas expand for a duration τ, and finally image the gas along the z axis. In such a 3D ToF, the gas first expands very fast along the initially strongly confined direction z. Thanks to this fast density drop, the interparticle interactions play nearly no role during the ToF and the slower evolution in the xy plane is governed essentially by the initial velocity distribution of the atoms. The ToF duration τ is chosen so that the size expected for a Boltzmann distribution $\tau\sqrt{k_B T/m}$ is at least twice the initial extent of the cloud. Typical examples of ToF images are given in figure 3.4. Whereas for the hottest and less dense configurations, the spatial distribution after ToF has a quasi-pure Gaussian shape, a clear non-Gaussian structure appears for larger N or smaller T. A sharp peak emerges at the center of the cloud of the ToF picture, signaling an increased occupation of the low-momentum states with respect to Boltzmann statistics, or equivalently a coherence length significantly larger than λ_{dB} the thermal wavelength ($\lambda_{dB} = h/\sqrt{2\pi M k_B T}$).

3.2.1.2 *Measuring the bimodality*

In order to analyze this velocity distribution, we chose as a fit function the sum

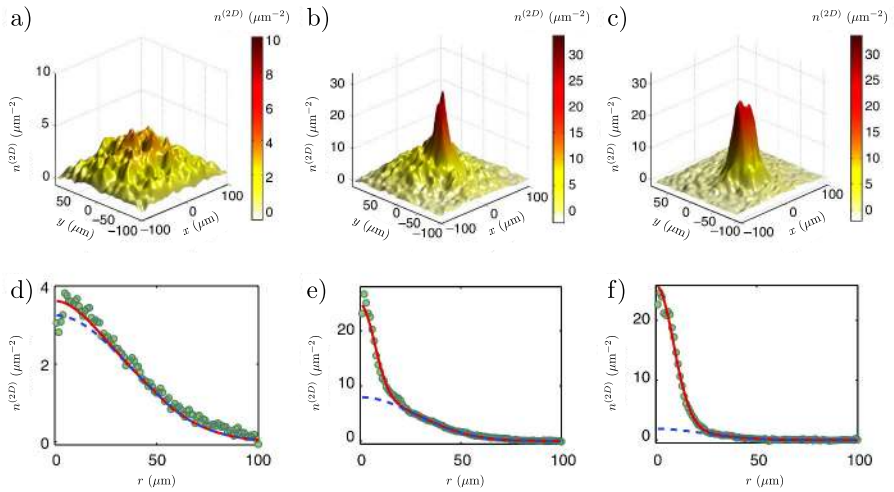

Figure 3.4: Surface density distribution $\rho(x, y)$ (first row) and corresponding radial distributions (green symbols) obtained by azimuthal average (second row). The distribution is measured after a 12 ms time-of-flight for a gas initially confined in a square of size $L = 24\,\mu$m, with a trapping frequency $\omega_z/2\pi = 365$ Hz along the z direction. The temperatures T and atom numbers N for these three realizations are (a) and (d): (155 nK, 28 000), (b) and (e): (155 nK, 38 000), (c) and (f): (31 nK, 19 000). The continuous red lines are fits to the data by a function consisting in the sum of two Gaussians corresponding to N_1 and N_2 atoms ($N = N_1 + N_2$). The Gaussian of largest width (N_2 atoms) is plotted as a blue dashed line. The bimodal parameter $\Delta = N_1/N$ equals (a) and (d): 0.01, (b) and (e): 0.12 and (c) and (f): 0.60.

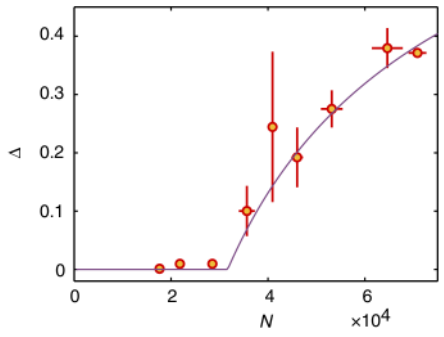

Figure 3.5: Variation of Δ with N for a gas in the same initial trapping configuration as figure 3.4 (a) and (d) and for $T = 155$ nK (red symbols). Error bars are the standard errors of the mean of the binned data set (with 4 images per point on average). The solid line is a fit to the data by the function $f(N) = (1 - (N_c/N)^{0.6})$ for$N > N_c$, and $f(N) = 0$ for $N \leqslant N_c$, from which we deduce $N_c(T)$. Here $N_c = 3.2\,(1) \times 10^4$, where the uncertainty range is obtained by a jackknife resampling method, i. e.fitting samples corresponding to a randomly chosen fraction of the global data set.

of two Gaussians of independent sizes and amplitudes, containing N_1 and N_2 atoms, respectively (see figure 3.4d–f). We consider the *bimodality parameter*

$$\Delta = N_1/N \tag{3.7}$$

defined as the ratio of the number of atoms N_1 in the sharpest Gaussian to the total atom number

$$N = N_1 + N_2 \tag{3.8}$$

A typical example for the variations of Δ with N at a given temperature is shown in figure 3.5 for an initial gas with a square shape (side length $L = 24\,\mu$m). It shows a a sharp crossover, with essentially no bimodality ($\Delta \ll 1$) below a critical atom number $N_c(T)$ and a fast increase of Δ for $N > N_c(T)$. We extract the value $N_c(T)$ by fitting the function

$$\Delta \propto (1 - (N_c/N)^{0.6}) \tag{3.9}$$

to the data. We chose this function as it provides a good representation of the predictions for an ideal Bose gas in similar conditions as explained in the following subsection.

3.2.1.3 *Choosing the fit function*

We estimate the behavior of $\Delta(N)$ at fixed T using Bose law for a ideal gas. We compute from Equation 1.6 the equilibrium velocity distribution $\tilde{n}(\boldsymbol{v})$. Then we estimate the spatial density after a ToF of duration τ (for a disk trap of radius R) via

$$n(\boldsymbol{r}) \propto \tilde{n}(\boldsymbol{r}/\tau) * \Theta\,(r \leqslant R) \tag{3.10}$$

where $*$ stands for the convolution operator and Θ for the Heaviside function. We fit $n(\boldsymbol{r})$ to a double Gaussian and compute the atom fraction in the sharpest Gaussian Δ, similarly to the processing of experimental data. To simulate our experimental results, we consider $\nu_z = 350\,$Hz, $R = 12\,\mu$m, $\tau = 14\,$ms and T varying from 100 to 250 nK.

For a given T, we record Δ while varying the total atom number N from 0.06 to 4 times the theoretical critical number for the transverse condensation $N_{c,th} = \zeta(\pi^2/6)\mathcal{A}/\lambda_{dB}^2$ (see chapter 1). We fit $\Delta(N)$ between $N_{min} = 0.06\ N_{c,th}$ and a varying N_{max} in 1.1 – 4 $N_{c,th}$, to $f(N) = \left(1 - (N_c/N)^{\alpha}\right)$ with N_c as a free parameter and a fixed α. For all considered T and N_{max}, choosing $\alpha = 0.6$ provides both a good estimate of N_c (between 0.93 and 0.99 $N_{c,th}$) and a satisfactory fit (average coefficient of determination 0.94).

3.2.2 *Phase coherence revealed by matter-wave interference*

Matter-wave interferences between independent atomic or molecular clouds is a powerful tool to monitor the emergence of extended coherence[17, 44, 55, 136, 137]. To observe these interferences in our uniform setup, we first produced two independent gases of similar density and temperature confined in two coplanar parallel rectangles, separated by a distance of 4.5 μm along the x direction (see

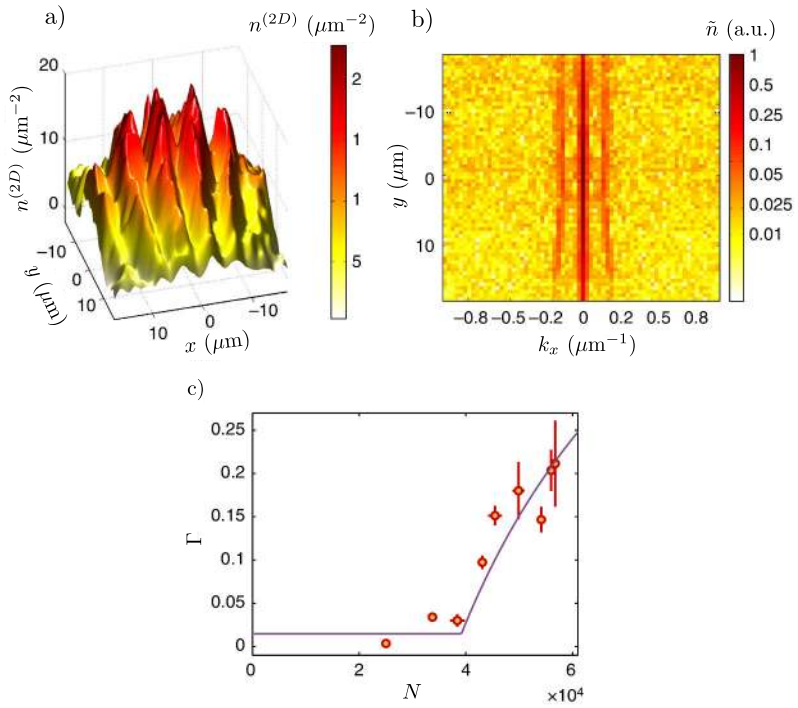

Figure 3.6: (a) Example of a density distribution after a 16 ms in–plane expansion of two coplanar clouds initially confined in rectangular boxes of size $24 \times 12\,\mu\text{m}^2$, spaced by $d = 4.5\,\mu$m ($\nu_z = 365$ Hz). The region of interest considered in our analysis consists of 56 lines and 74 columns (pixel width: $0.52\,\mu$m). (b) Amplitude of the 1D Fourier transform of each line of the density distribution. Each line y shows two characteristic side peaks at $\pm k_p(y)$ above the background noise, corresponding to the fringes pattern of (a). Here $\langle k_p \rangle = 0.17(2)\,\mu\text{m}^{-1}$. (c) Variation of the average contrast Γ (see text for its definition) for images of gases at $T = 155$ nK. Error bars show the standard errors of the mean of the binned data set (with on average 3 images per point). The solid line is a fit to the data of the function $f(N)$ defined as $f(N) = b$ for $N \leq N_c$ and $f(N) = b + a\ (1 - (N_c/N)^{0.6})$ for $N > N_c$. The parameter b is a constant for a data set with various T taken in the same experimental conditions. Here we deduce $N_c = 3.9\,(2) \times 10^4$, where the uncertainty range is obtained by a jackknife resampling method.

figure 3.3c). Then we suddenly released the box potential providing confinement in the xy plane, while keeping the confinement along the z direction (2D ToF). The latter point ensures that the atoms stay in focus with our imaging system, which allows us to observe interference fringes with a good resolution in the region where the two clouds overlap. A typical interference pattern is shown in figure 3.6a), where the fringes are (roughly) parallel to the y axis, and show some waviness that is linked to the initial phase fluctuations of the two interfering clouds.

We use these interference patterns to characterize quantitatively the level of coherence of the gases initially confined in the rectangles. For each line y of the pixelized image acquired on the CCD camera, we compute the x-Fourier transform $\tilde{n}(k, y)$ of the spatial density $n(x, y)$ (figure 3.6b). For a given y this function is peaked at a momentum $k_p(y) > 0$ that may depend (weakly) on the line index y. Then we consider the function that characterizes the correlation of the complex fringe contrast $\tilde{n}[k_p(y), y]$ along two lines separated by a distance d

$$\gamma(d) = \left| \, \langle \, \tilde{\rho}[k_p(y), y \,] \, \tilde{\rho}^*[k_p(y+d), y+d \,] \, \rangle \, \right| \tag{3.11}$$

Here * denotes the complex conjugation and the average is taken over the lines y that overlap with the initial rectangles. If the initial clouds were two infinite, parallel lines with the same $G_1(y)$, one would have $\gamma(d) = |G_1(d)|^2$ [138]. Here the non-zero extension of the rectangles along x and their finite initial size along y make it more difficult to provide an analytic relation between γ and the initial $G_1(r)$ of the gases. However $\gamma(d)$ remains a useful and quantitative tool to characterize the fringe pattern. For a gas described by Boltzmann statistics, the width at $1/e$ of $G_1(r)$ is $\lambda_{\mathrm{dB}}/\sqrt{\pi}$ and remains below $1\,\mu$m for the temperature range investigated in this work. Since we are interested in the emergence of coherence over a scale that significantly exceeds this value, we use the following average as a diagnosis tool

$$\Gamma = \langle \gamma(d) \rangle, \text{average taken over the range } 2\,\mu\text{m} < d < 5\,\mu\text{m} \tag{3.12}$$

For the parameter Γ to take a value significantly different from 0, one needs a relatively large contrast on each line, and relatively straight fringes over the relevant distances d, so that the phases of the different complex contrasts do not average out. For a given temperature T, the variation of Γ with N shows the same threshold-type behaviour as the bimodality parameter Δ. One example is given in figure 3.6c), from which we infer the threshold value for the atom number $N_c(T)$ needed to observe interference fringes with a significant contrast.

3.2.3 *Scaling laws for the emergence of coherence*

We have plotted in figure 3.7 the ensemble of our results for the threshold value of the total 2D phase-space-density $\mathcal{D}_c \equiv N_c \lambda_{\mathrm{dB}}^2/\mathcal{A}$ as a function of $\zeta = k_B T/h\nu_z$, determined both from the onset of bimodality as in figure 3.5 (closed symbols) or from the onset of visible interference as in figure 3.6c) (open symbols). Two trapping configurations have been used along the z direction,

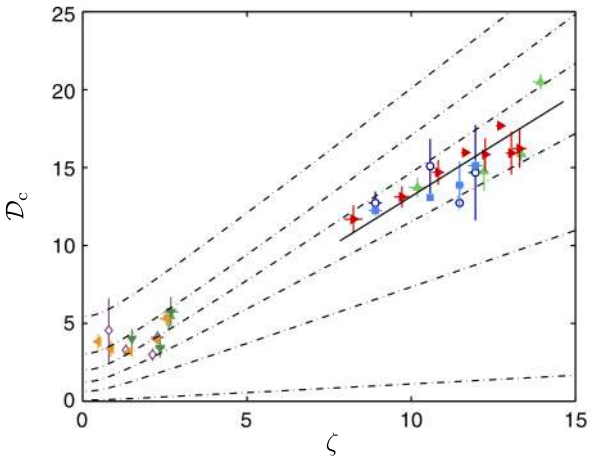

Figure 3.7: Variation of the threshold phase-space-density $\mathcal{D}_c = N_c \lambda_{dB}^2/\mathcal{A}$ for observing a non-Gaussian velocity distribution (full symbols) and distinct matter-wave interferences (open symbols), as a function of the dimensionless parameter $\zeta = k_B T/(\hbar\omega_z)$. For velocity distribution measurements: $\omega_z/2\pi = 365\,\text{Hz}$: disk of radius $R = 12\,\mu\text{m}$ (red right triangles), disk of $R = 9\,\mu\text{m}$ (light green up triangle), square of $L = 24\,\mu\text{m}$ (blue square), $\omega_z/2\pi = 1460\,\text{Hz}$: disk of $R = 12\,\mu\text{m}$ (orange right triangles), disk of $R = 9\,\mu\text{m}$ (dark green down triangles). For interference measurements: $\omega_z/2\pi = 365\,\text{Hz}$: dark blue open circles, $\omega_z/2\pi = 1460\,\text{Hz}$: violet open diamonds. Error bars show the 95% confidence bounds on the N_c parameter of the threshold fits to the data sets. The black solid line shows a linear fit to the data for $\zeta > 8$, leading to $\mathcal{D}_c = 1.4\,(3)\,\zeta$. The black dash-dotted lines show contours of identical ratios of the coherence range to the thermal wavelength λ_{dB}. The coherence range is evaluated by the value of r at which $G_1(r) = G_1(0)/20$ (see text) and we plot (in increasing $\mathcal{D}_{tot}$ order) ratios equal to 1, 1.2, 1.5, 2, 3 and 8. Boltzmann prediction corresponds to a ratio of ~ 0.98.

$\omega_z/2\pi = 1460\,\mathrm{Hz}$ and $\omega_z/2\pi = 365\,\mathrm{Hz}$. In the first case, the z direction is nearly frozen for the temperatures studied here ($\zeta \lesssim 2$). In the second one, the z direction is thermally unfrozen ($\zeta \gtrsim 8$). All points approximately fall on a common curve, independent of the shape and the size of the gas: $\mathcal{D}_c$ varies approximately linearly with ζ with the fitted slope $1.4\,(3)$ for $\zeta \gtrsim 8$ and approaches a finite value ~ 4 for $\zeta \lesssim 2$.

In the frozen case, a majority of atoms occupy the vibrational ground state $j_z = 0$ of the motion along the z direction, so that $\mathcal{D}$ essentially represents the 2D phase-space-density associated to this single transverse quantum state (see chapter 1). Then for $\mathcal{D} \geq 1$, we know from Equation 1.47 and the associated discussion that a broad component arises in G_1 with a characteristic length ℓ that increases exponentially with the phase-space-density. The observed onset of extended coherence around $\mathcal{D} \sim 4$ can be understood as the place where ℓ starts to exceed significantly λ_{dB}. The regime around $\mathcal{D} \sim 4$ is reminiscent of the presuperfluid state identified in [45, 86]. It is different from the truly superfluid phase, which is expected at a higher phase-space-density ($\mathcal{D} \sim 8$) for our parameters [99]. Therefore the threshold $\mathcal{D}_c$ is not associated to a true phase transition, but to a crossover where the spatial coherence of the gas increases rapidly with the control parameter N.

For $\omega_z/2\pi = 365\,\mathrm{Hz}$, the gas is in the "unfrozen regime" ($\zeta \gg 1$), which could be naively thought as irrelevant for 2D physics since according to Boltzmann statistics, many vibrational states along z should be significantly populated. However thanks to the transverse condensation phenomenon presented in chapter 1, a macroscopic fraction of the atoms can accumulate in the $j_z = 0$ state. This happens when the total phase-space-density exceeds the threshold for transverse condensation:

$$\mathcal{D}_{\mathrm{tot,c}} \approx \frac{\pi^2}{6}\,\zeta. \tag{3.13}$$

In the limit $\zeta \to \infty$, the transverse condensation corresponds to a phase transition of the same nature as the ideal gas BEC in 3D. In the present context of our work, we emphasize that although transverse condensation originates from the saturation of the occupation of the excited states along z, it also affects the coherence properties of the gas in the xy plane. In particular when $\mathcal{D}$ rises from 0 to $\mathcal{D}_c$, the coherence length in xy increases from $\sim \lambda_{\mathrm{dB}}$ (the non-degenerate result) to $\sim a_{\mathrm{ho}}$, the size of the ground state of the z motion. This increase can be interpreted by noting that when transverse condensation occurs (equation 3.13), the 3D spatial density in the central plane ($z = 0$) is equal to $g_{3/2}(1)/\lambda_{\mathrm{dB}}^3$, where g_s is the polylogarithm of order s and $g_{3/2}(1) \approx 2.612$. For an infinite uniform 3D Bose gas with this density, a true Bose-Einstein condensation occurs and the coherence length diverges. Because of the confinement along the z direction, such a divergence cannot occur in the present quasi-2D case. Instead, the coherence length along z is by essence limited to the size a_{ho} of the $j_z = 0$ state. When $\mathcal{D} = \mathcal{D}_c$ the same limitation applies in the transverse plane, giving rise to coherence volumes that are grossly speaking isotropic. When $\mathcal{D}$ is increased further, the coherence length in the xy plane increases, while remaining limited to a_{ho} along the z direction. The results shown in figure 3.7 are in line with this reasoning. For $\zeta \gg 1$, the emergence of coherence in the xy plane

occurs for a total phase-space-density $\mathcal{D}_c \propto \zeta$, with a proportionality coefficient $\alpha = 1.4\,(3)$ in good agreement with the prediction $\pi^2/6 \approx 1.6$ of equation 3.13.

We have also plotted in figure 3.7 contour lines characterizing the coherence range in terms of ζ and $\mathcal{D}$. Using ideal Bose gas theory, we calculated the one-body coherence function $G_1(r)$ and determined the distance r_f over which it decreases by a given factor f with respect to $G_1(0)$ (see also subsection 1.2.3). We choose the value $f = 20$ to explore the long tail that develops in G_1 when phase coherence emerges. The contour lines shown in figure 3.7 correspond to given values of r_{20}/λ_{dB}; they should not be considered as fits to the data, but as an indication of a coherence significantly larger than the one obtained from Boltzmann statistics (for which $r_{20} \approx \lambda_{dB}$). The fact that the threshold phase-space densities $\mathcal{D}_c$ follow quite accurately these contour lines validates the choice of tools (non Gaussian velocity distributions, matter-wave interferences) to characterize the onset of coherence.

3.3 CREATION OF TOPOLOGICAL DEFECTS BY QUENCH COOLING THE GAS

As explained in chapter 2, for a system undergoing a phase transition, a lot of information can be retrieved from studying the freezing out dynamics during a quench cooling as described by the Kibble-Zurek (KZ) mechanism. The density and scaling of topological defects with the quench duration can indicate which transition is being crossed and leading to the appearance of phase domains.

The Kibble-Zurek mechanism has already been experimentally studied in a variety of systems, such as liquid crystals[139], helium [140, 141], ion chains [142, 143], superconducting loops [144], hydrodynamic systems [145] and Bose-Einstein condensates [67, 68, 146, 147].

Here, we use the flexibility of our method to produce box potentials of different shapes to study this mechanism. In particular, having a uniform system brings us closer to the original proposal and scalings by Kibble and Zurek. However, note that recent experimental and theoretical studies have investigated the influence of introducing a harmonic trap on the Kibble-Zurek scaling [67, 142, 146, 148, 149].

We study the appearance of topological defects by quench cooling a gas of atoms in two different configurations. First, point vortices are revealed in short time-of-flight experiments. Second, supercurrents (i. e. phase windings) created in a ring of atoms are studied interferometrically by using a trap potential shaped as a "target" with a disk of atoms surrounded by a ring (see figure 3.3d). The preparation of the gas is similar for both cases and the scaling of the number of topological defects is recorded as a function of the quench duration to compare it to the predictions of the KZ mechanism (see chapter 2).

3.3.1 *Vortices in square geometries*

The text of this subsection was originally published in [82].

3.3.1.1 *Observation of topological defects*

From now on we use the weak trap along z ($\omega_z/2\pi = 365\,\mathrm{Hz}$) so that the onset of extended coherence is obtained thanks to the transverse condensation phenomenon. We are interested in the regime of strongly degenerate, interacting gases, which is obtained by pushing the evaporation down to a point where the residual thermal energy $k_B T$ becomes lower than the chemical potential μ (see 3.1.3.4). The final box potential is $\sim k_B \times 40\,\mathrm{nK}$, leading to an estimated temperature of $\sim 10\,\mathrm{nK}$, whereas the final density ($\sim 50\,\mu\mathrm{m}^{-2}$) leads to $\mu \approx k_B \times 14\,\mathrm{nK}$. In these conditions, for most realizations of the experiment, defects are present in the gas. They appear as randomly located density holes after a short 3D ToF (figure 3.8), with a number fluctuating between 0 and 5. To identify the nature of these defects, we have performed a statistical analysis of their size and contrast, as a function of their location and of the ToF duration τ (figure 3.8 c and d, and next subsection). For a given τ, all observed holes have similar sizes and contrasts. The core size increases approximately linearly with τ, with a nearly 100 % contrast. This favours the interpretation of these density holes as single vortices, for which the 2π phase winding around the core provides a topological protection during the ToF. This would be the case neither for vortex–antivortex pairs nor phonons, for which one would expect large fluctuations in the defect sizes and lower contrasts.

3.3.1.2 *Analysis of the density holes created by the vortices*

We first calculate the normalized density profile $n/\bar{n}$ where the average $\bar{n}$ is taken over the set of images with the same ToF duration τ. Then we look for density minima with a significant contrast and size. Finally for each significant density hole, we select a square region centered on it with a size that is ~ 3 times larger than the average hole size for this τ. In this region, we fit the function

$$A_0 \left[1 - c + c \tanh\left(\sqrt{x^2 + y^2}/\xi\right)\right] \tag{3.14}$$

to the normalized density profile, where A_0 accounts for density fluctuations. We also correct for imaging imperfections (finite imaging resolution and finite depth of field) by performing a convolution of the function defined in equation 3.14 by a Gaussian of width $1\,\mu\mathrm{m}$, which we determined from a preliminary analysis.

3.3.1.3 *Dynamical origin of the topological defects*

In principle the vortices observed in the gas could be due to steady-state thermal fluctuations. BKT theory indeed predicts that vortices should be present in an interacting 2D Bose gas around the superfluid transition point [85]. Such "thermal" vortices have been observed in non-homogeneous atomic gases, either interferometrically [44] or as density holes in the trap region corresponding to the critical region [133]. However, for the large and uniform phase-space densities that we obtain at the end of the cooling process ($n\lambda_{dB}^2 \geq 100$), Ref. [152] predicts a vanishingly small probability of occurrence for such thermal excitations. This supports a dynamical origin for the observed defects.

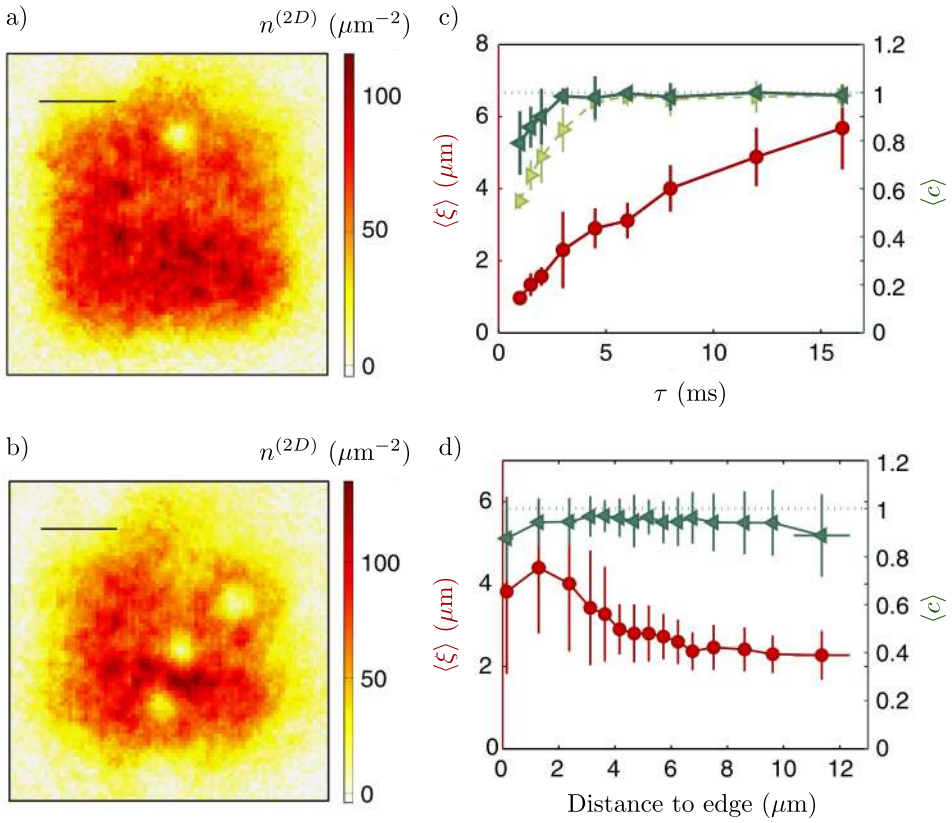

Figure 3.8: (a) and (b): Examples of density distributions after a 3D ToF of $\tau = 4.5\,\mathrm{ms}$ for a gas initially confined in a square of size $L = 30\,\mu\mathrm{m}$ ($\omega_z/2\pi = 365\,\mathrm{Hz}$). The two examples show respectively one (a) and three (b) holes of high contrast, corresponding to topologically protected expanding vortex cores. We fit each density hole by a hyperbolic tangent dip convoluted by a Gaussian of waist $w = 1\,\mu\mathrm{m}$ accounting for imaging imperfections (see subsection 3.3.1.2). (c) Evolution of the average size ξ (red circles, left labels) and contrast c (green triangles, right labels) of density holes with the expansion duration τ. No holes are visible for $\tau \lesssim 0.5\,\mathrm{ms}$. Red circles and dark green left triangles are results from a fit accounting for imaging imperfections while light green right triangles show contrast resulting from a fit without a convolution by a Gaussian. (d) Variation of the hole size ξ (red circles, left labels) and contrast c (green triangles, right labels) with the distance to the nearest edge of the box (same configuration than (a) and (b) : ToF of $\tau = 4.5\,\mathrm{ms}$ for a gas in a square of $L = 30\,\mu\mathrm{m}$). For a distance larger than $\sim 4\,\mu\mathrm{m}$, ξ and c are approximately independent from the vortex location. The average values in (c) are taken over all holes independent of their positions. One point in (c) (resp. d) corresponds to 15 (resp. 70) vortex fits. Error bars show standard deviations of the binned data set.

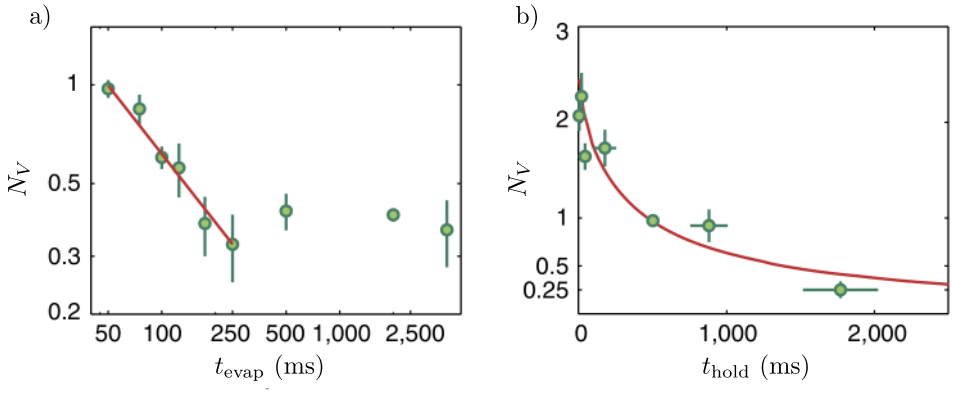

Figure 3.9: (a) Circle symbols: evolution of the mean vortex number N_V with the quench time t_{evap} (fixed $t_{\mathrm{hold}} = 500\,\mathrm{ms}$) for a gas initially confined in a square of size $L = 30\,\mu\mathrm{m}$ ($\omega_z/2\pi = 365\,\mathrm{Hz}$) and observed after a 3D ToF of $\tau = 4.5\,\mathrm{ms}$. The number of images per point ranges from 37 to 233, with a mean of 90. We restrict to $t_{\mathrm{evap}} \geqslant 50\,\mathrm{ms}$ to ensure that local thermal equilibrium is reached at any time during the evaporation ramp [150]. Red line: fit of a power-law decay to the short time data ($t_{\mathrm{evap}} \leq 250\,\mathrm{ms}$), giving the exponent $d = 0.69\,(17)$. The uncertainty range on d is the 95% confidence bounds of a linear fit to the evolution of $\log(N_V)$ with $\log(t_{\mathrm{evap}})$. For longer quench times, the mean vortex numbers are compatible with a plateau at $N_{\mathrm{V}} = 0.35\,(5)$. (b) Circle symbols: evolution of the mean vortex number N_V with the hold time t_{hold} (fixed $t_{\mathrm{evap}} = 50\,\mathrm{ms}$) in the same experimental configuration as (a). The number of images per point ranges from 24 to 181, with a mean of 59. In both figures error bars are obtained from a bootstrapping approach. Red line: results from a model describing the evolution of an initial number of vortices $N_{\mathrm{V},0} = 2.5(2)$ in the presence of a phenomenological damping coefficient [151]. The inferred superfluid fraction is $0.94\,(2)$. Confidence ranges on these parameters are obtained from a χ^2-analysis.

To investigate further this interpretation, we can vary the two times that characterize the evolution of the gas, the duration of evaporation t_{evap} and the hold duration after evaporation t_{hold} (see figure 3.1). For the results presented in this section, we fixed $t_{\mathrm{hold}} = 500\,\mathrm{ms}$ and studied the evolution of the average vortex number N_V as a function of t_{evap}. The corresponding data, given in figure 3.9a), show a decrease of N_V with t_{evap}, passing from $N_V \approx 1$ for $t_{\mathrm{evap}} = 50\,\mathrm{ms}$ to $N_V \approx 0.3$ for $t_{\mathrm{evap}} = 250\,\mathrm{ms}$. For longer evaporation times, N_V remains approximately constant around $0.35\,(5)$.

The decrease of N_V with t_{evap} suggests that the observed vortices are nucleated via a Kibble–Zurek (KZ) type mechanism [106, 107, 153], occurring when the transition to the phase coherent regime is crossed. However applying the KZ formalism to our set-up is not straightforward. In a weakly interacting, homogeneous 3D Bose gas, BEC occurs when the 3D phase-space-density reaches the critical value $g_{3/2}(1)$. For our quasi-2D geometry, transverse condensation occurs when the 3D phase-space-density in the central plane $z = 0$ reaches this value. At the transition point, the KZ formalism relates the size of phase-coherent domains to the cooling speed $\dot{T}$. For fast cooling, KZ theory predicts domain sizes for a 3D fluid that are smaller than or comparable to the thickness a_{ho} of the lowest vibrational state along z; it can thus provide a good description of our system. For a slower cooling, coherent domains much larger than a_{ho} would be expected in 3D at the transition point. The 2D nature of our gas leads in this case to a reduction of the in-plane correlation length. In the slow cooling regime, we thus expect to find an excess of topological defects with respect to the KZ prediction for standard 3D BEC.

More explicitly we expect for fast cooling, hence short t_{evap}, a power-law decay $N_V \propto t_{\mathrm{evap}}^{-d}$ with an exponent d given by the KZ formalism for 3D BEC. The fit of this function to the measured variation of N_V for $t_{\mathrm{evap}} \leq 250\,\mathrm{ms}$ leads to $d = 0.69\,(17)$ (see figure 3.9a). This is in good agreement with the prediction $d = 2/3$ obtained from the critical exponents of the so-called "F model" (see [105], subsubsection 2.1.1.5 and subsubsection 2.1.2.3), which is believed to describe the universality class of the 3D BEC phenomenon. For comparison, the prediction for a pure mean-field transition, $d = 1/2$, is notably lower than our result.

For longer t_{evap}, the above described excess of vortices due to the quasi-2D geometry should translate in a weakening of the decrease of N_V with t_{evap}. The non-zero plateau observed in figure 3.9a) for $t_{\mathrm{evap}} \geq 250\,\mathrm{ms}$ may be the signature of such a weakening. Other mechanisms could also play a role in the nucleation of vortices for slow cooling. For example due to the box potential residual rugosity, the gas could condense into several independent patches of fixed geometry, which would merge later during the evaporation ramp and stochastically form vortices with a constant probability.

3.3.1.4 *Lifetime of the topological defects*

The variation of the number of vortices N_V with the hold time t_{hold} allows one to study the fate of vortices that have been nucleated during the evaporation. We show in figure 3.9b) the results obtained when fixing the evaporation to a short value $t_{\mathrm{evap}} = 50\,\mathrm{ms}$. We observe a decay of N_V with the hold time,

from $N_V = 2.3$ initially to 0.3 at long t_{hold} (2 s). To interpret this decay, we modelled the dynamics of the vortices in the gas with two ingredients: (i) the conservative motion of a vortex in the velocity field created by the other vortices, including the vortex images from the boundaries of the box potential [154], (ii) the dissipation induced by the scattering of thermal excitations by the vortices, which we describe phenomenologically by a friction force that is proportional to the non-superfluid fraction of atoms in the gas [151]. During this motion, a vortex annihilates when it reaches the edge of the trap or encounters another vortex of opposite charge. The numerical solution of this model leads to a non-exponential decay of the average number of vortices, with details that depend on the initial number of vortices and their locations.

Assuming a uniform random distribution of vortices at the end of the evaporation, we have compared the predictions of this model to our data. It gives the following values of the two adjustable parameters of the model, the initial number of vortices $N_{\mathrm{V},0} = 2.5\,(2)$ and the superfluid fraction $0.94\,(2)$; the corresponding prediction is plotted as a continuous line in figure 3.9b). We note that at short t_{hold}, the images of the clouds are quite fuzzy, probably because of non-thermal phononic excitations produced (in addition to vortices) by the evaporation ramp. The difficulty to precisely count vortices in this case leads to fluctuations of N_V at short t_{hold} as visible in figure 3.9b). The choice $t_{\mathrm{hold}} = 500\,\mathrm{ms}$ in figure 3.9a) was made accordingly.

The finite lifetime of the vortices in our sample points to a general issue that one faces in the experimental studies on the KZ mechanism. In principle the KZ formalism gives a prediction on the state of the system just after crossing the critical point. Experimentally we observe the system at a later stage, at a moment when the various domains have merged, and we detect the topological defects formed from this merging. In spite of their robustness, the number of vortices is not strictly conserved after the crossing of the transition and its decrease depends on their initial positions. A precise comparison between our results and KZ theory should take this evolution into account, for example using stochastic mean-field methods [155–158].

3.3.2 *Supercurrents in ring geometries*

The text of this subsection was originally published in [159].

Fluids in annular geometry are ideally suited to investigate the role of topological numbers in quantum mechanics. The phase winding of the macroscopic wavefunction around the annulus must be a multiple of 2π, ensuring the quantization of the circulation of the fluid velocity. The resulting supercurrents have been observed in superfluid systems such as superconductors [160], liquid helium [161] and atomic gases [51, 162]. Studying these currents is crucial for the understanding of quantum fluids, as well as for realizing sensitive detectors like magnetometers [163] and rotation sensors [164].

Supercurrents in annular atomic Bose-Einstein condensates are usually created in a deterministic way by using laser beams to impart angular momentum on the atoms [51, 53, 162] or by rotating a weak link along the annulus [165]. Supercurrents can also have a stochastic origin. They may result from thermal

fluctuations or appear as topological defects following a rapid quench of the system. The latter mechanism was put forward by Kibble and Zurek, who studied the phase patterns that emerge in a fluid, when it undergoes a fast crossing of a phase transition point [106, 107].

For a superfluid confined in a ring geometry, which is the configuration originally considered by Zurek [107], the frozen phase of the wavefunction may lead to a supercurrent of charge q, i.e. a $2\pi q$ phase winding along the ring. In this section, we study a setup realizing this *gedanken* experiment using a quasi two-dimensional Bose gas trapped in an annular geometry. For each realization of the experiment, we use matter-wave interference between this annulus and a central disk acting as a phase reference, to measure the charge as well as the direction of the random supercurrent [4].

3.3.2.1 *Experimental sequence*

Our experiments are performed with a Bose gas of ^{87}Rb atoms. Along the vertical z direction the gas is confined using a harmonic potential with frequency $\omega_z/2\pi = 370\,\mathrm{Hz}$ (see section 3.1.2). In the horizontal xy plane, the atoms are trapped in the dark regions of a "box-potential" beam, engineered using an intensity mask located in a plane optically conjugated to the atom cloud (see figure 3.2 and 3.3e). We use a target-like mask, consisting of a disk of radius $R_0 = 4.5\,\mu\mathrm{m}$ surrounded by a ring of inner (resp. outer) radius of $R_{\mathrm{in}} = 9\,\mu\mathrm{m}$ (resp. $R_{\mathrm{out}} = 15\,\mu\mathrm{m}$) (figure 3.3d).

The typical time sequence for preparing the gas starts by loading a gas with a 3D phase-space density ≈ 2.4 slightly below the condensation threshold[5] with the box-potential beam at its maximal power. Then we linearly lower this power by a factor ~ 50 in a time t_{evap} to evaporatively cool the atomic cloud and cross the superfluid transition [100]. Last we keep the atoms at a constant box potential depth during a time t_{hold}. The final temperature is $\sim 10\,\mathrm{nK}$ (see subsection 3.1) with similar surface densities in the ring and the disk: $n \sim 80\,\mu\mathrm{m}^{-2}$. The typical interaction energy per atom is $E_{\mathrm{int}}/k_{\mathrm{B}} \approx 8\,\mathrm{nK}$, and the gas is marginally quasi-2D with $k_{\mathrm{B}}T$, $E_{\mathrm{int}} \sim \hbar\omega_z$. These parameters correspond to a large 2D phase-space density, $\mathcal{D} = n\lambda_{\mathrm{dB}}^2 \geqslant 100$, so that the gas is deeply in the superfluid regime at the end of the evaporation ramp.

At the end of the sequence, using the technique described in subsection 3.1.3.4 the chemical potential is computed for a disk-shaped trap of $R = 12\,\mu\mathrm{m}$ with $N_{\mathrm{at}} = 36\,000$ atoms (corresponding to the same surface density as in the experiments presented here: $n^{(2\mathrm{D})} = 80\,\mu\mathrm{m}^{-2}$). We find $E_{\mathrm{int}}/N_{\mathrm{at}} \approx k_B \times 8\,\mathrm{nK}$. We also checked that the residual anticonfinement along the y direction has little influence on the equilibrium distribution.

The fastest ramp of the box-potential beam we use (25 ms) is still slow enough for the evaporation process to take place and to identify this ramping down as a quench of the temperature of the system: we calculated the typical elastic collision time when crossing the transition to be a few milliseconds [150].

4 A similar method has recently been developed to investigate the supercurrent generated by a rotating weak link [166]

5 The estimated total atom number 76000 and the temperature is 210 nK. With these parameters, we never observe any interference fringes such as those of figure 3.10.

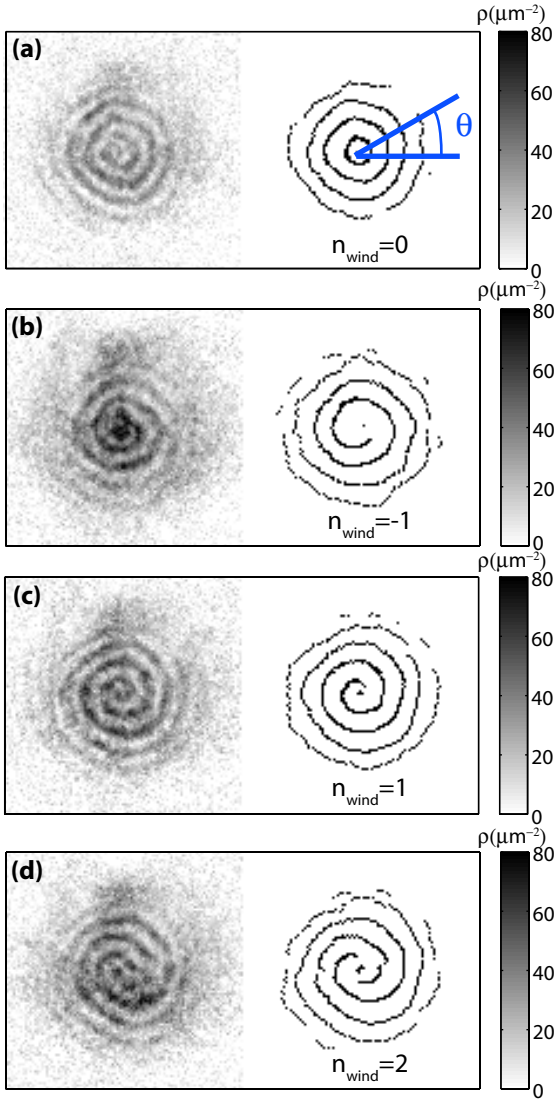

Figure 3.10: Experimental interference patterns. Examples of interference patterns after expansion in the 2D plane, along with constrast-amplified pictures. (a) without phase winding, (b) with phase winding -2π, (c) with phase winding $+2\pi$, (d) with phase winding $+4\pi$.

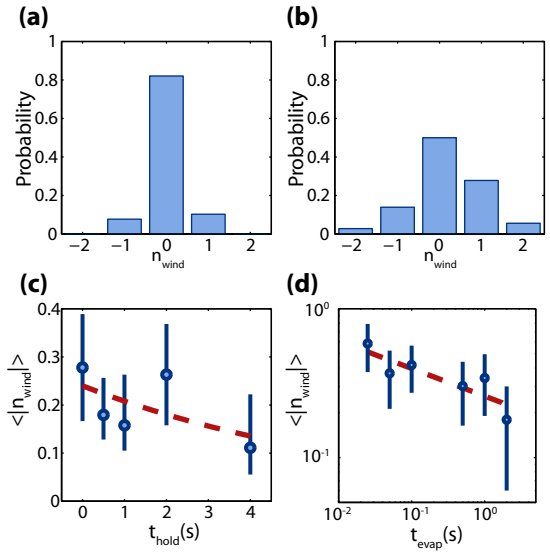

Figure 3.11: Study of the winding number. (a) and (b) Histograms showing the statistical appearance of winding number n_{wind} for $t_{\mathrm{hold}} = 0.5\,\mathrm{s}$. (a) We show the result of 39 realizations for $t_{\mathrm{evap}} = 2\,\mathrm{s}$. We get $\langle n_{\mathrm{wind}} \rangle = 0.03\,(8)$. (b) We show the result of 36 realizations for $t_{\mathrm{evap}} = 0.025\,\mathrm{s}$. We get $\langle n_{\mathrm{wind}} \rangle = 0.19\,(14)$. (c) Mean absolute winding number $\langle |n_{\mathrm{wind}}| \rangle$ as a function of hold time ($t_{\mathrm{evap}} = 2\,\mathrm{s}$). The data is fitted with an exponential with a time constant of 7 s. (d) Mean absolute winding number $\langle |n_{\mathrm{wind}}| \rangle$ as a function of evaporation time ($t_{\mathrm{hold}} = 0.5\,\mathrm{s}$) in log-log scale. The line is a power-law fit to the data, $\langle |n_{\mathrm{wind}}| \rangle \propto t_{\mathrm{evap}}^{-\alpha}$, gives $\alpha = 0.19\,(6)$. The uncertainty on $\langle n_{\mathrm{wind}} \rangle$ and the bars on figure (c) and (d) represent the statistical error determined with a bootstrapping approach.

3.3.2.2 *Interferometric detection of the supercurrent*

We use matter-wave interference to probe the relative phase distribution between the cloud in the central disk and the one in the ring. We abruptly switch off the box-potential while keeping the confinement along the z direction. The clouds experience a hydrodynamical expansion during which the initial interaction energy is converted into kinetic energy. After 7 ms of expansion, we record the interference pattern by imaging the atomic gas along the vertical direction. Typical interference patterns are shown in figure 3.10. Most of them consist in concentric rings, as expected for a quasi-uniform phase distribution in the disk and the annulus. However we also observe a significant fraction of spiral patterns, revealing the presence of a phase winding in the wavefunction of one of the two clouds.

We developed an automatized procedure to analyze these patterns, which reconstructs the phase $\phi(\theta)$ of the fringes along a line of azimuthal angle θ (see subsection 3.3.2.3). From the accumulated phase $\Delta\phi$ as the angle θ varies from 0 to 2π, we associate to each pattern a winding number $n_{\mathrm{wind}} = \Delta\phi/2\pi$, which is a positive, null or negative integer. This number is recorded for many realizations of the same experimental sequence. Examples of the probability distribution of n_{wind} are shown on figure 3.11 a and b. The measured histo-

grams are compatible with a zero mean value. The observed asymmetry on figure 3.11 b (mean value is 1.4 times the standard deviation) is compatible with the number of realizations: the probability to have a standard deviation equal or larger than this one is 17%. For example, if we use all the data presented on figure 3.11c and 3.11d we find $\langle n_{\mathrm{wind}} \rangle = 0.002\,(20)$. This confirms the stochastic nature of the mechanism at the origin of this phase winding.

Each data point in figure 3.11 is the average of 15 to 50 realizations. Error bars for the mean absolute winding number are obtained using a bootstrapping approach. From the initial set of data, 10 000 draws with replacement of datasets with the same length as the initial sample are made. For each draw, the mean absolute winding number is calculated. Then, using the bias corrected and accelerated percentile method [167], the one-standard deviation confidence interval is calculated[6].

3.3.2.3 *Reconstruction of the phase profile*

For each picture, the center is determined manually. The shot-to-shot variation of this center is small ($\approx 0.5\,\mu$m) and comparable to the independently measured position stability of the initial cloud. We checked that such an offset on the center does not lead to large modification of the results. Then we proceed in two steps to reconstruct the phase profile, contrast amplification and fit. To amplify the contrast, the pictures are first convoluted by a 2×2 matrix with constant coefficients. This filters out high frequency noise but does not blur the interference pattern. Then radial cuts with angle $\theta \in \{0, 2\pi/n, \cdots, 2\pi(1-1/n)\}$ are performed (typically $n = 150$), and the positions of local maxima are recorded, giving the contrast amplified picture.

To retrieve the phase, we perform a convolution of the contrast amplified picture with a gaussian of width 3 pixels and we fit radial cuts of the convoluted, contrast-amplified pictures with the following function

$$f(r, k, \phi, A, c) = A \sin(kr + \phi) + c \tag{3.15}$$

for points with distance to the center $r \in [r_{\mathrm{min}}, r_{\mathrm{max}}]$. First, the parameter k is left as a free parameter to fit the radial cuts. Then the averaged k_{mean} over all fits is taken as a fixed parameter and all the radial cuts are fitted again. The phase ϕ is recorded as a function of the angle θ of the radial cut.

3.3.2.4 *Location of the phase winding*

The first question that arises is the origin of the observed phase winding, which can be due either to a vortex in the central disk or to a quantized persistent current in the outer ring. We can experimentally eliminate the first possibility by noticing that when doing a 3D ballistic expansion (by switching-off both the box-potential beam and the confining beam in the z direction) we never observe any vortex signature in the small disk of radius $R_0 = 4.5\,\mu$m. By contrast, in larger structures such as the square represented in figure 3.3b), we can detect deep density holes revealing the presence of vortices as presented

6 For more information about bootstrapping, see Appendix D

in subsection 3.3.1. Hence we conclude that the spiral interference patterns of figure 3.10 reveal the presence of a supercurrent in the annulus, whose charge and orientation correspond to the modulus and sign of the winding number n_{wind}. The lifetime of this supercurrent is similar to the cloud lifetime (see figure 3.11c).

3.3.2.5 *Origin of the supercurrent*

We now discuss the origin of the observed supercurrents, which can be either thermal excitations or result from the quench cooling. If these currents had a thermal origin, their probability of occurrence would be given by the Boltzmann law $p(n_{\text{wind}}) \propto \exp\left[-E(n_{\text{wind}}) / k_B T\right]$, where the (kinetic) energy of the supercurrent is

$$E(n_{\text{wind}}) = n_{\text{wind}}^2 \frac{\pi\hbar^2 n^{(2D)}}{m} \ln\left(R_{\text{out}}/R_{\text{in}}\right) \tag{3.16}$$

This leads to

$$p(n_{\text{wind}}) \propto \left(R_{\text{in}}/R_{\text{out}}\right)^{n_{\text{wind}}^2 \mathcal{D}/2} \tag{3.17}$$

which is negligible for $n_{\text{wind}} \neq 0$ for our large phase space densities $\mathcal{D} \geqslant 100$, in clear disagreement with the typical 20-50% of pictures showing phase winding. Note that the probability for a vortex to appear in the central disk as a thermal excitation is even smaller than (3.17) because R_{in} and R_{out} should be replaced respectively by the healing length ($\lesssim 0.5\,\mu$m) and R_0.

To check that the quench cooling is indeed responsible for the formation of these supercurrents, we study the variation of $\langle|n_{\text{wind}}|\rangle$ for evaporation times spanning two orders of magnitude. The comparison between the results for a slow quench (figure 3.11a) and a fast quench (3.11b) show that the latter indeed increases the probability of occurrence of a supercurrent, as expected for the KZ mechanism [106, 107]. We summarize in figure 3.11d) the experimental variation of $\langle|n_{\text{wind}}|\rangle$ with t_{evap}, and find that it increases from 0.2 ($t_{\text{evap}} = 2\,$s) to 0.6 ($t_{\text{evap}} = 0.025\,$s). A power-law fit to the data, inspired by the prediction for the KZ mechanism, leads to $\langle|n_{\text{wind}}|\rangle \propto t_{\text{evap}}^{-\alpha}$ with $\alpha = 0.19\,(6)$.

3.3.2.6 *Comparison with the Kibble-Zurek scenario*

To interpret our results we have developed a simple one-dimensional (1D) model following the KZ scenario presented in [107, 157]. We consider a 1D ring of perimeter L and we assume that, when the normal-to-superfluid transition is crossed, N domains of uniform phase ϕ_j, $j = 1, \ldots, N$ are created. Each run of the experiment is modeled by a set $\{\phi_j\}$, where the phases ϕ_j are independent random variables drawn in $(-\pi, \pi]$ (with $\phi_1 = 0$ by convention). For each set of $\{\phi_j\}$ we calculate the total phase variation along the ring $\Phi = \sum_j \phi_j$ and define n_{wind} as the nearest integer to $\Phi/2\pi$. We then average over many draws of the set $\{\phi_j\}$.

We report on figure 3.12 the result of this calculation of the average absolute winding number $\langle|n_{\text{wind}}|\rangle$ obtained as a function of N the number of domains with different phases. For large values of N we find that $\langle|n_{\text{wind}}|\rangle$ scales like $\sqrt{N}$ as expected for a sum of a large number of independent random variables (see subsubsection 2.2.3.1). Our experimental range $0.2 \leq \langle|n_{\text{wind}}|\rangle \leq 0.6$ is

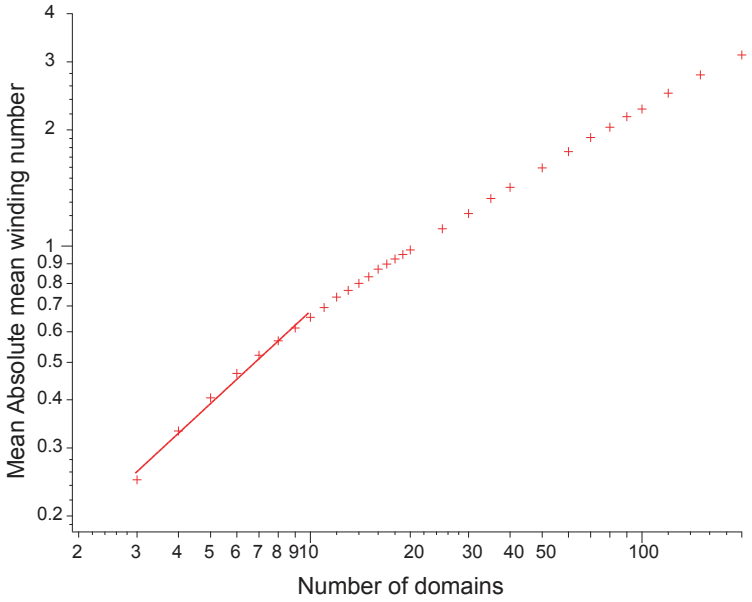

Figure 3.12: Average absolute winding number as a function of the number of phase domains in log-log scale. The points are the results of the simulation and the line is the power-law fit to the relevant points for the experiments described here.

obtained for $3 \leq N \leq 10$; in this range, we do not expect to recover an exact power-law behavior but we can still fit a power-law scaling to our data and get

$$\langle |n_{\text{wind}}| \rangle \propto N^{0.8} \tag{3.18}$$

Then we use the general prediction for the KZ mechanism to relate the typical length $\hat{\xi} = L/N$ of a domain to the quench time t_{evap} (see e.g. [157] and Equation 2.62)

$$\hat{\xi} \propto t_{\text{evap}}^{\nu/(1+\nu z)} \tag{3.19}$$

where ν and z define the universality class of the transition (see section 2.1): ν is the correlation length critical exponent and z the dynamic critical exponent. Using $z = 2$ and $\nu = 1/2$ relevant for a mean-field description of a 1D ring-shaped system [157], we get

$$\hat{\xi} = \frac{L}{N} \propto t_{\text{evap}}^{1/4} \tag{3.20}$$

Combining (3.19) and (3.20), we predict with this simple model

$$\langle |n_{\text{wind}}| \rangle \propto t_{\text{evap}}^{-1/4 \times 0.8} \approx t_{\text{evap}}^{-0.2} \tag{3.21}$$

which is in agreement with the experimental result $\alpha = 0.19\,(6)$.

3.3.2.7 *Discussion*

There are two main assumptions that could limit the validity of this model. First, our system is not uni-dimensional in terms of relevant single particle

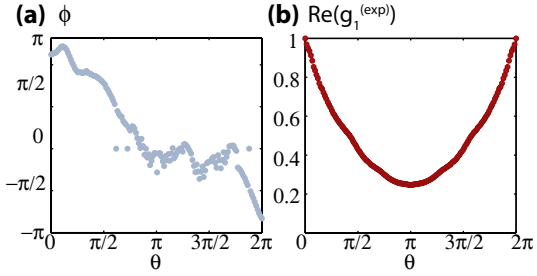

Figure 3.13: Analysis of the phase profiles. (a) Typical phase distribution reconstructed from the phase profile $\phi(\theta)$ of the interference pattern of figure 3.10b showing a winding number of -1. (b) Real value of the angular correlation function reconstructed from the phase of the interference patterns with 18 realizations of $t_{\mathrm{evap}} = 2\,\mathrm{s}$ and $t_{\mathrm{hold}} = 4\,\mathrm{s}$. When $n_{\mathrm{wind}} \neq 0$ the linear phase winding is substracted before computing g_1.

eigenstates. However, we find for our parameters that $\hat{\xi}$ is in the range 7–25 μm[7, 8]; this is always larger than the width of our annulus and justifies the use of a 1D model for describing the phase coherence properties of the gas. Second, this model does not take into account beyond mean-field effects, related to either the finite size of the system or the crossover between standard BEC and the Berezinskii–Kosterlitz–Thouless mechanism. This could change the value of the critical exponents and even lead to deviations with respect to the power-law scaling of (3.19) [168].

3.3.2.8 *Beyond topological defects: measurement of the phase fluctuations*

We show that one can extract information from the interference patterns, which goes beyond the determination of the topological number n_{wind}. In particular the ripples of the fringes are related to the phase distribution of the fluids in the central disk and the ring, which is characterized by the one-body correlation function g_1. This function plays a specially important role for low-dimensional systems, since it indicates how long-range order is destroyed by thermal phonons. To give an estimate of g_1, we study the angular dependance of the phase of the fringes $\phi(\theta)$ as shown on figure 3.13a). In particular we consider the periodic function

$$\delta\phi(\theta) = \phi(\theta) - n_{\mathrm{wind}}\,\theta \tag{3.22}$$

which describes the deviation of the reconstructed phase from a perfect linear winding. We construct the angular correlation function:

$$g_1^{(\mathrm{exp})}(\theta) = \langle e^{i[\delta\phi(\theta') - \delta\phi(\theta'+\theta)]} \rangle_{\theta',\,\mathrm{realizations}} \tag{3.23}$$

where the average is taken over all images irrespective of the value of n_{wind}, and which is expected to be real in the limit of a large number of realizations. A typical example for $\mathcal{R}e[g_1^{(\mathrm{exp})}]$ is given in figure 3.13b), where the minimum

7 An estimate of $\hat{\xi}$ for our geometry is $\pi\,(R_{\mathrm{in}} + R_{\mathrm{out}})/N$

8 We note that $\hat{\xi}$ is then larger than the size R_0 of the central disk. This confirms the fact that we do not expect the presence of vortices in this disk

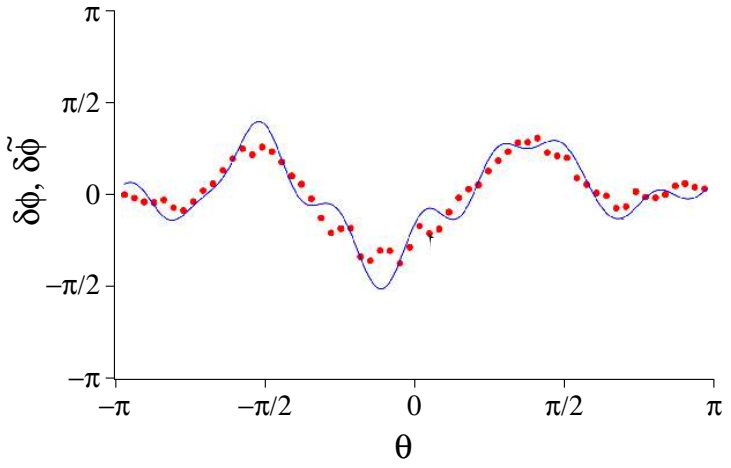

Figure 3.14: Comparison between the phase fluctuations of an initial state in the annulus ($\delta\tilde{\phi}$, solid line) and the phase profile deduced with the interference method used in the experiment ($\delta\phi$, red points).

for $\theta = \pi$ gives an indication of the phase coherence between diametrically opposite points. This measured angular correlation function $g_1^{(\mathrm{exp})}(\theta)$ can be used to reconstruct the first-order correlation function of the gas in the annulus.

To relate quantitatively $g_1^{(\mathrm{exp})}(\theta)$ to the coherence properties of the gas in the ring, two hypotheses are needed: (i) We suppose that the fluid in the central disk acts as a phase reference, so that the ripples of the fringes come essentially from the phase fluctuations in the ring. Indeed the small size of this disk guarantees that phonon modes are only weakly populated. (ii) We assume that the fluctuations of the phase of the fringe pattern directly reflect the phase of the atomic wave function along the ring. This is validated by the following numerical analysis, in which we simulate numerically the hydrodynamical expansion and calculate the wavy interference pattern originating from a given phase distribution along the ring. We use a spatial grid of size $36\,\mu\mathrm{m} \times 36\,\mu\mathrm{m}$ with pixel size $0.52\,\mu\mathrm{m}$. We first compute the ground state of $N_{\mathrm{at}} = 5 \times 10^4$ atoms in the target potential using the Gross-Pitaevskii equation, evolved with the split-step method in imaginary time (time step $10\,\mu\mathrm{s}$). A phase fluctuation $\delta\tilde{\phi}(\theta)$ is then added by hand to the wave function in the ring. We then simulate the hydrodynamical expansion by evolving the Gross-Pitaevskii equation in real time (time step $10\,\mu\mathrm{s}$) during 7 ms. The phase $\delta\phi(\theta)$ of the fringe pattern is finally obtained using the same procedure as for experimental pictures. A comparison between typical phase distributions $\delta\tilde{\phi}(\theta)$ and $\delta\phi(\theta)$ is given in figure 3.14. Both phase profiles are similar confirming that the phase reconstructed from the interference pattern correspond to the in-situ phase of the gas

This correlation function could allow one to extract the evolution of the phonon distribution during the thermalization of the fluid.

3.3.3 *Discussion on possible improvements on the measurements*

We now discuss the possible extensions of this work to a more thorough test of the KZ mechanism. As mentionned in chapter 3 section 2.3, power-law scaling is challenging to test in our situation because of the low value of the exponent (≈ 0.65 in the case of point vortices, ≈ 0.2 in the case of supercurrents) even if we span two orders of magnitude for t_{evap}. The extreme values of this range are experimentally limited:

- The evaporation time t_{evap} should be chosen long enough so that at any given time a local thermal equilibrium is achieved in the cloud.
- The largest evaporation time is set mainly by the cloud lifetime. For long evaporation times, the dynamics of the topological defects (merging of vortices, etc.) should also be taken into account as in section 3.3.1.4. Evaporation ramps that accelerate past the phase transition point can also be used to freeze the dynamics of the order parameter as was done in [68].

These two limits cannot be significantly modified, which fixes the relative range of variation of the number of phase domains. It could nevertheless be interesting to study cases where the freezing-out size $\hat{\xi}$ is much smaller than the typical size of the system L (size of the square, length of the ring). For a given density, the local equilibrium condition limits the lowest value of $\hat{\xi}$. Imprinting larger patterns onto the atoms would increase the ratio $L/\hat{\xi}$ which can be related to the number of phase "patches" in the system. The new experimental set-up described in chapter 4 enables us to double the area of the box potentials projected onto the atoms while keeping a constant surface density.

Last, in ultracold atom experiments as described here or as was realized in [67, 68], the quench cooling is usually realized by fast evaporative cooling. The decrease of the temperature might not be linear, but as long the time derivative of the temperature does not vary too much between the freezing-out time and the time at which the transition point is actually crossed, the Kibble-Zurek mechanism for a linear temperature quench described in chapter 2 section 2.2 can still be applied [90]. In addition, evaporative cooling decreases both the temperature and the atom number. As a consequence, the critical temperature also varies with time. For example, for the typical temperatures and atom numbers estimated for a gas at equilibrium at different points of the quench cooling (i. e. at different heights of the evaporation barrier) [90], the critical temperature for transverse condensation varies by 30 % during the total quench and by 10 % during the first third of the quench when the freezing-out should happen. Since this does not add any divergent behaviour and since the variation of the critical temperature with time is weak, the scaling should not be strongly affected.

3.4 CONCLUSION

In this chapter, we have presented two sets of experiments that illustrate the ideas described in chapter 1 and chapter 2.

The experimental set-up has been designed to produce 2D Bose gases by having a harmonic vertical confinement of varying strength ($\omega_z/2\pi$ ranges between

365 Hz and 1 500 Hz). We developed a versatile technique to produce uniform traps of arbitrary shape by imaging an intensity mask onto the atoms with a repulsive beam.

The first experiment which was carried out was to determine the phase-space density at which phase coherence appears in a uniform gas. It was measured using bimodality measurements in expanding clouds and by analysing matter-wave interference patterns. When the vertical trapping frequency is low, the threshold for the detection of coherence is consistent with the appearance of a large fraction of atoms in the ground state of the vertical harmonic oscillator due to bosonic amplification leading to transverse condensation (see chapter 1). When the vertical trapping frequency is high, coherence appears at $\mathcal{D} \sim 3$–4, which is a lower threshold than the expected critical phase-space density for the BEC or the BKT transitions (for which $\mathcal{D} \sim 8$–10, see chapter 1)..

The second experiment consists in observing topological defects that appear after quench cooling the gas in two different geometries and in comparing the scaling of the defect density with the quench duration with the Kibble-Zurek prediction (see chapter 2). These experiments were performed by observing the number of point vortices in squares of atoms in ToF experiments and the average charge of stochastic supercurrents created in atomic rings whose characteristics (including their direction) is revealed interferometrically. Fitting the defect density with a power-law behaviour yields exponents which are compatible with theoretical values, though the accuracy on the measurement only allows for a comparison in the critical regime at the 20% level.

The new experimental set-up presented in the next chapter could address some of the shortcomings of those experiments in a new set of experiments.

4

A NEW EXPERIMENTAL SET-UP FOR 2D PHYSICS

Due to the renovation work and the moving of the group to new facilities, the experimental set-up described in chapter 3 was dismantled and a new generation of rubidium 87 experiment has been designed and built in order to study 2D physics. In this chapter, I present the main technical choices that were made for the construction, focusing on their specificities without giving an in depth description of each. First, I describe the apparatus and the experimental sequence to obtain a Bose-Einstein condensate, to trap it in a uniform 2D trap and to image the clouds. Second, I present how we use a Digital Micromirror Device (DMD) to produce box potentials of arbitrary shape and an optical accordion lattice to provide strong 2D confinement of the cloud in the vertical direction, as well as a first demonstration of dynamical compression of a cloud in the vertical direction.

4.1 PRODUCING DEGENERATE GASES OF RUBIDIUM

4.1.1 *Design principle of the experiment*

This experiment was designed to pursue the same scientific goals as the previous set-up while improving the system. These goals are threefold:

- study bidimensional gases.
- confine the 2D gas in box potentials of arbitrary shape.
- in the long term, implement a strong effective magnetic field to produce strongly correlated many-body states.

To allow for those experiments, the following features have been introduced in the design:

- medium numerical aperture aspherical lenses[1] are positioned to allow for a horizontal beam to be focused into the cell. This will be used for the 2D confinement, produced by an angled lattice; it allows for tighter confinement and it should create less corrugation than the phase-plate technique used in the previous set-up. In addition, the spacing of this "accordion lattice" can be varied to optimize the loading of the atoms.
- a DMD is used to shape the beam of blue-detuned light which produces the box potentials. The resulting intensity mask is much more versatile than the clean-room fabricated ones used in the previous experiments. Its image is projected with high resolution ($\lesssim 1\,\mu$m) on the atoms using a vertical microscope objective.

1 Asphericon A50-100 LPX, numerical aperture 0.23

- a second vertical microscope objective is used to image the atoms with high resolution ($\lesssim 1\,\mu$m).
- the orientation of the three-dimensional magneto-optical trap (3D MOT) beams and the shape of the coils have been chosen to maximize the optical access around the science cell, allowing for triangular and square lattices to be installed.

The experiment was designed to be as simple as possible. A commercial two-dimensional magneto-optical trap (2D MOT) sends a beam of atoms through two stages of differential pumping to the science cell, where it is captured by a 3D MOT. Avoiding a transport stage, it is cooled down there and transferred to a magnetic trap to allow for radio-frequency evaporation. The BEC is obtained in a crossed dipole trap.

4.1.2 *Laser system*

The light for the laser cooling stage is provided by a 2.5 W Toptica TA pro laser at 780 nm. It is locked using the saturated absorption spectroscopy of a rubidium cell on the crossover line from the $|F' = 2\rangle$ to the $|F' = 3\rangle$ state. The frequency of the laser is red-detuned with respect to the "cooling transition" $|F = 2\rangle \rightarrow |F' = 3\rangle$ line by 258 MHz. To produce light close to the cooling frequency, we use double pass acousto-optical modulators working around the frequency of 120 MHz. We use a double-pass AOM around -110 MHz to produce light close to the $|F = 2\rangle \rightarrow |F' = 2\rangle$ transition in order to depump the atoms between two pictures during the imaging phase.

The repumping light for the laser-cooling stages is provided by an electro-optical modulator working around the frequency of 6.6 GHz [2]. The width of its resonance is 30 MHz, which allows to keep the relevant sideband at resonance with the $|F = 1\rangle \rightarrow |F' = 2\rangle$ transition even as the frequency of the carrier is shifted by changing the frequency of the microwave. A maximum power of 2 W is sent through the device. With the microwave at 6.6 GHz at maximum power, two sidebands are produced, each one having 8 % of the total optical power. This device is very sensitive to warming up and has to be turned on for one hour before running in steady state.

At the end of the experiment, the atoms are usually in the $|F = 1\rangle$ state; in order to be imaged using the $|F = 2\rangle \rightarrow |F' = 3\rangle$ transition, the atoms need to be transferred to the $|F = 2\rangle$ state. This can be done using several techniques; one of them is to optically pump the atoms using a short pulse of light resonant with the $|F = 1\rangle \rightarrow |F' = 2\rangle$ transition just before imaging the cloud. An interference filter stabilized diode laser[3] provides 10 mW of light to that purpose.

The laser set-up is depicted in figure 4.1.

2 visible phase modulator model 4851 from New Focus.
3 Radiant Dyes NarrowDiode

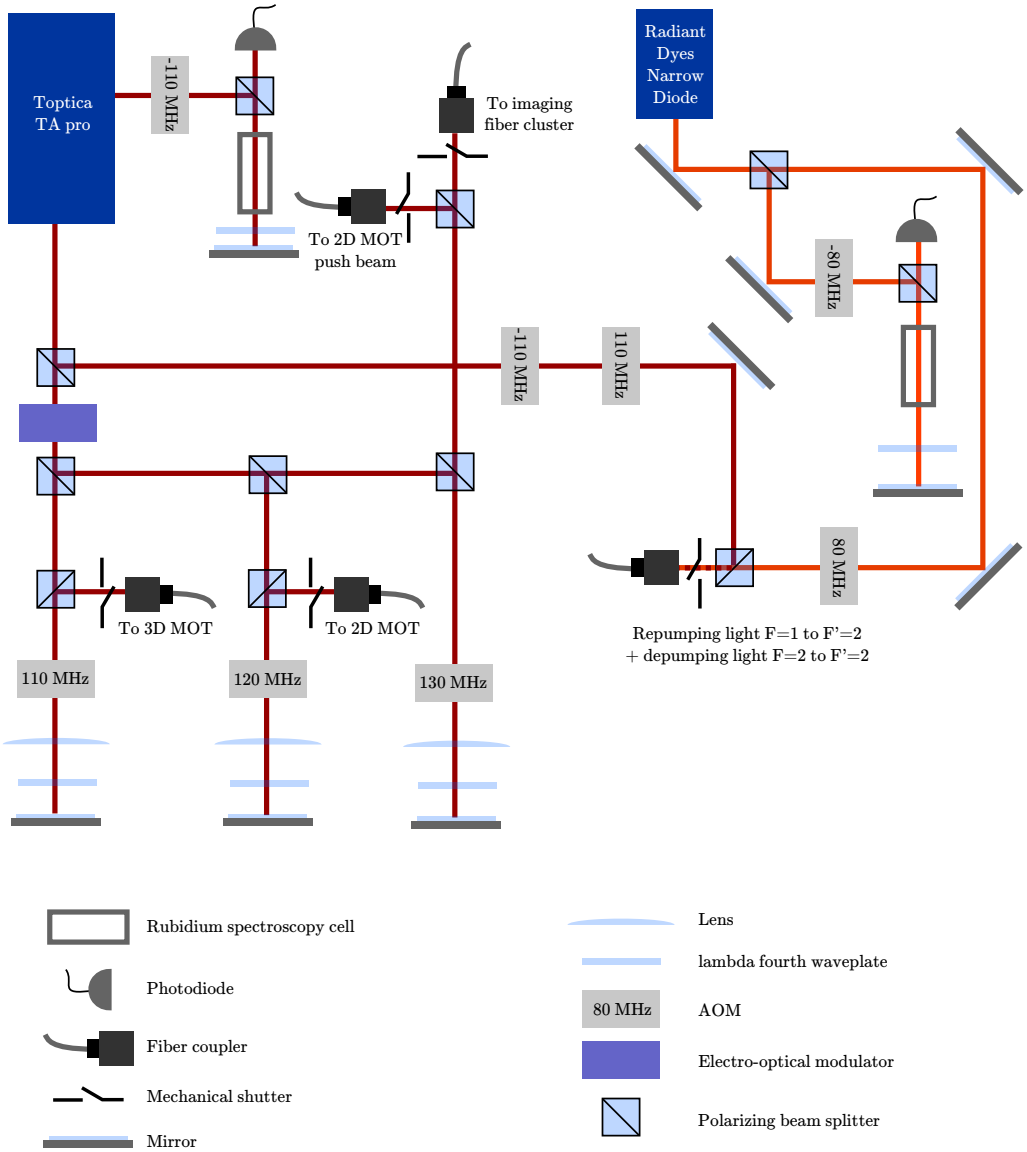

Figure 4.1: Principle of the laser set-up for the laser cooling and imaging phases.

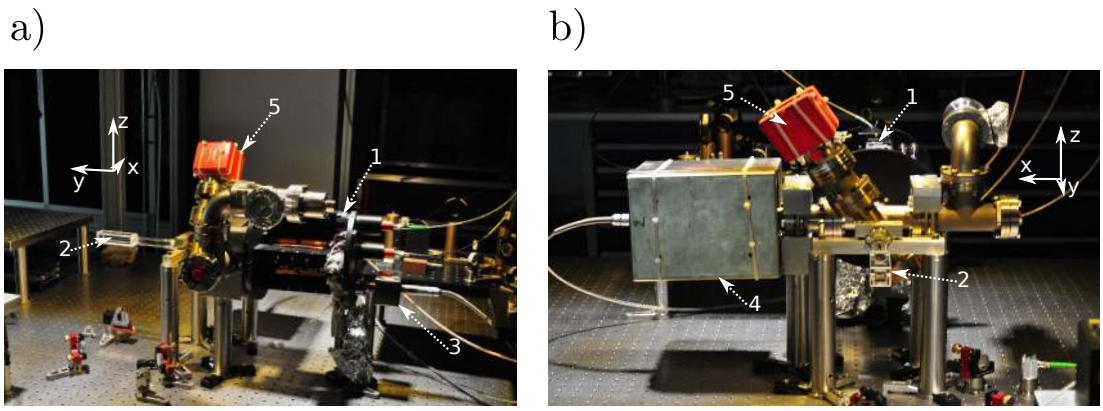

Figure 4.2: Pictures of the vacuum system: (a) side view; (b) front view. The main axis of the experimental set-up are indicated for each pictures. The following elements can be seen on the set-up: 1) 2D MOT, 2) science glass cell, 3) Agilent Technologies 2 L/s ion pump, 4) Agilent techologies VacIon 20 L/s, 5) SAES NEXTorr D200-5 ion getter pump.

4.1.3 *Vacuum system*

The vacuum system consists of two glass cells connected together by two metallic crosses. The first glass cell belongs to a commercial Two-dimensional Magneto-Optical Trap (2D MOT); its output is a hole of a diameter of 1.5 mm. It is pumped by an Agilent Technologies 2 L/s ion pump, and has an access flange for a turbo pump. The first cross is attached to a magnetically shielded Agilent technologies VacIon 20 L/s ion pump and to a turbo pump access flange. The second cross is separated from the first one by a differential pumping tube with a diameter of 1.5 mm, and pumped using a SAES NEXTorr D200-5 ion getter pump. The science glass cell is a parallelepipoid with external dimensions $25 \times 25 \times 105$ mm of 5 mm thick non coated glass, manufactured by Hellma. The distance between the output of the 2D MOT glass cell to the center of the science glass cell is 300 mm. It corresponds to the maximum advised distance between the 2D MOT and the MOT according to the datasheet of the commercial 2D MOT [169]. The vacuum system is shown in figure 4.2.

4.1.4 *Laser cooling*

4.1.4.1 *2D magneto-optical trap*

In order to produce a cold beam of atoms, we use a commercial 2D MOT [169–172] from Syrte which cools the atoms in the transverse direction while pushing them through a 1.5 mm diameter pumping tube.

A piece of solid rubidium is heated up to 65°C , corresponding to a pressure on the order of 10^{-7} mBar in the rectangular 2D MOT glass cell. In order to avoid bleaching of the windows as described in [173], the oven heating is reduced during the night. It turns on automatically in the morning thanks to a

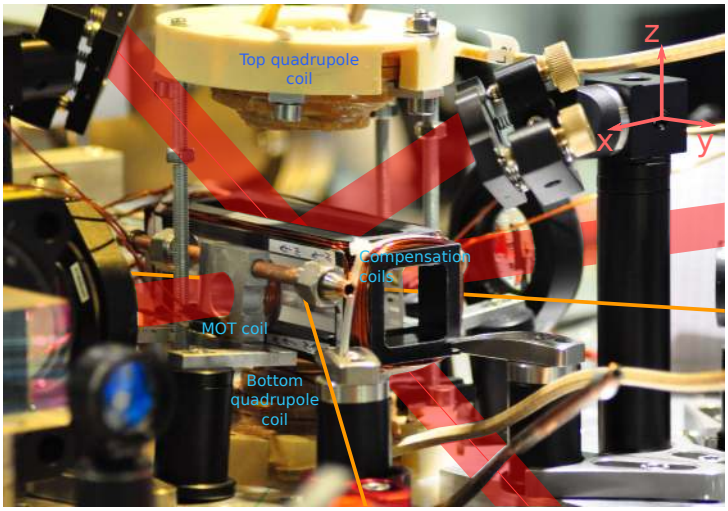

Figure 4.3: Picture of the science glass cell with the MOT beam (red), the optical dipole beams (orange) and the various coils. The top quadrupole coil is lifted with respect to its final position. The conical wiring allowing for the MOT beams to go through the cell can be seen.

mbed microcontroller which heats it up for one hour and a half before starting the experiment[4].

Four coils wound around the cell provide a magnetic gradient of 25 G/cm[173]. Additional compensation coils are required to load the MOT in an efficient way.

The 2D MOT has three cooling regions where circularly polarized light cool the transverse degrees of freedom of the atoms. We find the alignment of the beams of the cooling region closest to the differential pumping tube to be critical on the atom number captured later in the MOT stage. The light is red-detuned by 14 MHz (2.5Γ) with respect to the cooling transition $|F = 2\rangle \rightarrow |F' = 3\rangle$. It comes from two elliptical beams send to the side and the top of the 2D MOT, with a power of 60 mW for each beam. For stability purposes, we removed the commercial fiber couplers from their original mount: a beam pick-up was added to monitor the power of the laser beams.

An additional light beam pushes the atoms from the 2D MOT glass cell to the main glass cell of the experiment. It is blue-detuned by 12 MHz with respect to the cooling transition, has a power of 40 μW and a waist of 1 mm. The loading rate of the MOT is also very sensitive to the parameters and alignment of this beam.

4.1.4.2 *Magneto-optical trap*

The 2D MOT provides a cold atomic beam which is then captured by a standard 3D MOT. One pair of beams propagates along the x axis (see figure 4.2 for the definition of the axes). The two other pairs of beams are located in the yz plane, forming a 60° angle with the z axis (see figure 4.3). The power of the six beams is tuned using a Schäfter Kirchhof fiber cluster. Each beam has a waist of 7.4 mm, a diameter of 15 mm (being clipped by the MOT coil mounts) and a

4 Program available at https://github.com/lauracorman/mbedOven.

power on the order of 15 mW. They are red-detuned with respect to the cooling transition by 14 MHz.

The MOT coils are wound on a water-cooled mount that surrounds the horizontal beams. They provide a gradient of 22 G/cm at 20 A in the x axis (they are powered using a Delta Elektronika SM 7020D power supply). Large coils (meter sized) can compensate residual magnetic fields by producing fields up to 1 G.

With the 2D MOT switched on, the MOT loads for 7 s at a rate of $\sim 10^8$ atoms/s, resulting in a cloud with $\sim 8\,10^8$ atoms at a temperature of 250 μK. The lifetime of the MOT once the 2D MOT is switched off is of several minutes.

The power of the MOT beams is locked using the photodiode embedded in the fiber cluster. The lock is made using a mbed micro-controller[5].

4.1.4.3 *Compressed MOT and optical molasses phase*

During 15 ms, the power of the MOT beams is decreased and their frequency sweeped down to end 22 MHz away from resonance. The power of the repumper is reduced by 30% by decreasing the power of the microwave in the electro-optical modulator. This stage mainly cools the atoms by reducing light scattering; up to half of the atoms are in the $F = 1$ state due to the decrease in repumping light. At the end of this stage, the compressed MOT contains $6\,10^8$ atoms at a temperature of 50 μK.

After this stage, we cool further the cloud using a 4 ms optical molasses stage. The magnetic field gradient is turned off, the repumping intensity is increased again and the cooling light is further sweeped down to end red-detuned by 53 MHz with respect to the cooling transition. At the end of this stage, we have $6\,10^8$ atoms at a temperature of 10 to 15 μK.

4.1.5 *Quadrupole trap and radio-frequency evaporation*

4.1.5.1 *Quadrupole and radio-frequency set-up*

The quadrupole coils are conical with 14 turns of hollow copper wire (figure 4.3). They are water-cooled, and withstand a maximum current of 400 A without heating. Two safety circuits have been added to the system to shut down the current in the coils in case of a problem: a flow-meter stops the power supplies in case the water stop flowing, and a temperature sensor (Temperaturschalter TSM125) shuts down the power supplies in case the quadrupole coils overheat.

The coils are powered by two Delta Elektronika SM 15-200D power supplies in parallel. At the maximum current of 400 A, they create a gradient of $b_z = 240$ G/cm on the atoms. The current is switched using an insulated gate bipolar transistor. Switching on a current of 400 A takes 5 ms; switching off a current of 400 A takes $\sim 30\,\mu$s, with a strong transient increase in current. The eddy currents observed after switching off a current of 50 A have no significant effect on the atoms after 2 ms.

5 Program available at https://github.com/lauracorman/mbedPIDlockLasers.

The radio-frequency (RF) field for RF evaporation is provided by a general purpose interface bus (GPIB) controlled generator, a Rigol DG5071. It is amplified by a 4 W amplifier from HD communications (model HD19153) which works for frequencies between 150 kHz and 230 MHz. It is brought to the atoms by a two-turn antenna of typical radius of 7 cm.

4.1.5.2 *Loading the quadrupole trap*

At the end of the molasses phase, the atoms have to be transferred to the $F = 1$ state because we want to magnetically trap the atoms in the $|F = 1, m_F = -1\rangle$ state. Therefore, during 1 ms, the microwave power for the electro-optical modulator is completely switched off, the power of the MOT beams is increased and their detuning reaches 72 MHz with respect to the cooling transition. Detuning the laser brings its frequency closer to the $|F = 2\rangle \rightarrow |F' = 2\rangle$ transition from which the atoms can fall to the $|F = 1\rangle$ state.

The quadrupole is then switched on at $b_z = 58\,\mathrm{G/cm}$. This value is chosen to minimize heating due to the sudden change in potential energy for atoms which are far from the zero of the quadrupole trap. The mounts of the MOT and quadrupole coils have been designed and carefully mounted to have the zero of their gradient at the same position (distance between the two zeros smaller than 1 mm). The cloud of $2.5\,10^8$ atoms at a temperature of $190\,\mu$K is held for 1 s.

The quadrupole is compressed in 0.5 s to its maximum gradient to increase the collision rate of the atoms.

4.1.5.3 *RF evaporation*

During 12 s, the RF field is turned on at maximum power and its frequency is linearly swept from 34 MHz to 2.5 MHz. This evaporation ramp produces a cloud of $2.5\,10^7$ atoms at $16\,\mu$K. At the end of the evaporation ramp, the potential energy of an atom whose state can be flipped to a non trapped state is $U \sim k_B \cdot 125\,\mu$K. This corresponds to a ratio $\eta = U/k_B T \sim 8$, which is typical for such an evaporation.

4.1.6 *Production of Bose-Einstein condensates in a crossed dipole trap*

4.1.6.1 *Optical dipole trap set-up*

The optical dipole traps are provided by two lasers: (i) the 8.4 W single-mode Azurlight system 1064 nm laser described in chapter 3 working at 5 W; (ii) a 10 W multi-mode IPG laser at 1070 nm. Both lasers are sent through an acousto-optical modulator (AOM) to control the power sent on the atoms and fiber-coupled to the experiment table using large core fibers from Schäfter-Kirchhoff. The AOMs allow an extinction ratio of 100; they are also used to lock the power of the beams. We find that it is important to keep the AOM warm before shining the lasers at full power on the atoms. When the dipole beams are not used, the AOM are heated up by working at full power with a 30 MHz detuning in the incoming RF field. This deflects the laser beam to a beam dump.

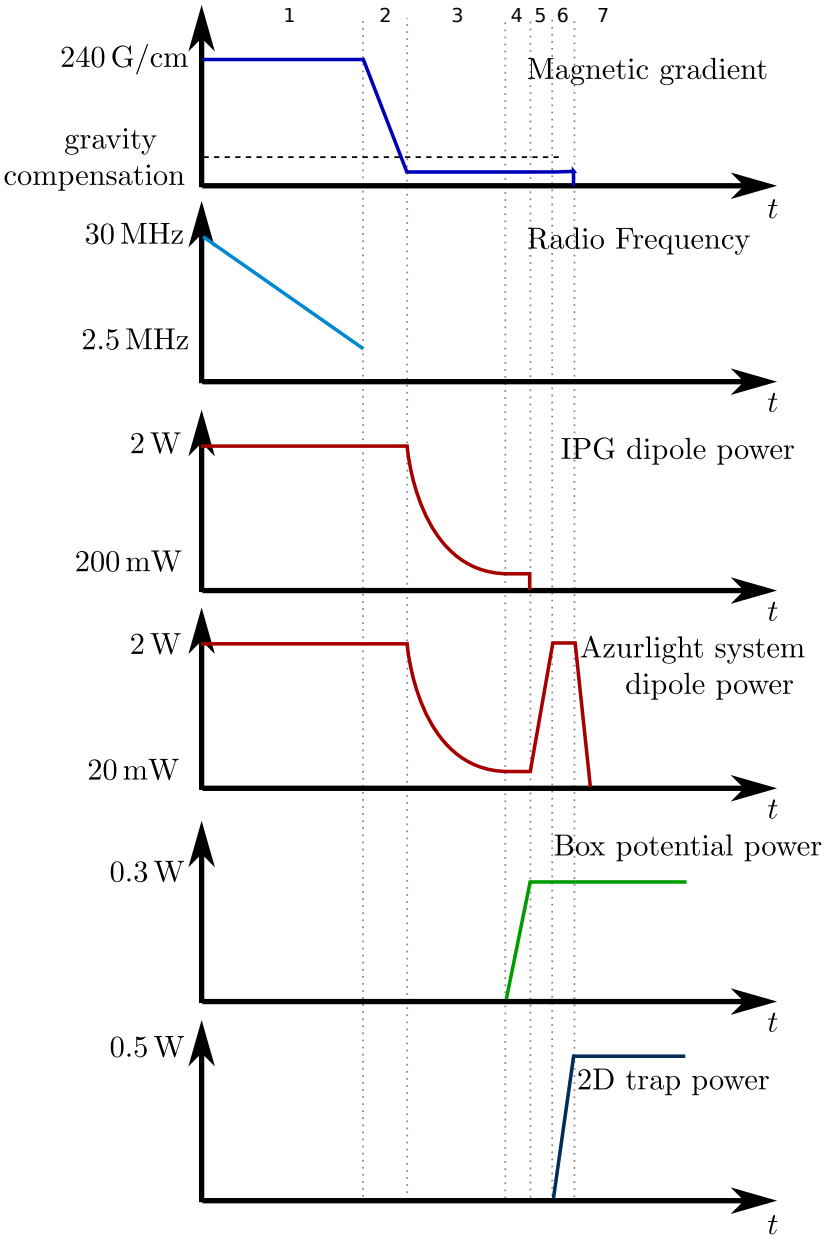

Figure 4.4: Main steps of the experimental sequence after the loading of the quadrupole. (1) RF evaporation (12 s). (2) Loading of the crossed optical dipole trap (0.5 s). (3) Evaporation in the optical trap (3 s). (4) Ramping up of the box potential (0.3 s). (5) Ramping up of the Azurlight dipole trap (0.125 ms). (6) Ramping up of the 2D confinement (25 ms). (7) Switching off of the Azurlight dipole trap (0.1 s). From there on the 2D cloud in a box potential is ready for further experimenting.

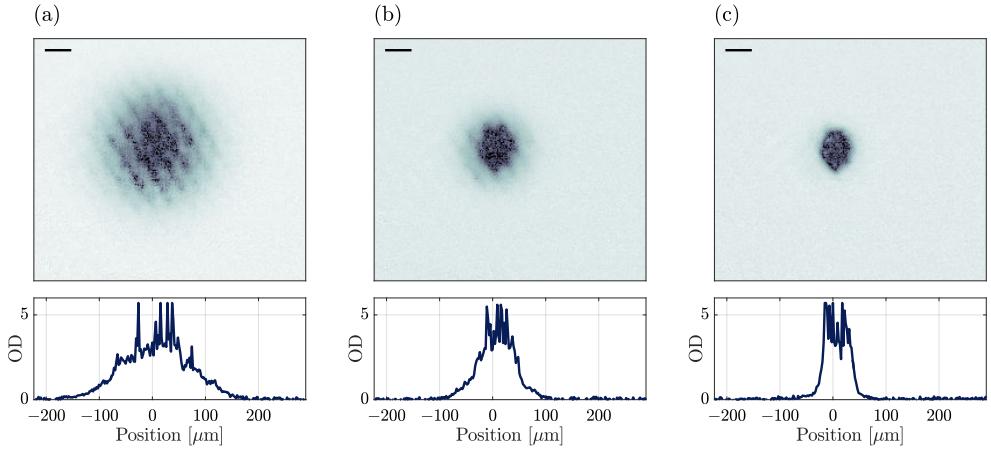

Figure 4.5: Pictures of the cloud during the evaporation in the crossed dipole trap after 12 ms of ToF expansion. In figure (a), the evaporation is stopped just before the condensation threshold, the distribution of atoms indicates a thermal cloud. In figure (b), the BEC threshold has been crossed, a condensed cloud appears surrounded by thermal wings. At the end of the evaporation (figure c), the cloud is fully condensed. Scale bars: 50 μm.

The dipole beams are in the xy plane, are orthogonal to each other and have a 45° angle with the x axis. They are depicted in orange in figure 4.3. They are focused in the glass cell with a vertical waist of 30 μm and a horizontal waist of 90 μm. The focus of both beams is located 50 μm below the zero of the magnetic gradient of the quadrupole trap.

The loaded cloud is therefore pancake-shaped, which will facilitate the 2D confinement in the following steps of the experiment. The positions of each beam can be finely tuned using a PicoMotor motorized mirror mount from New Focus.

4.1.6.2 *Loading the crossed optical dipole trap*

Two seconds before the end of the RF evaporation, the dipole beams are turned on at full power to ensure optimal heating of the control AOMs. At the end of the evaporation, the magnetic gradient is decreased in 0.5 s to a value of $b_z = 21\,\mathrm{G/cm}$. This magnetic gradient partially levitates the atoms; they experience a force equivalent to one third of the gravity force.

The relative position of the zero of the magnetic field and of the focus of the laser beams has to be controlled in order to load the cloud in a reliable fashion. This is achieved by adding compensation fields that displace the zero of the magnetic field using the pairs of coils shown in figure 4.3 which provide up to $\sim 10\,\mathrm{G}$ in the x and z direction (5 G in the y direction).

A cloud of $\sim 1.3\,10^7$ atoms at a temperature of $\sim 8\,\mu$K is loaded in the crossed optical dipole trap at its maximum power (2 W in each beam).

4.1.6.3 *Evaporation in the crossed dipole trap*

During 3 s, the power of the optical dipole trap beams are exponentially lowered. The power of the beam coming from the IPG laser is divided by 10 and the one from the Azurlight system laser is divided by 100 to reach the condensation threshold with $\sim$ 3.9 10^6 atoms at $\sim$ 255 nK. At the end of the evaporation ramp, we end up with a quasi pure BEC with 3 10^5 atoms (see figure 4.5).

4.1.6.4 *Loading the box potential and accordion lattice*

The degenerate cloud is then transferred to an all-optical, blue-detuned trap which is the combination of:

- a box potential provided by a hollow beam projecting the image of an intensity mask onto the atoms, confining the atoms in the xy plane
- an angled vertical optical lattice that confines the atoms in one or several planes in the z direction.

The realization of these traps is detailed in the following paragraphs. Let us focus here on the experimental sequence to load the whole cloud into a single plane of the vertical optical lattice which has a spacing of 12 μm. After the evaporation in the crossed optical dipole trap (see figure 4.4):

- the box potential beam is ramped at full power on the atoms in 300 ms.
- the dipole beam coming from the Azurlight system is ramped at its maximum power in 125 ms to reduce the vertical size of the cloud. The transverse size is limited by the box potential trap. This procedure is only performed with one laser because the efficiency of the acousto-optical modulator that controls its power (from AA optoelectronics) is less dependent on heating than the one of the other laser (from Crystal Tech).
- the power of the accordion lattice is ramped up to its maximum value in 25 ms.
- the power of the optical dipole traps are ramped to zero.

At this point, provided that the dark fringes of the accordion lattice stay at the same position, we can reliably load a single plane of atoms in the vertical direction (see figure 4.6), while having a box potential in the xy plane. This gas can be further evaporated by lowering the power in the box potential beam.

Thus, 2D gases in arbitrary shaped traps are produced in an experimental sequence of 30 s.

4.1.7 *Imaging the cloud*

4.1.7.1 *Repumping the cloud*

At the end of the cloud preparation, the atoms are in the $|F = 1, m_F = -1\rangle$ state. Before being imaged on the cycling transition $|F = 2\rangle \rightarrow |F' = 3\rangle$, they have to be transferred in the $|F = 2\rangle$ hyperfine state. This can be done using two methods:

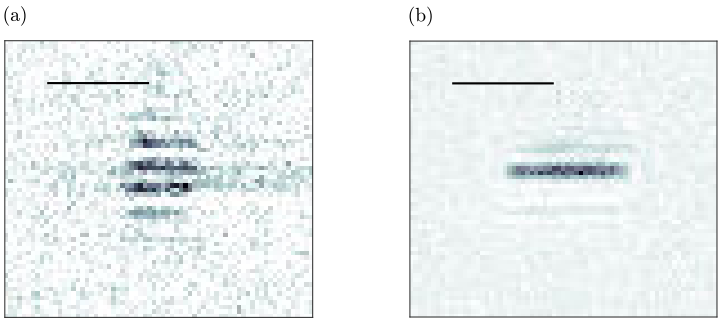

Figure 4.6: Loading of the accordion lattice for a lattice spacing of 12 μm. (a) Without compressing the optical dipole trap again, several planes of atoms are loaded. With the compression (b), one plane of atoms can be reliably loaded (the remaining fringes correspond to diffraction effects). Scale bars: 50 μm.

- Optical repumping is performed using a laser beam (with a power of $\sim$ 8 mW) resonant with the $|F = 1\rangle \rightarrow |F' = 2\rangle$ transition. An atom absorbs few photons before being transferred in the $|F = 2\rangle$ state. Depending on the density and position of the cloud, the repumping time is varied between 4 and 50 μs. The advantage of this method is that it is robust: the atoms can be imaged in-situ in the various traps (optical and magnetic), and the waist of the beam is large enough such that the atoms are also repumped after being released for several milliseconds from the traps (ToF). However, this repumping process can strongly modify the spatial distribution for dense clouds (see chapter 5). After a long time of flight, the cloud has to be repumped in a region where the intensity of the laser is less important; the repumping phase lasts for several tens of microseconds, which can also affect the shape of the cloud.

- The small displacement during the optical repumping might be a problem in measurements where the vertical extension is critical, as is the case for the experiment presented in chapter 5. In that case, it is preferable to use microwave repumping. It is performed in an all-optical trap; a bias field is ramped up to fix the quantization axis of the atoms. We choose this quantization axis to be along the x axis to avoid the main magnetic field perturbation which is caused by the subway (and is along the z axis). We choose a value of 2 G for the bias field. Then, we apply a microwave field (using a 10 W amplifier) for typical durations of a few microseconds. Its frequency is tuned to drive the $|F = 1, m_F = -1\rangle \rightarrow |F = 2, m_F = -2\rangle$ transition; the maximum coupling efficiency results in a Rabi frequency of 30 kHz. Although this technique can only be used after all magnetic traps are switched off, it does not transfer momentum to the atoms and allows for a precise control of the percentage of atoms transferred in the detected hyperfine state.

4.1.7.2 *Imaging axes*

The experimental set-up allows for several imaging axes:

- a main horizontal axis, with the imaging light propagating along the x direction. The absorption picture can be detected on two cameras, a Lumenera camera LM135M with magnification 0.4, mainly used to image the first steps of the experimental sequence (from the laser cooling to the quadrupole trap evaporation) and a Pixelfly PF-M-QE-PIV with magnification 3 used in interframed mode. Changing from one to the other camera is done using a flipping mirror.

- a second horizontal axis, with the imaging light copropagating with the optical dipole trap beam from the IPG laser. The pictures are detected on a Lumenera camera LM135M with magnification 1. This axis is mainly used to align the beam from the IPG laser.

- a vertical axis, with the imaging light propagating in the $-z$ (downwards) direction, which provides a very good imaging resolution (see 4.1.7.3). In this axis, two cameras are available: a Lumenera camera LM135M with magnification 2.5 and a Princeton Instrument PIXIS 1024 Excelon with a magnification of 11. The latter camera provides the highest quality pictures for the experiment. Its calibration and properties will be detailed in chapter 5 as they are an important part of the analysis. Changing from one to the other camera is done using a flipping mirror.

All the cameras are controlled by a Python program that I made available[6]; it is designed to work together with the experiment control software Cicero[7].

4.1.7.3 *Optical resolution in the vertical axis*

The vertical axis for the imaging is designed to have a high resolution both to image the cloud with light at 780 nm and to imprint light potentials with light at 532 nm on it. We use two custom microscope objectives[124] from Nachet with a numerical aperture of 0.45. They have been designed to work at 780 nm with a focal length of 10 mm with a 5 mm thick glass plate between them and their focal point.

Using a custom test target[8] with stripes of width 2 μm, 1 μm, 0.8 μm and 0.5 μm and a glass plate equivalent to those used for the vacuum cell, we measured the resolution of the objectives at the two wavelengths of interest. At 780 nm, the resolution is $\lesssim 1\,\mu$m (strong loss of contrast when imaging the 0.8 μm stripes with respect to the 1 μm ones). At 532 nm, the resolution is $< 0.8\,\mu$m. We were also able to measure the chromatic shift: the focal point at 780 nm is 50 μm closer to the objective than the focal point at 532 nm.

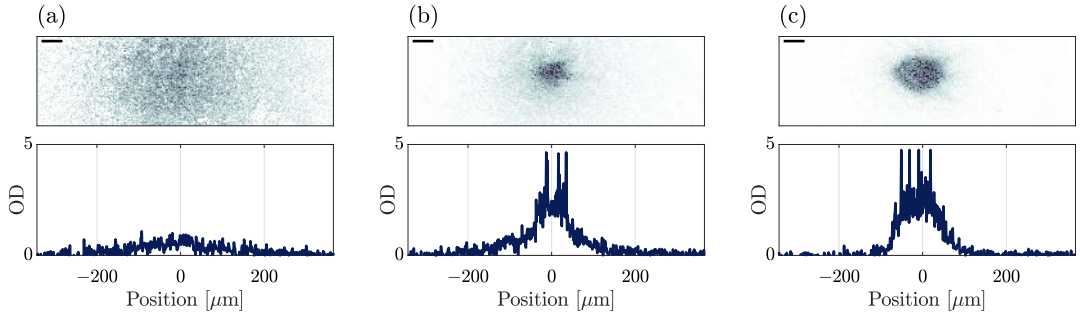

Figure 4.7: Condensation in an all-optical 2D box potential using the vertical imaging axis. The gas is initially trapped in a disk of radius 20 μm, and released for 8 ms of ToF. In (a), the box potential beam is kept at full power. The power of the box potential beam has been divided (in 0.1 s) by 2.4 in (b) and by 24 in (c). Starting from a thermal distribution, the cloud exhibits first a bimodal distribution then a strong occupation of low-momentum states. Scale bar 50 μm.

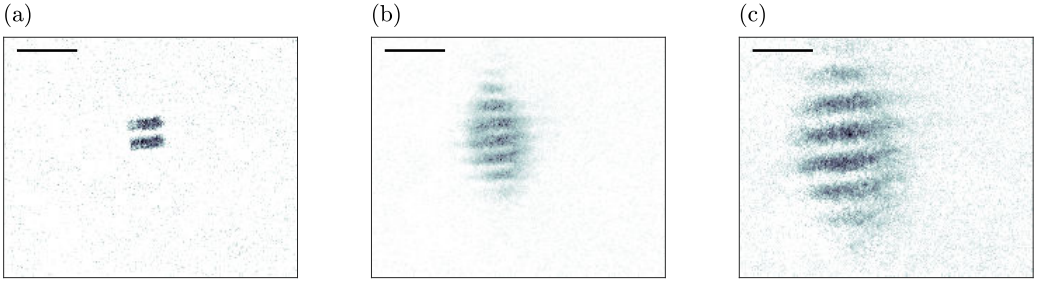

Figure 4.8: Matter-wave interferences in a 2D box potential in the xy plane observed using the vertical imaging axis. The gas is initially trapped in two rectangular boxes of size 15 μm $\times$ 5 μm, spaced by 3 μm (a). After being released for 10 ms (b) and 20 ms (c) ToF, interference fringes are clearly visible. Scale bar 50 μm.

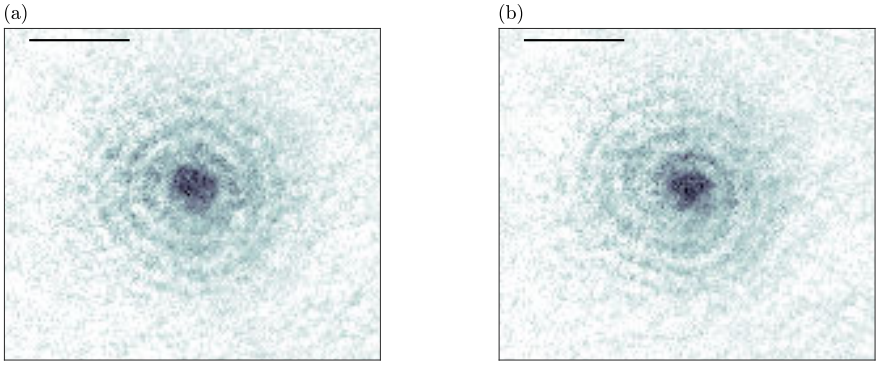

Figure 4.9: Matter-wave interferences from a two ring pattern using the vertical imaging axis. (a) Concentric fringes, (b) double spiral pattern. Scale bar 20 μm.

4.1.8 *Obtaining degenerate gases in shaped potentials*

Using the procedure and apparatus described in the previous sections, we have been able to produce degenerate gases with extended phase coherence in a 2D potential, as indicated by bimodal structures revealed in ToF measurements (figure 4.7) as well as by matter-wave interference fringes appearing when two degenerate clouds overlap (figure 4.8). We were also able to reproduce the spiral interference patterns produced on the former set-up after rapid evaporation (100 ms) of a two-ring pattern, thus validating the construction of the set-up (see figure 4.9).

4.2 SHAPING THE CLOUD

The aim of the experimental set-up is to produce 2D gases in arbitrary in-plane traps. In order to do so, two traps are projected onto the atoms:

- a hollow blue-detuned beam, the box potential beam, is shone from the top to provide in-plane confinement.
- a blue-detuned angled lattice, the "accordion" trap, is shone along the x axis, resulting in tight confinement along the z axis. The lattice spacing can be dynamically decreased in order to increase the confinement.

The order in which those beams are switched on in the sequence has been explained in paragraph 4.1.6.4. Here we detail how those traps are produced.

Both beams come from a single 10 W Verdi V10 laser. To provide a high quality spatial mode, the beams are fiber-coupled to the experiment; in order to limit Brillouin scattering, the fibers are kept as short as possible (50 cm for

6 https://github.com/lauracorman/cameraCicero
7 http://akeshet.github.io/Cicero-Word-Generator/
8 We thank José Palomo for the realization of the target in the clean room of the ENS.

the accordion trap and 1 m for the box potential beam) and we limit the output power to 1 W. The power of the beams is controlled using two crystalline quartz AOM from Gooch&Housego[9]; these AOM are robust against heating effects.

4.2.1 *Making box potentials*

We produce a box potential on the atoms by projecting the image of an intensity mask on the atoms, similar to what was described in chapter 3 subsection 3.1.3. Instead of using clean room fabricated intensity masks, we use a DMD (V7000 from Vialux) which acts as a programmable intensity mask.

The DMD is a micromirror array with 1024×784 square mirrors of size $13.8\,\mu$m. It is imaged onto the atoms with a magnification of $1/70$; each micromirror has an effective size of $0.2\,\mu$m on the atoms, well below the optical resolution of the system. The waist of the beam on the atoms when all the micromirrors are on is $45\,\mu$m. At maximal power (300 mW on the atoms), the maximum potential height created at the center of this beam is $k_B \cdot 6\,\mu$K. For a given laser power, the height of the potential barrier on the atoms depends on the typical size of the pattern which is created. For example, for a pattern of two rings with radii $R = 10\,\mu$m and $20\,\mu$m (similar to the configurations proposed in chapter 7 , the barrier height difference is on the order of 75%. This has not been a problem so far in our experiments, but some theoretical investigations have been done in order to study other evaporation mechanisms that do not depend on the size of the pattern (see chapter 6).

In order to produce uniform 2D gases, it is important to measure the quality of the hollow beam created by the DMD[10] [174]. Keeping potential corrugations small compared to the typical energy scales of the atomic cloud (chemical potential, temperature) is necessary to be able to study uniform gases. The three parameters that we want to investigate are:

- the root-mean-square deviation from the mean intensity at the center of the hollow region, which characterizes the overall roughness of the potential.
- the peak-to-peak amplitude of the defects at the center of the hollow region, which characterizes the maximal potential defects that can affect the atomic cloud.
- the sharpness of the edges, which characterizes on what distance the light intensity goes from its minimal to its maximal value. It is important to keep this distance as small as possible to investigate the physics of uniform gases [93].

These tests are performed using large square- or disk-shaped patterns with a length or diameter up to a size of $100\,\mu$m in the atomic plane. In order to avoid intensity ripples due to an abrupt variation of the coherent light, we allow for different "boundary width". For a width of d DMD pixels, we want to have

9 I-M110-2C10B6-3-GH26 with a A35-Series 5 W amplifier.
10 These analysis have been carried out by Jean-Loup Ville.

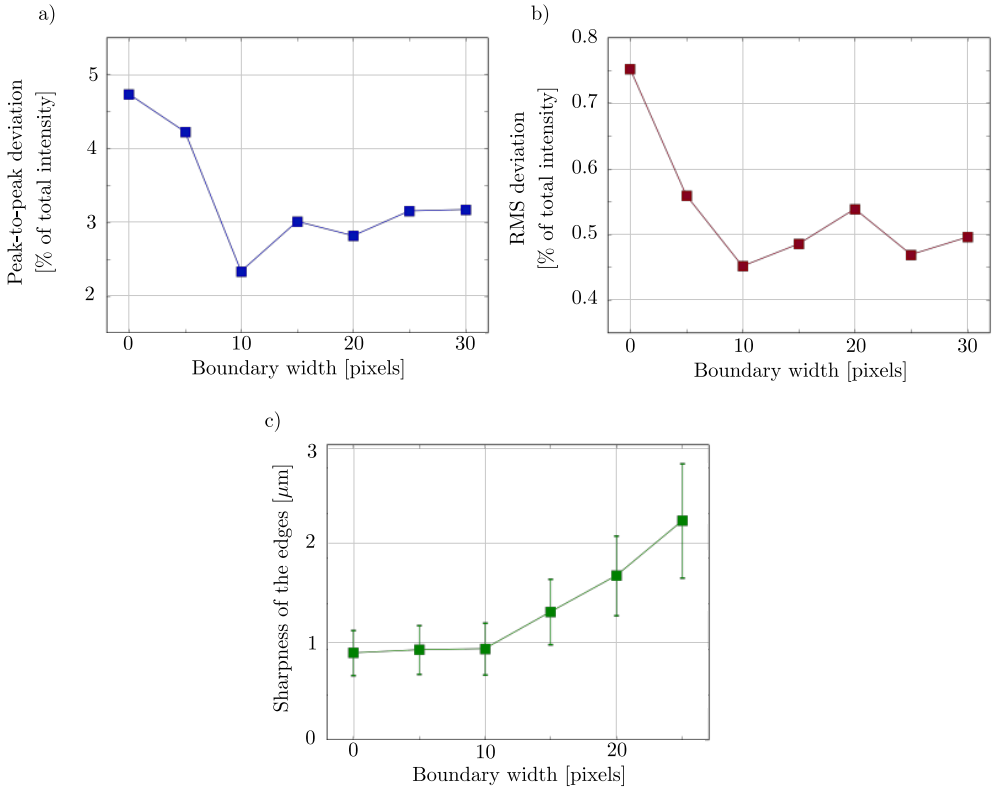

Figure 4.10: Characterization of the roughness and of the sharpness (defined in equation 4.1) of the potential created by the DMD as a function of the width (measured in DMD pixels) of the boundary for the pattern. On this boundary, micromirrors are randomly flipped to have an average linear increase of the light intensity. The characterization is performed with a disk of radius 30 μm in the atomic plane. The region on which the roughness is computed corresponds to a disk of radius 25 μm on the atoms. (a) Peak-to-peak deviation to the mean value, renormalized by the maximum intensity of the beam. (b) Root-mean-square deviation from the mean intensity, renormalized by the maximum intensity of the beam. Figure (c) characterizes the sharpness (in μm) of the DMD potential as a function of the width of the boundary characterization a square of size 50 μm in the atomic plane. The sharpness corresponds to the mean value of the fitted width of an error function on 80 cuts. The error bars indicate the standard deviation of the fitted width.

a gradual intensity increase. The DMD does not allow for analog control of the intensity, so we use the fact that the effective size of a micromirror on the atomic plane is much smaller than the imaging resolution. We randomly select the micromirrors that are turned on such that the mean value of the intensity increases linearly across the boundary.

For a sharp boundary ($d = 0$), the peak-to-peak variation of the intensity inside the desired region corresponds to 5% of the maximum intensity and the root-mean-square variation to 0.75% of the maximum intensity, which will not degrade the uniformity of the atomic sample. As the width of the boundary includes more and more pixels of the DMD, the coherent intensity ripples disappear and the peak-to-peak (resp. root-mean-square) variation decreases to 3% (resp. 0.5%) of the maximum intensity (see figure 4.10).

The sharpness of the imprinted potential is computed by taking many cuts perpendicular to the edges of the potential. These cuts are fitted with a Gauss error function

$$I = I_{\max}\mathrm{erf}\left(\frac{x - x_0}{\delta x}\right) + I_0 \tag{4.1}$$

with the fit parameters $I_{\max}$, x_0, δx and I_0. The mean value of δx over 80 cuts is the sharpness of the potential. The results reported on figure 4.10 show that as long as the width of the boundary does not exceed 10 micromirrors (corresponding to a size of 2 μm in the atomic plane), the sharpness is constant and on the order of 1 μm. It increases for larger boundary widths.

The potentials created by the DMD are of sufficient quality to created uniform gases or arbitrary shapes in 2D (see figure 4.11), since they present small corrugations ($< 5\%$ of the total barrier height) and sharp edges where the intensity rises in 1 μm. They are very convenient to produce because the intensity configuration can be easily changed thanks to the provided software.

We also tested that the DMD can be used to projects "movies" on the atoms (up to 16 kHz of switching frequency), which can be interesting for future projects [175].

At an early stage of the experiment, we tried to produce degenerate rings of atoms to implement the experiment proposal of chapter 7 by using a plugged quadrupole configuration (this did not work due to strong heating of the cloud in the quadrupole trap). We therefore projected DMD patterns during the quadrupole phase, for which it is very important that the patterns stay at the same position from one experimental run to the other. I developed a program to reposition the DMD pattern at the beginning of each experiment available on Github [11].

4.2.2 *Confining the gas to two dimensions*

4.2.2.1 *Producing a 2D gas using light potentials*

There are several techniques which can be used to provide a strong vertical harmonic confinement on the atoms and study 2D physics. Using a blue-detuned repulsive beam, we consider two options:

11 https://github.com/lauracorman/SlowLockPosition

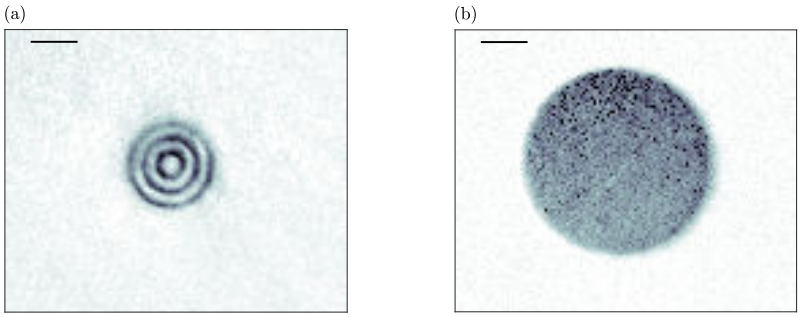

Figure 4.11: Example of a cloud of atoms trapped in (a) a potential made of three rings of radii $5\,\mu$m $-$ $6\,\mu$m, $10\,\mu$m $-$ $11\,\mu$m and $15\,\mu$m $-$ $16\,\mu$m (top view) (b) a disk of $80\,\mu$m diameter. Scale bar $20\,\mu$m.

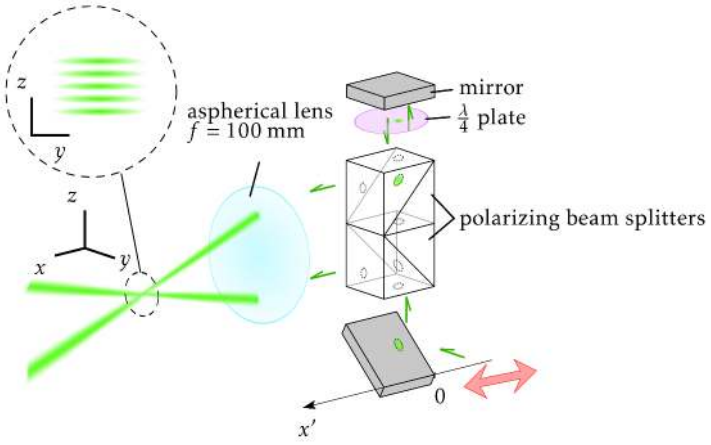

Figure 4.12: Working principle of the accordion lattice. A beam is sent up in two polarizing beam splitters. Part of the beam is reflected by the first cube. The remaining beam is polarized along the x' axis and is transmitted by both cubes. Its polarization is rotated by $\pi/2$ during the retroreflection on the top mirror thanks to the $\lambda/4$ plate; it is thus reflected by the second cube, yielding a second beam parallel to the first one with adjustable relative power. Depending on the input point of the beam along the x' axis, the reflection point of the beam of both cubes is shifted, leading to a variable spacing between the two beams.

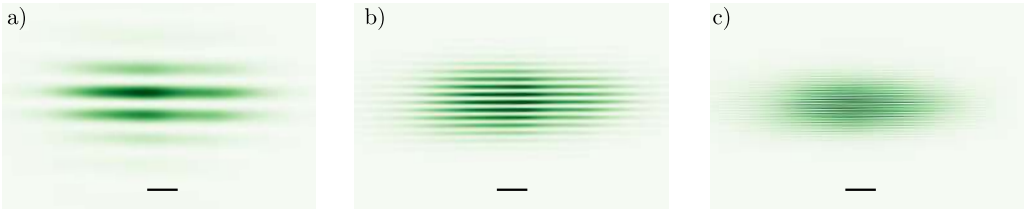

Figure 4.13: Examples of vertical lattices created using the optical accordion set-up proposed in [74]. Light intensities of lattices with spacing (a) 11 μm, (b) 3.6 μm and (c) 1.2 μm. Scale bars indicate a distance of 20 μm on the atoms.

- placing the cloud in a single-minimum potential using an evanescent field close to a surface [176] or a light sheet engineered as a Hermite-Gauss mode [177] (technique used in chapter 3).
- producing an optical lattice which provides several minima in which the atoms can be trapped.

The first technique easily allows to trap only one plane of atoms since the atoms which are not trapped in the central minima can be spilled out. However, the optical quality of the created traps contains some corrugations that are detrimental for uniform traps [90, 123], and it is difficult to reach very high confinements (with frequencies up to 10 kHz).

The second technique makes it possible to reach high confinements; however, this is realized with a small spacing lattice, for which single-plane loading is difficult. For a lattice spacing of a few μm, typically two planes can be loaded [44, 178]. Producing a single plane of atoms can require selectively removing all populated lattice planes but one [179].

To overcome the problem of single-plane loading, it is convenient to vary the lattice spacing during the experimental sequence: the loading takes place with a large lattice spacing ($\gtrsim 10\,\mu$m) to ensure that only a single node is populated with atoms; the lattice spacing is then decreased, resulting in an increase of the vertical confinement and enter the quasi-2D regime. Several techniques of such "optical accordions" have been tested, for example using acousto-optical deflectors to create 2D optical lattices with variable spacing [180] or using a beam reflected on a surface [181].

4.2.2.2 *Optical implementation of the accordion lattice*

Here, we implement on the atoms the set-up that was proposed and whose optical feasibility was demonstrated by the group of Raizen [74], illustrated in figure 4.12[12]. A system of polarizing beam splitters and quarter waveplate splits an incoming beam into two parallel beams. These beams are sent on an aspherical lens of focal length $f = 100$ mm that focuses the interfering beams onto the atoms.

The distance between the two beams d is controlled by the impact point of the beam on the polarizing beam splitters, which we tune using a motorized translation stage [13]. The lattice spacing Δz depends on the wavelength of the

12 These characterizations have been performed by Raphaël Saint-Jalm [182].
13 PI miCos LS-110 with the C6862 servo controller.

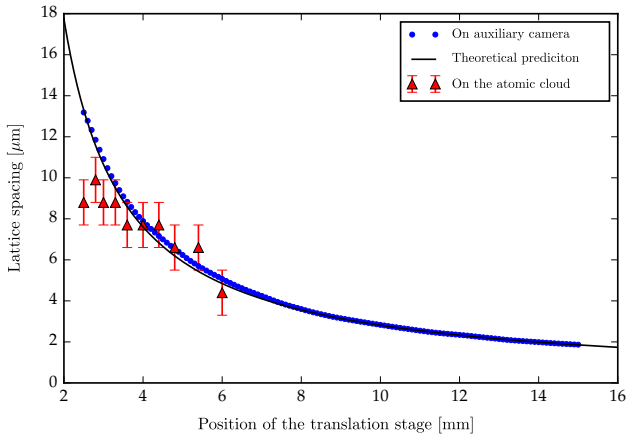

Figure 4.14: Lattice spacing of the accordion 2D confinement. The solid black line represents the theoretical prediction of equation 4.2. The blue dots represent measurements of the lattice spacing on an auxiliary camera. The red triangles represent direct measurements on the atoms, limited by the imaging resolution of the horizontal axis (on the order of 4 μm).

laser $\lambda = 532\,\text{nm}$, on the focal length of the lens f and on the distance between the two beams d or equivalently on the position of the translation stage x'_{stage} that controls the parameter d:

$$\Delta z = \frac{\lambda}{2}\sqrt{1+\left(\frac{2f}{d}\right)^2} = \frac{\lambda}{2}\sqrt{1+\left(\frac{f}{x'_{\text{stage}}}\right)^2} \tag{4.2}$$

By translating the beam on the bottom mirror by 2 cm, we can vary the lattice spacing from 12 μm to 2 μm (see figures 4.13 and 4.14). The lattice spacing can be checked from 12 μm to 4 μm (figure 4.14) using the horizontal imaging axis. These lattice spacings are limited on the one hand by the minimal distance between the two beams necessary so that none of them is clipped by one of the polarizing beam splitters, on the order of $d_{\text{min}} \sim 8.5\,\text{mm}$ (i. e. $\Delta z = 12\,\mu\text{m}$). On the other hand, the maximum spacing between the beams is limited by the numerical aperture of the imaging system. In the present configuration of the experiment, the MOT coils are the limiting factor, leading to $d_{\text{max}} \sim 45\,\text{mm}$ (i. e. $\Delta z = 2\,\mu\text{m}$).

The beams are elliptical on the atoms, with waists of $w_z = 35\,\mu\text{m}$ and $w_y = 100\,\mu\text{m}$. In the horizontal direction, having a large waist limits the anticonfinement due to the zero point energy $\hbar\omega_z/2$ (with ω_z the angular frequency of the vertical confinement) as well as the amplitude of defects due to a slight power imbalance or to a small misalignment of both beams. The potential created by the two beams has some remaining corrugations along the propagation axis; most of them are removed by cleaning their polarization after the two polarizing beam splitter set-up (by adding an additional polarizing beam splitter).

The polarizing beam splitters have been placed as close as possible to the aspherical lens in order to minimize the possible phase fluctuations between the two beams. The interference pattern indeed drifts slowly over time. When

the optics are well isolated from temperature variations and air turbulences, the dark fringe typically drifts by a third of the lattice spacing over one hour.

At full power ($\sim 0.75\,\mathrm{W}$ on the atoms), the lattice created on the atoms realizes a potential with a height of $\sim k_B \cdot 10\,\mu\mathrm{K}$. As explained in 4.1.6.4, a single plane of atoms can be loaded in a dark fringe of the accordion with the largest spacing of $12\,\mu\mathrm{m}$, which corresponds to a trapping frequency in the vertical direction of 2.4 kHz at full power.

4.2.2.3 *Increasing the vertical confinement using the optical accordion lattice*

We checked that the translation stage could be used dynamically for the compression of an atomic cloud. When moving the beam to change the interference pattern from the largest to the smallest lattice spacing, the central dark fringe moves by $1.5\,\mu\mathrm{m}$, due to small tilts of the beam during the displacement (within the specifications of the translation stage). This shaking should not significantly heat the atomic cloud. We find that the contrast of the interference patterns changes during the displacement of the the stage because of imperfections on the $f = 100\,\mathrm{mm}$ lens. Slight defects with respect to the theoretical profile of the lens indeed lead to a focal point that varies with the distance d between the beams.

We present here the preliminary test of this set-up: we try to load only one plane of atoms (see 4.1.6.4 and figure 4.6), then reduce the lattice spacing to work with stronger confinement in the vertical direction.

We can compress the cloud of atoms by dividing the lattice spacing by a factor of two. No significant heating was observed, and we loose half of the atoms. We could measure the frequency of the harmonic confinement in the vertical direction by measuring the breathing frequency of a thermal cloud when the lattice power is suddenly divided by two. The oscillation frequency for this reduced power corresponds to half of this value. The results are reported in figure 4.15. A maximum frequency of 4.2 kHz was measured at half of the maximum power.

We want to compare those results to the theoretical value of the oscillation frequency: it depends on the height of the potential U_0, on the mass of the atom M and on the lattice spacing Δz

$$\nu_z = \sqrt{\frac{U_0}{2M}}\frac{1}{\Delta z} \tag{4.3}$$

In our case, the frequency increases faster than the $1/\Delta z$ dependence (figure 4.15) because the cloud is not loaded in the most central dark fringe of the cloud. It is then brought to the most intense part of the accordion beam as it is compressed, changing the effective value of U_0.

4.3 CONCLUSION

In this chapter, we have described the new experimental set-up which has been built since June 2013. This experiment is aimed at studying the physics of 2D gases in arbitrary potentials. Loading a 3D MOT from a 2D MOT and using

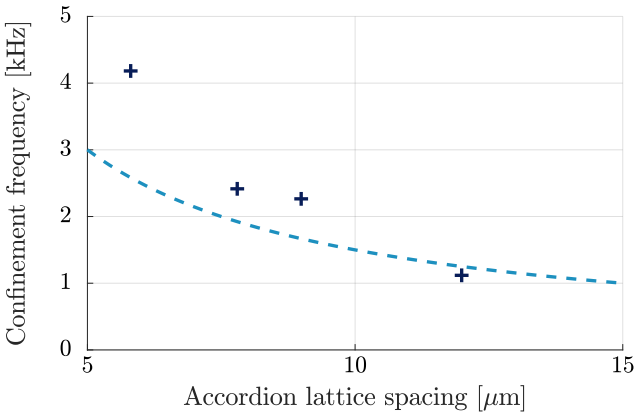

Figure 4.15: Measured oscillation frequencies in the compressed accordion lattice at half maximum power as a function of the lattice spacing. Crosses correspond to measured values. The dashed line corresponds to the theoretical value for a potential with a depth of $U_0 = k_B \cdot 9\,\mu$K. These measurements were realized with a horizontal waist of $w_y = 45\,\mu$m for the accordion beams. The discrepancy between theory and experiment can be explained by the displacement of the dark fringe in which the atoms are trapped from the edge to the center of the beams.

a crossed optical dipole trap, degenerate 2D gases are reliably produced every 30 s in a compact vacuum system.

The vertical confinement is provided by an angled lattice whose spacing can be dynamically varied in the experimental sequence, allowing to load a single plane of atoms and then accessing strong confinement. The in-plane trapping is provided by a hollow repulsive beam shaped using a DMD which is a flexible solution to produce arbitrary potentials. Two microscope objectives allow for high resolution imaging and projection of optical potentials ($\lesssim 1\,\mu$m).

5

COLLECTIVE EFFECTS IN LIGHT-MATTER INTERACTION

The experimental set-up whose design has been detailed in chapter 4 enables us to prepare dense atomic samples in 2D geometries. The typical atomic densities that are reached are on the order of $100\,\mathrm{at}/\mu\mathrm{m}^2$; at those densities, the mean inter-particle distance is on the order of $r = 0.1\,\mu\mathrm{m}$. If the atoms interact with light with a wavelength $\lambda = 780.24\,\mathrm{nm}$ (for the D_2 transition that we will consider), the distance between the particle is on the order of $\lambda/2\pi = 1/k$: the dipole-dipole interactions cannot be neglected. We therefore expect strong collective effects to take place when an atomic beam interacts with the cloud.

In this chapter, we will describe the *recurrent scattering* regime and the *multiple scattering* regime, following the nomenclature of [58]. The latter implies processes where a photon is absorbed and reemitted several times before escaping the cloud of atoms, without interacting several times with the same atom, and usually takes place in optically thick gases. The former includes the situation where a photon can interact many times with the same atom, for example while bouncing between the two atoms of a close pair (in addition to the processes considered in the multiple scattering regime).

We study these collective effects in light-matter interaction by monitoring the transmission of light through slabs of atoms of varying thicknesses and densities. This allows us to explore both multiple and recurrent scattering regimes.

After giving a quick overview of the problem of collective effects in light-matter interaction, I will present the model we choose to reproduce our experimental results. Then, the methods used to prepare a cloud of given density and thickness will be described. The main experimental results consist of fits of resonance curves, where the width and frequency shift are studied as a function of density and thickness. Last, we present a prospective series of experiments aiming at tracking the propagation of an excitation when a cloud of atoms is illuminated locally.

5.1 POSITION OF THE PROBLEM

5.1.1 *Importance of collective effects in atom-light interactions*

Light-atom interactions represent an ideal system to study many aspects of quantum mechanics. The interaction of one atom with the electromagnetic field is now well understood [183]. For instance, the controlled interaction between one atom and a mode of the electromagnetic field in the context of cavity quantum electrodynamics has led to the observation of Schrödinger cat states of light or to the first steps toward quantum information processing [184].

However, as soon as $N \gg 1$ atoms interact with the electromagnetic field, the collective response can be very different from the sum of individual behaviours. Let us take three examples that illustrate this.

5.1.1.1 *Imaging opaque disks*

First, consider the case of imaging a cloud of opaque disks of cross-section σ_d in the xy plane by looking at the light they block on a beam propagating along the z direction.

This is reminiscent of absorption imaging where atoms are considered as small disks of area σ_0, with σ_0 the scattering cross-section with light, with a value for a two-level atom at resonance of:

$$\sigma_0 = \frac{3\lambda^2}{2\pi} \tag{5.1}$$

As long as the cloud of opaque disks is dilute enough, the different atoms absorbing and reemitting light do not influence each other. Assuming a disk distribution with density $n(\boldsymbol{r})$ and light propagating along the z direction, a cloud of disks is dilute enough when the column density $n_c(x,y) = \int n(\boldsymbol{r})\,\mathrm{d}z$ is always much smaller than $1/\sigma_d$. Starting from a beam with uniform intensity I_{in} on an area $\mathcal{A} \gg \sigma_d$, the amount of transmitted light P_{out} when having N disks ($n_c = N/\mathcal{A}$) corresponds to [123]

$$P_{\text{out}} = I_{\text{in}}\mathcal{A}\left(1 - \frac{\sigma_d}{\mathcal{A}}\right)^N = P_{\text{in}}\, e^{-n_c\sigma_d} \tag{5.2}$$

We define the optical density (OD) as

$$\text{OD} = -\ln\left(\frac{P_{\text{out}}}{P_{\text{in}}}\right) \tag{5.3}$$

In the case that was just described, it takes a simple value

$$\text{OD} = n_c\sigma_d \tag{5.4}$$

and equation 5.2 corresponds to the well-known Beer-Lambert law.

In atomic clouds, the Beer-Lambert law is not always valid; in particular, since the light is not absorbed but scattered by the atoms, modification to this behaviour are expected for optically thick gases [185, 186], for which

$$\boxed{\sigma_0 n_c \gg 1} \tag{5.5}$$

This behaviour corresponds to the multiple scattering regime, and does not necessitate a dense cloud (where $nk^{-3} > 1$).

Note that in the case of a $|F = 2\rangle \rightarrow |F' = 3\rangle$ transition as is the case for the imaging transition of rubidium 87, the scattering cross-section is modified from that of equation 5.1 due to the Clebsch-Gordan coefficients characterizing the strength of the dipole transition between the various m_F states. We can consider an effective cross-section for a π polarized light considering equal populations in all m_F states [123]:

$$\sigma = \frac{7}{15}\sigma_0 = \frac{7}{15}\,\frac{3\lambda^2}{2\pi} \tag{5.6}$$

5.1.1.2 *Mean-field treatment of scattering in a dense medium*

As a second example, we present the mean-field treatment of scattering in a dense medium.

Light scattering in a dense medium has attracted a lot of interest from the condensed-matter community [187]. Interactions between classical, coupled dipoles are detailed in section 5.2. For an assembly of N dipoles located at positions $\{\boldsymbol{r}_i\}_{i\in[\![1,N]\!]}$, the total light field $\boldsymbol{E}_{\text{total}}$ is the sum of the incoming field $\boldsymbol{E}_{\text{in}}$ (with angular frequency ω) plus the field radiated $\boldsymbol{E}_{\text{radiated}}$ by each dipole excited in turn by the total field

$$\boldsymbol{E}_{\text{total}} = \boldsymbol{E}_{\text{in}} + \boldsymbol{E}_{\text{radiated}} \tag{5.7}$$

In the full treatment, the specific positions of the dipoles can strongly influence the final result and lead to non-local correlations of the field.

In the mean field treatment, the field radiated by all the dipoles is approximated by [188]

$$\boldsymbol{E}_{\text{radiated}}(\boldsymbol{r}) \simeq \frac{\boldsymbol{P}(\boldsymbol{r})}{3\epsilon_0} \tag{5.8}$$

where $\boldsymbol{P}(\boldsymbol{r})$ is the local polarization of the coarse-grained medium. The field no longer depends on the polarization of the material at $\boldsymbol{r} \neq \boldsymbol{r}'$, which constitutes the mean-field approximation in this context. We consider a 3D dipole density n. These dipoles have a bare susceptibility χ_0 and a single-atom polarizability $\alpha = \chi_0/n$ such that [188]

$$\boldsymbol{P} = \epsilon_0\chi_0\boldsymbol{E}_{\text{total}} \tag{5.9}$$

$$\boldsymbol{P} = \epsilon_0 n\alpha\boldsymbol{E}_{\text{total}} \tag{5.10}$$

We can also define the renormalized susceptibility χ which takes into account the fact that the dipoles radiate a field which retroacts on them. We thus have

$$\boldsymbol{P} = \epsilon_0\chi\boldsymbol{E}_{\text{in}} \tag{5.11}$$

These equations can be combined yielding the susceptibility as a function of the density of scatterers and of the single atom polarizability [188]

$$\chi = \frac{n\alpha}{1 - \frac{n\alpha}{3}} \tag{5.12}$$

In our case, the polarizability corresponds to the two-level atom result [189]

$$\alpha = -\frac{3\pi\Gamma}{k^3}\frac{1}{\Delta + i\frac{\Gamma}{2}} \tag{5.13}$$

where Γ is the natural linewidth, $\hbar ck = \hbar\omega_0$ the energy difference between the two levels, and $\Delta = \omega - \omega_0$ the detuning between the atomic frequency and the frequency of the light field (the Lamb shift is included in ω_0).

The new resonance frequency is defined as the value of Δ for which the real part of the denominator of χ vanishes

$$\Delta_{\text{MF}} = -2\pi\frac{n}{k^3}\frac{\Gamma}{2} \tag{5.14}$$

This shift, also called cooperative Lamb shift, is to the red of the natural resonance, and requires a dense cloud $nk^{-3} \gg 1$ in order to be significantly larger than Γ.

This mean-field theory can be developed further. For example, it is possible to include the influence of the field radiated by each dipole to the total field $\boldsymbol{E}_{\text{total}}$ to the lowest non-zero order [190]. This correction can be applied to the case of an atomic slab of width ℓ, leading to a shift

$$\Delta_{\text{slab}} = -|\Delta_{\text{MF}}| + \frac{3}{4}|\Delta_{\text{MF}}|\left(1 - \frac{\sin 2k\ell}{2k\ell}\right) \tag{5.15}$$

which was measured in a hot vapour of rubidium in nanocell [191] with excellent agreement with the theoretical prediction.

In the case of hot atomic vapours, it is possible that mean-field theory applies well thanks to the inhomogeneous broadening due to the Doppler shifts [192]. Difference in resonant frequencies due to the velocities of the atoms prevents long-range correlations to be built. In the case of cold clouds of atoms, where the Doppler shift

$$\Delta\omega_{\text{Doppler}} = \frac{\Delta v_{\text{atoms}}}{c}\omega_0 \tag{5.16}$$

is much smaller than the natural linewith Γ, a photon can be scattered several times by atoms which are far apart. It is thus necessary to take into account more precisely the scattering events that are important to recurrent scattering [58, 189, 192, 193].

5.1.1.3 *A pair of interacting atoms*

As a third example, consider a pair of two-level atoms interacting through the dipole-dipole interaction. The energy between the ground state $|g\rangle$ and the excited state with polarization ε, $|e:\varepsilon\rangle$, of each atom taken separately is $\hbar\omega_0 = \hbar c k_0$ (c is the speed of light), and the lifetime of the excited state is Γ^{-1}.

We will consider a light beam with angular frequency $\omega = ck$ propagating along z with a polarization ε_x incident on a pair of atoms such that $\boldsymbol{r}_2 = \boldsymbol{r}_1 + r\,\boldsymbol{e}_y$. Then, there are three manifolds of states which are interesting: (i) both atoms are in the ground state $|g_1, g_2\rangle$, (ii) one of the two atoms is in the excited state, $|g_1, e_2 : \varepsilon_x\rangle$ and $|e_1 : \varepsilon_x, g_2\rangle$, (iii) both atoms are in the excited state $|e_1 : \varepsilon_x, e_2 : \varepsilon_x\rangle$.

If the atoms are far apart, the two states of manifold (ii) have degenerate energies. If they are close enough, that is if their distance r is such that $k_0 r \lesssim 1$, the dipole-dipole interaction lifts the energy degeneracy between $|g_1, e_2 : \varepsilon_x\rangle$ and $|e_1 : \varepsilon_x, g_2\rangle$. The two new eigenstates $|eg^+\rangle$ and $|eg^-\rangle$ have energies E_+ and E_- and decay rates $\Gamma_+$and Γ_- different from the single atom picture:

$$E_\pm - \hbar\omega_0 \quad \propto \pm \quad \frac{\hbar\Gamma}{(k_0 r)^3} \tag{5.17}$$

$$\Gamma_+ \quad \xrightarrow[k_0 r \to 0]{} \quad 2\Gamma \tag{5.18}$$

$$\Gamma_- \quad \xrightarrow[k_0 r \to 0]{} \quad 0 \tag{5.19}$$

These results stem from the modelling described in section 5.2.

The equation 5.17 shows that the energies of the eigenstates are displaced. A similar phenomenon has been illustrated in the context of Rydberg atoms [194], which are states of atoms with a large dipole moment. In this regime, it is not possible to promote two atoms to a Rydberg state with the same laser, that is to go from manifold (ii) to (iii), because once one atom is promoted, the energy needed to promote the second one is no longer the same (the energy of the $|e_1 : \varepsilon_x, e_2 : \varepsilon_x\rangle$ is modified). This is called Rydberg blockade, and was observed experimentally [195, 196].

Equations 5.18 and 5.19 in turn show another aspect of the behaviour of two atoms interacting via the dipole-dipole interaction. Here, we see that coupling the two atoms leads to two states with different decay rates: while one state decays fast (corresponding to the case where the atoms oscillate in phase [197]) with a rate which is twice that of a single atom, the second state has a vanishingly small decay rate. These two states are called *superradiant* and *subradiant*. They have been observed in a variety of systems including cold ensemble of atoms [198–200], ions [201], molecules [202] and have also acoustical analog [203].

The two terms supperadiant and subradiant have been coined by Dicke in his seminal paper [204] where he studies the effect of dipole-dipole coupling. A quantum phase transition appears when this coupling is strong enough [33], which happens when an assembly of N atoms is confined in a volume small compared to λ^3.

For a pair of atoms, we see that collective effects starts to be important (energy shifts and modified decay rates) when the mean interparticle distance r is such that

$$\boxed{k_0 r \lesssim 1} \tag{5.20}$$

This condition puts more constraints on the atomic density than the condition to observe collective effects of a dilute but optically thick gas in equation 5.5. Both limits are described within the same modelling in section 5.2.

5.1.2 *Observation of collective effects*

The relevance of the mean-field description has been verified for solid materials, for hot atomic vapours and for Doppler-broadened clouds of cold atoms, including some corrections to include relevant multiple scattering events [186, 187, 191].

We will in the following focus on light-matter interaction experiments performed with cold to ultracold clouds of atoms, where experiment were performed both in the multiple and in the recurrent scattering regimes.

Signatures of multiple scattering were deduced from radiation pressure force modifications for atoms in optically thick but dilute clouds [185], and the cooperative Lamb shift was measured for largely spaced ions [205].

Many studies were performed by looking at the amount of light absorbed or fluoresced by an assembly of cold atoms [58, 59, 186, 206]. In this case, the amount of transmitted or fluoresced light is recorded for various detunings of the probe laser. As the density increases, the main effect which is seen is a broadening of the resonance fitted by a lorentzian curve with a width of more

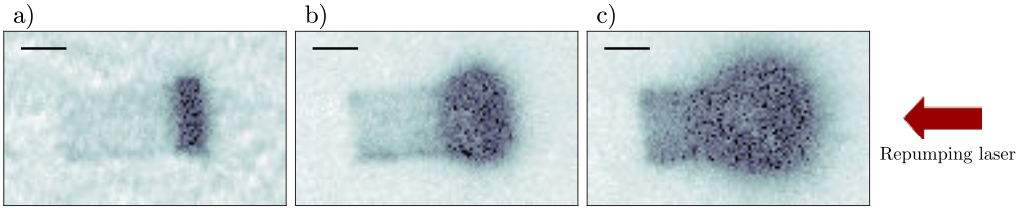

Figure 5.1: Cloud of $15\,\mu\text{m} \times 30\,\mu\text{m}$ at different repumping times: (a) $10\,\mu\text{s}$, (b) $25\,\mu\text{s}$, (c) $50\,\mu\text{s}$. The atoms acquire a velocity after being repumped from one hyperfine state to the other which is much larger than the recoil velocity. It can be explained by large light-mediated repulsion when one atom of a pair is in the excited $F' = 2$ state. Scale bars correspond to $10\,\mu\text{m}$.

than 3Γ both for strontium [186] and rubidium atoms [59]. A small red shift on the order of 0.2Γ has also been observed [59]. Such studies of resonance curves were performed both in the multiple scattering regime [186, 206] and in the recurrent scattering regime [58, 59].

Some experiments have also demonstrated the existence of sub- and superradiant states in atoms, molecules or ions [198–202] as predicted by Dicke [204]; decay rates up to 8Γ and down to 0.01Γ were observed.

5.1.3 *Relevance of collective effects for our systems*

In our system, the wavelength associated to the D_2 line of rubidium 87 is $\lambda_0 = 2\pi/k_0 \simeq 780.24\,\text{nm}$, so $k_0^{-1} \simeq k^{-1} = 2\pi/\lambda \simeq 0.12\,\mu\text{m}$.

When loading 2D box potentials as described in chapter 4, 2D densities $n^{(2D)}$ ranging from 50 to 150 atoms/μm^2 are achieved for disks of diameter 40 to $50\,\mu\text{m}$. These corresponds to optically thick gases since $\sigma n^{(2D)} \sim 14$. In addition, the mean interparticle distance r is then on the order of

$$r \sim 1/\sqrt{n^{(2D)}} \sim 0.08 \text{ to } 0.12\,\mu\text{m} \lesssim k^{-1} \tag{5.21}$$

Hence, we expect strong deviations from the single atom response in the interaction between a near-resonant probe light and our dense cloud of atoms in the regime of recurrent scattering. Our system is also well-suited to study the response of the cloud to a detuned probe beam: the cloud acts as a refractive medium, but the 2D geometry prevents strong lensing effects.

We get the first sign of strong collective effects when optically transferring the atoms from the $|F = 1\rangle$ to the $|F = 2\rangle$ state (see chapter 4 subsubsection 4.1.7.1). In this series of experiments, the optical repumping beam was propagating in the horizontal plane along the $-y$ direction (see chapter 4 Figure 4.2) and repumping the atoms that are trapped in the 2D box potential. As can be seen in figure 5.1, the atoms are repumped over $50\,\mu\text{s}$, and the front of repumped atoms can clearly be seen. In addition, after being repumped, the atoms travel $\sim 5\,\mu\text{m}$ in $\sim 15\,\mu\text{s}$ in spite of being trapped, meaning that they have a velocity on the order of 10 cm/s. This is incompatible with the recoil velocity that the atoms get after scattering one photon of the repumping beam, on the order of $v_{\text{recoil}} = 6\,\text{mm/s}$.

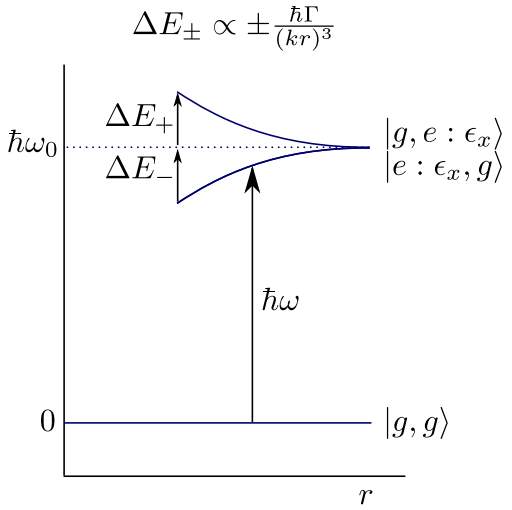

Figure 5.2: Energy diagram for two two-level atoms (ground state $|g\rangle$, excited state $|e\rangle$) interacting via the dipole interaction. As explained in section 5.1.1.3, the interaction lifts the degenerescence between the $|ge\rangle$ and $|eg\rangle$ states.

This large velocity can be understood from the simple case of a pair of atoms (see figure 5.2). The dipole-dipole interaction modifies the energies of the states where one atom of the pair is excited. These energies now depend on the vector $\boldsymbol{r}$ between the atoms. For two atoms separated by the distance r and excited along a direction orthogonal to $\boldsymbol{r}$

$$\Delta E_\pm \propto \mp \frac{\hbar\Gamma}{(kr)^3} \tag{5.22}$$

As a consequence, the atoms experience a force while one is in the excited state

$$|\boldsymbol{F}| \sim -3\frac{\hbar\Gamma}{r\,(kr)^3} \tag{5.23}$$

The atom spends a time on the order of Γ^{-1} in the excited state. The velocity acquired during this time is

$$v \sim \frac{|\boldsymbol{F}|\,\Gamma^{-1}}{M} \sim \frac{3v_{\text{recoil}}}{(kr)^4} \tag{5.24}$$

For a density of $150\,\text{at}/\mu\text{m}^2$, $v \sim 15\,v_{\text{recoil}} \sim 10\,\text{cm/s}$, which is on the order of the velocities which are deduced from figure 5.1.

5.2 MODELLING MULTIPLE AND RECURRENT SCATTERING EFFECTS

5.2.1 *Choice of the model*

The interaction of an assembly of atoms with light is difficult to simulate numerically; some approximations are needed, and we discuss in this section the possible treatments of the problem [207] and the reason we choose one of them to compare to our experimental system.

First, we neglect the motional degrees of freedom of the atoms; their initial velocities make their displacement short on the typical timescale of the interaction (this includes neglecting the Doppler effect). However, the light-mediated forces do induce larger velocities in the atoms as explained in 5.1.3, but it will be neglected here.

Second, we want to describe theoretically the interaction of an assembly of rubidium atoms that can interact with a light field close to resonance with the $|F = 2\rangle \rightarrow |F' = 3\rangle$ transitions, consisting of $L = 12$ states with $D = 15$ possible transitions. The interaction between the N atoms at positions $\boldsymbol{r}_i$ and the light field is treated within the dipole approximation (since the typical size of the atom is much smaller than the wavelength of the field)

$$\hat{H}_{\text{int}} = -\sum_{i=1}^{N} \hat{\boldsymbol{d}}_i \cdot \hat{\boldsymbol{E}}(\boldsymbol{r}_i) \tag{5.25}$$

where $\hat{\boldsymbol{d}}_i$ is the dipole moment of the ith atom, defined as the sum of all dipole operators for each of the D transitions $\left\{|g_j\rangle \rightarrow |e_j\rangle\right\}_{j\in[\![1,D]\!]}$

$$\hat{\boldsymbol{d}} = \sum_{j=1}^{D} \langle e_j|\hat{\boldsymbol{D}}|g_j\rangle |e_j\rangle\langle g_j| + \text{h.c.} \tag{5.26}$$

and $\hat{\boldsymbol{D}}$ is the dipole moment operator. The field $\hat{\boldsymbol{E}}(\boldsymbol{r})$ can usually be split into a classical and a quantum part; the classical part then describes the incoming laser field.

The full quantum mechanical treatment of the interaction of the electromagnetic field with the atoms can be done by considering both the field and the atomic degrees of freedom. However, the electromagnetic field has an infinite number of degrees of freedom, which makes it impractical. It is therefore more convenient to consider the density matrix of the atomic states after the field degrees of freedom have been traced out, as is described in [208]. The derivation of the master equation that describes the evolution of the density matrix relies on

- the Markov approximation, which assumes that the correlation time of the light field is much smaller than the correlation time of the atomic states. The state of the field thus always "follows" the state of the atoms.
- eliminating all terms in the master equation that oscillates on timescales comparable to the correlation time of the electromagnetic field. For a light field (resp. atomic transitions) of angular frequency ω (resp. ω_0), this eliminates terms in $e^{i(\omega+\omega_0)t}$ and $e^{-i(\omega+\omega_0)t}$ (see [207, 208] for a full description). Note that this kind of approximation, performed in the equation describing the evolution of the density matrix, is different from the rotating wave approximation which is usually done at the level of the interaction Hamiltonian $\hat{H}_{\text{int}}$ of equation 5.25.

The equation that has to be solved is therefore an equation on the density matrix reduced to the atomic space. This density matrix is a $12^N \times 12^N$ matrix: it is not

realistic to have computer simulations of large ensembles of atoms ($N \geqslant 100$) without further approximations.

These are the assumptions that are typically done in order to simplify the problem [207]:

- We can consider two-level atoms, reducing the size of the density matrix to a $2^N \times 2^N$ matrix. This is nevertheless still too computationally costly
- We can consider the weak excitation limit and restrict ourself to a non-degenerate ground state $|g\rangle$ for each atom. In that case, the state of the atoms is
$$|\psi\rangle = |gg\dots g\rangle + \sum_{i=1}^{N}\sum_{j=1}^{D} \beta_{i,j}|g\dots e_j^i\dots g\rangle \tag{5.27}$$
where $\left|\beta_{i,j}\right| \ll 1$. Under those conditions, the evolution reduces to a Schrödinger equation for $|\psi\rangle$ with an effective Hamiltonian H_{eff} which is non-hermitian [128, 207, 209]. The size of the matrix that has to be computed to solve the system is $DN \times DN$. Choosing $D = 3$ leads to systems which can be solved numerically. This choice, corresponding to a $J = 0 \to J = 1$ transition, actually corresponds to the situation of classical dipoles in an electromagnetic field [128]. This can be understood from the fact that having a weak excitation prevents any effect of bosonic amplification of the light field or saturation of the atomic transition to happen, hence the classical description of the field and atom is correct in this limit. Note also that a $J = 0 \to J = 1$ transition corresponds to a transition which has the same dimension as $\mathbb{R}^3$ in which classical dipoles exist.

In the following, we will model our system by an assembly of atoms with a $J = 0 \to J = 1$ transition in the weak excitation limit as was just described. We briefly describe the system to be solved from the point of view of classically coupled dipoles in the following subsection. Let us mention two additional approximations that can be done to solve this problem:

- Within the weak excitation limit, we can also consider that we have only two-level atoms, that is $D = 1$. This reduces the size of the matrix to be computed to $N \times N$.
- Last, for the weak excitation and a two-level atom system, it is possible to develop a mean-field theory called "Timed Dicke". The coefficient β_i corresponding to the amplitude of the excitation of the ith atom is replaced by
$$\beta_i = \bar{\beta} e^{i\boldsymbol{k}\cdot\boldsymbol{r}_i} \tag{5.28}$$
where $\bar{\beta}$ is now the only mean-field dipole to be solved.

5.2.2 *Coupled classical dipoles*

In a classical description, the light field $\boldsymbol{E}_L$ induces a dipole moment $\boldsymbol{d}_i$ on an atom at position $\boldsymbol{r}_i$ thanks to the atomic polarizability tensor $\underline{\underline{\alpha}}$

$$\boldsymbol{d}_i = \underline{\underline{\alpha}} \cdot \boldsymbol{E}_L\left(\boldsymbol{r}_i\right) \tag{5.29}$$

which in turn produces an electromagnetic field at position $\boldsymbol{r}$ described by the tensor $\underline{\underline{g}}$:

$$\boldsymbol{E}_{\text{radiated}}(\boldsymbol{r}) = \underline{\underline{g}}\left(\boldsymbol{r} - \boldsymbol{r}_i\right) \cdot \boldsymbol{d}_i \tag{5.30}$$

It is a common approximation to neglect the fact that the electromagnetic field can have different polarizations, which is called the scalar approximation [185, 210]. However, the anisotropy of the dipole-dipole interaction (stemming from the vectorial character of the excitation) is important for our densities so we will not neglect this.

The last two relations can be written in an implicit form to find either the total light field $\boldsymbol{E}_{\text{tot}}$ or the dipole moment of each atom $\boldsymbol{d}_j$ knowing the incoming field $\boldsymbol{E}_L$:

$$\boldsymbol{E}_{\text{tot}}(\boldsymbol{r}) = \boldsymbol{E}_L(\boldsymbol{r}) + \sum_i \underline{\underline{g}}\left(\boldsymbol{r} - \boldsymbol{r}_i\right) \cdot \underline{\underline{\alpha}} \cdot \boldsymbol{E}_{\text{tot}}(\boldsymbol{r}) \tag{5.31}$$

$$\boldsymbol{d}_i = \underline{\underline{\alpha}} \cdot \boldsymbol{E}_L\left(\boldsymbol{r}_i\right) + \sum_j \underline{\underline{\alpha}} \cdot \underline{\underline{g}}\left(\boldsymbol{r}_i - \boldsymbol{r}_j\right) \cdot \boldsymbol{d}_j \tag{5.32}$$

They can be expanded to have the expression of the field $\boldsymbol{E}_{\text{tot}}$ as an infinite sum depending on $\boldsymbol{E}_L$

$$\begin{aligned}\boldsymbol{E}_{\text{tot}}(\boldsymbol{r}) = \boldsymbol{E}_L(\boldsymbol{r}) &+ \sum_i \underline{\underline{g}}\left(\boldsymbol{r} - \boldsymbol{r}_i\right) \cdot \underline{\underline{\alpha}} \cdot \boldsymbol{E}_L\left(\boldsymbol{r}_i\right) \\ &+ \sum_{i,j} \underline{\underline{g}}\left(\boldsymbol{r} - \boldsymbol{r}_j\right) \cdot \underline{\underline{\alpha}} \cdot \underline{\underline{g}}\left(\boldsymbol{r}_j - \boldsymbol{r}_i\right) \cdot \underline{\underline{\alpha}} \cdot \boldsymbol{E}_L\left(\boldsymbol{r}_i\right) + \ldots\end{aligned} \tag{5.33}$$

or the expression of the dipole moment of each atom $\boldsymbol{d}_i$ as an infinite sum depending on $\boldsymbol{E}_L$:

$$\begin{aligned}\boldsymbol{d}_i = \underline{\underline{\alpha}} \cdot \boldsymbol{E}_L\left(\boldsymbol{r}_i\right) &+ \underbrace{\sum_j \underline{\underline{\alpha}} \cdot \underline{\underline{g}}\left(\boldsymbol{r}_i - \boldsymbol{r}_j\right) \cdot \underline{\underline{\alpha}} \cdot \boldsymbol{E}_L\left(\boldsymbol{r}_j\right)}_{\text{two atoms interactions}} \\ &+ \underbrace{\sum_{j,k} \underline{\underline{\alpha}} \cdot \underline{\underline{g}}\left(\boldsymbol{r}_i - \boldsymbol{r}_j\right) \cdot \underline{\underline{\alpha}} \cdot \underline{\underline{g}}\left(\boldsymbol{r}_j - \boldsymbol{r}_k\right) \cdot \underline{\underline{\alpha}} \cdot \boldsymbol{E}_L\left(\boldsymbol{r}_k\right) + \ldots}_{\text{three atoms interactions}}\end{aligned} \tag{5.34}$$

Starting from the third term of equation 5.33 and from the second term of equation 5.34, we see that the total electric field is different from the sum of individual contributions of each atom, corresponding to

$$\boldsymbol{E}_{\text{tot}}(\boldsymbol{r}) \neq \boldsymbol{E}_{\text{sum individual}}(\boldsymbol{r}) = \boldsymbol{E}_L(\boldsymbol{r}) + \sum_i \underline{\underline{g}}\left(\boldsymbol{r} - \boldsymbol{r}_i\right) \cdot \underline{\underline{\alpha}} \cdot \boldsymbol{E}_L\left(\boldsymbol{r}_i\right) \tag{5.35}$$

In some cases, it is possible to neglect the high-order terms in equation 5.33 and 5.34, for instance if the typical value of $\underline{\underline{g}}\left(\boldsymbol{r}_j - \boldsymbol{r}_i\right)$ for two atoms located at $\boldsymbol{r}_i$ and $\boldsymbol{r}_j$ is vanishingly small.

Although equations 5.31 and 5.32 are equivalent, it is easier to solve numerically the second one which only implies a finite number of degrees of freedom.

The tensor $\underline{\underline{\alpha}}$ is replaced by the atomic polarizability for an atom with a transition of energy $\hbar\omega_0$ and a linewidth Γ

$$\alpha = -\frac{6\pi}{k^3}\frac{\Gamma}{2}\frac{1}{\Delta + i\frac{\Gamma}{2}} \tag{5.36}$$

where $\Delta = \omega - \omega_0$ is the detuning of the electromagnetic field (of frequency ω) from the atomic resonance and $k = \omega/c$. We also need to compute the tensor $\left[\underline{\underline{g}}\left(\boldsymbol{r}_i - \boldsymbol{r}_j\right)\right]_{i,j\in[\![1,N]\!]}$, which induces correlations between the dipoles; calling $r_{ij} = \left|\boldsymbol{r}_{ij}\right| = \left|\boldsymbol{r}_i - \boldsymbol{r}_j\right|$, the amplitude of the field radiated by the dipole i at the position of dipole j is

$$\boldsymbol{E}_j\left(\boldsymbol{r}_i\right) = \frac{k^3}{6\pi\epsilon_0} G\left(kr_{ij}\right)\cdot\boldsymbol{d}_i \tag{5.37}$$

with $G\left(r_{ij}\right) = \underline{\underline{g}}\left(\boldsymbol{r}_i - \boldsymbol{r}_j\right)$ a 3×3 matrix equals to [128]

$$G\left(kr_{ij}\right) = h_1\left(kr_{ij}\right)\mathbb{1} + h_2\left(r_{ij}\right)\frac{\boldsymbol{r}_{ij}\otimes\boldsymbol{r}_{ij}}{r_{ij}^2} \tag{5.38}$$

(where $\otimes$ is the tensor product) and

$$h_1(u) = \frac{3}{2}\frac{e^{iu}}{u^3}\left(u^2 + iu - 1\right), h_2(u) = \frac{3}{2}\frac{e^{iu}}{u^3}\left(-u^2 - 3iu + 3\right) \tag{5.39}$$

Equation 5.32 becomes

$$\left(\Delta + i\frac{\Gamma}{2}\right)\boldsymbol{d}_{j,\alpha} + \frac{\Gamma}{2}\sum_{j'\neq j}\sum_{\alpha'=x,y,z} G_{\alpha,\alpha'}\left(kr_{jj'}\right)\cdot\boldsymbol{d}_{j',\alpha'} = d\Omega\boldsymbol{\epsilon}_\alpha e^{i\boldsymbol{k}\cdot\boldsymbol{r}_j} \tag{5.40}$$

with Ω and $\boldsymbol{\epsilon}$ the Rabi frequency and polarization of $\boldsymbol{E}_{\text{in}}$ and d is such that $\Gamma = d^2k_0^3/(3\pi\epsilon_0\hbar)$ that is

$$\underline{\underline{M}}\cdot\frac{\boldsymbol{d}}{d} = \boldsymbol{a} \tag{5.41}$$

with $\boldsymbol{d}$ the $3N\times 1$ vector containing the dipole moment along each polarization for all the atoms, $\underline{\underline{M}} = \left(\Delta + i\frac{\Gamma}{2}\right)\mathbb{1} + \underline{\underline{G}}$ the $3N\times 3N$ matrix containing the coefficients of the linear system to solve and $\boldsymbol{a}$ the excitation vector containing the amplitude, the phase and the polarization of the incoming light field.

After solving this linear system for $\boldsymbol{d}$, the values of the dipoles can be used to extract the field radiated by the atoms in each direction $\boldsymbol{k}_{\text{out}}$ and each polarization $\boldsymbol{\epsilon}_{\text{out}}$; in particular, for $\boldsymbol{k}_{\text{in}} = \boldsymbol{k}_{\text{out}}$, this allows to compute the theoretical value of the optical density after the assembly of atoms is imaged at the focal point of a lens as described in [128]. The field radiated by the atoms imaged at the focal point of a lens in the direction of the incoming field (i. e. $\boldsymbol{k}_{\text{in}} = \boldsymbol{k}_{\text{out}}$) with polarization $\boldsymbol{\epsilon}_{\text{out}}$ is:

$$\boldsymbol{E}_{\text{out}}^{\text{atoms}}\left(\boldsymbol{\epsilon}_{\text{out}}\right) = -\frac{\Omega}{d}\frac{i}{2}\sigma_0 n_c\sum_{j=1}^{N}\sum_{\alpha=x,y,z}\boldsymbol{d}_{j,\alpha}\boldsymbol{\epsilon}_{\text{out},\alpha} \tag{5.42}$$

with σ_0 the on-resonance scattering cross-section and n_c the column density; the optical density is thus:

$$\text{OD}_{\text{theo}} = -2\ln\left|1 + \boldsymbol{E}_{\text{out}}^{\text{atoms}}\left(\boldsymbol{\epsilon}_{\text{in}}\right)d/\Omega\right| \tag{5.43}$$

5.2.3 *Programs*

The programs that are used are described in Appendix C, and are available at https://github.com/lauracorman/multipleScattering.

Computing the OD requires solving a linear system of size $3N \times 3N$, where N is the number of simulated atoms whose positions are drawn in a disk of radius R. For a given Beer-Lambert OD, $\mathrm{OD}_{\mathrm{BL}} = \sigma_0 N / \left(\pi R^2\right)$, we compute $\mathrm{OD}_{\mathrm{theo}}(N)$ for various values of N to find when finite-size effects are negligible, and consider only values of $\mathrm{OD}_{\mathrm{theo}}(N)$ such that $\mathrm{OD}_{\mathrm{theo}}$ becomes independent of N.

We are able to simulate up to 4000 atoms. This allows us to compute the theoretical OD up to $\mathrm{OD}_{\mathrm{BL}} = 8$ for thin gases ($\Delta z \leqslant 0.2\,\mu\mathrm{m}$), and up to $\mathrm{OD}_{\mathrm{BL}} = 4$ for thick gases ($\Delta z \simeq 20\,\mu\mathrm{m}$).

5.3 PREPARING A SAMPLE

5.3.1 *Calibration of the imaging set-up*

5.3.1.1 *Camera properties*

In order to detect the atomic absorption, we image the cloud of atoms on a back-illuminated CCD camera from Princeton instruments, model Pixis 1024 Excelon. It is a 16 bit camera with a 1024×1024 pixel chip. We use it at maximum gain, which approximately corresponds to one count per electron.

In order to reduce the read-out noise, we cool it down to $-43°\mathrm{C}$ and the analog to digital converter is set to the slowest rate of 100 kHz. At this rate, reading the whole chip takes about 10 s.

The numerical aperture of the imaging system is relatively large (0.45). With this numerical aperture, on the order of 5% of the light absorbed by the atoms and reemitted in random directions is recaptured. To avoid recapturing that light that can hinder the optical density measurement, we insert an adjustable iris in the plane which is Fourier-conjugated to the atoms, typically limiting the numerical aperture to 0.2 by closing to a diameter of 6 mm (see figure 5.3a).

5.3.1.2 *Frame transfer mode*

We want to avoid a large delay between the picture taken with atoms and the picture taken without atoms. Since the read-out time is 10 s, we use the camera in kinetic mode: instead of performing a single exposure which is read at once, the camera perform a series of five exposures followed by transfer of the accumulated charges in the vertical direction. The final picture is therefore divided in five, each containing the light acquired at different times (figure 5.3). One fifth of the chip is exposed for $40\,\mu\mathrm{s}$, and the charges in the wells are transferred upwards in less that $700\,\mu\mathrm{s}$; this is much faster that reading them out. Four fifths of the chip are hidden from the imaging light thanks to a razor blade located in a plane conjugate to the atoms. After five sequences of exposure separated by charge transfer, the shutter of the camera closes and the chip is read. This process as well as the imaging system is illustrated in figure

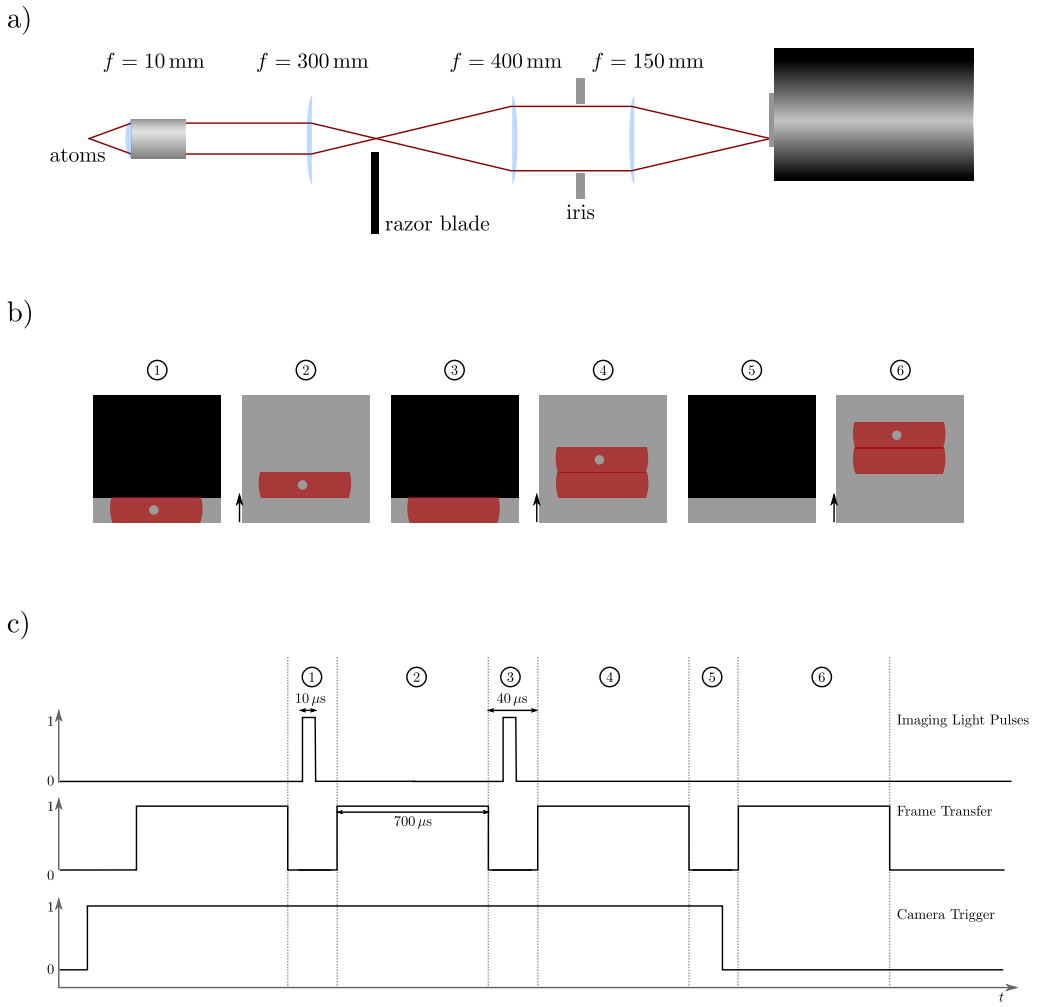

Figure 5.3: Sketch of the imaging system. (a) Optical system used for imaging the cloud. A first telescope with magnification 30 creates an image of the atoms where part of the light is blocked using a razor blade. A second telescope with magnification 0.375 images the atoms and the razor blade on the camera. (b) Schematic representation of the imaging sequence for the chip of the camera. Step 1 corresponds to the exposure of the picture with atoms, step 2 to the following frame transfer stage, step 3 to the exposure of the picture without atoms, step 4 to the following frame transfer stage, step 5 to the exposure of the background frame, step 6 to the following frame transfer stage. Each of these steps is also represented in the time sequence for the digital variable of (c), representing the trigger signal of the camera, the light pulses used and the frame transfer stages.

5.3. The chip is divided into five parts because the pixels are not perfectly hidden from the light sources when the shutter is opened; only three frames are of real interest to us:

- the first frame is exposed during the end of the preparation sequence because the shutter opens on the order of 3 s before the beginning of the imaging procedure; it is therefore unused.
- the second frame corresponds to the picture with atoms.
- the third frame corresponds to the picture without atoms.
- the fourth frame can be used as a background picture to be subtracted to the previous two.
- the fifth frame is exposed during several milliseconds, which correspond to the closing time of the shutter. It is therefore unused.

An exposure phase corresponds to a time where the charges in the different pixels are not transferred. However, during the frame transfer, one should be careful that the chip can accumulate photoelectrons (this is important for the depumping stage).

5.3.1.3 *Choice of the pixel size*

The pixel size of the camera is $13\,\mu\text{m} \times 13\,\mu\text{m}$, and the effective size of the pixel on the atoms is $1.16\,\mu\text{m} \times 1.16\,\mu\text{m}$ since the magnification of the optical system is 11.25 (see figure 5.3). This pixel size is chosen to be small enough to be able to check the uniformity of the cloud we prepare. It should also be chosen to be large enough such that the amount of light detected per pixel is much larger than the typical read-out noise (on the order of 5 counts per pixel). We want to probe the response of the cloud to the imaging light in the weakly saturating regime with an intensity $I \ll I_{\text{sat}} = 1.6\,\text{mW/cm}^2$ for the D_2 transition of rubidium 87. With this pixel size, a pulse of duration $10\,\mu\text{s}$ and taking into account the non coated surfaces, an imaging beam at the saturation intensity will generate 630 counts per pixels. In the following, we will only consider saturation parameters $s = I/I_{\text{sat}}$ below 0.2, which corresponds to an average number of counts per pixel N_{count} below 120.

5.3.2 *Computing the optical density of the cloud*

Standard, low-intensity absorption imaging yields the OD of the cloud (linked to the atomic density) through the formula

$$\text{OD} = -\ln\left(\frac{I_{\text{with}} - I_{\text{bgd}}}{I_{\text{without}} - I_{\text{bgd}}}\right) \tag{5.44}$$

where I_{with} is the intensity of the imaging beam going through the atoms, I_{without} the intensity of the imaging beam when there are no atoms and I_{bgd} the background intensity. For standard alignment procedure, we can use the

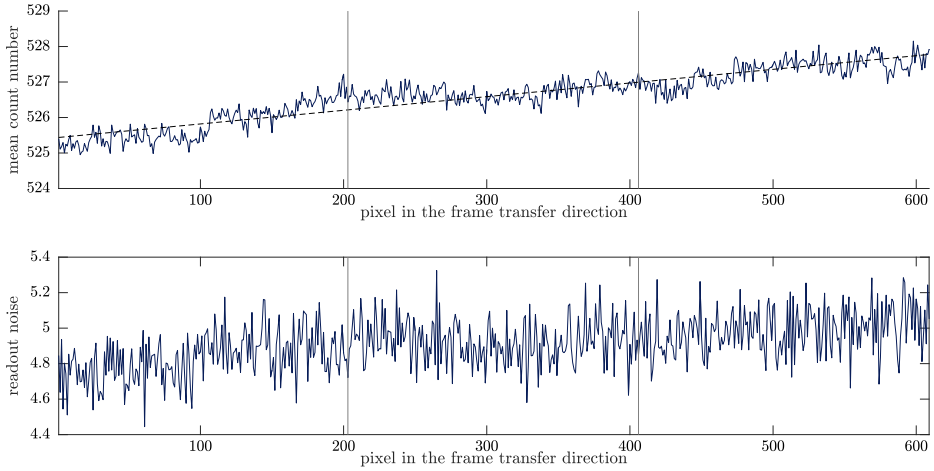

Figure 5.4: Systematic effects in the background part of the frame. A picture has been taken with a typical experimental sequence, but no atoms were captured and the imaging pulses were not triggered (see figure 5.3). The mean number of counts per line (top graph) and its standard deviation (bottom graph) are represented here for the relevant region of the chip: the region of the picture with atoms, without atoms and the background picture are delimited by light grey lines and are 203 pixel wide. The black dashed line of the top graph corresponds to a linear fit, showing a background increase of 3.84 counts for 1000 pixels.

fourth part of the chip as the background (as described in section 5.3.1.2). However, for an accurate determination of the OD, this is not sufficient, since several phenomena cause the background part of the frame to receive a different exposure from the parts of the frame with or without atoms:

- Using the kinetics mode that transfers the charges between each exposure sequence means that the frame with atoms (resp. without atoms) is exposed 1.5 ms (resp. 740 μs) longer than the background frame to the light that reaches the camera in spite of the razor blade, leading to an excess of counts for the frames that are exposed first.

- Reading out the chip with the slow, low-noise analog-to-digital converter takes up to 10 s. The frame with atoms is read several seconds before the background frame; during this time, dark counts can accumulate on the part of the chip which has not yet been read, leading to a systematically increased number of counts for the background frame. This effect is lowered when operating the CCD camera at low temperature.

Although these two causes have opposite effects, they do not compensate exactly, as seen on figure 5.4 representing an image without atoms and without imaging pulse, where only those systematic effects are seen. There is on average 1.56 counts (resp. 0.78 counts) more on a line of the background picture than on the corresponding line of the picture with (resp. without) atoms. For the evaluation of large OD, this represent an error which is too large. Therefore, in order to have an accurate determination of the OD, a background picture M_{bgd}

— that is a full picture without atoms and without imaging pulses — is taken at the end of each series of experiment. It is subtracted to the full data of the chip M_{data} (M_{bgd} and M_{data} are 1024×1024 matrices), which is then divided into two 1024×203 frames, M_{with} and M_{without}.

To compute the OD, the formula 5.44 can be used pixel by pixel and the mean OD can then be taken as the average value over all the relevant pixels, i. e. over the pixels that correspond to the position of the box potential $\mathbb{1}_{\text{box}}$. The maximum OD that can be measured depends on the number of counts per pixels N_{count}:

$$\text{OD}_{\text{max}} = \ln\left(N_{\text{count}}\right) \tag{5.45}$$

and varies between 3 and 4.8 for the imaging pulse and pixel size that are used. The error on the low values of the optical density is on the order of $\text{d}\,\text{OD} \simeq 0.37 - 0.09$ for $N_{\text{count}} = 30 - 120$ considering the read-out noise of $\text{d}N_{\text{count}}^{\text{read-out}} \simeq 5$ (see figure 5.4). This readout noise has to be considered twice, one for the image which is taken and the other for the background picture : $\text{d}N = \sqrt{2}\,\text{d}N_{\text{count}}^{\text{read-out}}$. For high values of OD, $\text{d}\,\text{OD} \simeq e^{\text{OD}}\text{d}N/N_{\text{count}} \sim 1$.

This large error can be avoided by computing the OD by summing the data beforehand. We therefore compute

$$N_{\text{with}} = \sum_{i,j} \mathbb{1}_{\text{box}}(i,j)\, M_{\text{with}}(i,j) \tag{5.46}$$

$$N_{\text{without}} = \sum_{i,j} \mathbb{1}_{\text{box}}(i,j)\, M_{\text{without}}(i,j) \tag{5.47}$$

where $\mathbb{1}_{\text{box}}$ is a 1024×203 matrix with ones at the location of pixels that are inside the box potential and zeros elsewhere. The number of pixels to be taken into account is $N_{\text{pix}} = \sum_{i,j} \mathbb{1}_{\text{box}}(i,j)$, typically on the order of 200. The relative error on $N_{\text{with}} = N_{\text{pix}} \langle N_{\text{count}} \rangle$ (and N_{without}) is reduced by a factor $\sqrt{N_{\text{pix}}} \simeq 14$ from the single pixel picture:

$$\frac{\text{d}N_{\text{with}}}{N_{\text{with}}} = \frac{\text{d}N}{\langle N_{\text{count}} \rangle} \frac{1}{\sqrt{N_{\text{pix}}}} = \frac{\sqrt{N_{\text{pix}}}\text{d}N}{N_{\text{with}}} \tag{5.48}$$

Decreasing the magnification to have all the atoms imaged on a single pixel would further decrease the relative error by a factor $\sqrt{N_{\text{pix}}}$, but we choose not to pursue this direction because this would prevent us from checking the uniformity of the cloud that is prepared.

The optical density is thus

$$\text{OD} = -\ln\left(\frac{\sum_{i,j} \mathbb{1}_{\text{box}}(i,j)\, M_{\text{with}}(i,j)}{\sum_{i,j} \mathbb{1}_{\text{box}}(i,j)\, M_{\text{without}}(i,j)}\right) = -\ln\left(\frac{N_{\text{with}}}{N_{\text{without}}}\right) \tag{5.49}$$

and the statistical error on the optical density is

$$\text{d}\,\text{OD} = \frac{\text{d}N}{\langle N_{\text{count}} \rangle} \frac{1}{\sqrt{N_{\text{pix}}}} \sqrt{e^{2\text{OD}} + 1} \sim 0.004\sqrt{e^{2\text{OD}} + 1} \text{ to } 0.015\sqrt{e^{2\text{OD}} + 1} \tag{5.50}$$

for a mean number of counts per pixel $\langle N_{\text{count}} \rangle$ between 30 and 120 and a read-out noise of $\text{d}N_{\text{count}}^{\text{read-out}} = 5$, i. e. $\text{d}N = 7$. For the largest $\text{OD} = 3$ that will be considered in the experimental analysis, the error is on the order of 0.12 (with a mean number of counts of 80).

5.3.3 *Preparation and properties of the atomic sample*

Using the experimental set-up described in chapter 4, we are able to produce clouds of atoms whose parameters are well suited to study collective scattering of light. The process starts by loading the same cloud of atoms in a 2D uniform trap. Then, we vary three parameters:

- the density of atoms interacting with the light by partially transferring them to an imaged state.
- the vertical extension of the cloud, which changes the mean interparticle distance without changing the column density.
- the frequency of the probe light with respect to the single atom resonance frequency.

5.3.3.1 *Preparation of the cloud*

The cloud is prepared using the sequence described in chapter 4. The atoms are trapped in a disk of 40 μm diameter and in a single fringe of the 12 μm accordion lattice. After loading the 2D uniform trap, the power of the box potential beam can be divided by 2.4 in 0.1 s; the power of the accordion can also be reduced during this timestep to change the vertical extension of the cloud. The powers of the beams are held constant for 0.5 s to allow for the thermalization of the cloud.

Then, a microwave pulse of variable duration (see 5.3.3.2) is applied in a bias field of 2 G to transfer part of the atoms to a detected state. The magnetic fields are then switched off, the atoms expand for a given time-of-flight period and a picture is taken. There a few milliseconds (from 0.7 to 10 ms) between the moment the current generating the bias magnetic field is switched off and the moment the picture is taken, to allow the eddy currents to decay to a level that does not influence the atoms. This is further confirmed by the fact that at low atomic densities, no inhomogeneous broadening has been seen.

5.3.3.2 *Repumping the atoms*

In order to avoid a large momentum kick to the atoms while transferring them from the $F = 1$ to the $F = 2$ state, we use a resonant microwave field in order to coherently transfer the atoms to the desired hyperfine state from the $|F = 1, m_F = -1\rangle$ to the $|F = 2, m_F = -2\rangle$ state. We choose this transition because it yields the highest Rabi frequency in our configuration. We choose the orientation of the magnetic bias field to minimize the residual gradient on the atoms. This leads to a Rabi frequency of 20.7(2) kHz.

We control the density of atoms that interact with the light by varying the duration of the microwave repumping pulse. The minimum duration accessible with the current status of the experiment control is 3 μs, corresponding to a transfer of 4% of the atoms to an imaged state. The mean interparticle distance between the atoms $\bar{r}$ is then on the order of $\sim 0.5\,\mu$m, such that coherent collective effects should not play a too strong role for this small density.

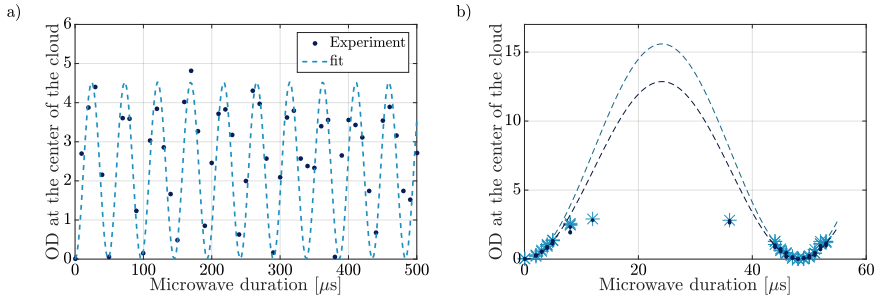

Figure 5.5: Rabi oscillation measurements. (a): Measurement of the Rabi oscillation frequency. The fitted frequency is 20.70 kHz with a 95% confidence interval of $(20.52, 20.87)$ kHz. (b) Extrapolation of the maximum OD for two configuration of in-situ gases (dark blue dots: accordion lattice at maximum power; light blue stars: accordion lattice at 23% of the maximum power), fixing the frequency and restricting the points to be fitted to those such that OD < 1.

The accuracy in the repumping is determined by the accuracy in the Rabi frequency of the microwave and the duration of the pulse. For a fluctuating magnetic field of order of magnitude 50 mG perpendicular to the direction of the bias field of 2 G (due to the fluctuating field generated by the subway), the Rabi frequency fluctuates around its mean value $20.7(2)$ kHz by 2%. This error leads to an error below 5% on the atom number in the range of repumping durations which are considered here.

The stability of the atom number is periodically checked using another imaging axis. It is stable at the 15% level. In order to determine accurately the atom number, we perform Rabi oscillations of the cloud. Knowing the Rabi frequency of the oscillation (see figure 5.5a) and limiting ourselves to OD smaller than 1 to avoid collective scattering effects, we extrapolate the maximum Beer-Lambert OD (equation 5.4 and figure 5.5b) for a π pulse. Over the different realizations, we find the maximum Beer-Lambert OD to be $14(2)$, corresponding to a maximum 2D density of $100(15)\,\text{atoms}/\mu\text{m}^2$, i. e. an atom number of $1.3(2) \cdot 10^5$. Therefore, using microwave repumping, the 2D density of the cloud can be tuned from 4 to $100\,\text{atoms}/\mu\text{m}^2$.

5.3.3.3 *Temperature of the atomic cloud*

We perform thermometry on the cloud of atoms with a technique similar to that described in [211]. Just after loading the 2D box trap, a small fraction of the atoms (between 10% and 18%) is transferred to the $F = 2$ hyperfine state using a short microwave pulse. The gas is then evaporated as usual, and finally released using a ToF of 5 ms. Only the atoms in $F = 2$ are being imaged.

The atoms in the $F = 2$ hyperfine state have had time to thermalize with the majority $F = 1$ atoms, but their density is too low to reach fugacities close to one, where quantum effects start to be important; it is a cold but non-degenerate sample. Their velocity distribution can therefore be approximated by a Maxwell-Boltzmann distribution.

In order to find the temperature of the atoms, we have to take into account the fact that the initial size of the cloud is not negligibly small compared to its

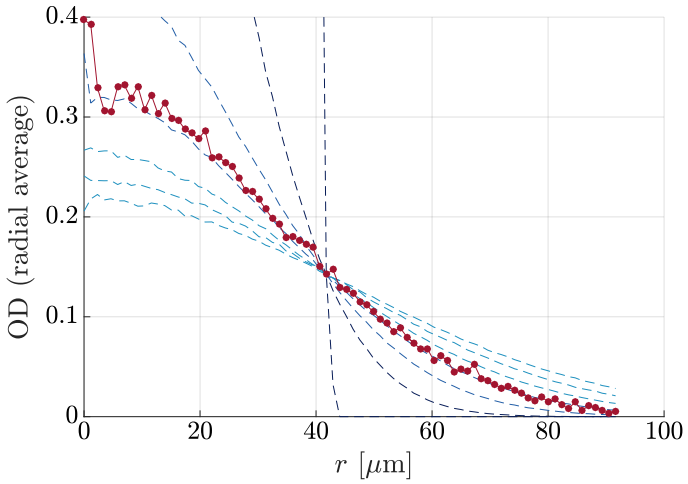

Figure 5.6: Example of temperature determination. The experimental curve (red dots) correspond to the radial average of the mean of ten pictures where 10% of the atoms were transferred to the $F = 2$ state before evaporation in the box potential, hold time for thermalization and time of flight of 5 ms. The dashed blue curves correspond to the same radial average of 100 simulated Maxwell-Boltzmann distribution after a ToF of 5 ms. The corresponding temperature from the light blue curve to the dark blue curve are 10, 100, 200, 300, 400, 500 and 600 nK. Here the experimental data follows the $T = 300$ nK curve best. More precise simulated curves lead to an estimate of $T = 310(10)$ nK.

size after a 5 ms ToF. In order to find the temperature of the cloud, we simulate the time-of-flight of a classical 2D gas of atoms whose initial spatial distribution corresponds to the trap in which the atoms are, a disk of radius R. The experimental atomic distribution and the simulated ones are radially averaged, and the experimental curve is compared to the simulated one to determine the temperature. The simulated curves are normalized such that they take the same value as the experimental curve for $r = 2R$. This corresponds to fixing the atom number. The simulated curve that matches best the experimental one for $r > 2R$ gives the temperature of the sample.

With this technique, as shown in figure 5.6, we estimate a temperature of 310(10) nK for the samples evaporated by dividing the power of the box potential beam by 2.4.

With an atom number of 10^5, this corresponds to a 2D phase-space density of $\mathcal{D} = n^{(2D)}\lambda_{dB}^2 \simeq 9.4$, meaning that the gas is in the degenerate regime. The repumped fraction of atoms used for thermometry therefore has a fugacity $z \sim 0.6$; the velocities for which the kinetic energy is on the order of the chemical potential correspond to $v \sim 5.5\,\mu$m/ms. Hence, looking at atoms 20 μm away from the edge of the disk and 40 μm away from the center of the disk after a 5 ms ToF means considering mainly atoms for which the kinetic energy is larger than the chemical potential, for which the Boltzmann weight is a valid approximation.

We also perform this analysis for a cloud where the power of the DMD is held constant for 0.5 s (without forced evaporation), for which the temperature is 450 nK.

5.3.3.4 *Extension along the vertical direction*

The spatial extension can be controlled using two techniques:

- by lowering the power of the accordion lattice before the microwave pulse, the vertical confinement decreases, allowing to tune the vertical extension of the cloud from a fraction of a micrometer to a few micrometers (trapped gas).
- by allowing the gas to expand for a time between 1 and 8 ms in ToF, allowing to tune the vertical extension of the cloud from a few micrometers to a few tens of micrometers (untrapped gas).

In this paragraph, we estimate the vertical extension of the cloud as a function of the power in the accordion lattice and of the ToF.

First, for the in-situ configuration, we want to check that having all atoms in the ground state of the vertical harmonic oscillator leads to a chemical potential μ which is smaller than the typical trapping frequency $\omega_z/2\pi$. There are three contributions to the energy for a cloud of atoms with the macroscopic wavefunction $\psi(\boldsymbol{r})$:

$$E_{\text{pot}} = \frac{N}{2} M\omega_z^2 \int z^2 \left|\psi\left(\boldsymbol{r}\right)\right|^2 \mathrm{d}^3 r \tag{5.51}$$

$$E_{\text{kin}} = \frac{N\hbar^2}{2M} \int \left|\boldsymbol{\nabla}\psi\left(\boldsymbol{r}\right)\right|^2 \mathrm{d}^3 r \tag{5.52}$$

$$E_{\text{int}} = N^2 \frac{2\pi\hbar^2 a_{\text{sc}}}{M} \int \left|\psi\left(\boldsymbol{r}\right)\right|^4 \mathrm{d}^3 r \tag{5.53}$$

where M is the mass of one atom, N the atom number and $a_{\text{sc}} \simeq 5.3\,\text{nm}$ the scattering length of rubidium 87. We consider the ground state wavefunction of a particle in a harmonic oscillator for ψ:

$$\psi\left(\boldsymbol{r}\right) = \frac{1}{\pi^{1/4}\sqrt{\mathcal{A}a_{\text{ho}}}} \mathbb{1}_{\text{box}}(x,y) \exp\left(-\frac{z^2}{2a_{\text{ho}}^2}\right) \tag{5.54}$$

where $\mathcal{A}$ is the area of the box potential (a disk of radius 20 μm), $a_{\text{ho}} = \sqrt{\hbar/(M\omega_z)}$ the natural length scale of the harmonic oscillator and $\mathbb{1}_{\text{box}}$ a function such that $\mathbb{1}_{\text{box}}(x,y) = 1$ if (x,y) is a point inside the box potential, and 0 elsewhere. The chemical potential corresponds to the derivative of the energy with respect to the atom number:

$$\mu = \frac{1}{N}\left(E_{\text{pot}} + E_{\text{kin}} + 2E_{\text{int}}\right) = \frac{\hbar\omega_z}{2} + 2\sqrt{2\pi}N\frac{\hbar^2}{M\mathcal{A}}\frac{a_{\text{sc}}}{a_{\text{ho}}} \tag{5.55}$$

For $\omega_z/2\pi = 2.4\,\text{kHz}$ (resp. 1.2 kHz), the interaction energy needed to add a particle in the ground state is $h \cdot 1.0\,\text{kHz}$ (resp $h \cdot 0.7\,\text{kHz}$) which is inferior to

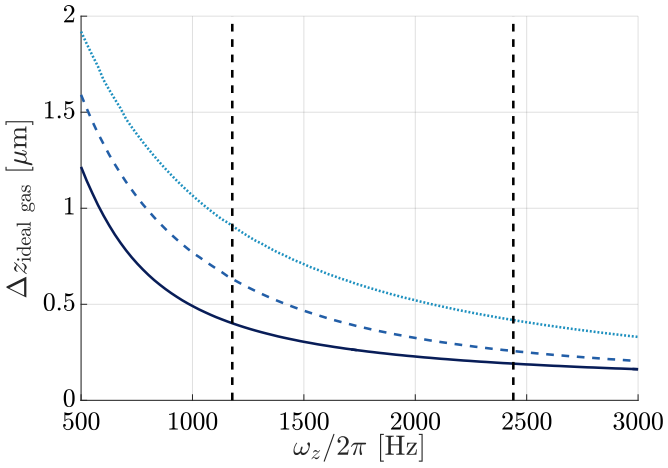

Figure 5.7: Vertical extension of an ideal Bose gas at a temperature of 200 nK (solid dark blue curve), 300 nK (dashed blue curve) and 500 nK (dotted light blue curve) as a function of the vertical confinement frequency $\omega_z/2\pi$. The two black dashed lines represent the extreme values of the in-situ confinement which were used: maximum at full power of the accordion lattice ($\omega_z/2\pi = 2.4$ kHz), minimum at 23% of the maximum power ($\omega_z/2\pi = 1.2$ kHz).

the energy spacing between the levels of the harmonic oscillator. Therefore, the broadening due to the interactions can be neglected.

For computing the in-situ vertical extension of the cloud, we thus only take into account the statistics of the ideal Bose gas, since the finite temperature will lead to some population of the excited states of the harmonic oscillator ($\zeta = k_B T/\hbar\omega_z$ ranges from 2.6 to 5.2) as in chapter 1. This consists in finding for a given value of ζ the fugacity z such that the total atom number

$$N_{\text{theo}} = \sum_{j=0}^{\infty} N_j = \sum_{j=0}^{\infty} -\frac{\lambda_{\text{dB}}}{\mathcal{A}} \ln\left(1 - ze^{-j/\zeta}\right) \tag{5.56}$$

is equal to the measured atom number N. Here, N_j represents the population of the jth state of the vertical harmonic oscillator. Then, knowing the spatial extension of the states of the harmonic oscillator Δz_j, the width of the cloud is given by

$$\Delta z = \Delta z_0 \sqrt{\sum_{j=0}^{\infty} \frac{N_j}{N} \frac{\Delta z_j^2}{\Delta z_0^2}} = \frac{a_{\text{ho}}}{\sqrt{2}} \sqrt{\sum_{j=0}^{\infty} \frac{N_j}{N} 2\left(j + \frac{1}{2}\right)} \tag{5.57}$$

The results in figure 5.7 show that for a power of the accordion lattice between 23% and 100% of its maximum value, the frequencies along the vertical direction vary between 1.2 kHz and 2.4 kHz and the spatial extension of an ideal Bose gas at 300 nK varies between 0.25 and 0.62 μm.

Then, we also want to compute the vertical extension of the cloud when suddenly released from the accordion lattice at full power. Knowing the initial trapping frequency, the initial spatial extension of the cloud Δz_0 and the duration of the ToF t, the spatial extension along z is given by [212]

$$\Delta z = \Delta z_0 \sqrt{1 + (\omega_z t)^2} \tag{5.58}$$

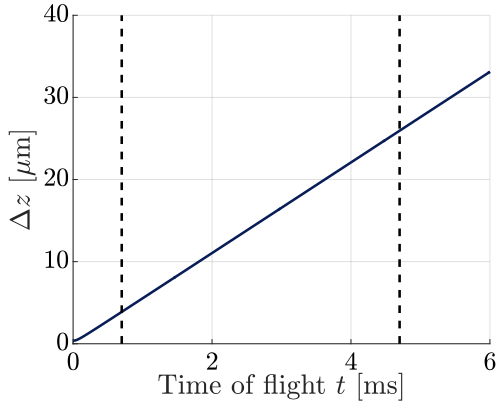

Figure 5.8: Vertical extension of an ideal Bose gas after time of flight. The initial conditions are those af a gas confined with the accordion lattice at maximum power, i. e. $\Delta z_0 = 0.36\,\mu$m and $\omega_z/2\pi = 2.4\,$kHz. The two dashed lines represent the time of flight of 0.7 ms and 4.7 ms.

The results of figure 5.8 show that the cloud rapidly reaches the far-field regime, i. e. the regime where $\Delta z \simeq \Delta z_0\,\omega_z t$. This is already valid for the shortest time of flight which is used on the experiment, 0.7 ms. When the atoms are imaged, they are not at rest, and have a typical velocity of a few centimeters per second, owing both to the release of kinetic energy from the initial 2D confinement and to the fact that they are under free fall for a few milliseconds. The Doppler shift associated to such velocities is on the order of 100 kHz, and is therefore neglected.

5.4 RESONANCES

We now turn to the experimental results, which consist in measuring the optical density of clouds varying their 2D atomic density, their thickness and the frequency of the probe beam.

5.4.1 *Resonance curves for dilute clouds*

First, we find the position of the resonance for a weakly repumped cloud of atoms, in a regime where collective effects in the light-matter interaction should be small. The experimental results which are presented in this section indeed require taking data for approximately ten hours, and it is necessary to regularly check that the characteristic properties of the low-density resonance curves are left unchanged. Six low-density resonances curves taken at several hours of interval have been analysed to that purpose.

Using a $3\,\mu$s microwave pulse, we transfer 4% of the atoms to the imaged state. The frequency of the probe laser $\nu = \omega/2\pi$ is varied on a 70 MHz range around the resonance of the atoms. Each of the six resonance curves is fitted by a lorentzian

$$\nu \mapsto \frac{\mathrm{OD}_0}{1 + 4\left(\frac{\nu-\nu_0}{\gamma}\right)^2} \tag{5.59}$$

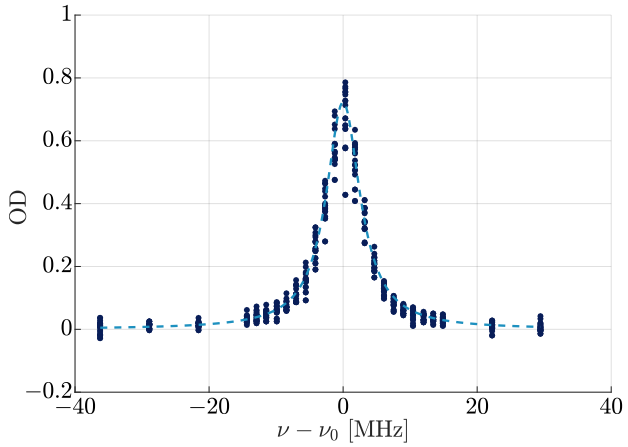

Figure 5.9: Resonance curve for weakly repumped clouds. The dark blue dots represent the data of the six resonance curves. The light blue dashed curve represents the lorentzian curve obtained from the averaged results of the fits.

Averaging over all the realizations we find a mean optical maximum density $OD_0 = 0.72(4)$, a mean width $\gamma = 6.1(3)\,MHz$ which is compatible with the natural linewidth of rubidium 87 $\Gamma = 6.06\,MHz$ and we use the fitted value of ν_0 to define the origin of all graphs in the rest of the analysis. The value of ν_0 is determined with an accuracy of 0.12 MHz. The results are presented in figure 5.9.

5.4.2 *Lorentzian fits*

We now prepare a cloud of atoms in the 2D box trap with maximum confinement in the vertical direction. The spatial extension of the cloud is $0.3\,\mu m$. We perform resonances by varying the duration of the microwave pulse, transferring $\sim$ 4%, 25%, 50%, 80% and 100% of the total atom number. The various resonances are shown on figure 5.10.

They are fitted using the equation 5.59. We limit ourselves to points with OD$<$ 3 where technical errors are not too important. The fit results are gathered in figure 5.11, whose main features we will now describe. First, the maximum OD which is fitted (5.11a) does not correspond to the Beer-Lambert law (see equation 5.4), represented with a dashed grey line, because of dipole interactions. The second observation is a strong broadening of the resonance. The fitted width follows the phenomenological law

$$\gamma \simeq \Gamma\sqrt{1+\left(\alpha n^{(2D)}\right)^2} \tag{5.60}$$

with $\alpha = 0.044(8)\,\mu m^2$, as can be seen on figure 5.11b. Last, at high densities, a blue shift is seen from the low-density resonance center (5.11c). This shift can be treated as a linear function in which case $\nu_0 = \beta n^{(2D)}$ with $\beta = 0.013(3)\,MHz\cdot\mu m^2$. This contrasts with the previous studies of dense clouds where either nothing or a slight red shift was observed [59, 186]. When letting the densest

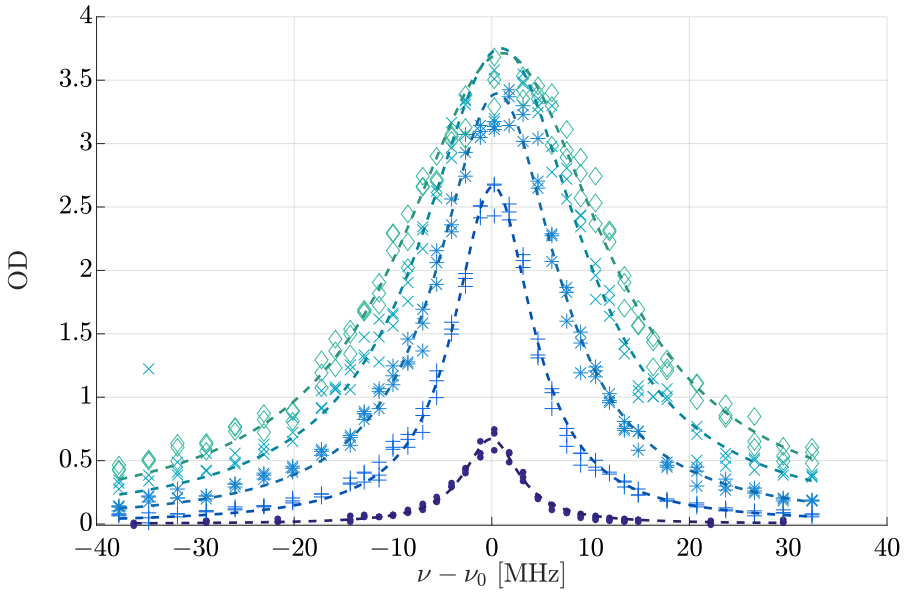

Figure 5.10: Resonance curve for in situ clouds. The various symbols correspond to varying densities: dots 4.0(6) at/μm^2, plus signs 25(4) at/μm^2, stars 50(7) at/μm^2, crosses 75(11) at/μm^2, diamonds 100(15) at/μm^2. Dashed lines correspond to the lorentzian fit of the curve with the corresponding colour.

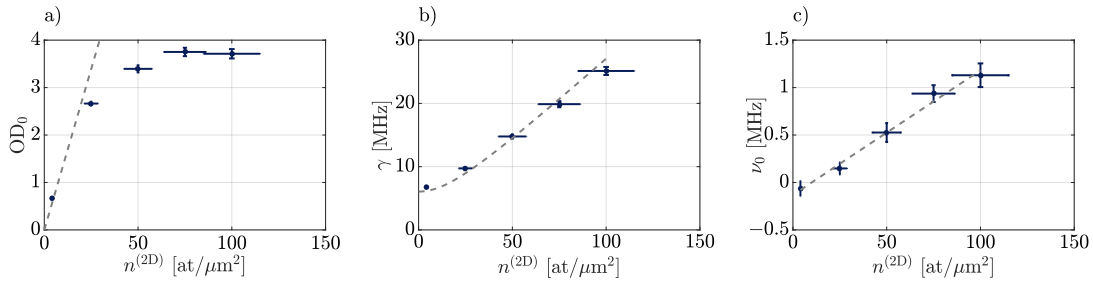

Figure 5.11: Fitted parameters of the lorentzian curves of figure 5.10 as a function of the atomic density (blue dots). Vertical error bars are found from a bootstrapping approach with 100 iterations (see Appendix D for more information on that technique). The horizontal error bars correspond to the uncertainty on the atom number. The dashed curve in a) corresponds to the Beer-Lambert prediction. The dashed curves in b) and c) correspond to phenomenological fits (see text).

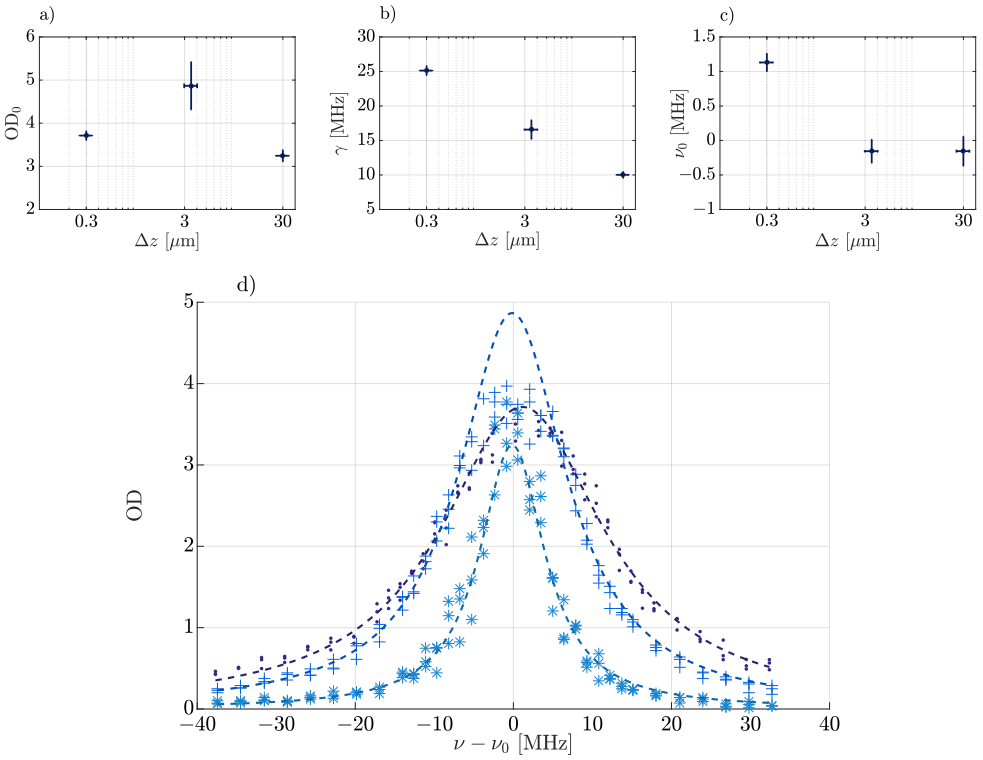

Figure 5.12: Resonance curve for a cloud at maximum column density. The various symbols in d) correspond to varying thicknesses: dots 0.3 μm, plus signs 3 μm, stars 30 μm. Dashed lines correspond to the lorentzian fit of the curve with the corresponding colour. The lorentzian fit was performed for all point with OD < 3 and for detunings $|\nu - \nu_0| \leqslant 30$ MHz. The parameters of the lorentzian fits are gathered in a-c.

cloud expand (figure 5.12), the blue shift vanishes and the resonance width becomes thinner. We also note that the optical density for the thickest cloud is reduced. This is mainly due to the fact that this thickness is obtained after a 4.7 ms of time-of-flight expansion, during which the cloud at 450 nK slightly expands in the xy plane[1].

We can compare this set of results to the simulations realized using the model described in 5.2. We simulate clouds of 3000 atoms with an effective Beer-Lambert OD $\mathrm{OD}_0 = \sigma_0 n^{(2\mathrm{D})}$ ranging from 0.1 to 8. We compute an "effective atom density" corresponding to the atomic density needed to have the same OD with the effective cross-section $\sigma = 7\sigma_0/15$. The positions of the atoms are drawn in a disk of appropriate radius to yield the expected density, and the vertical position is a random Gaussian number with a standard deviation of Δz. We fit the resulting curves using the exact same procedure as for the experimental data; in particular, we do not consider the points where OD > 3.

The results are shown in figure 5.13. Figure 5.13a-c corresponds to a gas with a thickness of $\Delta z = 0.2\,\mu$m and various values of $\mathrm{OD}_{\mathrm{BL}}$, translated in effective

1 In order to avoid computing the optical density in the lower-density wings, the region in which it is computed (corresponding to the function $\mathbb{1}_{\mathrm{box}}$ described in 5.3.2) is reduced compared to that for thinner gases.

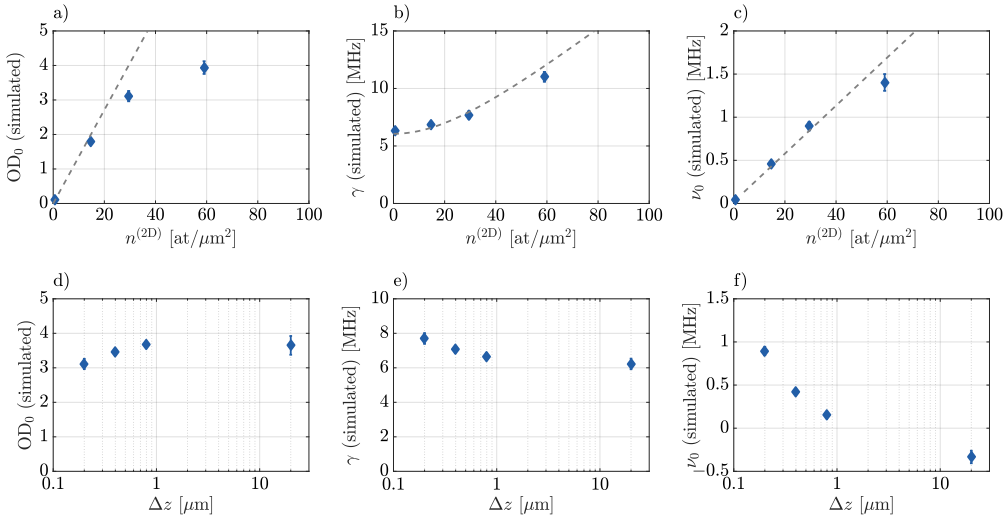

Figure 5.13: Fit results of the simulated resonance curves, corresponding to 9 repetitions with 3000 atoms. The error bars correspond to the statistical error. Figures (a)-(c) correspond to a cloud of thickness $\Delta z = 0.2\,\mu$m, with $\mathrm{OD}_{\mathrm{BL}} = 0.1$, 2, 4 and 8, corresponding to effective atomic densities $n^{(2D)} = 15\,\mathrm{OD}_{\mathrm{BL}}/(7\sigma_0) = 0.7$, 15, 30 and 60 at/$\mu$m^2. The dashed line in (a) corresponds to the Beer-Lambert prediction; the dashed lines in figure (b) and (c) correspond to phenomenological curves (see text). Figures (d)-(f) correspond to a cloud of density 30 at/μm^2 ($\mathrm{OD}_{\mathrm{BL}} = 4$) with a varying thickness: $\Delta z = 0.2$, 0.4, 0.8 and 20 μm. As in figure 5.12, the width of the lorentzian curve decreases and the shift in frequency decreases as the thickness increases (and goes from a large value to the blue of the resonance to a small value to the red of the resonance).

atom density. The grey dashed line in figure 5.13a also corresponds to the Beer-Lambert law, and those in figure 5.13b-c to the same phenomenological fits as in figure 5.11b-c. The fitted parameters $\alpha_{\mathrm{sim}} = 0.03(3)\,\mu\mathrm{m}^2$ and $\beta_{\mathrm{sim}} = 0.03(1)\,\mathrm{MHz}\cdot\mu\mathrm{m}^2$ are of the same order of magnitude than the experimental values. We indeed do not expect perfect agreement between the simulation and the experiment since (i) the transition which is modelled is a $J = 0 \to J = 1$ transition, while our transition is an $F = 2 \to F' = 3$ transition, whose effect has only been modelled by a reduction of the scattering cross-section; also, (ii) the motion of the atoms has been neglected, which might be true on the scale of the lifetime of one photon in the cloud but not necessarily on the scale of the imaging pulse. We also study the change of the shape of the lorentzian curve at a constant $\mathrm{OD}_{\mathrm{BL}} = 4$ (i. e. an effective density of 30 at/μm^2) as the thickness of the cloud is increased from $\Delta z = 0.2\,\mu$m to 20 μm. We are limited to this value of optical density for the reason exposed in section 5.2.3. The results of the fits are shown in figure 5.13d-f, which also reproduces the qualitative features of figure 5.11.

The experimental measurements are limited by the fact that while most atoms stay in the trap, some atoms acquire a large velocity during the 10 μs imaging pulse. A small fraction of the atoms can therefore be expulsed from the plane at a distance of 1 μm during the imaging process. However, the cloud initially

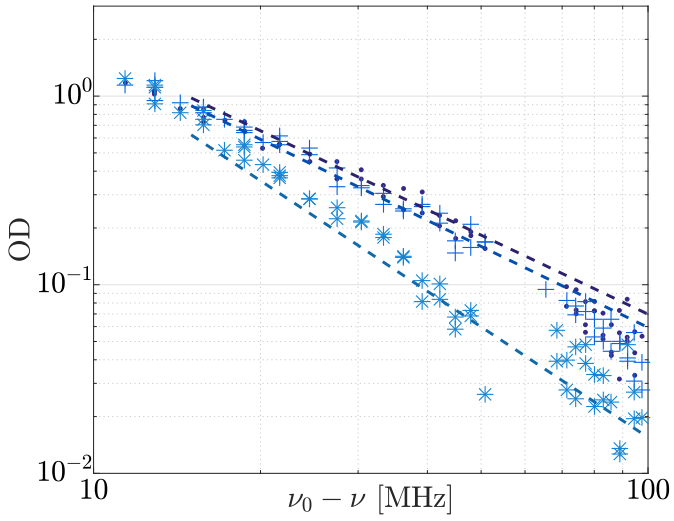

Figure 5.14: Resonance curve for a cloud at maximum column density in log-log scale. Only the negative detunings are shown. The various symbols correspond to varying thicknesses: dots 0.3 μm, plus signs 0.8 μm, stars 3 μm. Dashed lines correspond to the power-law fit of the curve with the corresponding colour; the fitted exponents are $-1.39(2)$ for the gas of thickness 0.3 μm, $-1.43(5)$ for the gas of thickness 0.8 μm, $-1.95(7)$ for the gas of thickness 3.5 μm.

has the predicted thickness, and the comparison with the simulations shows that the qualitative behaviour is still correct. The increasing width of the cloud can therefore have a systematic effect on the measurements that still has to be investigated, but the main features of figures 5.11 and 5.12 should be robust to that effect.

5.4.3 *Wing fits*

Some further information can be extracted by looking at the decay of the atomic response as the detuning of the probe laser is varied. For the densest cloud ($n^{(2D)} = 100\,\text{at}/\mu\text{m}^2$), the optical density for negative detunings between -15 MHz and -100 MHz are fitted by a power-law. As can be seen from figure 5.14, the exponent that is fitted is close to the expected value of -2 for a pure lorentzian behaviour for the gas of thickness 3.5 μm. However, for the clouds of thicknesses 0.3 μm and 0.8 μm, the exponents are incompatible with the value of -2. This deviation from the lorentzian behaviour can be explained by the presence of close pairs whose resonance frequency is strongly shifted due to dipole-dipole interactions [128].

5.5 LOCAL EXCITATION OF A CLOUD OF ATOM

In this series of experiment, we prepare a disk of atoms with a diameter of 60 μm. Instead of using an imaging beam that covers the whole cloud, we

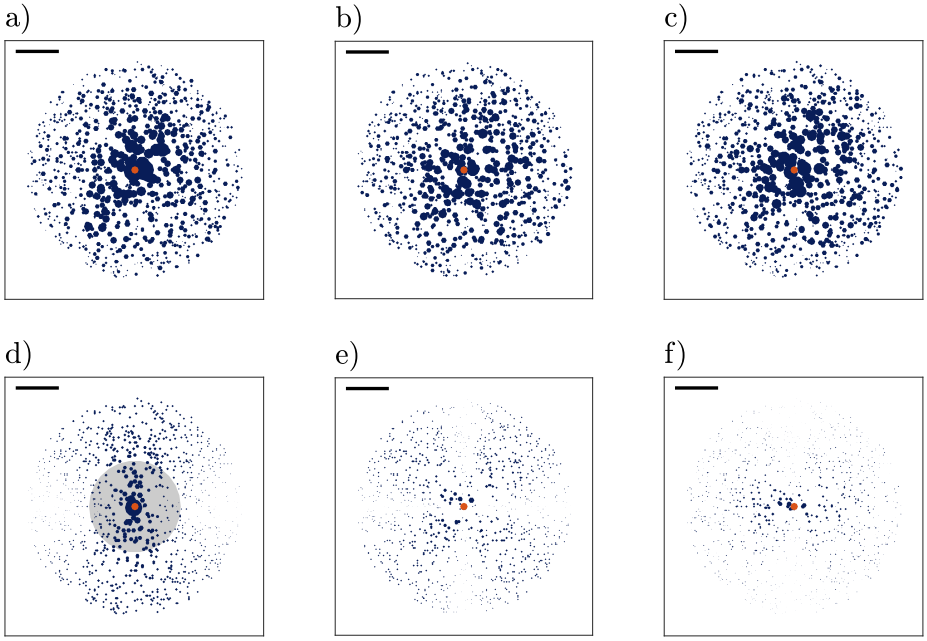

Figure 5.15: Simulation of the propagation of a single excitation along the x direction initially on the atom with a red dot for a dense cloud with $n_c = 50\,\mathrm{at}/\mu\mathrm{m}^2$ (a)-(c) and for a dilute cloud with $n_c = 5 \cdot 10^{-3}$ at$/\mu$m^2(d)-(f). In each case, the cloud has a thickness of $0.2\,\mu$m. Each dot is located at the position of an atom, and the area of the disk represent the amplitude of the dipole in the x, $|\boldsymbol{d}_{i,x}|$(a and c), y,$\left|\boldsymbol{d}_{i,y}\right|$ (b and e) and z, $|\boldsymbol{d}_{i,z}|$ (c and f) directions. The amplitude of the dipole of the central atom excited without interaction with the other atoms is almost the same as in the dilute case, and is represented by the grey disk. In the dilute case, the patterns are characteristic of the dipolar scattering diagram. Scale bar $1\,\mu$m for pictures (a)-(c), $100\,\mu$m for pictures (d)-(f).

image a pinhole on the atoms, illuminating a small disk of atoms of diameter $17\,\mu$m with an intensity $I = 0.2 I_{\mathrm{sat}}$. All the photons are then collected on the camera during an exposure time of $100\,\mu$s.

The light intensity collected on each pixel is the sum of the incoming light field and of the field radiated by each atom. Here, we create a situation where the incoming field is zero on some atoms; detecting some photons coming from these atoms means that they have been excited by the field radiated by other atoms, that is that the excitation has propagated in the cloud.

This situation can be simulated using the model described in section 5.2. In figure 5.15, we simulate an assembly of 1000 atoms where only the central one is excited (in red on the picture). The cloud has a thickness of $0.2\,\mu$m, and the column density of atoms is $50\,\mathrm{at}/\mu\mathrm{m}^2$ for pictures a-c, and $5 \cdot 10^{-3}\,\mathrm{at}/\mu\mathrm{m}^2$ for pictures d-f. We represent the modulus of each component of the dipole moment $\boldsymbol{d}_i$ of each atom at the position of the atoms $\boldsymbol{r}_i$. Figures 5.15a-d (resp b-e, c-f) are made of disks of area $|\boldsymbol{d}_{i,x}|$ (resp. $\left|\boldsymbol{d}_{i,y}\right|$, $|\boldsymbol{d}_{i,z}|$) at positions $\boldsymbol{r}_i$. In figure 5.15d, the amplitude of the central, initially excited atom is not represented in blue but with a grey disk which is almost equal to the amplitude it

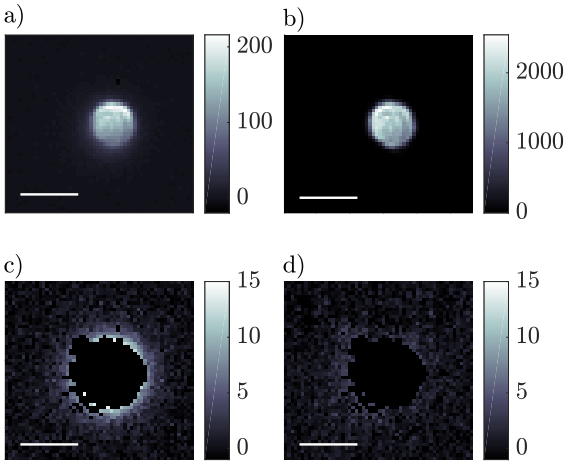

Figure 5.16: Local excitation experiment (averages over 104 realizations). Figure (a) corresponds to the light transmitted through the cloud (unit: camera counts) I_{with}. Figure (b) corresponds to the light transmitted to the camera without atoms I_{without}. Figure (c) (resp. d) correspond to figure (a) and (resp. b) where all the pixels such that $I_{\text{without}} \geqslant 4$ are removed. The halo visible on the picture with atoms shows some propagation of the excitation in the cloud. Scale bars 20 μm.

would have without any dipole-dipole interactions. For the low atomic density, dipole-dipole interactions have only a small effect and the emission diagram of a single dipole excited along the x direction can be recognized in the excitation amplitude of the other atoms. For the high atomic density, the excitation initially located on the central atom is spread on the whole cloud. The cloud has a radius of 2.5 μm, meaning that the excitation can spread on more than a micrometer away from the location of the excitation.

The preliminary results of the local excitation of a thin dense cloud are presented in figures 5.16 and 5.17, where 104 realizations are averaged. As expected, the light passing through the pinhole is absorbed by the cloud (5.16a and b). We call $I_{\text{without}}(i,j)$ (resp. $I_{\text{with}}(i,j)$) the amount of light on pixel (i,j) in the pictures where the atoms are removed (resp. where the atoms are present). In order to see whether the light excitation can propagate through the cloud, we look at all the pixels where $I_{\text{without}}(i,j) < 4$. On pixels such that $I_{\text{without}}(i,j) \geqslant 4$, the signal is difficult to interpret, since it is the sum of the incoming light and of the light radiated by the atoms, and we want to isolate the second contribution. This is represented on figure 5.16c and d. On the pictures with atoms, a clear halo is visible, which is absent from the picture without atoms.

Although some atoms can gain high velocities when absorbing a photon (see section 5.1.3), these velocities on the order of ten centimeters per second cannot explain this halo. When a photon excites the cloud of atoms, it can decay on timescales which are much larger than the single atom decay rate according to Dicke's description [204]. However, it is unlikely that the a group of atoms stays in a subradiant subradiant mode while moving. It is therefore unrealistic that an excited atom acquiring some velocity and being deexcited outside of

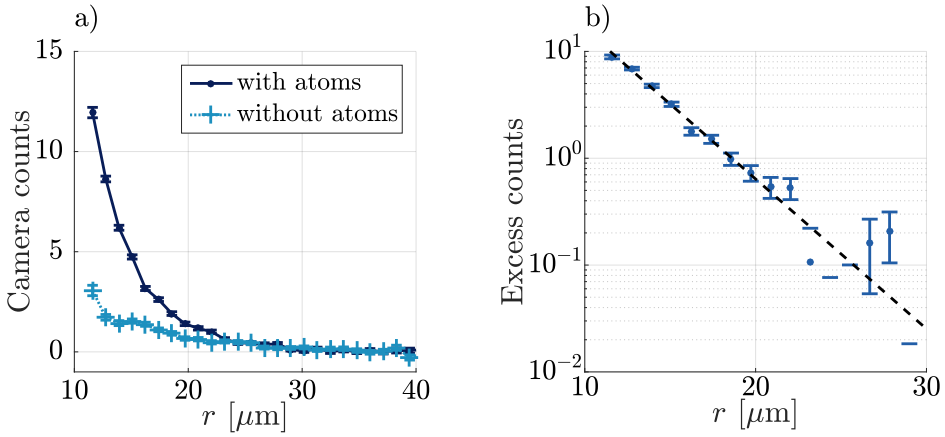

Figure 5.17: Local excitation experiment (averages over 104 realizations). Figure (a) corresponds to radial averages of the figure 5.16c) $\langle I_{\text{with}}(r)\rangle$ (with atoms, dark blue dots) and 5.16c) $\langle I_{\text{without}}(r)\rangle$ (without atoms, light blue crosses). The error bars on the number of camera counts correspond to the detection noise. The mean number of camera counts is plotted against the distance to the center of the pinhole. The edge of the pinhole is located at $r = 8.5\,\mu$m. Figure (b) corresponds to the difference in counts between the pictures with and without atoms $\langle I_{\text{with}}(r)\rangle - \langle I_{\text{without}}(r)\rangle$ (light blue dot). The dashed black line represents an exponential fit to the data $r \mapsto A\exp(-r/r_0)$. Here, $r_0 = 3.1(2)\,\mu$m.

the illuminated region can explain the halo of figure 5.16c, the positions of the atoms can be considered to be frozen on the timescales of the light-interaction processes as assumed in section 5.2. However, the movement of the atoms during the imaging time (100 μs for this experiment) might have to be considered.

We represent the excess of count on the camera in the picture with atoms with respect to the picture without atoms in figure 5.17. When fitted by an exponential decay, the typical length on which the halo decays is $3.1(2)\,\mu$m.[2]

5.6 CONCLUSION

The experimental set-up presented in chapter 4 constitutes an excellent platform to test collective effects in light-matter interaction. We are able to produce dense gases in which the mean interparticle distance is smaller than $\lambda/2\pi$ (λ is the imaging wavelength), where the atoms interact strongly via resonant dipole-dipole interactions.

We study the response of a slab of atom with a varying thickness and density as a function of the probe beam detuning in the weakly saturating regime. We observe a blue shift of the resonance on the order of $\Gamma/4$ for the densest cloud, scaling linearly with the atom density. The width of the resonance is strongly increased up to 5Γ, and the maximum optical density saturates to ~ 4 although

2 Measurements performed after the writing of this work have showed that most of the halo is due to geometrical abberations of our imaging system. Nevertheless, taking them into account, we were still able to observe the decay of the excitation in the cloud for certain densities (article in preparation).

we estimate a density of $100\,\mathrm{at}/\mu\mathrm{m}^2$, which should give a Beer-Lambert optical density of 14. As the thickness of the cloud is increased, the blue shift decreases to zero and the broadening is less important; the gas of atoms goes from the recurrent scattering regime ($kr \lesssim 1$) to the multiple scattering regime ($kr > 1$ but $n^{(2D)}\sigma > 1$). Strong deviations from a lorentzian behaviour were also seen by looking at the power-law decay of the optical density for large probe detuning. While for a gas with a thickness of several micrometers, the fitted power-law is compatible with the lorentzian value of -2, it has a value of $-1.39(2)$ for the thinnest gas.

We also performed some preliminary work to study the propagation of the excitation in the atoms by locally illuminating the cloud and studying the fluorescence of atoms who have not been exposed to the probe beam. We observe a halo of fluorescence photons with a typical extension of $3.1(2)\,\mu$m beyond the illuminated region.

These experiments could be improved by reducing the imaging pulse duration, which would limit the extension of the cloud due to large velocities acquired via dipole-dipole interactions. This would nevertheless reduce the amount of signal on the camera, whose magnification might have to be modified. Last, an important part of the study of dipole-dipole interactions addresses the observation of sub- or superradiant states. These states are not detected on our set-up, and might require time-resolved detector.

6

PROSPECTIVE EXPERIMENT: EVAPORATION IN A TILTED LATTICE

Experiments using cold atoms have entered the quantum degenerate regime thanks to the experimental technique of evaporative cooling [213]. This technique allows one to lower the temperature of the gas by loosing the most energetic particles followed by a thermalization of the remaining atoms through collisions [213]. When the resulting decrease in temperature is more important than the loss of atoms, this leads to an increase in phase-space density. This technique has proved to be very successful in a variety of experimental set-ups, including quadrupole traps, other magnetic traps, dipole traps or hybrid dipole and magnetic traps. In most set-ups, a particle will be evaporated if its energy is larger than some threshold and if it crosses a region in space whose geometry is defined by the type of trap which is used. This region can be the ellipsoid in space at which the magnetic state of the atom is flipped for radio-frequency evaporation, the edge of the dipole potential for an optical dipole trap, etc.

The fact that a particle is ejected not only because of its energy but also because of its position limits the efficiency of the evaporation. The energy is removed at specific positions in the atomic cloud, and this "information" has to spread to the inner parts of the cloud to allow full thermalization. This is not much of an issue in many experiments; for example, when studying the equilibrium properties of a cloud of ultra cold atoms, an appropriate waiting time can be added to allow the gas to reach thermal equilibrium before performing any measurements. However, when studying out-of-equilibrium phenomena, the additional thermalization time coming from the inhomogeneous condition for evaporation can prevent the experiment to access short timescales. This can be problematic for example in the case of the experimental study of the Kibble-Zurek mechanism as described in chapter 2 and chapter 3, which relies on having a uniform gas of atoms with a uniform temperature.

Having an evaporation scheme where any particle whose energy is higher than a fixed threshold could be evaporated, independent of its position, would allow for better controlled studies of non-equilibrium phenomena and would also lead to more efficient evaporation with the removal of the constraints on the position of the particle.

In the experimental set-up described in chapter 4, 2D gases of atoms are produced in an optical trap combining a box potential and a lattice in the vertical direction produced by the optical accordion detailed in subsection 4.2.2. In addition to this optical confinement, gravity or a quadrupole magnetic field provide a linear potential, leading to a tilted lattice potential in the vertical direction. This set-up has already been studied in cold atom experiments, though not in the perspective of evaporating a gas towards degeneracy [214]. In this chapter, we study how we can evaporate the atoms in the tilted lattice potential. First, we concentrate in section 6.1 on solving the quantum mechanical

problem of an atom in a tilted lattice following the approach of [75], finding the scattering states and their associated lifetime. The aim here is to find a suitable set of parameters (lattice spacing, lattice depth, tilt) such that there is one long-lived state localized in a given well, while the other states have a much smaller lifetime. This calculation aims at computing how fast an atom initially in the first excited state of the vertical potential well escapes. However, after some standard evaporation (in our case usually provided by the lowering of the box potential), the atoms hardly ever have enough energy to reach that first excited state in the well of the cloud. Collision-assisted tunnelling can nevertheless allow for some evaporation. When two particles collide, the result of the collision can yield one particle in the initial well in the ground state of the vertical motion and one particle in the first excited state of the neighbouring well. This process is studied in section 6.2 using collision simulations based on the Bird method [215].

6.1 SOLVING THE SCATTERING PROBLEM OF AN ATOM IN A TILTED LATTICE

6.1.1 *Position of the problem — Outline of the resolution*

We follow the line of reasoning of [75], but writing the calculations in dimension full units such that they are easily applicable to the experiment. We consider the single-particle one-dimensional problem of a particle in a tilted lattice potential

$$\hat{H} = \frac{\hat{p}^2}{2M} + V_0\left(1 - \cos(k_0\hat{z})\right) - b\hat{z} = \frac{\hat{p}^2}{2M} + V_{\text{laser}}\sin^2(k_{\text{laser}}\hat{z}) - b\hat{z} \tag{6.1}$$

where $2V_0$ is the potential depth, $k_0 = 2\pi/d$ with d the distance between two wells of the lattice and $b > 0$ characterizes the strength of the tilt. Note that the recoil energy of a lattice is usually defined using the parameters k_{laser} and V_{laser}. These are related to k_0 and V_0 by $E_r = \frac{\hbar k_{\text{laser}}^2}{2M}$ with $k_{\text{laser}} = k_0/2$, and $V_{\text{laser}} = 2V_0$. In this part, we will consider the tilt Hamiltonian

$$\hat{H}_0 = \frac{\hat{p}^2}{2M} - b\hat{z} \tag{6.2}$$

as the unperturbed Hamiltonian, and regard the lattice potential as a perturbation. The solutions to the Hamiltonian 6.2 are well known. They can be expressed as translated Airy functions in real space or, as will be more relevant in our case, have the following expression in reciprocal space:

$$\psi_0(k, E) = \exp\left(-i\left(\frac{\hbar^2 k^3}{6bM} - \frac{Ek}{b}\right)\right) \tag{6.3}$$

Our aim is to find relatively stable states that appear when the lattice potential is added, meaning functions of space $\psi_S(z, \mathcal{E})$ whose time evolution will be characterized by the complex number $\mathcal{E} = E - i\Gamma/2$. These stable states can be detected via a scattering experiment; if a particle is injected from $z > 0$ onto the potential with an energy E, it will resonate with the state ψ_S leading to a high

scattering cross-section. The resonant complex energies can thus be detected as the pole of the scattering matrix.

The procedure will thus be the following:

- Define the scattering matrix in real space, and find its expression in momentum space.
- Define the Bloch-Stark states as the solutions of the evolution over a Bloch period $\tau_B = \hbar k_0 / b$.
- Compute the scattering matrix using the Fourier decomposition of the Bloch-Stark states.
- Find the poles of the scattering matrix and record the corresponding complex energies and wave function.

6.1.2 *Scattering matrix in real and reciprocal space*

In order to define the scattering matrix, we define the incoming and outgoing wave functions for the perturbed (indicated by the subscript S) and unperturbed (indicated by the subscript 0) cases:

$$\psi^{\text{in}}_{0,S}(z,E) \propto \int_{-\infty}^{0} e^{-ikz}\psi_{0,S}(k,E)\mathrm{d}k \tag{6.4}$$

$$\psi^{\text{out}}_{0,S}(z,E) \propto \int_{0}^{\infty} e^{-ikz}\psi_{0,S}(k,E)\mathrm{d}k \tag{6.5}$$

We are only interested in the bound states that appear as the lattice potential is added; hence the scattering matrix is defined as the asymptotic ratio of the outgoing and incoming wave function normalized by the unperturbed case:

$$\boxed{S(E) = \lim_{z\to\infty} \frac{\psi^{\text{out}}_S(z,E)}{\psi^{\text{out}}_0(z,E)} \frac{\psi^{\text{in}}_0(z,E)}{\psi^{\text{in}}_S(z,E)}} \tag{6.6}$$

The scattering matrix characterizes the output state, result of the scattering of an incoming wavefunction on a potential. Here, since the potential goes to infinity when $z \to -\infty$, the incoming waves are necessarily those with $k < 0$ and the outgoing waves those with $k > 0$, and the scattering matrix is a ratio of outgoing over incoming waves. In addition, the incoming and outgoing states are normalized by their unperturbed form in order to isolate the contribution of the lattice to the scattering properties.

The solutions of the unperturbed potential have a very simple expression in reciprocal space as shown in equation 6.3, which is why we will try to express the scattering matrix in the reciprocal space too. First, we need to express ψ_S as a function of ψ_0. Let us define φ and ϑ by

$$\psi_S(k,E) = e^{i\varphi(k,E)}\psi_0(k,E) \tag{6.7}$$

$$\psi^{\text{out (in)}}_S(z,E) = e^{i\vartheta_{\text{out (in)}}(z,E)}\psi_0(z,E) \tag{6.8}$$

Note that $\varphi(k)$ and $\vartheta(x)$ are a priori complex numbers. However, at large distance $z \gg 0$ the effect of the scattering lattice potential can be reduced to that of a pure dephasing of the perturbed wave functions with respect to the unperturbed ones:

$$\vartheta_{\text{out (in)}}(z, E) \xrightarrow[z\to\infty]{} \vartheta_{\text{out (in)}}(E) \in \mathbb{R} \tag{6.9}$$

We can relate this asymptotic behaviour to that of φ:

$$\begin{aligned}\psi_S^{\text{out}}(z, E) = \int_0^\infty \exp\left[i\left(k\left(z + \frac{E}{b}\right) - \frac{\hbar^2 k^3}{6bM} + \varphi(k)\right)\right] \mathrm{d}k \\ = \int_0^\infty \exp\left[i\left(\Theta_0(z, k) + \varphi(k)\right)\right] \mathrm{d}k\end{aligned} \tag{6.10}$$

so subtracting equation 6.8 to equation 6.10

$$\mathcal{I}(z, E) = \int_0^\infty \underbrace{\exp\left(i\Theta_0(z, k)\right)}_{\text{oscillating term}} \underbrace{\left[e^{i\vartheta_{\text{out}}(z)} - e^{i\varphi(k)}\right]}_{\text{phase term}} \mathrm{d}k \equiv 0 \tag{6.11}$$

For a given large z, $k \mapsto \exp\left(i\Theta_0(z, k)\right)$ is an oscillating function. The integral can thus be approximated using a saddle-point technique; let $\tilde{k}$ be the point such that $\frac{\mathrm{d}\Theta_0}{\mathrm{d}k}(\tilde{k}) = \Theta_0'(\tilde{k}) = 0$. Then, calling $\frac{\mathrm{d}^2\Theta_0}{\mathrm{d}k^2}(\tilde{k}) = \Theta_0''(\tilde{k})$,

$$\mathcal{I}(z, E) \simeq \frac{\exp\left(i\Theta_0(z, \tilde{k})\right)}{\sqrt{\Theta_0''(z, \tilde{k})}} \left[e^{i\vartheta_{\text{out}}(z)} - e^{i\varphi(\tilde{k})}\right] \tag{6.12}$$

and

$$\tilde{k} = \frac{\sqrt{2\left(E + bz\right)M}}{\hbar} \tag{6.13}$$

Hence asymptotically the function φ tends toward a constant:

$$\varphi(k, E) \xrightarrow[k\to+\infty]{} \varphi_+(E) \in \mathbb{R} \tag{6.14}$$

and similar reasoning on ψ_S^{in} yields

$$\varphi(k, E) \xrightarrow[k\to-\infty]{} \varphi_-(E) \in \mathbb{R} \tag{6.15}$$

Using the saddle point approximation on the scattered function $\psi_S(z, E) = \int_{-\infty}^{\infty} \exp\left[i\Theta(z, k)\right] \mathrm{d}k$ on large positive z (neglecting the derivative of φ for large k),

$$\psi_S^{\text{in}}(z, E) \propto \frac{\exp\left(i\Theta(z, -\tilde{k})\right)}{\sqrt{\Theta''(z, -\tilde{k})}} \tag{6.16}$$

$$\psi_S^{\text{out}}(z, E) \propto \frac{\exp\left(i\Theta(z, \tilde{k})\right)}{\sqrt{\Theta''(z, \tilde{k})}} \tag{6.17}$$

Taking the $z \to \infty$ limit in the definition of the scattering matrix 6.6 is thus equivalent to taking the $k \to \pm\infty$ limit

$$\boxed{S(E) = \lim_{k\to\infty} \frac{\psi_S(k,E)}{\psi_0(k,E)} \frac{\psi_0(-k,E)}{\psi_S(-k,E)}} \tag{6.18}$$

The fact that the real-space coordinate can be "replaced" by the momentum-space coordinate is not surprising if one considers that *(i)* the result of the unperturbed Hamiltonian is an Airy function which oscillates faster the further away from the origin *(ii)* the lattice potential has little influence at sufficiently large z (typically for $(z - E/b) \gg d$) such that the substitution can still be done.

The expression for the scattering matrix 6.18 is especially convenient in the case when ψ_S and ψ_0 are periodic functions of z; in this case, using the Fourier coefficients $\left\{c_n^S\right\}_{n\in\mathbb{Z}}$ (resp. $\left\{c_n^0\right\}_{n\in\mathbb{Z}}$) of ψ_S (resp. ψ_0), we obtain

$$\boxed{S(E) = \lim_{n\to\infty} \frac{c_n^S}{c_n^0} \frac{c_{-n}^0}{c_{-n}^S}} \tag{6.19}$$

6.1.3 *Definition of the Bloch-Stark states*

In this section, we aim at finding periodic solutions of the scattering problem in order to be able to use the simple expression of the scattering matrix 6.19. We will proceed in the following way:

- First we will perform a gauge transform on the Hamiltonian to a space-periodic time-dependent Hamiltonian.
- Then we will construct a family of functions being the product of a plane wave and a periodic function that are eigenfunctions of the evolution operator at a certain time.
- Last we will write the equation system obeyed by the Fourier coefficients of the periodic function for further replacement in equation 6.19.

The family of functions which is going to be constructed is called the Bloch-Stark states. It relates to the Wannier-Stark states the same way that Bloch states in lattices relate to Wannier states. The Wannier-Stark ladder are translated from the Wannier states of the lattice in energy (by an energy proportional to one over the Bloch period) and space (by the lattice spacing). The Bloch states will be constructed using the same procedure.

6.1.3.1 *Gauge transformation*

Let $\hat{A}$ be a unitary transformation (which can depend on time, space, momentum...); it is equivalent to consider the evolution of the wave function ψ under the Hamiltonian $\hat{H}$ or to consider the evolution of the wave function $\hat{A}\psi$ under the Hamiltonian $\hat{\tilde{H}}$:

$$\hat{\tilde{H}} = \hat{A}H\hat{A}^\dagger + i\hbar\frac{\mathrm{d}\hat{A}}{\mathrm{d}t}\hat{A}^\dagger \tag{6.20}$$

The evolution operator $\hat{\tilde{U}}$ associated to $\hat{\tilde{H}}$ can also be related to the evolution operator $\hat{U}$ associated to $\hat{H}$:

$$\hat{U}(t) = \hat{A}^\dagger(t)\hat{\tilde{U}}(t)\hat{A}(0) \tag{6.21}$$

We now want to transform the Hamiltonian $\hat{H}$ of equation 6.1 to a space-periodic time-dependent Hamiltonian. The unitary operator that we consider is the following:

$$\hat{A}(t) = \exp\left(-i\frac{bt}{\hbar}\hat{z}\right) \tag{6.22}$$

The new Hamiltonian now reads

$$\hat{\tilde{H}} = \frac{(\hat{p}+bt)^2}{2M} + V_0\left(1-\cos(k_0\hat{z})\right) \tag{6.23}$$

and the evolution operators read

$$\hat{\tilde{U}}(t) = \hat{\exp}\left[-\frac{i}{\hbar}\int_0^t\left(\frac{(\hat{p}+bt')^2}{2M} + V_0\left(1-\cos(k_0\hat{z})\right)\right)\mathrm{d}t'\right] \tag{6.24}$$

$$\hat{U}(t) = \hat{\exp}\left(-i\frac{bt}{\hbar}\hat{z}\right)\hat{\tilde{U}}(t) \tag{6.25}$$

Here the notation $\hat{\exp}$ stands for the time ordered operator, i. e.

$$\boxed{\hat{\tilde{U}}(t) = \lim_{\delta t\to 0}\prod_{n=0}^{n=t/\delta t}\left[\mathbb{1} - \frac{i}{\hbar}\hat{\tilde{H}}(n\,\delta t)\delta t\right]} \tag{6.26}$$

6.1.3.2 *Construction of the Bloch-Stark states*

Consider ψ an eigenfunction of the Hamiltonian $\hat{H}$ with eigenvalue E. We call $\tau_B = \hbar k_0/b = h/(bd)$ the Bloch period corresponding to the time-scale associated with the energy offset between two neighbouring sites and define

$$\lambda = e^{-iE\tau_B/\hbar} = e^{-iEk_0/b} \tag{6.27}$$

We can then define the Bloch-Stark function associated to ψ with quasi-momentum κ as

$$\phi_\kappa(z) = \sum_{\ell\in\mathbb{Z}}\exp(i\ell d\kappa)\psi(z-\ell d) \tag{6.28}$$

The function $\kappa \mapsto \phi_\kappa(z)$ is k_0-periodic and the function $z \mapsto e^{-ix\kappa}\phi_\kappa(z)$ is d-periodic, justifying the name of quasi-momentum for κ given usually in the context of Bloch eigenfunction in lattices. This transformation corresponds to the relation between Bloch states and Wannier states in lattices.

The starting wave function can be recovered by the standard transformation that turns Bloch functions into Wannier functions for space-periodic potentials

$$\psi(z) = \sqrt{\frac{2\pi}{d}}\int_{-k_0/2}^{k_0/2}\phi_\kappa(z)\mathrm{d}\kappa \tag{6.29}$$

We now look at the action of the evolution operator on the Bloch-Stark function:

$$\begin{aligned}\hat{U}(t)\phi_\kappa(z) &= \sum_{\ell\in\mathbb{Z}} e^{i\ell d\kappa} e^{-iEt/\hbar + ibd\ell t/\hbar}\psi(z-\ell d) \\ &= e^{-iEt/\hbar}\sum_{\ell\in\mathbb{Z}} e^{i\ell d(\kappa+bt/\hbar)}\psi(z-\ell d) \\ &= e^{-iEt/\hbar}\phi_{\kappa+bt/\hbar}(z) \end{aligned} \tag{6.30}$$

which is consistent with the evolution of the quasi-momentum in Bloch oscillations. In particular, for $t = \tau_B$, we call $\hat{U}(\tau_B) = \hat{U}_B$ (and $\hat{\tilde{U}}(\tau_B) = \hat{\tilde{U}}_B$) and get

$$\hat{U}_B\phi_\kappa(z) = \lambda\phi_\kappa(z) \tag{6.31}$$

This equation shows that the Bloch-Stark wave functions are eigenfunctions of the operator $\hat{U}_B$ with an eigenvalue λ which does not depend on the quasi-momentum (which will be important in the numerical simulation).

6.1.3.3 *Fourier decomposition of the Bloch-Stark states*

Using standard Bloch decomposition, the Bloch-Stark states can be expressed as such

$$\phi_\kappa(z) = \sum_{n\in\mathbb{Z}} c_n^\kappa e^{i(nk_0+\kappa)z} \tag{6.32}$$

and this line of reasoning holds for both the perturbed and the unperturbed cases:

$$\phi_\kappa^0(z) = \sum_{n\in\mathbb{Z}} c_n^{\kappa,0} e^{i(nk_0+\kappa)z} = \sum_{n\in\mathbb{Z}} c_n^{\kappa,0}|nk_0+\kappa\rangle \tag{6.33}$$

$$\phi_\kappa^S(z) = \sum_{n\in\mathbb{Z}} c_n^{\kappa,S} e^{i(nk_0+\kappa)z} = \sum_{n\in\mathbb{Z}} c_n^{\kappa,S}|nk_0+\kappa\rangle \tag{6.34}$$

We now consider the matrix elements of the evolution operators over a Bloch period for a given quasi momentum:

$$\hat{\tilde{U}}_{B,\kappa}^{m,n} = \langle mk_0+\kappa|\hat{\tilde{U}}_B|nk_0+\kappa\rangle \tag{6.35}$$

$$\hat{U}_{B,\kappa}^{m,n} = \langle mk_0+\kappa|\hat{U}_B|nk_0+\kappa\rangle = \hat{\tilde{U}}_{B,\kappa}^{m+1,n} \tag{6.36}$$

where the last line uses the result of equation 6.25. The Fourier coefficients of the Bloch-Stark equations thus obey the following linear system:

$$\sum_{n\in\mathbb{Z}} \hat{U}_{B,\kappa}^{m,n} c_n^{\kappa,S} = \lambda c_m^{\kappa,S} \tag{6.37}$$

For numerical simulations, it turns out to be easier to work with the operator $\hat{\tilde{U}}_B$ which can be expressed in momentum space alone:

$$\boxed{\sum_{n\in\mathbb{Z}} \hat{\tilde{U}}_{B,\kappa}^{m+1,n} c_n^{\kappa,S} = \lambda c_m^{\kappa,S}} \tag{6.38}$$

6.1.4 *Expression of the scattering matrix*

Now we have all the elements to find the poles of the scattering matrix. First, for a given quasi-momentum κ we numerically compute the matrix elements of the evolution operator at the Bloch period, $\hat{\tilde{U}}_{\mathrm{B},\kappa}$, using the formula 6.26 and using a truncation in momentum space $n \in [\![-N, N]\!]$. Then, using equation 6.38, the eigenvalues of $\hat{U}_{\mathrm{B},\kappa}$ — or equivalently of the shifted operator $\hat{\tilde{U}}_{\mathrm{B},\kappa}$ — can be found and Fourier coefficients of the Bloch-Stark functions calculated. These can be inserted in the definition of the scattering matrix 6.19, whose poles are then computed.

The scattering matrix reads in the Bloch-Stark basis

$$S(E) = \lim_{n\to\infty} \frac{c_n^{\kappa,S}\, c_{-n}^{\kappa,0}}{c_n^{\kappa,0}\, c_{-n}^{\kappa,S}} \tag{6.39}$$

and the result must be independent of κ as was seen in equation 6.31. The unperturbed Fourier coefficients are easily computed using the equation 6.3

$$c_n^{\kappa,0} = \exp\left[-i\left(\frac{\hbar^2\,(nk_0+\kappa)^3}{6bM} - \frac{E\,(nk_0+\kappa)}{b}\right)\right] \tag{6.40}$$

and the ratio of coefficients appearing in the scattering matrix is:

$$\frac{c_N^{\kappa,0}}{c_{-N}^{\kappa,0}} = \alpha(N,E,\kappa) = \frac{\exp\left[-i\left(\frac{\hbar^2(Nk_0+\kappa)^3}{6bM} - \frac{E(Nk_0+\kappa)}{b}\right)\right]}{\exp\left[-i\left(\frac{\hbar^2(-Nk_0+\kappa)^3}{6bM} - \frac{E(-Nk_0+\kappa)}{b}\right)\right]} \tag{6.41}$$

We now turn to the computation of the Fourier coefficient in the perturbed case. The matrix elements of the operator $\hat{\tilde{U}}_{\mathrm{B},\kappa}$ form a $(2N+1)\times(2N+1)$ matrix that we call $\underline{\underline{W}}$; we also define the following vectors (S exponents are momentarily omitted):

$$\underline{c}^{\kappa} = \begin{pmatrix} 0 \\ c_N^{\kappa} \\ c_{N-1}^{\kappa} \\ \vdots \\ c_{-N+1}^{\kappa} \\ c_{-N}^{\kappa} \end{pmatrix}, \quad \underline{e}_1 = \begin{pmatrix} 0 \\ \vdots \\ 0 \\ 1 \end{pmatrix}, \quad \underline{e}_2 = \begin{pmatrix} 0 \\ 1 \\ 0 \\ \vdots \\ 0 \end{pmatrix} \tag{6.42}$$

The central equation 6.38 now reads

$$\underline{\underline{B}} \cdot \underline{c}^{\kappa} = \begin{pmatrix} 0 & & \\ \vdots & \underline{\underline{W}} & \\ 0 & \cdots\ 0 & \end{pmatrix} \cdot \underline{c}^{\kappa} = \lambda \underline{c}^{\kappa} - \lambda c_{-N}^{\kappa} \underline{e}_1 \tag{6.43}$$

Calling $\underline{\underline{\mathbb{1}}}$ the identity matrix of size $(2N+2)\times(2N+2)$:

$$\left(\underline{\underline{B}} - \lambda \underline{\underline{\mathbb{1}}}\right) \cdot \underline{c}^{\kappa} = -\lambda c_{-N}^{\kappa} \underline{e}_1 \tag{6.44}$$

If the matrix $\underline{\underline{B}} - \lambda \underline{\underline{\mathbb{1}}}$ can be inverted, the ratio of coefficients appearing in the expression of the scattering matrix is:

$$\frac{c_N^{\kappa,S}}{c_{-N}^{\kappa,S}} = -\lambda \, \underline{e}_2 \cdot \left(\underline{\underline{B}} - \lambda \underline{\underline{\mathbb{1}}}\right)^{-1} \cdot \underline{e}_1 \tag{6.45}$$

Bringing together equations 6.41 and 6.45 yields the following expression of the scattering matrix:

$$S(E) = \lim_{N\to\infty} -\lambda \, \left[\alpha(N, E, \kappa)\right]^{-1} \, \underline{e}_2 \cdot \left(\underline{\underline{B}} - \lambda \underline{\underline{\mathbb{1}}}\right)^{-1} \cdot \underline{e}_1 \tag{6.46}$$

As mentioned in 6.1.1, the poles of the scattering matrix are of interest because they indicate resonances. These poles are located in the complex plane at $\mathcal{E} = E - i\Gamma/2$. In the expression of $S(E)$, divergences appear at points where the matrix $\underline{\underline{B}} - \lambda \underline{\underline{\mathbb{1}}}$ cannot be inverted, i. e. when λ is an eigenvalue of $\underline{\underline{B}}$. Finding the resonances of the scattering matrix thus amounts to finding the eigenvalues of $\underline{\underline{B}}$. The energies and decay rates of the corresponding eigenstates are related to the eigenvalue by

$$\lambda = \exp\left(-\frac{\Gamma \tau_\mathrm{B}}{2\hbar}\right) \exp\left(-i\frac{E\tau_\mathrm{B}}{\hbar}\right) \tag{6.47}$$

The steps of the simulation are the following:

- Pick a quasi-momentum κ.
- Construct the Hamiltonian of the system $\hat{\hat{H}}$ which has diagonal coefficients of $\hbar\left(nk_0 + \kappa + bt\right)^2/(2M)$, and where the first terms above and under the diagonal are $-V_0/2$ to account for the lattice potential.
- Compute the evolution operator $\hat{\hat{U}}_{\mathrm{B},\kappa}$ using 6.26 in the truncated momentum space, thus yielding the matrices $\underline{\underline{W}}$ and $\underline{\underline{B}}$.
- Find the eigenvalues and eigenvectors of $\underline{\underline{B}}$. The eigenvectors correspond to the scattering states which are rather stable states, i. e. one can define an energy and lifetime for those states thanks to the corresponding eigenvalue.

According to the definition of the scattering matrix, the truncation in momentum space should be made larger and larger in order to see which eigenvalues actually correspond to resonances of the full problem. However, this rapidly leads to handle impractically large matrices. In order to distinguish real resonances from numerical artefacts owing to the finite size of the Hilbert space we are considering, we use the fact that the eigenvalues are independent of the quasi-momentum κ chosen (according to equation 6.31). For a given truncation in momentum space, the calculation is repeated for several quasi-momenta and only the eigenvalues which are common to all calculations are kept. Only a finite number of scattering states can be found using this procedure due to the finite size of the matrices which are considered.

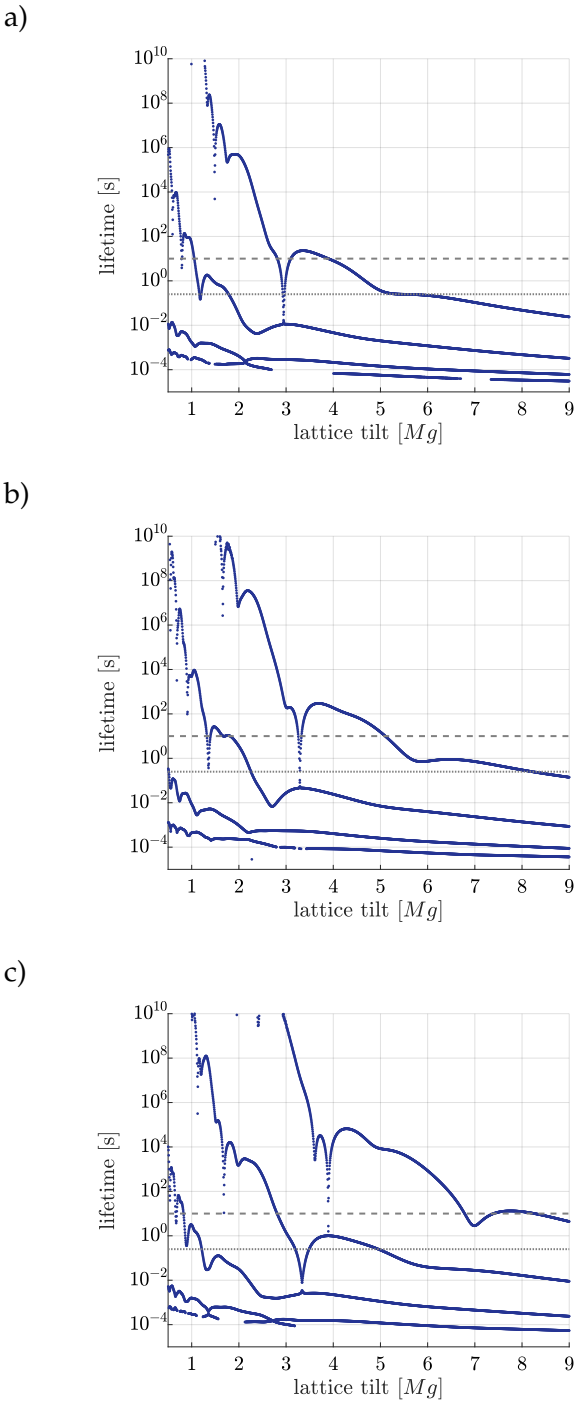

Figure 6.1: Lifetimes of the various scattering states in the tilted lattice, as a function of tilt (expressed in units of gravity) with (a) $V_{\text{laser}} = 20\,E_{\text{r}}$, (b) $V_{\text{laser}} = 24\,E_{\text{r}}$, (c) $V_{\text{laser}} = 32\,E_{\text{r}}$. For all graphs, $d = 1.2\,\mu$m. The dotted line represents the longest lifetime allowed for the first excited state taken to be 25 ms, while the dashed line represents the shortest lifetime allowed for the ground state, taken to be 10 s.

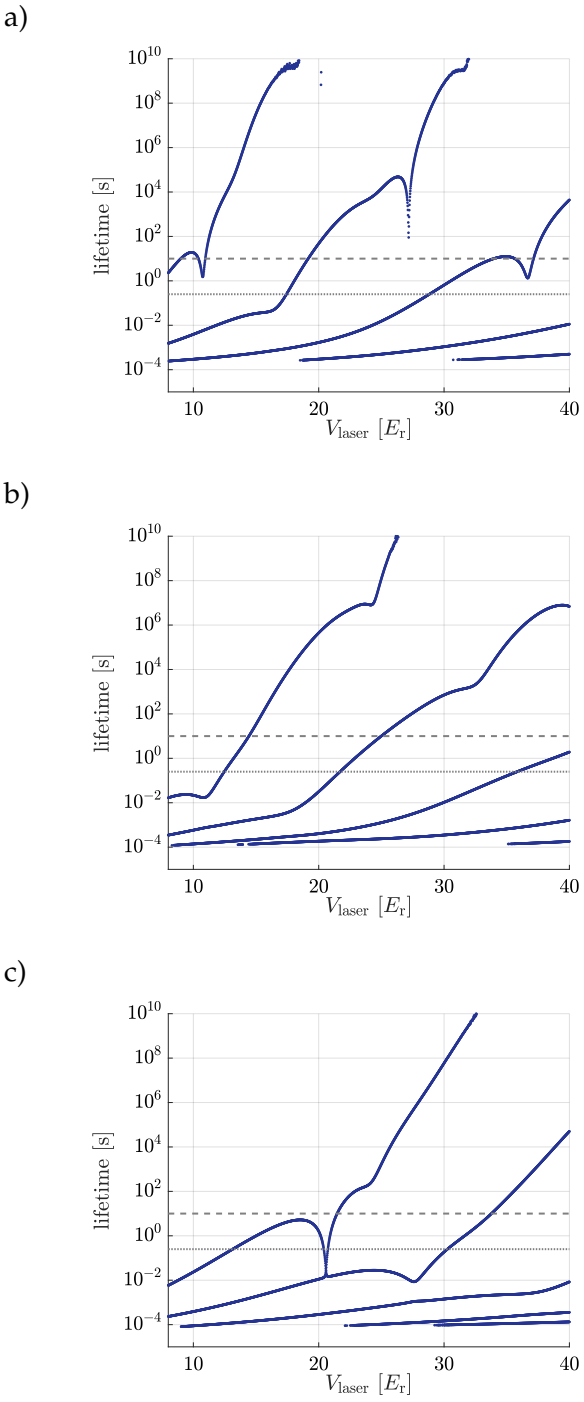

Figure 6.2: Lifetimes of the various scattering states in the tilted lattice, as a function of the depth of the lattice with a tilt of (a) $b = Mg$, (b) $b = 2Mg$, (c) $b = 3Mg$. For all graphs, $d = 1.2\,\mu$m. The dotted line represents the longest lifetime allowed for the first excited state taken to be 25 ms, while the dashed line represents the shortest lifetime allowed for the ground state, taken to be 10 s.

6.1.5 *Results*

In the simulations, the parameters that can be varied are the lattice depth V_0, the lattice spacing d and the tilt of the lattice b. We check the validity of our results by reproducing the results of [75].

In order to estimate if evaporation is possible in the new experimental set-up described in chapter 4, we will restrict the values of the simulation to experimentally achievable ones. We will concentrate on the smallest lattice spacing $d = 1.2\,\mu$m. The maximum depth of the lattice that we can obtain with our current laser set-up is

$$V_0^{\max} = k_B\, 18\mu\mathrm{K} = 950\, E_r \tag{6.48}$$

where $E_r = \frac{\hbar^2 k_0^2}{8M} \simeq h\,410\,\mathrm{Hz}$. The tilt provided by gravity is

$$b_{\text{gravity}} = Mg \simeq 6.2\,\frac{E_r}{d} \tag{6.49}$$

and tuning the position of the zero and the magnitude of the magnetic gradient provided by the quadrupole coils allow to vary b from 0 to $b_{\max} = 9\,Mg = 56\,E_r/d$.

Our aim is to find a regime of parameters where the lifetime τ_1 of the longest-lived state is on the order of seconds or more – we choose $\tau_1 = 10\,\mathrm{s}$ – while that of the second longest-lived state τ_2 is short compared to the time-scales of the experiment, i. e. on the order of one to tens of milliseconds– we choose $\tau_2 = 25\,\mathrm{ms}$.

Figure 6.1 shows the lifetimes as a function of the tilt of the lattice and figure 6.2 shows the lifetimes as a function of the depth of the lattice. For all cases considered, it is possible to find a range of parameter where the lifetimes of the scattering states are within the desired range. For example, with the tilt provided by gravity, a lattice with a depth 60 times smaller than its maximal value provides a lifetime of the ground state on the order of $10^7\,\mathrm{s}$ while that of the first excited state is 15 ms. For a tilt three times larger than gravity, acceptable lifetimes can be obtained at a power 30 times lower than the maximum power of the lattice, which corresponds to a typical power decrease during evaporation.

6.2 EVAPORATION USING PARTICLE INTERACTIONS

6.2.1 *Principle*

The previous studies have shown how atoms in the excited vibrational states of the vertical lattice can be removed by tuning the tilt to out-couple them much faster than the ground state. This procedure removes atoms whose energy is higher than that associated to a vibration quantum. For the case of a lattice with a spacing of $1.2\,\mu$m and a depth of $V_{\text{laser}} = 20E_r$, this corresponds to an energy of $\hbar\omega = \hbar \cdot 2\pi \cdot 3.6\,\mathrm{kHz} = k_B \cdot 180\,\mathrm{nK}$. For a cloud whose temperature and chemical potential are much below this energy scale, the probability that an atom reaches the first excited state becomes exponentially small because the

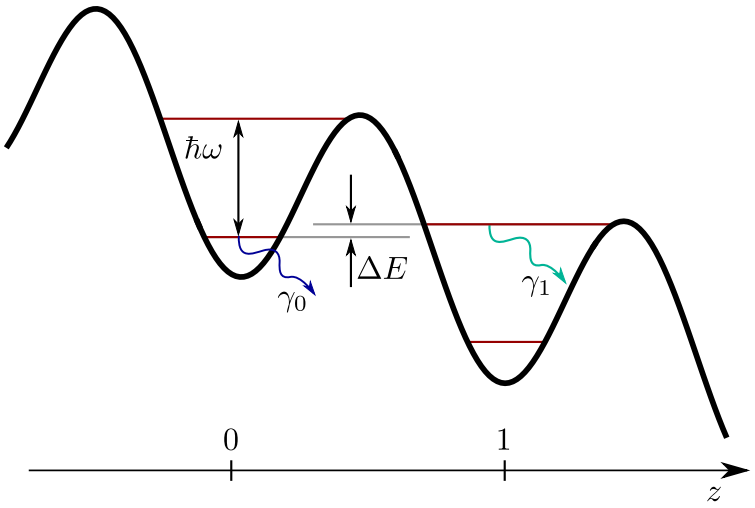

Figure 6.3: Two adjacent potential wells with almost-matching energy levels.

gas is in the deeply 2D regime. The evaporation is efficient as long as the gas does not enter this regime.

However, we would like to be able to evaporate the atomic cloud even when its vertical degree of motion is frozen. To this purpose, we consider atoms localized in the potential well centred on $z = 0$, thermalizing via collisions. We also include the closest level in energy, which is the nth excited level of the well centred on $z = 1$. The energy difference between the two levels is

$$\Delta E = n\hbar\omega - bd \tag{6.50}$$

Both levels have a finite lifetime which is γ_0 (resp. γ_1) for the localized state of lowest energy (resp. for the localized state in the neighbouring well which is the closest in energy). Those parameters are illustrated in figure 6.3.

In this configuration, it becomes possible for two colliding particles to end up in a situation with one atom in the initial state for the vertical degrees of freedom and the other one in the closest state in the neighbouring well. If the energy difference is negative $\Delta E < 0$, this is always possible. If $\Delta E > 0$, the initial kinetic energy associated to the relative velocity of the two particles has to be larger than ΔE for this type of collision to be possible. Given that the well-changing collision is possible, it happens with a probability $p_{\neq}$. The precise value of this parameter will be discussed in section 6.2.3. Each of these collisions reduces the total energy by a quantity ϵ related to the energy difference between the two levels and to the kinetic energy of the particle. We assume the particle that has changed well is lost, that is $\gamma_1 \gg \gamma_0$. For the atoms remaining in the initial well, the energy as well as the atom number has decreased, which can lead to an increase in phase-space density.

Let us present a simplification of the problem using classical particles before presenting the numerical simulations which were performed.

We consider a gas of N classical particles confined in the lowest level of a potential well of the tilted lattice and in a box potential of area $\mathcal{A}$ in the two other directions x and y. They are at thermal equilibrium with a temperature

T, and are thus uniformly distributed in the xy plane with a density n. The probability distribution of atoms in phase-space is

$$f(\boldsymbol{r},\boldsymbol{p}) = \frac{1}{2\pi\mathcal{A}Mk_{\mathrm{B}}T}\exp\left(-\frac{p^2}{2Mk_{\mathrm{B}}T}\right) \tag{6.51}$$

$$f(\boldsymbol{v},\boldsymbol{p}) = \frac{M}{2\pi\mathcal{A}k_{\mathrm{B}}T}\exp\left(-\frac{Mv^2}{2k_{\mathrm{B}}T}\right) \tag{6.52}$$

and the mean energy

$$\langle E\rangle = Nk_{\mathrm{B}}T \tag{6.53}$$

In the following, we will assume that $p_{\neq} \leqslant 1/4$ such that there are at least on average three non lattice-site-changing collisions between two lattice-site-changing collisions. In typical evaporation processes, it was measured that a gas typically thermalizes after three collisions [216]. Thus, we can assume that the lattice-site-changing collisions are rare enough such that position and momentum distribution is always at thermal equilibrium. We call the collision probability per unit time per particle γ_{coll} and the probability that two colliding particles have a relative kinetic energy larger that ΔE, $p_{\Delta E}$. For a Maxwell-Boltzmann distribution,

$$p_{\Delta E} = \begin{cases} 1 & \text{if } \Delta E < 0 \\ \exp\left(-\frac{\Delta E}{k_{\mathrm{B}}T}\right) & \text{if } \Delta E > 0 \end{cases} \tag{6.54}$$

The calculation is explicitly done in Appendix B, yielding the result in Equation B.6. During a time δt, the number of lattice-site-changing collisions is

$$\#\text{collisions} = p_{\neq}\,\gamma_{\mathrm{coll}}\delta t\,p_{\Delta E}\,\frac{N}{2} = p\frac{N}{2}\delta t \tag{6.55}$$

The probability of having a lattice-site-changing collision per particle has been aggregated to a single number γ_p. This number depends on the temperature of the gas, on the relative velocity of the atoms, etc. We neglect the dependence with the relative velocity and assume that it stays constant over the time interval δt that we consider. The atom number has changed by

$$\delta N = -\gamma_p\frac{N}{2}\delta t \tag{6.56}$$

since one particle is lost for each collision and the energy has changed by

$$\delta E = -\gamma_p\frac{N}{2}\epsilon\delta t \tag{6.57}$$

where ϵ is the mean energy which is carried away by an atom. For two colliding particles with initial velocities $\boldsymbol{v}_1$ and $\boldsymbol{v}_2$, the center-of-mass velocity is defined as $\boldsymbol{v}_{\mathrm{CoM}} = (\boldsymbol{v}_1+\boldsymbol{v}_2)/2$ and the relative velocity as $\boldsymbol{v}_{\mathrm{rel}} = (\boldsymbol{v}_1-\boldsymbol{v}_2)$. The initial energy (considering the two particles in the initial trap) is

$$E^{\mathrm{i}} = M\boldsymbol{v}_{\mathrm{CoM}}^2 + \frac{M}{4}\boldsymbol{v}_{\mathrm{rel}}^2 \tag{6.58}$$

The center-of-mass velocity is left unchanged to ensure conservation of momentum. The norm of the relative velocity is changed to ensure energy conservation. If $\boldsymbol{v}_{\mathrm{rel,\,f}}$ is the relative velocity after the collision,

$$E^{\mathrm{rel}}_{\mathrm{kin,\,f}} = \frac{M}{4}\boldsymbol{v}^2_{\mathrm{rel,\,f}} = \frac{M}{4}\boldsymbol{v}^2_{\mathrm{rel}} - \Delta E \tag{6.59}$$

The final energy of the single particle remaining in the initial potential well reads

$$E^{\mathrm{f}} = \frac{1}{2}M\boldsymbol{v}^2_{\mathrm{CoM}} + \frac{1}{8}M\boldsymbol{v}^2_{\mathrm{rel,\,f}} = \frac{1}{2}M\boldsymbol{v}^2_{\mathrm{CoM}} + \frac{1}{8}M\boldsymbol{v}^2_{\mathrm{rel}} - \frac{\Delta E}{2} \tag{6.60}$$

hence

$$\epsilon = -\left(E^{\mathrm{f}} - E^{\mathrm{i}}\right) = \frac{\Delta E}{2} + \frac{1}{2}M\boldsymbol{v}^2_{\mathrm{CoM}} + \frac{1}{8}M\boldsymbol{v}^2_{\mathrm{rel}} \tag{6.61}$$

The average of the square of the center-of-mass velocity is calculated using the fact that

$$\left\langle \boldsymbol{v}^2 \right\rangle = 2k_{\mathrm{B}}T/M \tag{6.62}$$

and that

$$\left\langle \boldsymbol{v}^2_{\mathrm{CoM}} \right\rangle = \left\langle \boldsymbol{v}^2 \right\rangle /2 = k_{\mathrm{B}}T/M \tag{6.63}$$

The expectation value $\left\langle \boldsymbol{v}^2_{\mathrm{rel}} \right\rangle$ has to be calculated taking into account the fact that if the collision takes place. The explicit calculation is done in Appendix B. Plugging the results of Equation B.11 and Equation B.12 into equation 6.61 yields:

$$\langle \epsilon \rangle = \begin{cases} \frac{\Delta E}{2} + k_{\mathrm{B}}T & \text{if } \Delta E < 0 \\ \Delta E + k_{\mathrm{B}}T & \text{if } \Delta E > 0 \end{cases} \tag{6.64}$$

In the following, we will only consider average values and write ϵ instead of $\langle \epsilon \rangle$.

Assuming that equation 6.53 always holds (since the gas is always at thermal equilibrium), differentiating it and using equations 6.56 and 6.57 we obtain

$$k_{\mathrm{B}}\delta T = -\frac{\gamma_p}{2}\left(\epsilon - k_{\mathrm{B}}T\right)\delta t \tag{6.65}$$

Hence, the temperature will decrease if

$$\epsilon > k_{\mathrm{B}}T \tag{6.66}$$

which is natural because it means that the mean energy carried away by an escaping particle has to be larger than the mean energy per particle, meaning for the energy difference between the two levels

$$\Delta E > 0 \tag{6.67}$$

However, we are not interested in just cooling the gas but in increasing its degeneracy, that is increasing its 2D phase-space density

$$\mathcal{D} = n\lambda^2_{\mathrm{dB}} = \frac{N}{\mathcal{A}}\frac{h^2}{2\pi M k_{\mathrm{B}}T} \tag{6.68}$$

where $\mathcal{A}$ is the area of the box potential in which the atoms are confined and λ_{dB} the de Broglie wavelength associated to the temperature of the atoms. Differentiating the above equation yields

$$\begin{aligned}\frac{\delta\mathcal{D}}{\mathcal{D}} &= \frac{\delta N}{N} - \frac{\delta k_{\mathrm{B}}T}{k_{\mathrm{B}}T} \\ &= \gamma_p \left(\frac{\epsilon}{2k_{\mathrm{B}}T} - 1\right)\delta t \qquad (6.69) \\ &= \frac{\gamma_p}{2}\left[\frac{\Delta E}{k_{\mathrm{B}}T} - 1\right]\delta t \qquad (6.70)\end{aligned}$$

As expected, a decrease in temperature does not necessarily lead to an increase in phase-space density because the atom number decreases too. The phase-space density will increase if

$$\epsilon > 2\,k_{\mathrm{B}}T \qquad (6.71)$$

or equivalently

$$\Delta E > k_{\mathrm{B}}T \qquad (6.72)$$

Moreover, the relative increase in phase-space density can be expressed as a function of the ratio $\Delta E/k_{\mathrm{B}}T$:

$$\frac{\delta\mathcal{D}}{\mathcal{D}} = \frac{1}{2}\left(\frac{\Delta E}{k_{\mathrm{B}}T} - 1\right) e^{-\frac{\Delta E}{k_{\mathrm{B}}T}}\,\gamma_{\mathrm{coll}}\,p_{\neq}\delta t \qquad (6.73)$$

For a given collision rate, it is maximum at $\Delta E/k_{\mathrm{B}}T = 2$ with a value of $e^{-2}\gamma_{\mathrm{coll}}\,p_{\neq} \simeq 0.13$ for a collision rate of $8\,\mathrm{s}^{-1}$. A lattice-site-changing collision probability of $p_{\neq} = 0.25$ gives a relative increase of 13 % per unit time.

In case the vertical confinement (a harmonic oscillator of characteristic frequency ω) is not very large compared to the typical energy of the atoms, a second mechanism of collision-induced evaporation has to be considered. If two particles collide with a large enough relative kinetic energy, the particles can end up in different vibrational states of the vertical harmonic oscillator. Owing to the short lifetime of the particles in these states, they will be quickly lost (see6.1).

For symmetry reasons, calling n_1 and n_2 the two vibrational states of the products of the collisions, $n_1 + n_2$ has to be an even number. In the following, we will restrict ourselves to two cases:

$$\text{process 1} \quad : \quad (n_1 = 0,\, n_2 = 0) \rightarrow (n_1 = 1,\, n_2 = 1) \qquad (6.74)$$

$$\text{process 2} \quad : \quad (n_1 = 0,\, n_2 = 0) \rightarrow (n_1 = 0,\, n_2 = 2) \qquad (6.75)$$

meaning that the two particles must have a relative kinetic energy larger than $2\hbar\omega$ for this process to be allowed. We call $\psi_n(z)$ the wavefunction of the harmonic oscillator along the z axis, and define the (non normalized) collision coefficients:

$$c_0 = \int |\psi_0(z)|^4\,\mathrm{d}z \qquad (6.76)$$

$$c_1 = \int (\psi_0(z))^2\,(\psi_1(z))^2\,\mathrm{d}z \qquad (6.77)$$

$$c_2 = \int (\psi_0(z))^3\,\psi_2(z)\,\mathrm{d}z \qquad (6.78)$$

Knowing that the particles have enough energy (and assuming that there are no well-changing collisions, $p_{\neq} = 0$), the first process happens with a probability

$$p_1 = \frac{c_1}{c_0 + c_1 + c_2} = \frac{1/2}{1 + 1/2 + 1/\sqrt{8}} \tag{6.79}$$

and the second with probability

$$p_2 = \frac{c_2}{c_0 + c_1 + c_2} = \frac{1/\sqrt{8}}{1 + 1/2 + 1/\sqrt{8}} \tag{6.80}$$

With the same line of reasoning as for the previous evaporation mechanism, the gain of phase space density during a time δt is

$$\frac{\delta \mathcal{D}}{\mathcal{D}} = \left(\sqrt{2} \frac{\hbar \omega}{k_B T} - 1 \right) \frac{\gamma_p}{\sqrt{2}} \delta t \tag{6.81}$$

where $\gamma_p = (p_1 + p_2) \gamma_{\text{coll}} p \left(E_{\text{kin}}^{\text{rel}} \geqslant 2\hbar\omega \right)$.

6.2.2 *Simulations*

To simulate the problem, we use molecular dynamics techniques which have already been successfully describing evaporation for cold atom experiments [217, 218]. This technique alternates between collision-less evolution of the trajectories of a given number of particles and random collision events between close-by particles.

We start with N atoms whose positions are drawn uniformly in a square box with size L and whose velocities are drawn following the Maxwell-Boltzmann distribution. The walls of the box in the xy plane have a finite height U_{box}, allowing for standard evaporation. The scattering cross-section for the atoms reads

$$\sigma = 2 \cdot 4\pi a_{\text{scatt}}^2 \tag{6.82}$$

with a_{scatt} the s-wave scattering length, which is the only channel in which the atoms can collide owing to their low temperatures. The factor of two accounts for the scattering enhancement due to the fact that our atoms are non-condensed bosons (the phase-space distribution is considered to be classical).

We assume that the confinement provided by the lattice is harmonic with an angular frequency ω and a characteristic extension of the ground state $a_{\text{ho}} = \sqrt{\hbar/(M\omega)}$.

We also use the length scale $\delta\ell$ which defines a two-dimensional grid onto the atoms. It is chosen such that the probability of having two atoms in the same box is small:

$$N \ll \left(\frac{L}{\delta \ell} \right)^2 \tag{6.83}$$

Time evolves in discrete steps of duration δt. This duration is chosen such that the probability of having a collision when two particles are in the same cell of the grid is small

$$p_{\text{coll}} = \frac{\sigma \left| \boldsymbol{v}_{\text{rel}} \right|}{\left(a_{\text{ho}} / \sqrt{2} \right) \delta \ell^2} \delta t \ll 1 \tag{6.84}$$

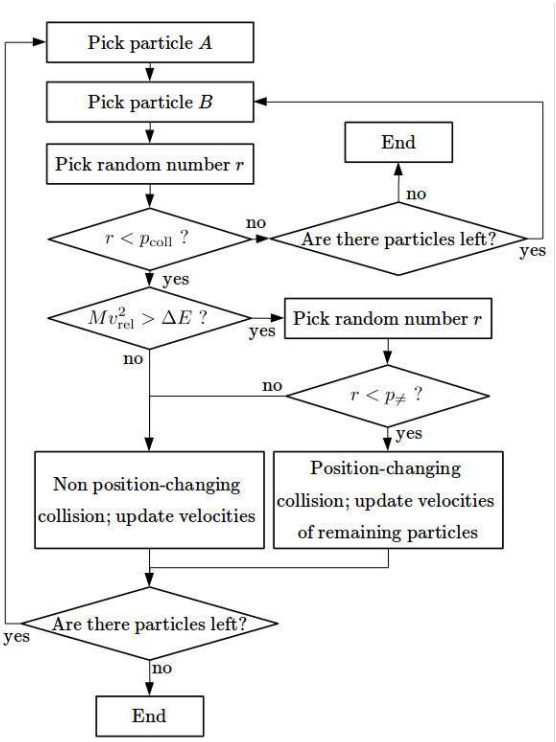

Figure 6.4: Process used to decide for collision events.

This probability expresses the fact that, in the frame of one particle, a second particle spans the volume $V_{\text{scatt}} = \sigma |\boldsymbol{v}_{\text{rel}}| \delta t$ during one time step; hence the probability to hit the first particle corresponds to the ratio of the volume V_{scatt} over the volume of the cell $\left(a_{\text{ho}}/\sqrt{2}\right) \delta \ell^2$.

From this the simulation goes as follow. For each time step:

- Let the particles evolve freely during δt. In our case, having only a box potential to confine the atoms makes the evolution rather simple; only the reflections on the walls have to be accounted for. In case a particle with a kinetic energy larger than U_{box} crosses the boundary of the box, remove it.

- Compute the outcome of collisions according to the flow chart in figure 6.4. According to the previous section, the velocity of the center-of-mass is left unchanged; the norm of the relative velocity is changed if there is a lattice-site-changing collision according to equation 6.59, and its angle is drawn randomly.

- Remove particles with probability $\gamma_0 \delta t$ to account for the finite lifetime, for example due to imperfect vacuum.

- Compute the interesting quantities: atom number, energy, temperature (computed either by a fit of the velocity distribution or, assuming the gas is at thermal equilibrium, using equation 6.53), phase-space density, mean energy lost per lattice-site-changing collision, etc.

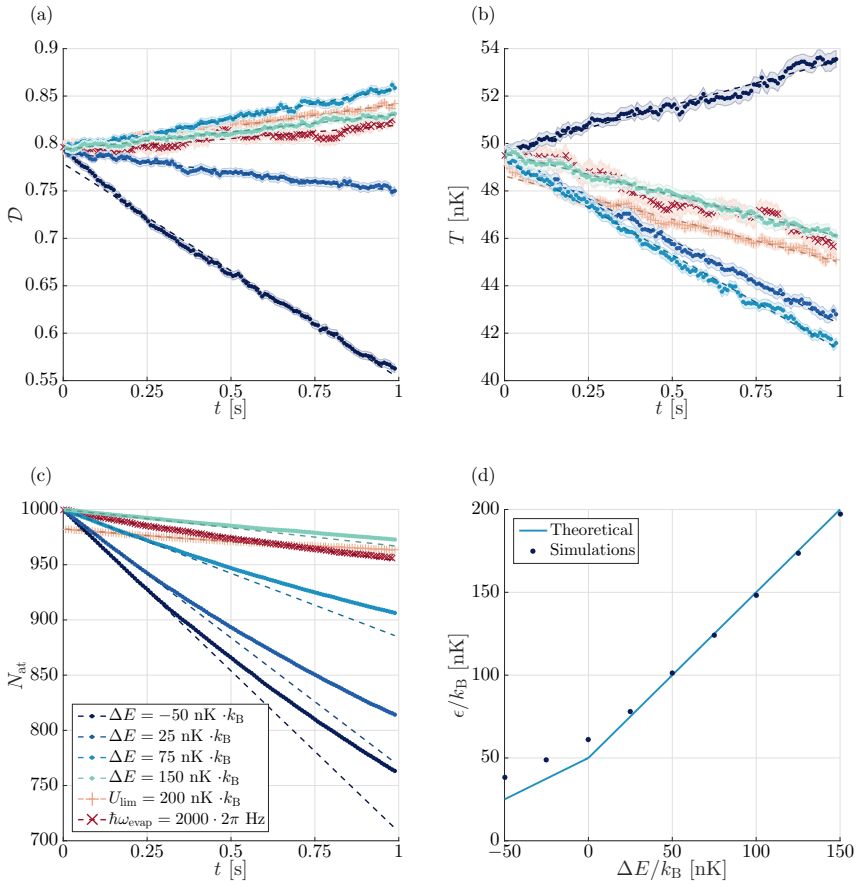

Figure 6.5: Results of the molecular dynamics simulations. Various energy offsets between the neighbouring sites $\Delta E = k_{\mathrm{B}}[-50, 25, 75, 150]$ nK are represented by dark to light blue dots. Standard evaporation with an energy height of the box potential of $k_{\mathrm{B}}200$ nK is in light red (plus signs); results of the evaporation using the different vibrational states in the vertical direction are represented with dark red crosses. Dashed lines represent the linear fits to the simulation data. Shaded areas correspond to the standard error on the results (averaged over 50 measurements for the dark red curves, 100 measurements for the others). (a) Phase-space density, (b) Temperature, (c) Atom number, (d) Mean energy removed by a particle which is lost.

6.2.3 *Results*

In the simulation, we consider a gas of 1000 atoms in a square box of length 30 μm. The initial temperature of the gas is taken to be 50 nK, the confinement frequency in the vertical direction is taken to be 2 kHz and the probability to have a lattice-site-changing collision is $p_{\neq} = 0.25$.

In a first series of simulations, the height of the barrier potential at the edge of the box is taken to be much larger than the typical kinetic energy of an atom. This prevents standard evaporation to take place. The energy difference between the two closest levels in energy ΔE is varied between -50 nK and 150 nK. The results of the molecular dynamics simulation are presented in figure 6.5 and follow the results derived in section 6.2.1. The average energy removed per particle is slightly larger than the one which was calculated in

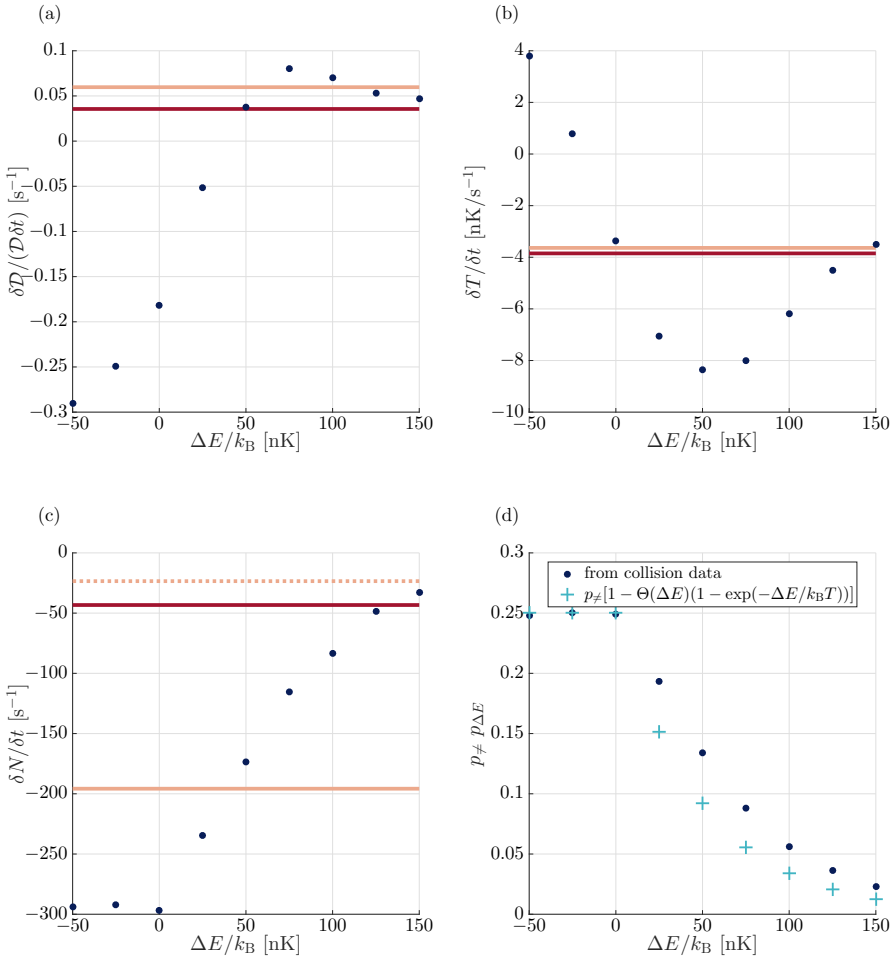

Figure 6.6: Results of the fits of the molecular dynamics simulations for various energy offsets between the neighbouring sites (dark blue curve), for evaporation using the different vibrational state (dark red line) for standard evaporation with an energy height of the box potential of $k_{\mathrm{B}}200\,\mathrm{nK}$ (light red line). (a) Variation of phase-space density. (b) Variation of temperature. (c) Variation of atom number; there are two possible way of computing the atom number variation for the standard evaporation. The coefficient of the linear fit of 6.5c is represented as a dotted line. The atom loss during the first 0.1 s is represented as a solid line.(d) Probability that a collision is lattice-site-changing, knowing that there is a collision. In the program, $p_{\neq} = 0.25$. Dark blue dots represent the results of the simulation, light blue crosses represent theoretical values computed from equation 6.54.

equation 6.64 as seen from figure 6.5d. This is due to the fact that the collision probability is not independent of the relative velocity between the particles, as shown in equation 6.84. The larger the relative velocity, the higher the probability to collide so the mean of $\boldsymbol{v}_{\mathrm{rel}}^2$ knowing that there is a collision is different from what is calculated for equation 6.64.

We perform linear fits of the various curves (the atom number is fitted during the first 10 % of the total simulation time), whose values are reported in figure 6.6. As expected, the evaporation mechanism can lead to an increase in phase-space density for an energy difference of $\Delta E \gtrsim k_{\mathrm{B}} T$.

In figures 6.5 and 6.6, the light red curves represent a simulation of "standard evaporation" with no possibility to have lattice-site-changing collisions. The evaporation is provided by the finite height of the in-plane box potential which allows particles whose kinetic energy is higher than $U_{\mathrm{lim}} = k_{\mathrm{B}} \cdot 200\,\mathrm{nK}$ to be lost. This corresponds to a ratio between the height of the barrier and the temperature of the gas of $\eta = 4$, which is reasonable for this type of evaporative cooling. The loss of atom is less important but the decrease in temperature too, so that the increase of phase-space density is smaller than the one due to lattice-site-changing collisions for some values of ΔE.

The second evaporation process of evaporation relying on atoms changing of vibrational state after a collision has also been simulated. The vertical confinement has been chosen such that $\hbar\omega_{\mathrm{evap}} = \hbar \cdot 2\pi \cdot 2\,\mathrm{kHz}$. The results of this simulation is represented by the dark red curves in figures 6.5 and 6.6.

We can also define the efficiency of the evaporation as

$$e = \frac{\mathrm{d}\mathcal{D}}{\mathcal{D}} \frac{N}{\mathrm{d}N} \tag{6.85}$$

which indicates the increase in phase-space density (in orders of magnitude) when one order of magnitude is lost in atom number. The results are presented in figure 6.7. For the standard evaporation, computing the quantity $\delta N/N$ can be performed using two methods. This is due to the fact that at the beginning of the simulation, many particles are lost at once (about 2 %). It is therefore different (i) to fit the decay of the atom number or (ii) to compute the percent of atoms lost after 0.1 s: $[N(t = 0.1\,\mathrm{s}) - N(0)]\,/N(0)$. The first method seems to indicate that standard evaporation is always more efficient than the two other collision-assisted processes. However, it does not take into account the initial atom loss. According to the results for (ii), it is possible to reach similar or higher efficiencies with either of the two collision-assisted evaporation methods.

Last, we discuss the probability of having a lattice-site-changing collision knowing that there is a collision with high enough energy $p_{\neq}$; it was taken to be $p_{\neq} = 0.25$ in the simulation, taking the highest possible value such that the reasoning of section 6.2.1 holds. This probability actually depends on the overlap of the wave functions localized in two different potential wells. We give a rough estimate of this probability by assuming that the lattice is deep enough to support several bound states; we can then approximate the wave functions in the vertical direction by eigenfunctions of the harmonic oscillator instead of taking into account the full Wannier functions. Calling ψ_0 (resp. ψ_1)

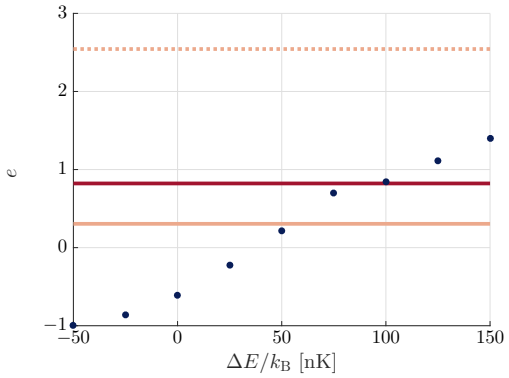

Figure 6.7: Efficiency of the evaporation for the collision-assisted evaporation (blue dots) as a function of the energy difference between the two levels, compared with that of standard evaporation with $\eta = U_{\text{lim}}/k_B T = 4$ (light red line) and with collision-assisted evaporation using the different vibrational states of the lattice well. The dotted and solid lines for the standard evaporation correspond to the two possible way to compute the atom loss: coefficient of the linear fit of 6.5c (dotted line) and atom loss during the first 0.1 s (solid line).

the wave function of the ground state (resp. of the first excited state), we get an approximate value of $p_{\neq}$ by computing

$$p_{\neq} \simeq \frac{p_1}{p_0 + p_1} \tag{6.86}$$

with

$$p_0 = \int \psi_0^4(z)\,\mathrm{d}z = \frac{1}{a_{\text{ho}}\sqrt{2\pi}} \tag{6.87}$$

$$p_1 = \int \psi_0^3(z)\,\psi_1(z-d)\,\mathrm{d}z = \frac{d}{a_{\text{ho}}^2\sqrt{2\pi}} e^{-d^2/2a_{\text{ho}}^2} \tag{6.88}$$

where $a_{\text{ho}} = \sqrt{\hbar/(M\omega)}$, $\omega = \sqrt{2V_{\text{laser}}k_{\text{laser}}^2/M}$ and d is the lattice spacing. This gives

$$p_{\neq} \simeq \frac{d e^{-d^2/2a_{\text{ho}}^2}}{a_{\text{ho}} + d e^{-d^2/2a_{\text{ho}}^2}} \tag{6.89}$$

The approximate value of $p_{\neq}$ is shown in figure 6.8. For lattice depths on the order of $10\,E_{\text{r}}$ (computed with a lattice spacing of $1.2\,\mu$m), we have $p_{\neq} \simeq 10^{-4}$ if $d = 1.2\,\mu$m or $p_{\neq} \simeq 10^{-7}$ if $d = 2\,\mu$m. The relative variations of atom number, temperature and phase-space density are all proportional to $p_{\neq}$, meaning that unless the tunnelling is important and the lattice shallow, the first collision-assisted evaporation scheme will not be practical. Tilting the lattice in the regime defined thanks to 6.1 can therefore lead to efficient evaporation at reasonable lattice depths via collision-assisted evaporation where the particles change their vibrational state within a lattice well.

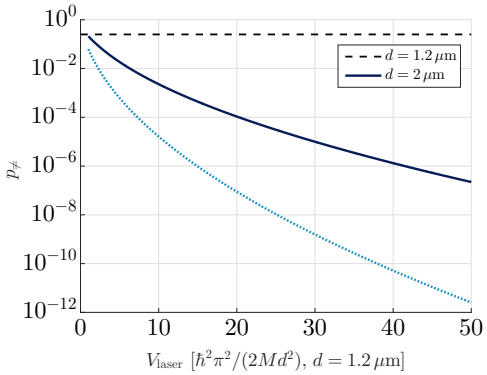

Figure 6.8: Estimated value of $p_{\neq}$ for overlapping eigenfunctions of the harmonic oscillator as a function of the lattice depth. The lattice depth is depicted in units of E_r for a lattice spacing of $d = 1.2\,\mu$m. The overlap $p_{\neq}$ is shown for a lattice spacing of $d = 1.2\,\mu$m (dark blue solid curve) and of $d = 2\,\mu$m (light blue dotted curve). The dashed line represents the value which mas used in the simulations $p_{\neq} = 0.25$.

6.3 CONCLUSION

In this chapter, we have studied how the tilted lattice can lead to new evaporation mechanisms.

First, we looked at the influence of having a lattice potential and a linear potential on the poles of the scattering matrix. We saw that it is possible to find a combination of lattice depth and tilt with realistic values for our experimental set-up such that the lowest energy localized state is long-lived ($\tau_0 > 10\,$s) and the first excited and localized state is short-lived ($\tau_1 < 25\,$ms). Going into this regime means that atoms whose vertical degree of freedom is not frozen are quickly lost. This can help to maintain a two-dimensional gas by removing vibration excitations in the vertical direction.

Then, we studied two ways of evaporating the atomic cloud using collisions. We start with all the atoms in the localized ground state of one well and consider the possibility of two atoms to collide and to end up either with one particle in the initial state while the other particle has been transferred to another localized in a neighbouring well or with one or two particles in a different vibrational state of the same lattice well.

For the first mechanism, the ability of the atoms to be cooled or their phase-space density to be increased by this mechanism depends on the energy difference between the initial state and the state in the neighbouring well ΔE. As is seen from approximate calculations as well as from molecular dynamics simulation, the temperature of the gas decreases if $\Delta E \gtrsim 0$ and the phase-space density increases if $\Delta E \gtrsim k_\text{B}T$. While the increase in phase-space density can be greater with this type of evaporation than with a standard evaporation using finite-height potentials, the dynamics of this evaporation relies on the overlap between the two possible states of the atoms in the two different potential wells. For the deep lattices, this overlap becomes exponentially small, which hinders this mechanism.

For the second mechanism, with a vertical confinement induced by the lattice of $h \cdot 2\,\mathrm{kHz}$ (within experimental reach), the evaporation is shown to be as efficient as the standard evaporation technique. Therefore, tilting the lattice can provide additional and uniform evaporation of the atomic cloud.

This uniform evaporation can be very interesting in the context of the Kibble-Zurek mechanism described in 2 and experimentally investigated in 3: if we want to investigate large clouds of atoms, standard evaporation could lead to a non-uniform temperature due to the fact that particles only escape at the edges of the trap. Having a uniform evaporation that makes the system cross the phase transition temperature would lead to a more controlled test of this mechanism.

7

PROSPECTIVE EXPERIMENT: USING MAGNETIC TEXTURE TO PRODUCE SUPERCURRENTS

The experimental set-up which has been developed and described in chapter 4 enables us to produce planar gases of degenerate atoms with various shapes. In that respect, ring geometries are very interesting because they support supercurrents, i. e. states of the macroscopic matter wave with a quantized angular momentum that are metastable owing to the superfluid character of the gas. These supercurrents have already been produced and studied in various ultracold atom experiments [51, 53] using several techniques:

- In chapter 3, we saw that they can be created stochastically by quench cooling ultracold atoms.
- They can also be optically generated as a metastable state by imprinting a phase winding on a ring-shaped cloud of atoms using Laguerre-Gauss beams [53, 162].
- They can also be created as the ground state in the rotating frame of a stirred torus of atoms [51].
- Those supercurrents could also be generated as the ground state of the Hamiltonian written in the laboratory frame, when applying on the neutral atoms a potential equivalent to a magnetic field for charged particles – named "artificial gauge field" – the amplitude of which corresponds to several flux quanta for the ring, as was done for mesoscopic rings of metal or of semiconductor material [219–221].

However, although ultracold atoms have been the subject of intense research for the past twenty years due to the high degree of control they offer on many experimental parameters, there is still a parameter which the ultracold atom community is trying to implement in a reliable fashion: gauge fields of large amplitude [39]. Schemes to produce an artificial magnetic field have received a lot of theoretical and experimental interest in order to address some of the most intriguing puzzles of condensed matter physics. While obtaining gauge field amplitudes high enough to reach regimes analogous to the quantum Hall effect [222, 223] has remained out of reach for the moment, implementations in bulk [57] or lattice systems [224–227] have been demonstrated.

In this chapter, we will describe how we can produce an artificial magnetic field on the atoms using the quadrupole coils available in our experiment and discuss possible experiments that follow on from that set-up. In this geometry, the strength of the gauge field is characterized equivalently by its amplitude or by its flux through the ring. Using a static magnetic field configuration will allow to produce artificial gauge fields with an amplitude of a few flux quanta.

Among the many techniques which have been developed to produce artificial gauge fields [39], we will take advantage of the magnetic moment of the atoms which gives them an internal degree of freedom, and describe the artificial gauge potential that is obtained in Section 7.1. As a result of the presence of the gauge field, the atoms can condense in different states of angular momentum depending on the parameters of the ring potential; ground states of the system as well as possible detection scheme for the supercurrents are discussed in Section 7.2. Having an artificial gauge field can also be phrased in the framework of the Berry phase (generalization of the Aharonov-Bohm phase), as will be done in Section 7.3. Then, the case of a time-periodic magnetic field will be considered in Section 7.4; we will show that the periodic magnetic field can be engineered such that the charge of the supercurrent increases by two at each period, implementing a "vortex pump". The topological aspects of this time-periodic Hamiltonian will also be discussed.

7.1 A RING OF ATOMS IN A QUADRUPOLE FIELD

7.1.1 *A neutral atom in a real magnetic field interpreted as a charge in an artificial magnetic field*

Let us assume we have a neutral atom in an external potential $V(\hat{\boldsymbol{r}})$ and a magnetic field that depends on position $\boldsymbol{B}(\boldsymbol{r})$:

$$\hat{H} = \frac{\hat{\boldsymbol{p}}^2}{2M} + V(\hat{\boldsymbol{r}}) - g\mu_{\mathrm{B}}\hat{\boldsymbol{F}} \cdot \boldsymbol{B}(\boldsymbol{r}) \tag{7.1}$$

where $\hat{\boldsymbol{p}}$ is the momentum of the atom, M its mass, $\hat{\boldsymbol{F}}$ its spin associated to the gyromagnetic ratio g, and μ_{B} is the Bohr magneton.

An atom localized in $\boldsymbol{r}$ minimizes its energy by aligning its spin with the local magnetic field (for a positive g). The internal state minimizing the energy thus depends on position $|m_+\left[\boldsymbol{B}(\boldsymbol{r})\right]\rangle = |m_+\rangle_{\boldsymbol{B}}$. We will assume in the following that the atom stays in this "local ground state" during its evolution, since the time-scale of the evolution of the spin (on the order of $1/\nu_{\mathrm{Larmor}} \sim 1.4\,\mu$s for a magnetic field of 1 G) is much smaller than the time-scale of the evolution of the motional degrees of freedom of the atom (on the order of 125 μs for the highest trapping frequencies we can produce). This assumption thus relies on the adiabatic approximation, similar to the Born-Oppenheimer approximation of quantum chemistry where the time-scales for the evolution of the electrons are much shorter than the time-scales for the evolution of the nuclei. We will come back in the following on the validity of this approximation in our experiment.

The internal degree of freedom has a dimension $2F+1$ where F is the integer or half-integer labelling the spin manifold in which the atom is, and the local eigenstates for the magnetic Hamiltonian are

$$\{|m_{-F}\rangle_{\boldsymbol{B}},\ |m_{-F+1}\rangle_{\boldsymbol{B}},\ \cdots,\ |m_F\rangle_{\boldsymbol{B}} = |m_+\rangle_{\boldsymbol{B}}\} \tag{7.2}$$

A spinor wave function $\Psi(\boldsymbol{r}, t)$ can be decomposed on this basis

$$\Psi(\boldsymbol{r}, t) = \sum_{i=-F}^{F} \varphi_i(\boldsymbol{r}, t) \, |m_i\rangle_{\boldsymbol{B}} \tag{7.3}$$

The adiabatic approximation consists in considering that an atom initially prepared in the internal state $|m_F\rangle_{\boldsymbol{B}}$ will remain there; we therefore only consider the evolution of φ_F. By applying the Hamiltonian 7.1 on the wave function 7.3 and then projecting on $|m_+\rangle_{\boldsymbol{B}}$, we obtain the evolution equation for φ_F [39]

$$i\hbar \frac{\partial \varphi_F}{\partial t} = \left[\frac{(\boldsymbol{p} - \boldsymbol{A})^2}{2M} + V(\boldsymbol{r}) + W(\boldsymbol{r}) \right] \varphi_F \tag{7.4}$$

which involves the vector potential

$$\boldsymbol{A}(\boldsymbol{r}) = i\hbar \langle m_F |_{\boldsymbol{B}} \boldsymbol{\nabla} | m_F \rangle_{\boldsymbol{B}} \tag{7.5}$$

and the scalar potential

$$W(\boldsymbol{r}) = \frac{\hbar^2}{2M} \sum_{i=-F}^{F-1} \left| \langle m_i | \boldsymbol{\nabla} m_F \rangle \right|^2 \tag{7.6}$$

The neutral atom thus behaves as a charged particle in the artificial magnetic field $\boldsymbol{\mathcal{B}}$ obtained from the vector potential $\boldsymbol{A}(\boldsymbol{r})$:

$$\boldsymbol{\mathcal{B}}(\boldsymbol{r}) = \boldsymbol{\nabla} \times \boldsymbol{A}(\boldsymbol{r}) \tag{7.7}$$

The idea to use a real magnetic field on neutral atoms to simulate an artificial magnetic field on them has been experimentally demonstrated previously: the zero of a magnetic trap was moved completely through the cloud of atom, leading to the production of vortices of charge two at MIT as described in [228]. In Amherst as described in [229, 230], the zero of a quadrupole field was placed in a BEC and interpreted as a magnetic monopole. In Seoul, the zero of a quadrupole field was moved in an atomic cloud and described as a skyrmion texture [231].

7.1.2 *Case of a spin 1 atom*

In our experiment, we prepare a degenerate cloud of rubidium 87 atoms in the lower hyperfine state, so we will consider the $F = 1$ manifold in the following unless mentioned. In order to give literal expressions for $\boldsymbol{A}$ and W, the local eigenstates $\{|m_i\rangle_{\boldsymbol{B}}\}_{i \in \{+,0,-\}}$ have to be computed.

The magnetic field $\boldsymbol{B}(\boldsymbol{r})$ can be parametrized in the following way

$$\boldsymbol{B}(\boldsymbol{r}) = B \begin{pmatrix} \sin\vartheta \cos\varphi \\ \sin\vartheta \sin\varphi \\ \cos\vartheta \end{pmatrix} \tag{7.8}$$

Here, φ and ϑ are position-dependent, they can be expressed using the angles of the spherical coordinates ϕ and θ without being equal to them as depicted

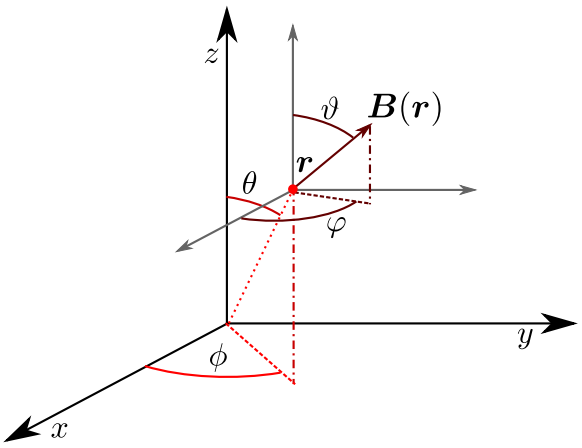

Figure 7.1: Parametrization of the magnetic field $\boldsymbol{B}(\boldsymbol{r})$ by the angles ϑ and φ, along with the angles of the spherical coordinates θ and ϕ.

in figure 7.1. In this situation, the local eigenstates for the internal degree of freedom in the $m_z = -1, 0, +1$ basis (corresponding to a quantization axis of the magnetic moment along the z-axis) read

$$|m_+\rangle_{\boldsymbol{B}} = \frac{1}{2}\begin{pmatrix} 1+\cos\vartheta \\ \sqrt{2}e^{i\varphi}\sin\vartheta \\ e^{2i\varphi}(1-\cos\vartheta) \end{pmatrix} \tag{7.9}$$

$$|m_0\rangle_{\boldsymbol{B}} = \frac{1}{2}\begin{pmatrix} -\sqrt{2}e^{-i\varphi}\sin\vartheta \\ 2\cos\vartheta \\ \sqrt{2}e^{i\varphi}\sin\vartheta \end{pmatrix} \tag{7.10}$$

$$|m_-\rangle_{\boldsymbol{B}} = \frac{1}{2}\begin{pmatrix} e^{-2i\varphi}(1-\cos\vartheta) \\ -\sqrt{2}e^{-i\varphi}\sin\vartheta \\ 1+\cos\vartheta \end{pmatrix} \tag{7.11}$$

Replacing 7.9 in 7.5 we obtain the expression for the vector potential

$$\boldsymbol{A}(\boldsymbol{r}) = \hbar\,(\cos\vartheta - 1)\,\boldsymbol{\nabla}\varphi \tag{7.12}$$

Note that this quantity is gauge dependent. If all the local eigenstates are multiplied by a space-dependent phase $e^{-if(\boldsymbol{r})}$ (where $\boldsymbol{r}$ is the position of the atom), the vector potential becomes:

$$\boldsymbol{A} = \hbar\boldsymbol{\nabla}f + i\hbar\langle m_F|_{\boldsymbol{B}}\boldsymbol{\nabla}|m_F\rangle_{\boldsymbol{B}} \tag{7.13}$$

This does not change the physical observables of the system, which depend only on the effective magnetic field $\boldsymbol{\mathcal{B}}$. For instance, taking $f(\boldsymbol{r}) = -\varphi(\boldsymbol{r})$, the vector potential becomes in this gauge

$$\boldsymbol{A}(\boldsymbol{r}) = \hbar\cos\vartheta\boldsymbol{\nabla}\varphi \tag{7.14}$$

The scalar potential reads (using 7.6)

$$W(\boldsymbol{r}) = \frac{\hbar^2}{4M}\left(|\boldsymbol{\nabla}\vartheta|^2 + \sin^2\vartheta\,|\boldsymbol{\nabla}\varphi|^2\right) \tag{7.15}$$

7.1.3 *Higher order spins*

The effective vector potential for an atom in a manifold which is different from $F = 1$ is actually similar to 7.12. The local eigenstate of the system is indeed obtained starting from an eigenvector of the magnetic Hamiltonian for $\boldsymbol{B} = B\boldsymbol{e}_z$, $|m_z\rangle$, rotated first around the axis y by an angle ϑ then around the axis z with an angle φ

$$|m_i\rangle_{\boldsymbol{B}} = \hat{\mathcal{R}}_{\boldsymbol{e}_z}(\varphi)\hat{\mathcal{R}}_{\boldsymbol{e}_y}(\vartheta)|m_z\rangle \tag{7.16}$$

Using the standard expression for the rotation matrices

$$\hat{\mathcal{R}}_{\boldsymbol{u}}(\alpha) = e^{-\frac{i}{\hbar}\alpha\hat{\boldsymbol{F}}\cdot\boldsymbol{u}} \tag{7.17}$$

we obtain for the gradient:

$$\begin{aligned}\boldsymbol{\nabla}|m_+\rangle_{\boldsymbol{B}} = -\boldsymbol{\nabla}\varphi\frac{i}{\hbar}\left[\hat{\boldsymbol{F}}\cdot\boldsymbol{e}_z\right]\hat{\mathcal{R}}_{\boldsymbol{e}_z}(\varphi)\hat{\mathcal{R}}_{\boldsymbol{e}_y}(\vartheta)|m_z\rangle \\ -\boldsymbol{\nabla}\vartheta\frac{i}{\hbar}\hat{\mathcal{R}}_{\boldsymbol{e}_z}(\varphi)\left[\hat{\boldsymbol{F}}\cdot\boldsymbol{e}_y\right]\hat{\mathcal{R}}_{\boldsymbol{e}_y}(\vartheta)|m_z\rangle\end{aligned} \tag{7.18}$$

After the first rotation around the y-axis, the spin vector is still orthogonal to $\boldsymbol{e}_y$ so the second term in 7.18 vanishes, and the scalar product with the vector $\boldsymbol{e}_z$ yields $m_z\hbar\cos\vartheta$ after the two rotations. Hence, the vector potential for the wave function projected on the local eigenstate $|m_i\rangle_{\boldsymbol{B}}$ is

$$\boxed{\boldsymbol{A} = m\hbar\cos\vartheta\boldsymbol{\nabla}\varphi} \tag{7.19}$$

with $m \in [\![-F, F]\!]$, which is equivalent to 7.14. By working in the $F = 2$ manifold or by considering another atomic species whose hyperfine manifold are characterized by a higher number (for example $F = 8$ for dysprosium 164 [31]), the amplitude of the vector potential can be enhanced.

7.1.4 *Case of the quadrupole field*

The magnetic field created by two opposing coils with current flowing in opposite directions is called a quadrupole field. Due to the symmetry of the system, there is a zero of the magnetic field on the central symmetry point of the current distribution. This type of magnetic field is very important from an experimental point of view since the MOT stage and the magnetic trapping stage use this current configuration. Hence, such coils are readily available on our experimental set-up, which makes it especially relevant for direct implementation of an experimental scheme using a quadrupole configuration.

The atoms are located close to the zero of the magnetic field where this field can be expanded to the first order as

$$\boldsymbol{B}(\boldsymbol{r}) = b'\begin{pmatrix} -x/2 \\ -y/2 \\ z \end{pmatrix} \tag{7.20}$$

where b' is the value of the magnetic field gradient (up to 240 G/cm on our new set-up) and where the factors $1/2$ ensure that the divergence of $\boldsymbol{B}$ is zero. Calling $R = \sqrt{x^2 + y^2}$, we get the following expression to define B, ϑ and φ:

$$B = b' \sqrt{z^2 + R^2/4} \tag{7.21}$$

$$\cos\vartheta = \frac{z}{\sqrt{z^2 + R^2/4}}, \qquad \sin\vartheta = \frac{-R/2}{\sqrt{z^2 + R^2/4}} \tag{7.22}$$

$$x = -R\cos\varphi, \qquad y = -R\sin\varphi \tag{7.23}$$

We can relate the angles ϑ and φ to the angles of the spherical coordinates θ and ϕ:

$$\varphi = \phi + \pi \tag{7.24}$$

$$\cos\vartheta = \frac{2\cos\theta}{\sqrt{1 + 3\cos^2\theta}} \tag{7.25}$$

Using the expression of the gradient and the standard basis vectors in spherical coordinates, we obtain

$$\boldsymbol{\nabla}\vartheta = \frac{2\sin\theta}{R\left(1 + 3\cos^2\theta\right)}\boldsymbol{e_\theta} \tag{7.26}$$

$$\boldsymbol{\nabla}\varphi = \frac{1}{R}\boldsymbol{e_\phi} \tag{7.27}$$

The vector potential of 7.12 now reads:

$$\boxed{\boldsymbol{A} = \frac{\hbar\left(\cos\vartheta - 1\right)}{R}\boldsymbol{e_\phi}} \tag{7.28}$$

and the scalar potential

$$W = \frac{\hbar^2}{4MR^2}\,\sin^2\vartheta\left(2 + 3\sin^2\vartheta\right) \tag{7.29}$$

In the case of a ring of atoms centred on the revolution axis of the quadrupole field at the height z_r and of radius R, the vector and scalar potentials are constant in modulus and the vector potential is oriented along the azimuthal direction.

7.1.5 *Higher order fields*

The quadrupole field is readily available on an experiment, which makes it natural to use it for further experiments. However, it is also possible to consider other magnetic field configurations. A family of magnetic fields of interest are the multipolar fields. These configurations use the fact that a field $\boldsymbol{B} = (B_x, B_y, B_z)$ with equation

$$B_z = \text{constant} \tag{7.30}$$

$$B_x + iB_y = b^{(n)}\left(x + iy\right)^n \tag{7.31}$$

is a solution of the Maxwell equations for $n \in \mathbb{N}$. Similarly to what has been done in 7.1.4, the field can be parametrized by two angles ϑ and φ and a scalar B as in 7.8. These two angles can in turn be expressed as a function of the spherical coordinates r, θ and ϕ :

$$\varphi = n\phi \tag{7.32}$$

$$\cos\vartheta = \frac{B_z}{\sqrt{B_z^2 + \left(b^{(n)}\right)^2 r^{2n} \sin^{2n}\theta}} \tag{7.33}$$

Replacing the expression 7.32 in 7.12, we obtain

$$\boldsymbol{A} = \frac{\hbar n\left(\cos\vartheta - 1\right)}{R}\boldsymbol{e}_\phi \tag{7.34}$$

where the amplitude of the vector potential has been enhanced by a factor n.

7.1.6 *Artificial magnetic field*

It is interesting to compute the effective magnetic field generated by the gauge potential 7.28. For this, we use the expression of the rotational operator in the spherical basis $\left(\boldsymbol{e}_\rho, \boldsymbol{e}_\vartheta, \boldsymbol{e}_\varphi\right)$ such that $\boldsymbol{e}_\rho = \boldsymbol{B}/\left|\boldsymbol{B}\right|$, $\boldsymbol{e}_\varphi = -\sin\varphi\,\boldsymbol{e}_x + \cos\varphi\,\boldsymbol{e}_y$ and $\boldsymbol{e}_\vartheta = \boldsymbol{e}_\varphi \times \boldsymbol{e}_\rho$ and find

$$\boxed{\boldsymbol{\mathcal{B}} = \boldsymbol{\nabla} \times \boldsymbol{A} = -\frac{\hbar}{\rho^2}\boldsymbol{e}_\rho} \tag{7.35}$$

where $\rho = \sqrt{z^2 + R^2/4}$. This effective magnetic field is close to the Dirac magnetic monopole where $\boldsymbol{B} = \alpha/r^2\boldsymbol{e}_r$; this mapping has been studied recently in a cloud of ultracold atoms in [229, 230]. However, the coordinate system used in 7.35 is not that of the spherical coordinates of $\boldsymbol{r}$.

7.2 CONDENSATION IN PRESENCE OF AN ARTIFICIAL GAUGE FIELD

7.2.1 *Computing the ground state*

Similarly to what has been done in mesoscopic physics [219–221], it would be interesting to probe the change of the ground state of the system as the magnitude of the artificial magnetic field is increased, leading to ground states bearing a non-zero supercurrent. Knowing the expression of the artificial gauge potential 7.28, we will now compute the ground state of an atom in a ring to look for configurations where it has a non zero angular momentum.

Consider a particle in a ring potential centred on the z axis characterized by its size (R) and height (given by the angle θ). We consider in the following only the azimuthal degree of freedom ϕ (which would be exact for a strongly confining ring potential). The momentum operator of the particle is

$$\hat{p}_\phi = \frac{\hbar}{i}\frac{1}{R}\partial_\phi \tag{7.36}$$

so the Hamiltonian describing the motion of the particle that adiabatically follows the local ground state for the spin state is

$$\hat{H} = \frac{\hbar^2}{2MR^2}\left(i\partial_\phi + \cos\vartheta - 1\right)^2 \tag{7.37}$$

The eigenfunctions of this Hamiltonian are scalar functions ψ of the azimuthal coordinate ϕ with periodic boundary conditions $\psi(\phi + 2\pi) = \psi(\phi)$. They have the following form:

$$\psi(\phi) = \frac{1}{\sqrt{2\pi}} e^{i\ell\phi}, \qquad \ell \in \mathbb{Z} \tag{7.38}$$

The corresponding energies are

$$\boxed{E_\ell = \frac{\hbar^2}{2MR^2}\left(\ell - \cos\vartheta + 1\right)^2} \tag{7.39}$$

which are depicted in figure 7.2.

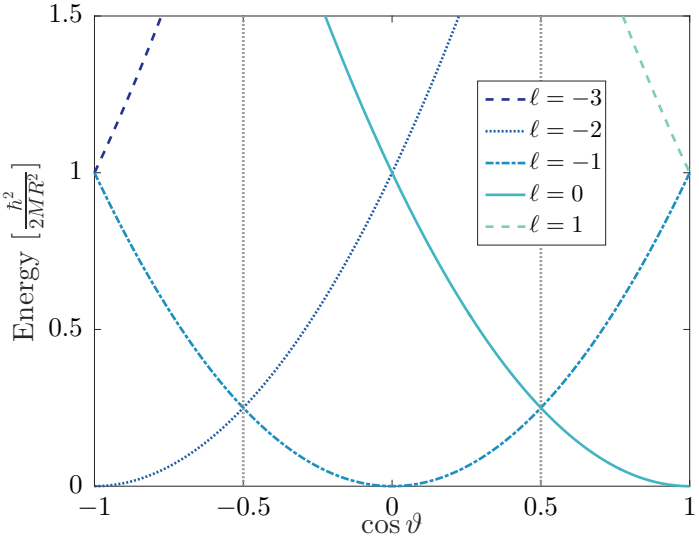

Figure 7.2: Energies of the eigenfunctions with $\ell = -3, -2, -1, 0$ and 1 as a function of the height characterized by $\cos\vartheta$. The dotted lines represent the critical height at which the angular momentum of the ground state changes.

The number of angular momentum quanta (corresponding to the charge of the supercurrent) of the ground state wave function depends on the height of the ring:

1. if $\cos\vartheta < -1/2$, the ground state is in the $\ell = -2$ state
2. if $|\cos\vartheta| < 1/2$, the ground state is in the $\ell = -1$ state
3. if $\cos\vartheta > 1/2$, the ground state is in the $\ell = 0$ state

The presence of a gauge field can thus lead atoms in a ring to condense in a state of non zero angular momentum. Unlike experiments which were performed in solid-state systems [219–221], the magnitude of the artificial magnetic field is limited; hence we cannot access high number of angular momentum quanta.

The angular momentum state in which the atoms condense depends on the height of the ring on the rotation symmetry axis of the magnetic field. The derivative of the energy of the ground state with respect to the height of the ring is discontinuous for $\cos\vartheta = \pm 1/2$ i. e.

$$\boxed{z_c = \pm\frac{R}{2\sqrt{3}}} \tag{7.40}$$

According to Ehrenfest's classification of phase transitions, since the derivative of the energy is discontinuous at $\pm z_c$, this could be considered as a first-order phase transition.

7.2.2 *Higher order spins or multipolar fields*

As was shown in 7.19 and 7.34, the vector potential can be enhanced by considering a particle with a high spin F and using a multipolar field of order n instead of a quadrupole field. The Hamiltonian 7.37 thus becomes

$$\hat{H} = \frac{\hbar^2}{2MR^2}\left(i\partial_\phi + nF\left(\cos\vartheta - 1\right)\right)^2 \tag{7.41}$$

and the corresponding energies

$$E_\ell = \frac{\hbar^2}{2MR^2}\left(\ell - nF\left(\cos\vartheta - 1\right)\right)^2 \tag{7.42}$$

The state in which the atoms can condense thus range from $\ell = -2nF$ to $\ell = 0$, with a transition for each height such that

$$\cos\vartheta = -1 - \frac{1}{2nF} + \frac{k}{nF}, \qquad k \in [\![1, 2nF]\!] \tag{7.43}$$

7.2.3 *Spinor and choice of gauge*

The total wave function of the atom in the ground state of the Hamiltonian 7.37 is obtained by reintroducing the spinor wave functions of section 7.1.2.

1. In case $\cos\vartheta < -1/2$:

$$\Psi(\phi) = \frac{1}{\sqrt{8\pi}}\begin{pmatrix} (1+\cos\vartheta)\, e^{-2i\phi} \\ -\sqrt{2}\sin\vartheta\, e^{-i\phi} \\ (1-\cos\vartheta) \end{pmatrix} \tag{7.44}$$

2. In case $|\cos\vartheta| < 1/2$:

$$\Psi(\phi) = \frac{1}{\sqrt{8\pi}}\begin{pmatrix} (1+\cos\vartheta)\, e^{-i\phi} \\ -\sqrt{2}\sin\vartheta \\ (1-\cos\vartheta)\, e^{i\phi} \end{pmatrix} \tag{7.45}$$

3. In case $\cos\vartheta > 1/2$:

$$\Psi(\phi) = \frac{1}{\sqrt{8\pi}} \begin{pmatrix} 1+\cos\vartheta \\ -\sqrt{2}\sin\vartheta\, e^{i\phi} \\ (1-\cos\vartheta)\, e^{2i\phi} \end{pmatrix} \tag{7.46}$$

These expression are independent of the gauge choice (up to a phase factor that is independent of the position); a different gauge would have changed the expression of the spinor 7.9, which would have in turn modified the vector potential 7.28, leading to the same spinor wavefunctions as here.

7.2.4 *Detecting the angular momentum*

After having cooled down a ring of atoms through the BEC transition at a given height given by the parameter $\cos\vartheta$, we would like to detect the height-dependent angular momentum.

7.2.4.1 *Projection of the spin on the $|m_z = +1\rangle$ state*

A first way to detect the phase winding picked up by the wavefunction is to perform a fast rotation of the spin. The spinor wavefunction can be rotated to be aligned with the z-axis.

1. In the case $\cos\vartheta > 1/2$:

$$\Psi_f(\phi) = \hat{\mathcal{R}}_{\boldsymbol{e}_\varphi}(-\vartheta)\,\Psi(\phi) = \frac{1}{\sqrt{2\pi}} \begin{pmatrix} 1 \\ 0 \\ 0 \end{pmatrix} \tag{7.47}$$

2. In the case $|\cos\vartheta| < 1/2$:

$$\Psi_f(\phi) = \hat{\mathcal{R}}_{\boldsymbol{e}_\varphi}(-\vartheta)\,\Psi(\phi) = \frac{e^{i\phi}}{\sqrt{2\pi}} \begin{pmatrix} 1 \\ 0 \\ 0 \end{pmatrix} \tag{7.48}$$

3. In the case $\cos\vartheta < -1/2$:

$$\Psi_f(\phi) = \hat{\mathcal{R}}_{\boldsymbol{e}_\varphi}(-\vartheta)\,\Psi(\phi) = \frac{e^{2i\phi}}{\sqrt{2\pi}} \begin{pmatrix} 1 \\ 0 \\ 0 \end{pmatrix} \tag{7.49}$$

After having performed the spin rotation, the angular momentum can be detected using standard techniques for rings of atoms. For instance, it is possible to lower the depth of the trap potential and to observe a hole in a ToF measurement whose width indicates the magnitude of the angular momentum ([51, 162, 232]).

The experimental feasability of condensing atoms in a ring will be discussed in 7.2.4.3. Let us here consider the feasability of the projection of the spin. It can be realized experimentally by ramping up a bias field on the z-axis $\boldsymbol{B}_{\text{bias}} = B_z(t)\boldsymbol{e}_z = \dot{B}_z\, t\, \boldsymbol{e}_z$.

On the one hand, if the ramp is slow compared to the Larmor frequency of the atoms, their spin will adiabatically follow the orientation of the magnetic field, realizing the situation described previously.

Assuming that the ramp of the bias magnetic field is such that $\vartheta = \pi/2$ at $t = 0$ yields:

$$\vartheta = \arctan\left(-\frac{B_\perp}{B_z}\right) = \arctan\left(-\frac{b'R}{2\dot{B}_z t}\right) \tag{7.50}$$

with $B_\perp = \sqrt{B_x^2 + B_y^2}$. The derivative of the angle is thus:

$$\frac{\mathrm{d}\vartheta}{\mathrm{d}t} = \frac{\omega}{1+\omega^2 t^2} \tag{7.51}$$

with $\omega = 2\dot{B}_z/(b'R)$. The Larmor frequency is

$$\omega_{\text{Larmor}} = \frac{g\mu_{\text{B}}}{\hbar}\frac{b'R}{2}\sqrt{1+\omega^2 t^2} \tag{7.52}$$

The condition $|\mathrm{d}\vartheta/\mathrm{d}t| \ll \omega_{\text{Larmor}}$ at $t = 0$ is thus equivalent to

$$\dot{B}_z \ll \frac{g\mu_{\text{B}}}{\hbar}\left(\frac{b'R}{2}\right)^2 \tag{7.53}$$

Typically, $R = 10\,\mu$m and the value of b' can range from 10 G/cm to 240 G/cm. For a gradient of 30 G/cm, we obtain $\dot{B}_z \ll 160$ G/s which does not put so much constraint on the experiment.

On the other hand, if the ramp is too slow, the phase winding created during condensation will decay because it will no longer be the true ground state of the Hamiltonian but a metastable state as the bias field is ramped up.

In a trap the roughness of which is small compared to the relevant energy scales for the cloud of atoms, the lifetime of a supercurrent can be on the order of seconds [162]. A linear ramp of the bias field can only reach the complete rotation of the spins asymptotically. Let us assume that it is sufficient to go from a situation where $\cos\vartheta = -0.99$ to a situtation where $\cos\vartheta = 0.99$. The duration of the ramp will be, using 7.50

$$t = \frac{b'R}{\dot{B}_z \cdot 0.14} \ll 1\,\text{second} \tag{7.54}$$

which gives the condition on $\dot{B}_z$

$$\dot{B}_z \gg b'R \cdot 7.1\,\text{Hz} \tag{7.55}$$

For a gradient of 30 G/cm and a radius of 10 μm, this means $\dot{B}_z \gg 200$ mG/s which is also easily fulfilled.

7.2.4.2 *Interference of two rings*

While projecting the spin in the $|m_z = +1\rangle$ state allows for the detection of a phase winding in the cloud, it relies on transforming the initial spinor into a metastable supercurrent state.

This is not necessary to observe the condensation in different states of angular momentum. Thanks to the flexibility of the DMD, we can project on the atoms two coplanar rings with radii $R_1 < R_2$ and place them at a distance z_R of the zero of the magnetic field as shown on figure 7.3. The difference of angular momentum in each ring can be probed via interference experiments such as those described in chapter 3 in subsection 3.3.2.

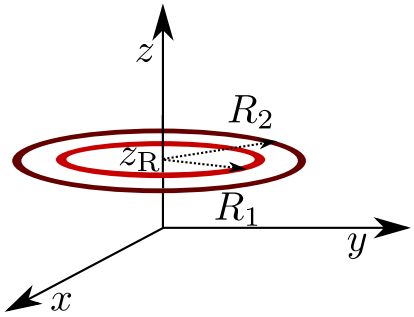

Figure 7.3: Schematic of the experiment to reveal the different states of angular momentum in which the atoms condense. Two coplanar rings of atoms with radii R_1 and R_2 are at a height z_R above the zero of the magnetic field.

For a ring of radius R, the critical heights at which the angular momentum changes are, as shown in 7.2.1

$$z_c = \pm \frac{R}{2\sqrt{3}} \tag{7.56}$$

In a two-ring setup, it is thus possible to distinguish several regimes for the difference of angular momentum $\Delta\ell = \ell_2 - \ell_1$ as a function of the height of the ring as depicted in figure 7.4. Let $z_c^{(1)}$ and $z_c^{(2)}$ be the critical heights for the two rings with radii R_1 and R_2 according to equation 7.56; in the case $z_R > 0$:

- if $z_R > z_c^{(1)}, z_c^{(2)}$, both rings condense in the $\ell = 0$ state, and the interference pattern will consist in concentric rings.
- if $z_c^{(2)} > z_R > z_c^{(1)}$, the inner ring will condense in the $\ell = 0$ state and the outer one in the $\ell = -1$ state; the interference pattern will be a spiral of charge minus one.
- if $z_R < z_c^{(1)}, z_c^{(2)}$, both rings condense in the $\ell = -1$ state, and the interference pattern will consist in concentric rings.

7.2.4.3 *Experimental requirements*

Experimentally, the magnetic field has to be controlled well enough to move the zero of the magnetic field in the relevant range. We assume that the ring

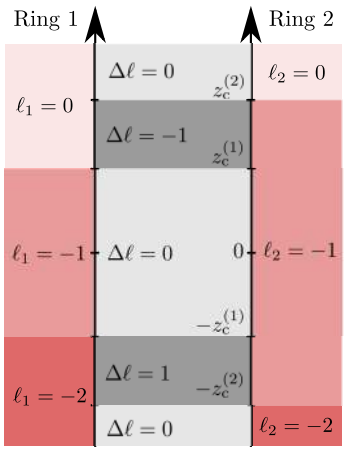

Figure 7.4: Angular momentum of the ground state of each ring as a function of position; regions where interference pattern will yield concentric fringes (resp. spiral fringes) are depicted in light (resp. dark) grey.

is originally produced at $z_R = 0$ and that a bias field B_z is added to move the position of the zero of the quadrupole. There are several conditions to be fulfilled so that the scheme is experimentally feasible:

1. The fluctuations of the ambient magnetic field B_{fluct} and the experimental resolution on the bias field B_{res} have to be small enough to allow the zero to be scanned in the $|\Delta\ell| = 1$ region of height $(R_2 - R_1)/(2\sqrt{3}) = \Delta R/(2\sqrt{3})$; they must also be smaller than the field generated by the quadrupole on the rings:

$$\delta B = \max\left(B_{\text{fluct}}, B_{\text{res}}\right) \ll \min\left(\frac{b'\Delta R}{2\sqrt{3}}, \frac{b'R_1}{2}\right) \tag{7.57}$$

2. The bias field has to be large enough to allow for a maximal displacement of the zero of the quadrupole field of $z_{\max} > R_2/(2\sqrt{3})$, typically on the order of 100 μm in the vertical direction

$$b'z_{\max} < B_{\max} \tag{7.58}$$

3. The speed of the atoms must be small enough so that the change in magnetic field orientation in time is small compared to the Larmor frequency (adiabatic approximation)

$$\dot{\varphi} = \frac{v}{R} \ll \omega_{\text{Larmor}} = \frac{g\mu_B b'R}{\hbar} \tag{7.59}$$

4. The fluctuations of the magnetic field or the residual field δB have to induce a potential difference between diametrically opposite points on the rings which is small with respect to the chemical potential of the gas μ. In the case where $\delta B \ll b'R_i/2$ (fulfillled thanks to equation 7.57), it reads:

$$2g\mu_B \sin\vartheta_i\, \delta B \ll \frac{\mu}{\hbar} \tag{7.60}$$

In our experimental setup, it is reasonable to consider radii such that $R_1 = 7\,\mu$m and $R_2 = 17\,\mu$m; the gradient that can be produced ranges from 0 to 240 G/cm; the bias coils provide a field up to 4.5 G with a resolution on the order of 10 mG, which is also the amplitude of the magnetic fluctuations close to the experiment (due to the magnetic field of the subway); the degenerate ring gases which were produced so far have an estimated chemical potential of $h \cdot 2\,$kHz.

For this typical experimental values, the condition 7.60 is the most stringent. At the critical height for the change of angular momentum, the chemical potential of the gas has to be large compared to $\sqrt{3} g \mu_B \delta B = h \cdot 12\,$kHz. This implies that the chemical potential of the gas has to be increased for example by compressing the accordion lattice as described in subsection 4.2.2 in order to become less sensitive to the residual magnetic fields (this will also increase the zero-point energy of the gas, and hence its relevant energy scale). It is also possible to improve the stability of the magnetic fields in the experiment using for example active compensation, which can reach residual magnetic fields of $300\,\mu$G according to [233]. This would lead to $\sqrt{3} g \mu_B \delta B = h \cdot 0.4\,$kHz, avoiding unwanted tilts of the ring potential. One can also resort to magnetic shielding (although this would be difficult given the current set-up).

The possible values for the quadrupole are bounded by equations 7.57 and 7.58. Under our typical parameters, the quadrupole field can take values

$$30\,\text{G/cm} < b' < 500\,\text{G/cm} \tag{7.61}$$

which is well within experimental reach.

Last, for a velocity of the atoms on the order of 1 mm/s (on the order of the thermal temperature and of the velocity field induced by the presence of the angular momentum), we obtain $\dot{\varphi} \simeq 2\pi \cdot 1.6\,$Hz. This means that for a ring of radius $R = 7\,\mu$m, the gradient has to be much larger than 2.3 mG/cm, also easily done on the experiment.

7.3 MEASURING BERRY'S PHASE

The problem of adiabatic following as described in section 7.1.1 can be phrased in many different ways. It was first brought forward by Berry in [234] who explained that if there is a way to split the degrees of freedom between a slow- and a rapidly-varying, a particle moving through a closed loop in the slowly-varying parameter space while adiabatically following the state of the fast degrees of freedom ends up in the same state that the one from which it originally started, up to a phase factor. This phase has two contributions, one which is dependent on the speed at which the atom travels through the closed loop in the slowly-varying degrees of freedom, called the dynamical phase, and another one which is independent of the speed. The latter contribution, which depends on the contour, is called the Berry phase, or geometrical phase. It is of great interest for ultracold atom physics due to the analogy that can be made with the Aharonov-Bohm phase of a charged particle moving in a magnetic field.

For a particle that adiabatically follows the state $|\chi(\boldsymbol{s})\rangle$, where $\boldsymbol{s}$ is the coordinates characterizing the slowly-varying degrees of freedom, the Berry phase accumulated on a closed contour $\mathcal{C}$ in the $\boldsymbol{s}$ parameter space is

$$\varphi_{\text{Berry}}(\mathcal{C}) = i\int_{\mathcal{C}}\langle\chi(\boldsymbol{s})|\boldsymbol{\nabla}_{\boldsymbol{s}}|\chi(\boldsymbol{s})\rangle\cdot\mathrm{d}\boldsymbol{s} \tag{7.62}$$

From this expression and from equation 7.5, there is a clear connection between the Berry phase and the vector potential $\boldsymbol{A}$:

$$\varphi_{\text{Berry}}(\mathcal{C}) = \frac{1}{\hbar}\int_{\mathcal{C}}\boldsymbol{A}(\boldsymbol{s})\cdot\mathrm{d}\boldsymbol{s} \tag{7.63}$$

For a spin in an m_F state aligned with a changing magnetic field, the Berry phase has another simple expression, as derived in [234]. While moving in the $\boldsymbol{s}$ parameter space, the spin takes orientations parametrized by two angles ϑ and φ that are the polar angles describing the orientation of the magnetic field (see figure 7.1). Using equation 7.19 and the Green theorem one gets

$$\varphi_{\text{Berry}}(\mathcal{C}) \quad = \quad -m_F\Omega(\mathcal{C}) \tag{7.64}$$

where $\Omega(\mathcal{C})$ is the solid angle enclosed by the tip of the unitary vector $\boldsymbol{B}/B$ as it moves along $\mathcal{C}$. This generalizes what was computed for a ring centered on the symmetry axis of a quadrupole magnetic field: an atom moving around a closed contour in a magnetic field picks up a phase which is m_F times the solid angle (computed with the angles ϑ and φ) under which it sees the zero of the magnetic field. The critical heights for condensation as computed in 7.2.1 correspond to heights where $\varphi_{\text{Berry}}(\mathcal{C}) = \pi \ [2\pi]$, i. e. heights at which the closest multiple of 2π changes.

Using our experimental setup, it would become possible to measure the Berry phase of a contour.

Consider a ring potential at a height characterized by ϑ. Using the dynamical possibilities of the DMD, a cloud of degenerate atoms can be produced on one side of the ring, e. g. around $\varphi = 0$, then released in the ring potential. The atoms will start to expand hydrodynamically, spreading symmetrically on the ring, and then interfere at the opposite point of the ring. The interference pattern is characterized by a phase φ_{interf} which indicates the amplitude of the interfering matter-wave at the point $\varphi = \pi$. If the situation is perfectly symmetric, the interference at $\varphi = \pi$ is constructive: $\varphi_{\text{interf}} = 0$. Assume now that the quadrupole field is ramped up just before the atoms are released in the ring potential. The quadrupole field might induce some energy shifts but as long as the ring is centered, these effects will cancel out in the constructive interference at $\varphi = \pi$. However, due to the adiabatic following of the ground state, the atoms going in the $\varphi > 0$ path will pick up a geometrical phase opposite to that picked by the atoms going along the $\varphi < 0$ path. The amplitude of the interference at $\varphi = \pi$ will thus give a direct measurement of the Berry phase

$$\varphi_{\text{interf}} = \frac{R}{\hbar}\left(\underbrace{\int_0^{\pi}|\boldsymbol{A}(\varphi)|\,\mathrm{d}\varphi}_{\text{atoms going in }\varphi>0} - \underbrace{\int_0^{-\pi}|\boldsymbol{A}(\varphi)|\,\mathrm{d}\varphi}_{\text{atoms going in }\varphi<0}\right) = \varphi_{\text{Berry}}(\mathcal{C}=\text{ring}) \tag{7.65}$$

An asymmetry in the positioning of the ring with respect to the symmetry axis of the magnetic field will result in a shift of the interference pattern which is due to (i) the Berry phase (ii) the dynamical phase caused by slight energy shifts between the two paths. The second contribution to the phase shift will be linear with the magnitude of the gradient b'. Thus, the limit for $b' \to 0$ of the phase shift of the interference pattern will lead to the value of the Berry phase.

7.4 A VORTEX PUMP

7.4.1 *Basic idea*

So far, we have considered experimental schemes during which the zero of the quadrupole field stays at the same position – except for the projection of the spinor of section 7.2.4.1, which is serving detection purposes. However, building on this detection scheme and on the imprinting of topological vortices described in [228], we can use our system to pump quanta of angular momentum in a ring of atoms.

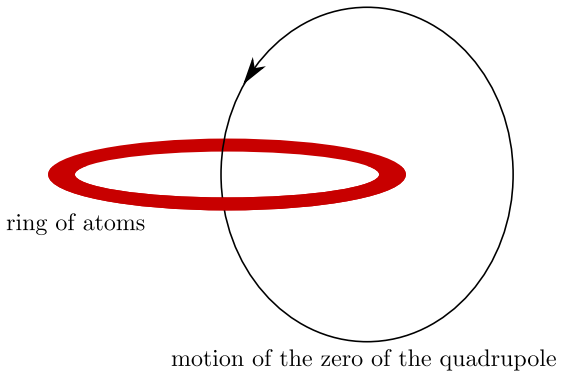

Figure 7.5: Basic idea of the vortex pump. The zero of the quadrupole field is moved on a periodic trajectory that pierces once through the ring. According to the previous calculations, this motion leads to a decrease of ℓ by 2 at each cycle.

The basic idea of the "vortex pump" can be understood in terms of the Berry phase described in the previous section. Starting with a zero of the magnetic field infinitely far above the ring of atoms, the Berry phase is going to be 0. As the zero is moved down, closer to the ring, the solid angle under which the ring sees the zero will increase. As it passes in the plane of the ring, there are two possibilities:

1. the zero goes through the ring, inducing a solid angle of 2π
2. the zero goes outside of the ring, inducing a solid angle of 0

As the zero is moved further down, the solid angle goes to zero again; in case 1, the total phase winding picked up by the atoms is -4π while in case 2 it is 0; in both cases, the spins now point toward the same direction. In the previous section we saw that a change of Berry phase of -2π is equivalent to changing the number of angular momentum quanta from ℓ to $\ell - 1$. Hence, in case 1, if

the adiabatic approximation is valid, the atoms in the ring will go from an ℓ state to an $\ell - 2$ state; in case 2 the ℓ quantum number will stay the same. It is possible to repeat a cycle where the zero of the magnetic field is moved from a position well above the ring of atoms down through it, and then back to its original position avoiding going through the ring, as illustrated in figure 7.5. Each cycle leads to an increase of angular momentum of -2.

7.4.2 *Topological interpretation of the vortex pump*

7.4.2.1 *Topology of mappings from a torus to a sphere*

We would now like to give a topological interpretation of the vortex pump. In mathematics, topology studies properties of objects which are not affected by continuous deformations of those objects. An emblematic example is that of closed, orientable surfaces in $\mathbb{R}^3$. These surfaces can be classified according to their genus which is the number of holes they have: for instance, a sphere has genus 0 while a torus has genus 1 and this number stays the same under continuous deformations of those surfaces (no "gluing" or "cutting" allowed).

It is very interesting in physics to produce topological excitations of matter, meaning states of matters that cannot be brought back to the ground state by continuous transformations, because these excitations are robust to perturbations which usually induce continuous deformations of the initial state. In the case of flux lattices, optical lattices which are non topologically trivial can be realized to produce artificial magnetic fields of large amplitude on clouds of ultracold atoms [222, 223, 235].

Topological properties are usually characterized by a set of integer numbers. In some cases, these integers can be computed from geometrical properties of the objects. In the case of orientable surfaces in $\mathbb{R}^3$ without boundary, the genus can be computed using the Gauss-Bonnet theorem: the integral of the curvature of the surface divided by 2π is an integer equals to two minus the genus of the surface.

In the following, we will focus on characterizing the topological properties of functions that associate to each point of a torus $\mathcal{T}$ a point on a sphere $\mathcal{S}$

$$\begin{aligned} f : \quad \mathcal{T} \quad &\mapsto \mathcal{S} \\ M(\alpha, \phi) \quad &\to P(\vartheta(\alpha, \phi), \varphi(\alpha, \phi)) \end{aligned} \tag{7.66}$$

where (ϕ, α) are two angles going from 0 to 2π that represent the point M on $\mathcal{T}$ and (ϑ, φ) the two angles of the spherical coordinates representing the point P on $\mathcal{S}$. Characterizing those functions from a topological point of view is very relevant in physics, for example to understand flux lattices. The properties of a lattice are well described in reciprocal space in the Brillouin zone which, for a square lattice, is also a square with periodic boundary conditions: it is thus equivalent to a torus. In addition, these non topologically trivial lattices usually couple several atomic internal states. In the case where two atomic states are available, they can be mapped onto a spin 1/2 system, represented by a point on the Bloch sphere. Hence knowing the topological properties of the lattice means knowing the topological properties of the mapping from the Brillouin

zone (represented by a torus) onto the atomic state (represented by a point on a sphere).

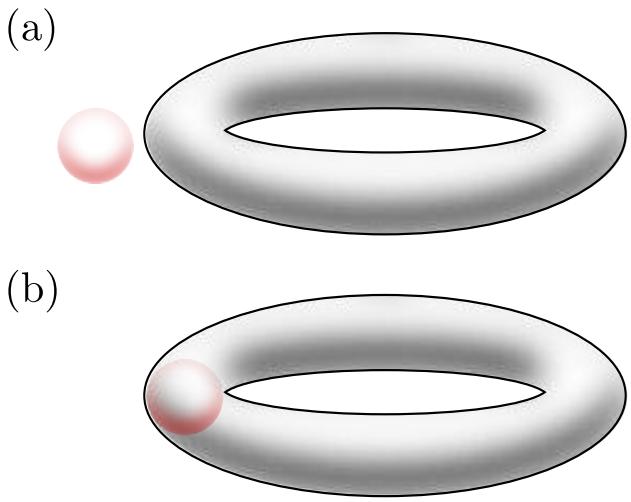

Figure 7.6: Two possible mappings of the torus onto the sphere. In figure (a), the Chern number is 0, while it is 1 on figure (b)

Functions $f : \mathcal{T} \mapsto \mathcal{S}$ are characterized by an integer number called the Chern number. Two functions with the same Chern number can be continuously transformed into each other. In a schematic way, the Chern number represents the number of times $f(\mathcal{T})$ wraps around the sphere. Let us illustrate this using the functions f_a and f_b defined thanks to figure 7.6. Each function associates a point of the sphere to a point of the torus in the following way:

- Pick a point of the torus M defined by the coordinates (ϕ_M, α_M)
- Draw the line starting at the center of the sphere C_i $(i = a, b)$ passing by M. This line will intersect the sphere once at P which has the coordinates (ϑ_P, φ_P)
- Define the function

$$\begin{array}{rccc} f_i : & \mathcal{T} & \mapsto \mathcal{S} \\ & (\phi_M, \alpha_M) & \to (\vartheta_P, \varphi_P) \end{array} \tag{7.67}$$

In case a), the center of the sphere C_a is outside of the torus and $f(\mathcal{T})$ only represents a small part of the sphere: the Chern number of f_a is 0. In case b), the center of the sphere C_b is inside the torus and the torus wraps once around the sphere: the Chern number of f_b is 1.

Just as the genus of a closed orientable surface in $\mathbb{R}^3$ can be computed from its curvature thanks to the Gauss-Bonnet theorem, the Chern number of a function f can be computed by integrating the area spanned by the elementary vectors $\partial_\phi f$ and $\partial_\alpha f$ over the torus, which is defined as follows:

$$\Omega_f(\phi, \alpha) = \left(\partial_\phi f \times \partial_\alpha f\right) \cdot f = \partial_\alpha \varphi \partial_\phi \cos\vartheta - \partial_\phi \varphi \partial_\alpha \cos\vartheta \tag{7.68}$$

The integral of Ω_f over the torus is zero provided that:

- the integrated functions $\varphi(\phi, \alpha)$ and $\cos\vartheta(\phi, \alpha)$ obey periodic boundary conditions
- the integrated functions have no singularity.

While the first condition is always fulfilled on a torus, the second is not: the singularities will have a non-zero contribution to the integral and

$$\iint \Omega_f(\phi, \alpha)\, \mathrm{d}\phi\, \mathrm{d}\alpha = 4\pi\nu_f \tag{7.69}$$

where ν_f is the Chern number of f (related to the number and nature of singularities).

The Chern number can also be defined for any function $h = g \circ f$ such that f is a function like those defined in equation 7.66 and g is a function from the sphere to the unit vectors of $\mathbb{C}^n$

$$\begin{array}{rccc} g: & \mathcal{S}(\mathbb{R}^3) & \mapsto & \mathcal{S}(\mathbb{C}^n) \\ & (\cos\vartheta, \varphi) & \to & |m\rangle \end{array} \tag{7.70}$$

as the integral

$$\nu_h = \frac{1}{2\pi} \iint \Omega(\phi, \alpha)\, \mathrm{d}\phi\, \mathrm{d}\alpha \tag{7.71}$$

where α has been rescaled to vary from 0 to 1 (for example redefining α by $\cos\alpha$) and where the Berry curvature is defined as:

$$\Omega(\phi, \alpha) = i\left(\langle\partial_\phi m|\partial_\alpha m\rangle - \langle\partial_\alpha m|\partial_\phi m\rangle\right) \tag{7.72}$$

7.4.2.2 *Chern number of the vortex pump*

Given a magnetic field configuration, there are three possible states in the $F = 1$ manifold that the atoms can follow adiabatically, corresponding to the states $|m = -1, 0, 1\rangle_{\boldsymbol{B}}$ described in 7.1.2. Choosing for example $|m = 1\rangle_{\boldsymbol{B}}$ defines a vector field on the ring. If the magnetic field is time-dependent, so is the vector field. It can be repesented as a vector field on a cylinder where the height of the cylinder represents the time, as depicted in figure 7.7 (a). In the case of a periodic variation of the magnetic field, the time axis can be wrapped on itself; the local ground state can be represented as a vector field on a torus, as depicted in figure 7.7 (b). We are therefore brought back to the problem of the previous subsection of a mapping of a torus on a sphere in the framework of periodic Hamiltonians whose topological properties have already been the object of studies [76, 236].

The coordinates on the torus are $\phi \in [0, 2\pi[$ the position on the ring and $\alpha \equiv \omega t/(2\pi)$ modulo 1 the time. To each point on the torus corresponds a point on a sphere, which is the orientation of the spin, characterized by two angles ϑ and φ as defined previously.

The idea of the vortex pump corresponds to the following mapping (up to a continuous function of α and ϕ):

$$\cos\vartheta = \begin{cases} -(1 - 4\alpha) & \text{for } \alpha \in [0, 1/2] \\ -(4\alpha - 3) & \text{for } \alpha \in [1/2, 1] \end{cases} \tag{7.73}$$

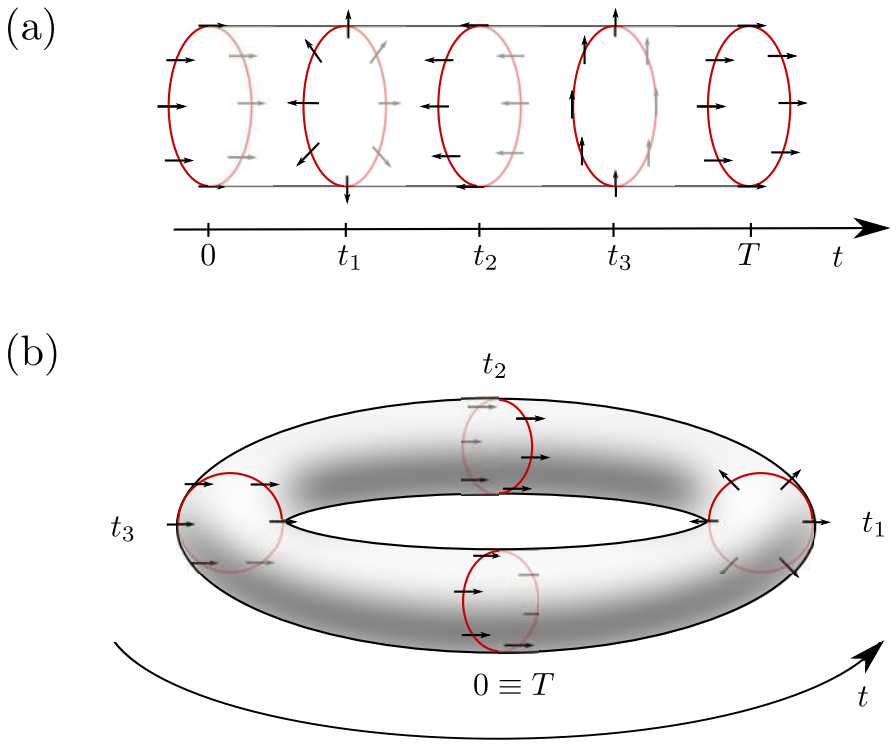

Figure 7.7: (a) Orientation of the spins on the ring as a function of time. At $t = 0$, all the atoms point up. The zero of the quadrupole is moved up through the cloud between 0 and t_2. At $t = t_1$, the zero lies exactly at the center of the ring. Then, from t_2 to T, the quadrupole is switched off and a uniform bias field rotates the spins (equivalent to the zero of the quadrupole being infinitely far). At $t = t_3$, the bias field is directed along the x axis. At $t = T$, the spins are back to their original position. (b) Having a phenomenon perodic in time, the figure (a) can be wrapped around, thus becoming a torus. The study of the vortex pump – i. e. the configuration of the spins on a ring in a time-periodic setup – thus becomes equivalent to the study of a vector field on a torus which is an emblematic problem in topology.

$$\varphi = \begin{cases} \pi + \phi & \text{for } \alpha \in [0, 1/2] \\ 0 & \text{for } \alpha \in [1/2, 1] \end{cases} \tag{7.74}$$

Given this mapping, we compute the Berry curvature $\Omega(\phi, \alpha)$ for an atom following the $|m = -1, 0, 1\rangle_{\boldsymbol{B}}$ states, whose integral yields the Chern number:

$$\Omega(\phi, \alpha) = i \left(\langle \partial_\phi m_i | \partial_\alpha m_i \rangle_{\boldsymbol{B}} - \langle \partial_\alpha m_i | \partial_\phi m_i \rangle_{\boldsymbol{B}} \right) \tag{7.75}$$

It gives for $i = -1, 0, 1$ and for $\alpha \in [0, 1/2]$:

$$\Omega_{+1}(\phi, \alpha) = -8\,(1 - 2\alpha) \tag{7.76}$$
$$\Omega_{0}(\phi, \alpha) = 0 \tag{7.77}$$
$$\Omega_{-1}(\phi, \alpha) = 8\,(1 - 2\alpha) \tag{7.78}$$

and $\Omega_i(\phi, \alpha) = 0$ for $\alpha \in [1/2, 1]$. The Chern number can now be calculated using the formula 7.71 which yields

$$\nu_1 = -2 \tag{7.79}$$
$$\nu_0 = 0 \tag{7.80}$$
$$\nu_{-1} = 2 \tag{7.81}$$

This corresponds to the increase or decrease of two in the number of angular momentum quanta depending on the local eigenstates that the atoms are following.

7.4.2.3 *The vortex pump as a topological charge pump*

By considering the Hamiltonian of the system in momentum space, it is possible to interpret the vortex pump as a charge pump. The Hamiltonian 7.1 can be written with ϕ as the only degree of freedom; a convenient basis to express it is the set $\{|\ell, m\rangle\}_{\ell\in\mathbb{Z},\, m\in\{-1,0,1\}}$ with ℓ the integer characterizing the orbital angular momentum as in 7.38, and m being the projection of the spin on the z axis for a spin one particle.

In this basis, with a quadrupole field of amplitude $b' = -\hbar\omega_{\mathrm{L}}/(g\mu_{\mathrm{B}}R)$ at $z = 0$ and two bias fields, one along the x axis $B_x = \hbar\omega_x/(g\mu_{\mathrm{B}})$ and one along the z axis $B_z = \hbar\omega_z/(g\mu_{\mathrm{B}})$, the Hamiltonian reads:

$$\begin{aligned}\hat{H} &= \frac{\hbar^2}{2MR^2}\sum_{\ell,m}\ell^2|\ell,m\rangle\langle\ell,m| \\ &+ \frac{\hbar\omega_{\mathrm{L}}}{2}\sum_{\ell,m}(|\ell,m\rangle\langle\ell+1,m-1| + \text{h.c.}) \\ &+ \hbar\omega_z\sum_{\ell}(|\ell,1\rangle\langle\ell,1| - |\ell,-1\rangle\langle\ell,-1|) \\ &+ \frac{\hbar\omega_x}{\sqrt{2}}\sum_{\ell}(|\ell,1\rangle\langle\ell,0| + |\ell,0\rangle\langle\ell,-1| + \text{h.c.})\end{aligned} \tag{7.82}$$

The second line comes from the spatial dependence of the quadrupole field at $z = 0$: the magnetic Hamiltonian is

$$-g\mu_{\mathrm{B}}\hat{\boldsymbol{F}}\cdot\boldsymbol{B}(\boldsymbol{r}) = g\mu_{\mathrm{B}}\frac{b'}{2}\left(x\hat{F}_x + y\hat{F}_y\right) = g\mu_{\mathrm{B}}\frac{b'R}{4}\left(e^{i\phi}\hat{F}_- + e^{-i\phi}\hat{F}_+\right) \tag{7.83}$$

The energy scale of the kinetic term for our typical experimental parameter $\hbar^2/(2MR^2) = h\cdot 0.6\,\mathrm{Hz}$ is much smaller than the other energy scales of the system $\hbar\omega_i$ (for the quadrupole field at $30\,\mathrm{G/cm}$ and a radius of $10\,\mu\mathrm{m}$, $\hbar\omega_{\mathrm{L}} = h\cdot 21\,\mathrm{kHz}$). If we neglect it, the remaining Hamiltonian can be seen as a one-dimension tight-binding Hamiltonian where the unit cells are labelled by the integer ℓ and where each unit cell has three sites labelled m. The energy scales $\hbar\omega_{\mathrm{L}}$ and $\hbar\omega_x$ correspond to tunnelling terms between the sites, while the energy $\hbar\omega_z$ corresponds to an energy offset between the three sites in one unit cell, as illustrated in figure 7.8.

The vortex pump consists in four steps, starting for example with a negative z bias, a quadrupole on and in the $|\ell = 0, m = -1\rangle$ state (corresponding

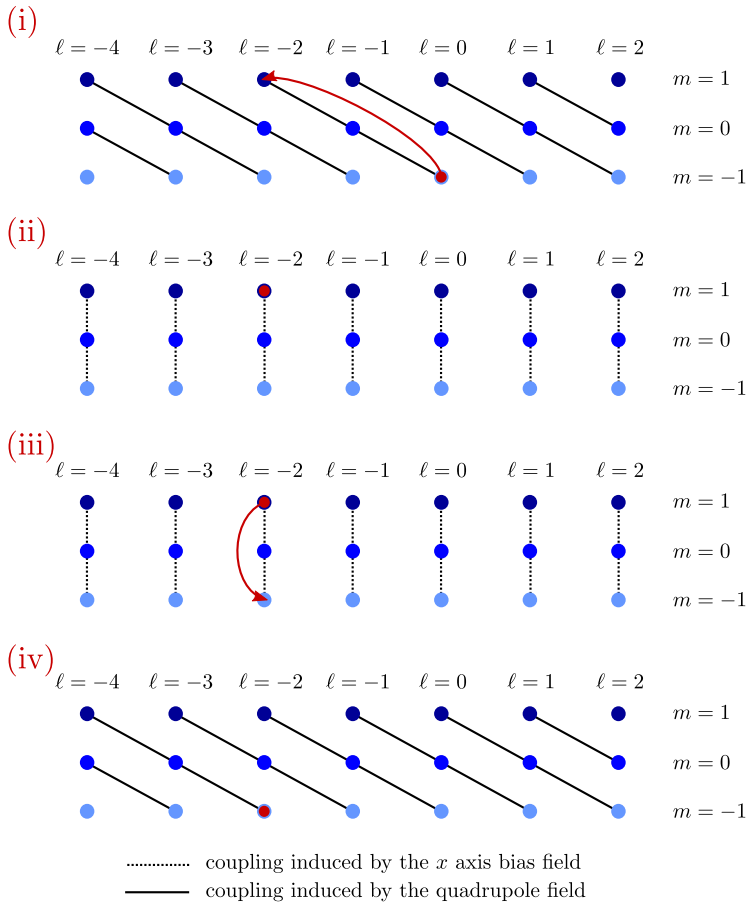

Figure 7.8: Tight binding model in the basis of the $\{|\ell, m\rangle\}_{\ell\in\mathbb{Z}, m\in\{-1,0,1\}}$ states. The m states are offset in energy due to the bias field on the z axis. Coupling between the m states is provided by the x bias field and tunnelling between different ℓ states is provided by the quadrupole. The description of steps (i) to (iv) are given in the text.

to the $|m_+\rangle_{\boldsymbol{B}}$ state described previously): (i) inverting the bias in z with the quadrupole on, thus moving the initial state to the $|\ell = -2, m = 1\rangle$ state; (ii) switching off the quadrupole (dark solid lines) and turning on the x bias field (dotted lines); (iii) inverting the z bias with the x bias field on, yielding the state $|\ell = -2, m = -1\rangle$; (iv) switching off the x bias field and turning on the quadrupole to come back to the initial situation (see figure 7.8).

Thus, a periodic Hamiltonian in this lattice configuration will induce a "charge" transport (with ℓ being the charge) of two lattice sites, which is similar to recent experiments [77, 237] implementing the original idea of the Thouless pump [76]. The Chern number can be computed with the same formula as in equation 7.71, which can in this context be interpreted as the Chern number of the bands of this lattice as in [238] (here the equivalent of the quasi-momentum is the phase ϕ).

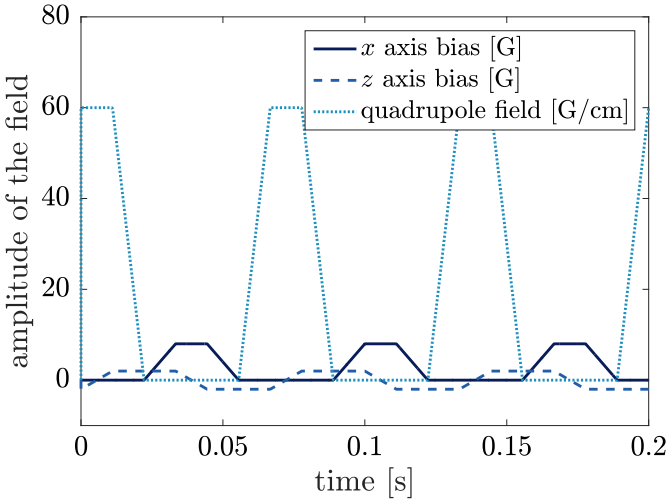

Figure 7.9: The Hamiltonian 7.82 is periodic with a frequency of $\omega = 2\pi \cdot 15\,\mathrm{Hz}$; all fields vary in a piecewise linear manner with $b'_{\max} = 60\,\mathrm{G/cm}$, $B_{x,\max} = 8\,\mathrm{G}$, $B_{z,\max} = 2\,\mathrm{G/cm}$ and $B_{z,\min} = -2\,\mathrm{G/cm}$. Here the value of the magnetic fields are represented at all times for three periods.

7.4.3 *Simulation of experimentally relevant parameters*

7.4.3.1 *Non interacting case*

The Hamiltonian can be numerically integrated starting from a wavefunction $|\Psi(t=0)\rangle$ in the $|\ell = 0, m = -1\rangle$ state. A time sequence for the magnetic fields has to be chosen to implement a spin texture on the atoms close to the mapping presented in equations 7.73 and 7.74. Piecewise linear magnetic fields are chosen, as depicted in figure 7.9. Their amplitude are realistic for our experiment.

To monitor the efficiency of the vortex pump, we compute for each value of ℓ the quantity

$$\langle \ell(t) \rangle = \sum_m \langle \ell, m | \Psi(t) \rangle \tag{7.84}$$

with $|\Psi(t)\rangle$ the wavefunction evolved from the initial state $|\ell = 0, m = -1\rangle$. For an efficient pumping, $\langle \ell(t) \rangle$ increases by two for each pump cycle. As can be seen from figure 7.10 (a), the pumping is efficient for the magnetic fields depicted in figure 7.9. However, if the period of the Hamiltonian is too short as in (b), the adiabatic approximation is no longer valid and the pumping is no longer efficient. If the quadrupole (resp. the x axis bias) field is not switched off perfectly as in (c) (resp. (d)), not all the atoms are going to be transferred to a state of higher angular momentum. This is easily seen in the tight-binding picture of 7.4.2.3, since the dotted and full lines of figure 7.8 are going to be switched on at the same time. Reverting the z bias will therefore lead to a beamsplitter type of behaviour. The control of the in-plane magnetic bias thus has to be very accurate in order not to induce partial pumping of the atoms into states of higher angular momentum.

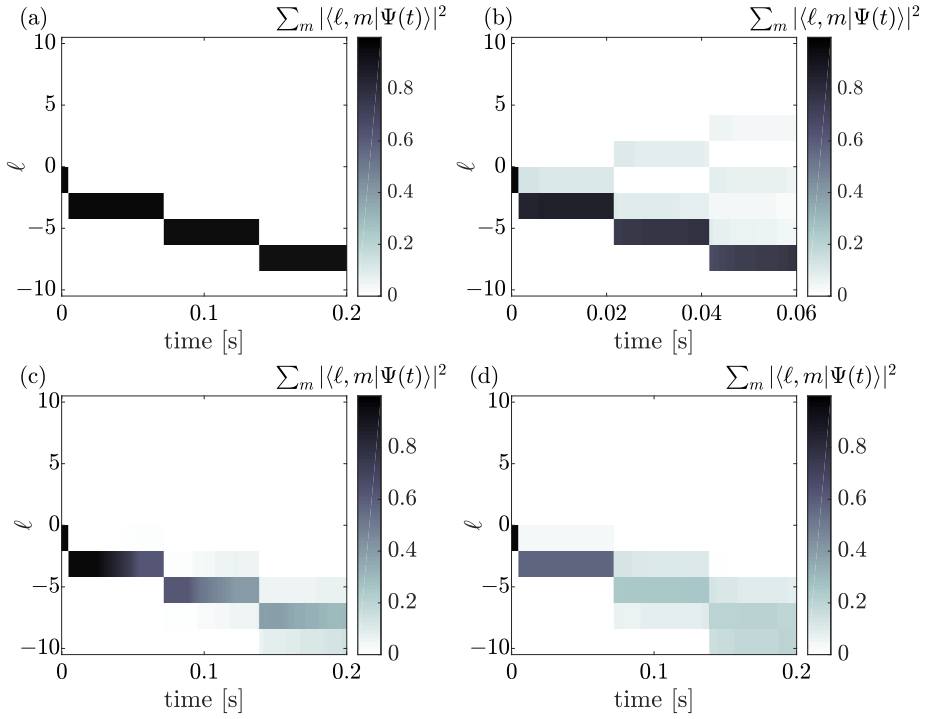

Figure 7.10: A wavefunction initially in $|\ell = 0, m = -1\rangle$ is evolved in time according to equation 7.82. The different figures represent the projection of the wavefunction on the different ℓ states. In (a), it is the exact situation of figure 7.9. In (b), the frequency of the Hamiltonian is changed to $\omega = 2\pi \cdot 50\,\mathrm{Hz}$; the adiabaticity condition does not hold anymore. In (c), the quadrupole field does not go to zero but to 2 G/cm and in (d) the bias field along the x axis does not go to zero but to 1 mG.

7.4.3.2 *Effect of the interactions*

In this section, we analyze the interactions (that we assume to be spin-independent) which have been neglected so far. The mean-field energy created by an atom cloud of spatial density $|\Psi(\boldsymbol{r})|^2$ on a given atom is:

$$E_{\mathrm{int}} = \frac{4\pi\hbar^2 a_{\mathrm{sc}}}{M} N\, |\Psi(\boldsymbol{r})|^2 \tag{7.85}$$

where a_{sc} is the scattering length of the atoms, N the number of atoms in the system and $\Psi(\boldsymbol{r})$ the wavefunction of the system normalized to one. We consider a function Ψ which is confined in the z axis by a tight confinement characterized by the frequency $\omega_{z,\mathrm{conf}}$ and where the density is independent of the radial coordinate in the ring

$$|\Psi(\boldsymbol{r})|^2 = \frac{e^{-z^2/a_{\mathrm{ho}}^2}}{\sqrt{\pi} a_{\mathrm{ho}}} \cdot \frac{\Theta\left(r - R_{\mathrm{min}}\right)\Theta\left(R_{\mathrm{max}} - r\right)}{\mathcal{A}_{\mathrm{ring}}} \cdot |\Psi(\phi)|^2 \tag{7.86}$$

where $a_{\mathrm{ho}} = \sqrt{\hbar/(M\omega_{z,\mathrm{conf}})}$ is the characteristic length of the harmonic oscillator providing the vertical confinement, $\mathcal{A}_{\mathrm{ring}}$ the area of the ring of atoms, $x \mapsto \Theta(x)$ the Heaviside function (equals to 1 for $x > 0$ and 0 otherwise) and R_{min}

and R_{max} the inner and outer radii of the atom ring. Calling $\tilde{g} = \sqrt{8\pi}a_{\text{sc}}/a_{\text{ho}}$ the dimensionless parameter characterizing the interaction strength for bidimensional gases, the interaction energy thus reads $\Psi(\phi)$:

$$E_{\text{int}} = \frac{\hbar^2}{M}\tilde{g}\frac{N}{\mathcal{A}_{\text{ring}}}|\Psi(\phi)|^2 \tag{7.87}$$

In the following, we will assume that the interaction strength is the same for all spin states. The wavefunction Ψ can be decomposed on the basis we have used so far

$$|\Psi\rangle = \sum_{\ell,m} c_{\ell,m}|\ell,m\rangle \tag{7.88}$$

Hence

$$\Psi(\phi) = \left(\sum_{\ell,m} c^*_{\ell,m}\langle\ell,m|\right)\left(\sum_{\ell,m} e^{i\ell\phi}c_{\ell,m}|\ell,m\rangle\right) = \sum_{\ell}\alpha_\ell e^{i\ell\phi} \tag{7.89}$$

with $\alpha_\ell = \sum_m |c_{\ell,m}|^2$. The density thus reads:

$$|\Psi(\phi)|^2 = \sum_{\ell} A_\ell e^{i\ell\phi} \tag{7.90}$$

with $A_\ell = \sum_{\ell'}\alpha_{\ell'+\ell}\alpha_{\ell'}$. The interaction term in the Hamiltonian will thus couple different states of orbital momentum depending on the spatial dependence of the density. Writing Gross-Pitaevskii equation in the basis of interest for us, we obtain the total Hamiltonian in momentum space which consists of the sum of equation 7.82 with the interaction term

$$\hat{H}_{\text{int}} = \frac{\hbar^2}{M}\tilde{g}\frac{N}{\mathcal{A}_{\text{ring}}}\sum_{\ell,\ell',m} A_{\ell-\ell'}|\ell,m\rangle\langle\ell',m| \tag{7.91}$$

The energy scale corresponding to the interactions is

$$E_{\text{int}} = \hbar^2\tilde{g}N/(M\mathcal{A}_{\text{ring}}) \simeq h\cdot 162\,\text{Hz} \tag{7.92}$$

for a ring of atoms of internal (resp. external) radius of 8.5 μm (resp. 11.5 μm) with a 2D density of 13 at/μm^2. If the projection of the wavefunction on the ℓ states $\langle\ell(t)\rangle$ consists only of one ℓ state, all the A_ℓ are zero except for A_0 and the atoms stay in that state of angular momentum, because it is not favorable from the point of view of the interactions to create a density modulation when there is none. However, if the wavefunction is spread over several ℓ states – as is the case when the zero of the quadrupole is close to the ring, as shown by the exact form of the spinor given in 7.1.2 – the interaction term can lead to a diffusion in the various angular momentum states. This diffusion will be prevented if the time spent with the zero of the magnetic field close to the ring is small compared to h/E_{int}. In the case of the magnetic field configuration presented in figure 7.9, with a frequency ω for the Hamiltonian, the zero of the quadrupole is close to the ring during a time $T \simeq 2\pi/(12\omega)$; the condition thus becomes

$$\omega > 2\pi\cdot 13\,\text{Hz} \tag{7.93}$$

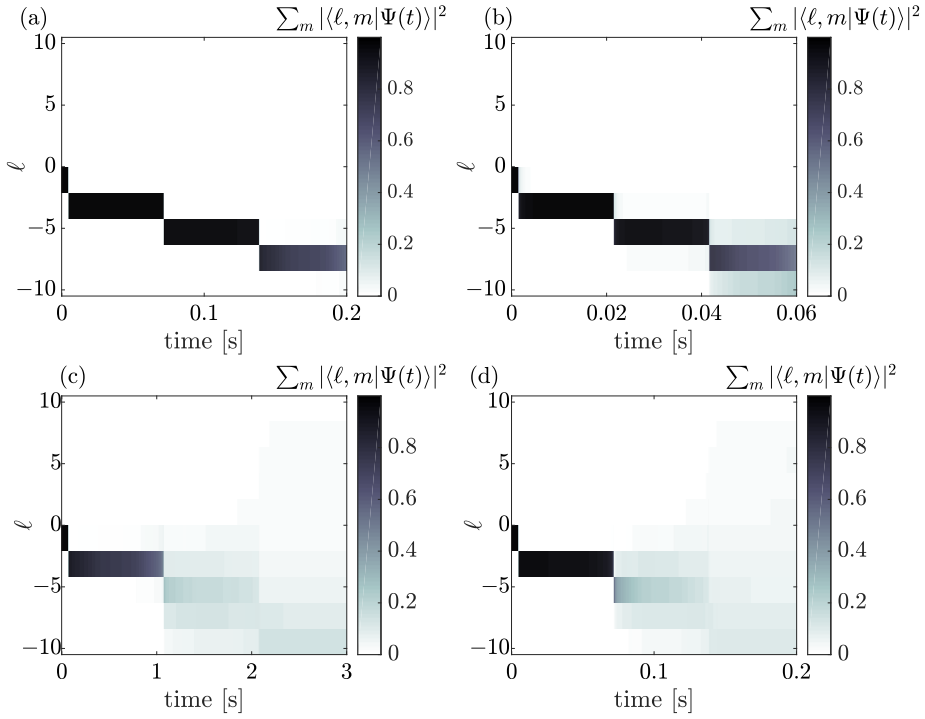

Figure 7.11: A wavefunction initially in $|\ell = 0, m = -1\rangle$ is evolved in time according to equation 7.82 plus the interaction term of equation 7.91 with the same parameters as in figure 7.10. The different figures represent the projection of the wavefunction on the different ℓ states. In (a), $E_{\text{int}} \simeq h \cdot 162\,\text{Hz}$ and $\omega = 2\pi{\cdot}15\,\text{Hz}$. In (b), $E_{\text{int}} \simeq h \cdot 162\,\text{Hz}$ and $\omega = 2\pi{\cdot}50\,\text{Hz}$; the pumping is now more efficient than without interactions. In (c) $E_{\text{int}} \simeq h \cdot 162\,\text{Hz}$ and $\omega = 2\pi{\cdot}1\,\text{Hz}$; the slow evolution favours diffusion in the different ℓ states. In (d), $E_{\text{int}} \simeq h \cdot 325\,\text{Hz}$ and $\omega = 2\pi{\cdot}15\,\text{Hz}$; the high density leads to faster diffusion in the ℓ states too.

Various configurations have been simulated on figure 7.11. With the parameters of figure 7.9, it is still possible to pump efficiently the atoms to states with higher angular momentum. Having interactions also favours faster dynamics as illustrated by figure 7.11 (b) and (c). The scheme of the vortex pump should be able to work even in the presence of interactions.

7.5 CONCLUSION

In this chapter, we have studied what happens to a ring of atoms placed in a magnetic field when the orientation of the atoms follows the local eigenstates of its spin degree of freedom. For a well-chosen magnetic field, for example a quadrupole field, this leads to an artificial magnetic field on the atoms.

From there two possible experimental schemes have been investigated. First, we have studied the possibility of probing the ground state of the ring of atoms in this artificial magnetic field by condensing in presence of the quadrupole field. Depending on the relative position of the ring and the zero of the magnetic field, the atoms can condense in different angular momentum states which

can be detected either by projecting the internal state of the atoms on a single magnetic state or by letting two coplanar rings interfere. The problem of having a gauge field on the atoms was also phrased in term of a Berry phase; this phase could be detected in an interference experiment.

Then we studied the possibility to "pump" quanta of angular momentum in the ring of atoms by controlling the quadrupole field as well as the vertical and in-plane bias fields in a periodic manner. This vortex pump can be expressed in a simple way by a mapping of a torus on a sphere, which is a typical problem of topology. The Chern number characterizing the evolution of a local eigenstate of the internal degree of freedom is either 0, +2 or -2 according to the number of angular momentum quanta that are added to the system in one cycle.

Both experiments make use of the main features of the new experimental set-up described in chapter 4. However, they will require careful control of the magnetic fields, which is not implemented yet.

CONCLUSION

In this work, I have presented some experiments and some proposals which are made possible thanks to the development of techniques to produce 2D clouds of degenerate atoms in arbitrary potentials. These techniques, first developed on an existing set-up for the experiments presented in chapter 3, were implemented in an improved version in the new experiment which was build during my thesis and described in chapter 4. They consist of (i) a 2D confinement provided by an "accordion lattice" whose spacing can be dynamically changed in the experimental sequence, optimizing both the loading and the strength of the confinement; (ii) a programmable intensity mask which is imaged onto the atoms, which are then trapped in the dark regions of a light beam if it creates a repulsive potential.

In a first series of experiments, we studied the crossover between the three- to the two-dimensional regime. Driven by the bosonic statistics of the atoms, a 2D cloud can exist even if the energy scale associated to temperature is not small compared to the 2D confinement: this is a phase transition called transverse condensation, whose mechanism was detailed in chapter 1. In chapter 3, we demonstrated that the appearance of extended coherence in the cloud (revealed by interference or time-of-flight measurements) is due to the crossing of this transition, at phase-space densities which are too low to reveal Bose-Einstein condensation of a finite system or the Berezinskii-Kosterlitz-Thouless transition emblematic of 2D systems.

In a second series of experiments, the dynamical properties of the phase transition were tested. By quench cooling gases in uniform ring or square traps, we observe the formation of topological defects (supercurrents or point vortices) and study their density as a function of the quench duration. These measurements are compared to the predictions of Kibble and Zurek, explained in chapter 2: the variation of the number of topological defects with quench duration is compatible with the different theoretical models relevant for the superfluid transition in a Bose gas, but the precision of our measurement does not allow us to distinguish between them.

A third series of experiments allowed us to study collective effects between light and atoms, as described in chapter 5. We used our ability to produce homogeneous slabs of atoms with a varying density and thickness and study their optical density when probed by a weak, near resonant laser. Instead of the one atom Lorentzian line, we observed broadened resonances that are shifted to the blue, in agreement with simulations of classical dipoles. We also reported on the first experimental study of the propagation of an excitation in a quasi 2D cloud illuminated locally.

We have also presented two possible experiments which are easily accessible in the new set-up of chapter 4.

The first one consists in taking advantage of the low dimensionality of the system to implement "bulk" evaporative cooling. The 2D confinement provided by

the accordion lattice, combined with a tilted potential, will allow us to evaporate a uniform cloud in a uniform way without having to rely on atoms escaping at the edge of the cloud as shown in chapter 6. This would be an improvement on the previous measurement related to the Kibble-Zurek mechanism, which requires a homogeneous temperature over the whole sample.

The second planned experiment analysed in this thesis is related to artificial gauge felds. It is possible to take advantage of the internal states of the Rubidium atom to create supercurrents in a ring trap combined with a quadrupole magnetic field, as described in chapter 7. This is realized either by having the atoms condense in a static artificial magnetic field or by implementing the equivalent of a Thouless "vortex pump" on the atoms.

More generally, the ability to project tailored potentials with a high resolution on a cloud of degenerate atoms is at the heart of the recent development of "atomtronics", aiming at harnessing the transport of atoms through circuits of light in the same way the transport of electrons through different materials was controlled in the past. In that respect, the new experimental set-up that has been built is an excellent platform to explore these questions thanks to the ability to project arbitrary dynamical potentials on the atoms.

Last, the possibility to have a gas of bosons in a uniform trap with a strong 2D confinement (thanks to the accordion lattice) opens the way to implementing some of the proposals to create large artificial magnetic fields [222], and access the strongly correlated states of the quantum Hall effect.

A

FIT-FREE DETERMINATION OF SCALE INVARIANT EQUATIONS OF STATE: APPLICATION TO THE TWO-DIMENSIONAL BOSE GAS

Determination of Scale-Invariant Equations of State without Fitting Parameters: Application to the Two-Dimensional Bose Gas Across the Berezinskii-Kosterlitz-Thouless Transition

Rémi Desbuquois,[1] Tarik Yefsah,[2] Lauriane Chomaz,[3,4] Christof Weitenberg,[5] Laura Corman,[3] Sylvain Nascimbène,[3] and Jean Dalibard[3,4]

[1]*Institute for Quantum Electronics, ETH Zurich, 8093 Zurich, Switzerland*
[2]*MIT-Harvard Center for Ultracold Atoms, Research Laboratory of Electronics, Department of Physics, Massachusetts Institute of Technology, Cambridge, Massachusetts 02139, USA*
[3]*Laboratoire Kastler Brossel, CNRS, UPMC, ENS, 24 rue Lhomond, F-75005 Paris, France*
[4]*Collège de France, 11 Place Marcelin Berthelot, 75231 Paris Cedex 05, France*
[5]*Institut für Laserphysik, Universität Hamburg, Luruper Chaussee 149, D-22761 Hamburg, Germany*

(Received 17 March 2014; revised manuscript received 2 June 2014; published 8 July 2014)

We present a general "fit-free" method for measuring the equation of state (EoS) of a scale-invariant gas. This method, which is inspired from the procedure introduced by Ku *et al.* [Science 335, 563 (2012)] for the unitary three-dimensional Fermi gas, provides a general formalism which can be readily applied to any quantum gas in a known trapping potential, in the frame of the local density approximation. We implement this method on a weakly interacting two-dimensional Bose gas across the Berezinskii-Kosterlitz-Thouless transition and determine its EoS with unprecedented accuracy in the critical region. Our measurements provide an important experimental benchmark for classical-field approaches which are believed to accurately describe quantum systems in the weakly interacting but nonperturbative regime.

DOI: 10.1103/PhysRevLett.113.020404 PACS numbers: 05.30.Jp, 03.75.Hh, 05.70.Ce, 67.85.-d

Homogeneous matter at thermal equilibrium is described by an equation of state (EoS), i.e., a functional relation between thermodynamic variables of the system. While the EoS is analytically known for ideal gases, one must resort to approximations or numerical calculations to determine the EoS of interacting fluids, which must then be compared to experiments. Thanks to a precise control of temperature, confining potential, and interaction strength, cold atomic gases constitute a system of choice for the experimental determination of quantum matter EoS [1]. While performed on atomic systems, such measurements often provide crucial insight on generic physical problems, well beyond the atomic physics perspective. Prominent examples are the recent measurements of the EoS of atomic Fermi gases [2–5], which provided a precious quantitative support for our understanding of strongly interacting fermions at low temperatures. Another important paradigm accessible to atomic gases is found in two-dimensional quantum systems, where the low temperature state is established via a defect-driven transition. This generic phenomenon of two-dimensional systems is described by the celebrated Berezinskii-Kosterlitz-Thouless (BKT) theory, with a scope that ranges from superconductivity to quantum Hall bilayer physics to high energy physics.

In this context, the weakly interacting two-dimensional Bose gas is of particular interest as it supports the fundamental principles of the BKT theory, while allowing for a simplified theoretical description. Indeed, for small enough interparticle interactions, the thermodynamics of the two-dimensional Bose gas is well captured by a classical-field model [6,7], which is itself described by a dimensionless coupling constant and exhibits scale invariance [8]. In general, scale invariance occurs in any fluid where no explicit energy or length scale is associated with the (binary) interaction potential. For the weakly interacting two-dimensional case, the 3D scattering length is normalized by the extension of the system in the third dimension, and this dimensionless ratio characterizes the effective 2D interaction strength. Scale invariance also occurs in the unitary Fermi gas, where the scattering length describing s-wave interactions diverges (for a review, see [12]). This property considerably simplifies the EoS structure, as general dimensionless quantities such as the phase space density $\mathcal{D}$ which usually depend separately on the chemical potential μ and the temperature T can only be expressed as the ratio $\mu/k_{\mathrm{B}}T$ owing to the absence of other energy scales [13,14].

The usual method for determining the EoS of a cold atomic gas starts with the measurement of the density distribution $n(\boldsymbol{r})$ in a smoothly varying, confining potential $V(\boldsymbol{r})$. Using the local density approximation (LDA), the measured $\mathcal{D}(\boldsymbol{r})$ is linked to that of a uniform fluid with the same interaction strength and temperature, and with chemical potential $\mu(\boldsymbol{r}) = \mu - V(\boldsymbol{r})$, μ being its value at the center of the trap [1]. For a given realization of the gas, T and μ are obtained by comparing the low-density wings of $n(\boldsymbol{r})$ with the known theoretical result for a dilute fluid. However, any systematic error in the determination of the density, e.g., due to imperfect calibration of the probing system, will lead to inaccurate values of μ and T and thus

affect the measurement of the EoS $\mathcal{D}(\mu, T)$. Recently, an alternative fit-free method that does not suffer from this limitation has been put forward in [4] for the measurement of the EoS of the scale-invariant 3D Fermi gas. It is based on the use of two specific thermodynamic variables, pressure and compressibility; in addition, absolute energy scales T and μ were replaced by a single relative scale $d\mu$, which was itself determined by the LDA through $d\mu = -dV$.

The purpose of the present Letter is twofold. First, we describe a method that generalizes the procedure introduced in [4], which does not rely on specific thermodynamic variables but rather provides a generic formalism that can readily be applied to other quantum systems. Second, we implement this method on a two-dimensional (Bose) fluid, for which the spatial density $n(\boldsymbol{r})$ is directly accessible from an image of the cloud. The precision of the reconstructed EoS makes it suitable for a quantitative comparison to the classical-field Monte Carlo calculation [7] in the critical region, which could not be conclusive from previous measurements [13,14]. Our measurement, with a relative statistical error smaller than 1% on the detectivity, is in excellent agreement (better than 5%) with the prediction obtained from [7] at the critical point and deeper in the superfluid regime. In the normal regime close to the transition point, we observe a deviation on the order of 15%, which might be due to beyond classical-field effects.

We start our analysis by considering an atomic gas in thermodynamic equilibrium confined in a known potential $V(\boldsymbol{r})$. The only hypothesis for the method is the LDA, which entails that $n(\boldsymbol{r})$ depends on position only through the local value of the trapping potential: $n(\boldsymbol{r}) = n[V(\boldsymbol{r})]$. Although this method is applicable to any dimension, we focus here on the particular case of the two-dimensional gas for the sake of clarity. Let us introduce the energy $E[V(\boldsymbol{r}))]$ with $\boldsymbol{r} = (x, y)$, defined by [15]

$$E = \frac{\hbar^2}{m} n, \tag{1}$$

which we want to combine with other relevant energies in order to form useful dimensionless variables. Though no absolute energy scales are readily available, a relative energy scale is provided by the variation of the trapping potential $\mathrm{d}V$. Furthermore, quantities formed in this manner are directly connected by the LDA to the properties of the uniform gas using the relation $d\mu = -dV$. Thus, we define the dimensionless quantities

$$X_\nu \equiv E^{\nu-1} \frac{\partial^\nu E}{\partial \mu^\nu} = (-1)^\nu E^{\nu-1} \frac{\mathrm{d}^\nu E}{\mathrm{d}V^\nu}, \tag{2}$$

where ν is an integer. By convention, $X_0 = 1$ and a negative ν will instead correspond to $|\nu|$ successive integrations of E with respect to V, with, for example,

$$X_{-1} = \frac{1}{E^2} \int_V^\infty E(V') dV'. \tag{3}$$

From a given image of the gas $n(\boldsymbol{r})$, one can thus construct all functions $X_\nu(V)$. In the case of a scale-invariant system, the knowledge of a single thermodynamic variable X_ν is sufficient to determine the state of the fluid and, hence, the values of all other variables $X_{\nu'}$. In other words, all individual measurements must collapse on a single line in each plane $\{X_\nu, X_{\nu'}\}$, irrespective of their temperature and chemical potential. Such a line is a valid EoS of the fluid under consideration.

Once the X_ν are known, all other thermodynamic quantities can be determined, up to an integration constant. In particular, one can derive the phase-space density $\mathcal{D}$ and the ratio $\alpha = \mu/k_\mathrm{B}T$. Let us suppose that a point $(X_\nu^{(0)}, X_{\nu'}^{(0)})$ can be identified in a known portion of the EoS and that it corresponds to the values α_0 and $\mathcal{D}_0$. The link between the set $\{X_\nu\}$ and $(\alpha, \mathcal{D})$ is provided by

$$\mathcal{D}(X_\nu^{(1)}) = \mathcal{D}_0 \exp\left(\int_{X_\nu^{(0)}}^{X_\nu^{(1)}} \frac{X_1}{(\nu-1)X_1X_\nu + X_{\nu+1}} dX_\nu \right), \tag{4}$$

$$\alpha(X_\nu^{(1)}) = \alpha_0 + \frac{1}{2\pi} \int_{X_\nu^{(0)}}^{X_\nu^{(1)}} \frac{\mathcal{D}(X_\nu)}{(\nu-1)X_1X_\nu + X_{\nu+1}} dX_\nu. \tag{5}$$

The determination of $(\alpha, \mathcal{D})$ thus requires the knowledge of a triplet $\{X_1, X_\nu, X_{\nu+1}\}$. This requirement can be weakened by choosing $\nu = 1$ or $\nu = -1$, in which case only the pairs $\{X_1, X_{-1}\}$ or $\{X_1, X_2\}$ are needed.

We illustrate this general procedure with a few examples. For the simple case of a Maxwell-Boltzmann gas, the EoS in terms of the X_ν's can be obtained analytically, and one gets, for example, $X_1X_{-1} = 1$ and $X_2 = X_1^2$. For an interacting 2D gas, the EoS is not known analytically; however, for the bosonic case, it can be approximated in two limiting cases. For $\mu < 0$, the gas is only weakly degenerate and the mean-field energy of an atom in the gas can be written as $2\tilde{g}(\hbar^2 n/m)$, where the dimensionless coefficient $\tilde{g}$ (assumed here to be $\ll 1$) characterizes the strength of the interaction. The thermodynamics is then well described by the prediction of the Hartree-Fock theory [16],

$$\mathcal{D} = -\ln(1 - e^{\alpha - \tilde{g}\mathcal{D}/\pi}), \tag{6}$$

from which we extracted numerically the values of X_{-1} and X_1 and plotted the corresponding EoS in Fig. 1. In the opposite case of a strongly degenerate gas (with a chemical potential that is positive and larger than $k_\mathrm{B}T$), the gas is described by the Thomas-Fermi equation $\mathcal{D} = 2\pi\alpha/\tilde{g}$. All X_ν are then constant, with $X_{-1} = \tilde{g}/2$, $X_1 = 1/\tilde{g}$, and $X_2 = 0$.

We now turn to the practical implementation of this method for processing data obtained with a quasi-2D

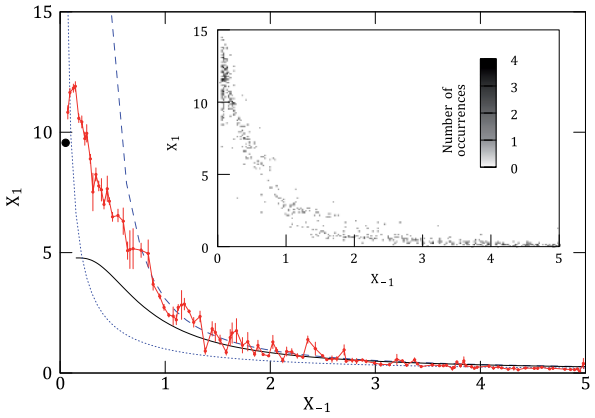

FIG. 1 (color online). Determination of the EoS with variables X_{-1} and X_1, along with known limits. The simple cases of the ideal Bose gas (Boltzmann gas) are shown as a blue dashed (dotted) line. The known limits of the EoS of the weakly interacting 2D Bose gas are indicated by a black point for the Thomas-Fermi limit and by a black solid line for the Hartree-Fock mean-field theory. The red line results from the averaging over all the separate intensity profiles, with the error bars corresponding to the standard error introduced by the averaging procedure. The data shown here contain ~100 different values of X_{-1}. Inset: Distribution of measured values of X_{-1} and X_1. The gray level indicates the number of individual data points falling in each pixel.

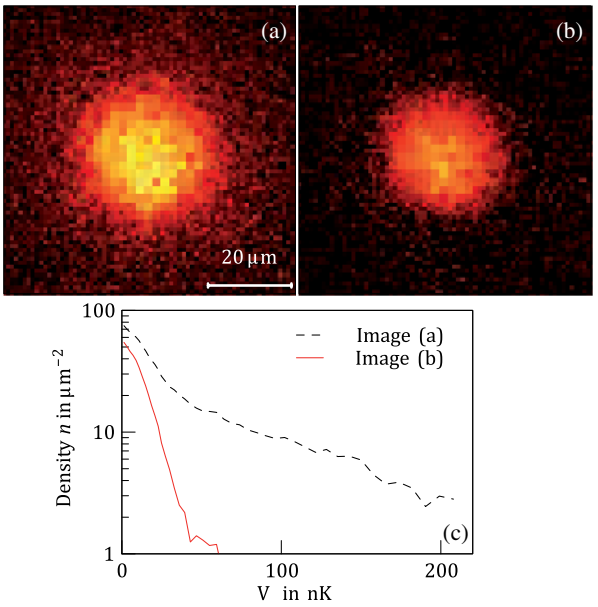

FIG. 2 (color online). (a) and (b): Density distributions of 2D atomic samples of ^{87}Rb corresponding to a partially degenerate (a) and a strongly degenerate cloud (b). (c): Corresponding function $n[V(\boldsymbol{r})]$ resulting from azimuthal averaging. The distributions are obtained with high intensity imaging.

rubidium gas. Our experimental preparation follows along the lines detailed in [14,17]. We start with a 3D gas of ^{87}Rb atoms, confined in their $F = m_F = 2$ state in a magnetic trap. To create a 2D system, we shine an off-resonant blue-detuned laser beam on the atoms, with an intensity node in the plane $z = 0$. The resulting potential provides a strong confinement perpendicular to this plane, with oscillation frequency $\omega_z/2\pi = 1.9(2)$ kHz, which decreases at most by 5% over typical distribution radii. This corresponds to the interaction strength $\tilde{g} = \sqrt{8\pi}a/l_z \approx 0.1$, where a is the 3D scattering length and $l_z = \sqrt{\hbar/m\omega_z}$ [18]. The energy $\hbar\omega_z$ is comparable to the thermal energy $k_B T$, which ensures that most of the atoms occupy the ground state of the potential along z (see [14] and [19]). The magnetic trap provides a harmonic confinement in the xy plane, with mean oscillation frequency $\omega_r/2\pi = 20.6(1)$ Hz. *In situ* density distributions of our clouds are measured via absorption imaging with a probe beam perpendicular to the atomic plane. For the analysis presented below, we used a data set of 80 samples, with temperatures ranging from 30 nK to 150 nK and atom numbers from 25 000 to 120 000.

In Fig. 2 we show typical density distributions of 2D atomic clouds, together with the corresponding function $n[V(\boldsymbol{r})]$. The cloud (a) exhibits a significant thermal fraction, contrarily to cloud (b), which is essentially in the Thomas-Fermi regime. The latter illustrates the power of this fit-free method since it can be incorporated as such in our determination of the EoS. On the other hand, it would be discarded in a conventional approach, owing to the impossibility of assigning it a temperature.

Though both choices of variables (X_{-1}, X_1) and (X_1, X_2) are, in principle, possible, the latter requires the experimental evaluation of a second-order derivative, which often suffers from a poor signal-to-noise ratio. By contrast, the choice (X_{-1}, X_1), also adopted in [4] when writing the EoS in terms of pressure and compressibility, appears particularly robust [23]. For each image, we perform an azimuthal average and compute a set of ≈70 data points (X_{-1}, X_1), where the low (high) values of X_{-1} correspond to the high (low) density regions of the image.

In a first step, we combine all sets obtained from images acquired at various temperatures and various atom numbers to test the scale invariance. As explained above, each individual measurement should sit on the same universal curve in the (X_{-1}, X_1) plane, provided the interaction strength $\tilde{g}$ is constant. We show in the inset of Fig. 1 the repartition of data points in the (X_{-1}, X_1) plane, which fall as expected around a single curve. In the main panel we plot the corresponding average curve, which provides the EoS of our gas [24]. In order to reexpress this EoS in terms of the more traditional variables α and $\mathcal{D}$, we now need to apply the transformations of Eqs. (4) and (5). However, these transformations must be adapted to account for possible imperfections in the calibration of the detectivity of our imaging setup. Indeed, as in most cold atom experiments, we only measure the density up to a global

multiplicative factor β [25], which is defined as the ratio between the unknown actual absorption cross-section and the ideal one expected for monochromatic probe light in the absence of stray magnetic fields. Taking this calibration factor into account amounts to replacing Eqs. (4) and (5) by

$$\mathcal{D}(X_\nu^{(1)}) = \mathcal{D}_0 \exp\left(\int_{X_\nu^{(0)}/\beta^\nu}^{X_\nu^{(1)}/\beta^\nu} \frac{X_1}{(\nu-1)X_1X_\nu + X_{\nu+1}} dX_\nu\right), \quad (7)$$

$$\alpha(X_\nu^{(1)}) = \alpha_0 + \frac{\beta}{2\pi}\int_{X_\nu^{(0)}/\beta^\nu}^{X_\nu^{(1)}/\beta^\nu} \frac{\mathcal{D}(X_\nu)}{(\nu-1)X_1X_\nu + X_{\nu+1}} dX_\nu, \quad (8)$$

where the bounds of the integrals now depend on β and where $X_\nu^{(0)}/\beta^\nu$ corresponds to the reference values α_0 and $\mathcal{D}_0$. The value of β is *a priori* unknown; however, it can be determined by fitting the measured EoS to the Hartree-Fock mean-field theory, which is a good approximation in the region $\alpha < 0$. This procedure applies to any other quantum gas, provided one has a good knowledge of the EoS in a given segment of the parameter space.

We choose the bound of Eqs. (7) and (8) at $X_{-1}^0 = 3$, which corresponds to a phase-space density $\mathcal{D}_0 = 1.45$ and $\alpha_0 = -0.22$, well within the Hartree-Fock mean-field regime, and find a detectivity factor $\beta = 0.456(1)$ [26]. The EoS in terms of the variables $(\alpha, \mathcal{D})$—obtained after a small correction due to excited states of the z motion (see [19])—is shown in Fig. 3(a), along with the numerical prediction $\mathcal{D}_{\text{th}}$ [7]. The reconstructed EoS is remarkably smooth and does not display any particular feature at the transition point. This observation is also made on the EoS for pressure, entropy, and heat capacity [19]. This illustrates the "infinite-order" nature of the BKT transition, which is not associated with any singularity of thermodynamic quantities [27], as opposed to phase transitions driven by the breaking of a continuous symmetry, such as the second-order lambda transition observed at MIT [4]. To compare quantitatively the reconstructed EoS with the numerical prediction, we plot the quantity $\mathcal{D}/\mathcal{D}_{\text{th}} - 1$ in Fig. 3(c) and find that it lies consistently below 15%, and even below 5% around the phase transition, which occurs at $\mu_C/k_BT \approx 0.17$ [7]. The deviation observed in the fluctuation region below the critical chemical potential might signal deviations to the classical-field picture which is expected to be accurate for $\tilde{g} \ll 1$ [6,7]. Theoretically this deviation could be addressed using quantum Monte Carlo methods [28,29].

In conclusion, we have presented a method to determine the EoS of a scale-invariant fluid. This method does not rely on thermometry of individual images, nor on the precise calibration of the detectivity, and it leads to a strong reduction of the noise level in the measurement. We have applied it to the case of a weakly interacting Bose gas and obtained its EoS with a precision of a few percent, in excellent agreement with the theoretical prediction obtained from a classical Monte Carlo simulation. Using the response of the gas to a gauge field, originating, for example, from a rotation, this method could be extended to access the superfluid fraction of the gas along the lines proposed in [1]. In principle, this method is not limited to scale-invariant systems and could be extended to any situation described by two independent dimensionless parameters, such as the zero temperature limit of the Fermi gas, either for a spin-balanced gas with varying interactions [3] or for a unitary spin-imbalanced Fermi gas [30].

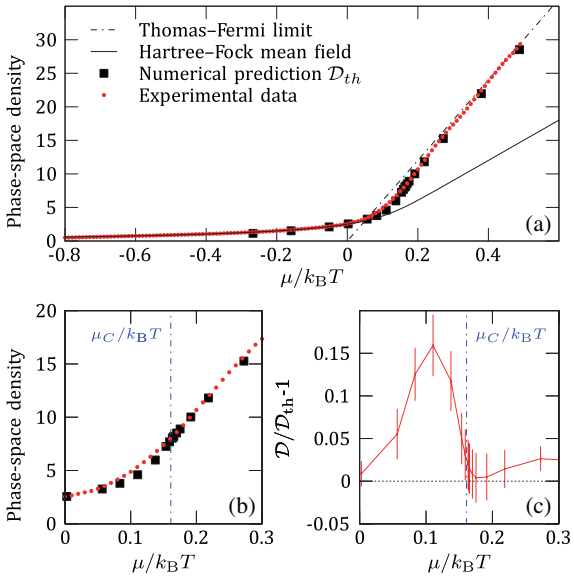

FIG. 3 (color online). (a) Equation of state of the 2D Bose gas, determined with Eqs. (4) and (5) (red points), with a detailed view of the critical region around the BKT transition (blue dash-dotted line) in (b). Statistical error bars are too small to be shown on these plots. We show, for comparison, the classical-field Monte Carlo prediction $\mathcal{D}_{\text{th}}$ [7] in black squares, the Thomas-Fermi limit in the black dash-dotted line, and the Hartree-Fock mean-field theory in the black solid line. We provide a quantitative estimate of the difference between measurement and prediction in (c). There, we plot $\mathcal{D}/\mathcal{D}_{\text{th}} - 1$, where zero indicates perfect agreement. The error bars result from a bootstrap analysis of the experimental data.

We thank Jérôme Beugnon, Jason Ho, Boris Svistunov, and Martin Zwierlein for useful discussions and comments. This work is supported by IFRAF, ANR (ANR-12- BLAN-AGAFON), and ERC (Synergy UQUAM). L. Chomaz and L. Corman acknowledge the support from DGA, and C. W. acknowledges the support from the EU (PIEF-GA-2011-299731).

[1] T.-L. Ho and Q. Zhou, Nat. Phys. **6**, 131 (2009).
[2] S. Nascimbéne, N. Navon, K. J. Jiang, F. Chevy, and C. Salomon, Nature (London) **463**, 1057 (2010).

[3] N. Navon, S. Nascimbéne, F. Chevy, and C. Salomon, Science **328**, 729 (2010).
[4] M. J. H. Ku, A. T. Sommer, L. W. Cheuk, and M. W. Zwierlein, Science **335**, 563 (2012).
[5] K. Van Houcke, F. Werner, E. Kozik, N. Prokof'ev, B. Svistunov, M. J. H. Ku, A. T. Sommer, L. W. Cheuk, A. Schirotzek, and M. W. Zwierlein, Nat. Phys. **8**, 366 (2012).
[6] N. Prokof'ev, O. Ruebenacker, and B. Svistunov, Phys. Rev. Lett. **87**, 270402 (2001).
[7] N. V. Prokof'ev and B. V. Svistunov, Phys. Rev. A **66**, 043608 (2002).
[8] Beyond the classical-field level the scale invariance is broken [9], but the deviation can be neglected for small enough interaction strengths [10,11].
[9] E. Vogt, M. Feld, B. Fröhlich, D. Pertot, M. Koschorreck, and M. Köhl, Phys. Rev. Lett. **108**, 070404 (2012).
[10] M. Olshanii, H. Perrin, and V. Lorent, Phys. Rev. Lett. **105**, 095302 (2010).
[11] C. Langmack, M. Barth, W. Zwerger, and E. Braaten, Phys. Rev. Lett. **108**, 060402 (2012).
[12] S. Giorgini, L. P. Pitaevskii, and S. Stringari, Rev. Mod. Phys. **80**, 1215 (2008).
[13] C.-L. Hung, X. Zhang, N. Gemelke, and C. Chin, Nature (London) **470**, 236 (2011).
[14] T. Yefsah, R. Desbuquois, L. Chomaz, K. J. Günter, and J. Dalibard, Phys. Rev. Lett. **107**, 130401 (2011).
[15] In dimension d, this equation takes the general form $E = \hbar^2 n^{2/d}/m$.
[16] Z. Hadzibabic and J. Dalibard, Riv. Nuovo Cimento **34**, 389 (2011).
[17] S. P. Rath, T. Yefsah, K. J. Günter, M. Cheneau, R. Desbuquois, M. Holzmann, W. Krauth, and J. Dalibard, Phys. Rev. A **82**, 013609 (2010).
[18] D. S. Petrov, M. Holzmann, and G. V. Shlyapnikov, Phys. Rev. Lett. **84**, 2551 (2000).
[19] See Supplemental Material at http://link.aps.org/supplemental/10.1103/PhysRevLett.113.020404 which refers to the works [20–22]. There, we detail the imaging procedure, as well as the procedure followed in order to subtract the contribution of the excited states of the z motion to the EoS. We also give the EoS's for other thermodynamic variables (pressure, entropy, heat capacity).
[20] L. Chomaz, L. Corman, T. Yefsah, R. Desbuquois, and J. Dalibard, New J. Phys. **14**, 055001 (2012).
[21] G. Reinaudi, T. Lahaye, Z. Wang, and D. Guéry-Odelin, Opt. Lett. **32**, 3143 (2007).
[22] S. Tung, G. Lamporesi, D. Lobser, L. Xia, and E. A. Cornell, Phys. Rev. Lett. **105**, 230408 (2010).
[23] In our case, the compressibility is given by $\kappa = X_1/(n^2h^2/m)$ and the pressure by $P = X_{-1}n^2h^2/m$.
[24] We extract data points with $X_{-1} < 2.5$ ($X_{-1} > 2.5$) from high (low) intensity imaging.
[25] This factor is taken into account in Eq. (1) by $E = \beta(\hbar^2/m)n$. The definition of X_ν is unchanged.
[26] The error bar on this value is calculated through a bootstrap analysis. The result is consistent with our (less precise) previous estimate for the same setup, $\beta = 0.40(2)$, which was based on a different method [14].
[27] A singularity, however, appears in the superfluid density, which has to be distinguished from the total density, as the former enters only in the response of the system to an external drag or rotation.
[28] M. Holzmann and W. Krauth, Phys. Rev. Lett. **100**, 190402 (2008).
[29] A. Rançon and N. Dupuis, Phys. Rev. A **85**, 063607 (2012).
[30] Y.-I. Shin, Phys. Rev. A **77**, 041603 (2008).

B

CALCULATION OF THE PROBABILITY DISTRIBUTION OF THE RELATIVE VELOCITY

We consider the situation described in chapter 6 of a gas of atoms with mass M following the Maxwell-Boltzmann distribution such that the probability distribution of the atoms in phase space is

$$f(\boldsymbol{r},\boldsymbol{p}) = \frac{1}{2\pi\mathcal{A}Mk_BT}\exp\left(-\frac{p^2}{2Mk_BT}\right) \tag{B.1}$$

$$f(\boldsymbol{v},\boldsymbol{p}) = \frac{M}{2\pi\mathcal{A}k_BT}\exp\left(-\frac{Mv^2}{2k_BT}\right) \tag{B.2}$$

We now consider two particles with velocities $\boldsymbol{v}_1$ and $\boldsymbol{v}_2$. We want to compute the probability for the relative velocity $\boldsymbol{v}_{\text{rel}} = \boldsymbol{v}_r = \boldsymbol{v}_2 - \boldsymbol{v}_1$ to have a modulus v_r equal to v_0.

Calling $v^2 = 2k_BT/M$, the quantity that must be computed is

$$p\left(v_r = v_0\right) = \frac{1}{\pi^2 v^4}\int e^{-\frac{v_1^2}{v^2}}e^{-\frac{v_2^2}{v^2}}\delta\left(|\boldsymbol{v}_2 - \boldsymbol{v}_1| - v_0\right)\mathrm{d}^2v_1\, d^2v_2 \tag{B.3}$$

Because the relative velocity and the center-of-mass velocity are two quadratic degrees for the system of the two atoms, we have :

$$\boxed{p\left(v_r = v_0\right) = \frac{(M/2)}{k_BT}v_0\exp\left(-\frac{(M/2)v_0^2}{2k_BT}\right)} \tag{B.4}$$

The probability distribution of $\boldsymbol{v}_{\text{rel}} = \boldsymbol{v}_r$ is that of a Maxwell-Boltzmann distribution with temperature T and mass $M/2$.

From this it follows that the probability for the kinetic energy in the relative degree of freedom, $E_{\text{kin}}^{\text{rel}} = M\boldsymbol{v}_{\text{rel}}^2/4$ to be superior to an energy barrier $\Delta E > 0$ is:

$$p\left(v_r \geqslant \sqrt{\frac{4\Delta E}{M}}\right) = \int_{\sqrt{\frac{2\Delta E}{M}}}^{\infty} p(v = v_0)\,\mathrm{d}v \tag{B.5}$$

that is

$$\boxed{p\left(v_r \geqslant \sqrt{\frac{4\Delta E}{M}}\right) = \exp\left(-\frac{\Delta E}{k_BT}\right)} \tag{B.6}$$

and $p\left(v_r \geqslant \sqrt{\frac{4\Delta E}{M}}\right) = 1$ if $\Delta E < 0$ as in Equation 6.54.

We also want to compute the mean kinetic energy $E_{\text{kin}}^{\text{rel}}$ knowing that $E_{\text{kin}}^{\text{rel}} \geqslant \Delta E$:

$$\left\langle \boldsymbol{v}_{\text{rel}}^2\right\rangle_{\text{knowing } E_{\text{kin}}^{\text{rel}} \geqslant \Delta E} = \frac{\left\langle \boldsymbol{v}_{\text{rel}}^2\right\rangle_{E_{\text{kin}}^{\text{rel}} \geqslant \Delta E}}{p\left(v_r \geqslant \sqrt{\frac{4\Delta E}{M}}\right)} \tag{B.7}$$

In the case $\Delta E \geqslant 0$:

$$\left\langle \boldsymbol{v}_{\text{rel}}^2 \right\rangle_{E_{\text{kin}}^{\text{rel}} \geqslant \Delta E} = \frac{M}{2k_{\text{B}}T} \int_{\sqrt{4\Delta E/M}}^{\infty} v^3 \exp\left(-\frac{Mv^2}{4k_{\text{B}}T}\right) \mathrm{d}v \tag{B.8}$$

$$= \frac{k_{\text{B}}T}{M} \int_{\frac{2\Delta E}{k_{\text{B}}T}}^{\infty} u\, e^{-u/2} \mathrm{d}u \tag{B.9}$$

$$= \frac{4}{M} \left(\Delta E + k_{\text{B}}T\right) e^{-\Delta E/k_{\text{B}}T} \tag{B.10}$$

such that

$$\boxed{\left\langle E_{\text{kin}}^{\text{rel}} \right\rangle_{\text{knowing } E_{\text{kin}}^{\text{rel}} \geqslant \Delta E} = \Delta E + k_{\text{B}}T} \tag{B.11}$$

if $\Delta E > 0$ and

$$\boxed{\left\langle E_{\text{kin}}^{\text{rel}} \right\rangle_{\text{knowing } E_{\text{kin}}^{\text{rel}} \geqslant \Delta E} = k_{\text{B}}T} \tag{B.12}$$

if $\Delta E \leqslant 0$.

C

DESCRIPTION OF THE COUPLED DIPOLE PROGRAMS

Here, we describe the main functions of the python program used to simulate multiple and recurrent scattering in chapter 5 available in the `diffmult.py` file. at https://github.com/lauracorman/multipleScattering

C.1 `drawpositions`

C.1.1 *Inputs*

`nat` number of atoms simulated; default 200

`rad` radius of disk in xy plane in which the positions are drawn (in the unit length of the program, defaults µm); default 25

`dz` size in z direction (in the unit length of the program, defaults µm); default 0.2

`core` minimal distance between 2 atoms (in the unit length of the program, defaults µm); default 0.05

`avoid` boolean indicating whether the minimal distance between atoms should be taken into account; default is true

`methodz` method used to drow the positions in the z axis. 1 is gaussian, 0 is uniform; default is 1

C.1.2 *Output*

`r` 3×`Nat` matrix containing the positions (in the unit length of the program, defaults µm)

C.2 `heff`

Computes the resolvant matrix $((\hbar\omega - H + i0_+)^{-1}$ of equation (30) of the paper[128]).

C.2.1 *Inputs*

`r` 3×`Nat` matrix containing the positions (in the unit length of the program defined by `k0`, defaults µm)

`delta` detuning in units of $\Gamma/2$; default 0

`k0` value of the wavevector, which sets the unit length of the program; default $2\pi/0.78$ (units in µm) (if 1 units in $\lambda/2\pi$)

C.2.2 *Output*

`h` `3Nat`×`3Nat` resolvant matrix

C.3 `excvector`

Computes the vector that indicates the excitation of the light field on the atoms (vector $|\mathcal{E}_{j,x}\rangle$ of equation (30) of reference [128]).

C.3.1 *Inputs*

`r` 3×`Nat` matrix containing the positions (in the unit length of the program defined by `k0`, defaults µm)

`pol` 3×1 vector indicating the polarization of the light field; default is x polarization ($(1, 0, 0)$).

`k` 3×1 vector indicating the propagation direction of the light field; default is along z ($(0, 0, 1)$).

`k0` value of the wavevector, which sets the unit length of the program; default $2\pi/0.78$ (units in µm) (if 1 units in $\lambda/2\pi$)

C.3.2 *Output*

`a` `3Nat`×1 excitation vector.

C.4 `transmission`

Compute the mean OD (and standard deviation), the mean phase (and standard deviation) and the mean complex transmission (and standard deviation) according to equation (21), (22), (23), (37)-(41) of reference [128], averaged over some repetitions.

C.4.1 *Inputs*

`nat` number of atoms simulated; default 1000

`nrepeat` number of repetition; default 10

`rad` radius of disk in xy plane in which the positions are drawn (in the unit length of the program, defaults µm); default 1.75

`dz` size in z direction (in the unit length of the program, defaults µm); default 0.2

`core` minimal distance between 2 atoms (in the unit length of the program, defaults µm); default 0.01

`delta` detuning in units of $\Gamma/2$; default 0

`avoid` boolean indicating whether the minimal distance between atoms should be taken into account; default is true

`methodz` method used to drow the positions in the z axis. 1 is gaussian, 0 is uniform; default is 1

C.4.2 *Output*

`trans` 3×1 vector containing the mean of the complex transmission

`transstd` 3×1 vector containing the standard deviation of the complex transmission

`od` mean OD

`odstd` standard deviation of the OD

`phi` mean dephasing

`phistd` standard deviation of the dephasing

C.5 doresonancesvaryod

Does many transmission experiments varying the atom density and the detuning (resonance curves). Stores the data in matlab and python readable files in `./Results/doResonancesVaryOD_(datetag).mat` or `.npz`.

C.5.1 *Inputs*

`nat` number of atoms simulated; default 1000

`od0s` `nOD`$\times 1$ densities of atoms to be tested, expressed by their Beer-Lambert OD; default is $[0.1, 1, 2, 4, 8]$

`dz` size in z direction (in µm); default 0

`delta` `nDetunings`$\times 1$ detuning in units of $\Gamma/2$; default `linspace(-25,25,1)`

`nrepeat` number of repetition per point; default 3

`core` minimal distance between 2 atoms (in µm); default 0.01

`avoid` boolean indicating whether the minimal distance between atoms should be taken into account; default is true

`methodz` method used to drow the positions in the z axis. 1 is gaussian, 0 is uniform; default is 1

C.5.2 *Output*

`trans` 3×1 vector containing the mean of the complex transmission

`transstd` 3×1 vector containing the standard deviation of the complex transmission

`ods` `nOD`$\times$`nDetunings` matrix containing the mean OD for all values of density and detuning

`odsstd` `nOD`$\times$`nDetunings` matrix containing the standard deviation of the OD for all values of density and detuning

`phis` `nOD`$\times$`nDetunings` matrix containing the mean dephasing for all values of density and detuning

`phisstd` `nOD`$\times$`nDetunings` matrix containing the standard deviation of the dephasing for all values of density and detuning

`nod` number of densities considered

`delta` the input parameter

`od0` `nOD`$\times$`nDetunings` matrix containing the Beer-Lambert OD for all values of density and detuning

`n` `nOD`$\times 1$ vector with all the densities (in at/μm^2)

`nat` the input parameter

`od0s` the input parameter

`dz` the input parameter

`delta` the input parameter

`core` the input parameter

`avoid` the input parameter

`methodz` the input parameter

D

ESTIMATING CONFIDENCE INTERVALS USING THE BOOTSTRAPPING METHOD

In many experimental studies, some data is gathered from which a meaningful parameter needs to be extracted. The error on this parameter is also wanted. Bootstrapping allows to determine a confidence interval in such a situation.

D.1 POSITION OF THE PROBLEM

Let us consider the probablity distribution P, and assume that we want to find the mean $\bar{x}$ and standard deviation σ, or any quantity $\theta(P)$ associated to P. If P is defined on (a well-chosen set of ensembles of) $\mathbb{R}$:

$$\bar{x} = \int x\, P(X = x)\, \mathrm{d}x \tag{D.1}$$

$$\sigma = \sqrt{\int (x - \bar{x})^2\, P(X = x)\, \mathrm{d}x} \tag{D.2}$$

To do this in an empirical manner, we will draw N random numbers $\boldsymbol{x} = (x_1, \ldots, x_N)$ following the distribution P and compute the estimated values of the mean and the standard deviation:

$$\hat{\bar{x}} = \frac{1}{N} \sum_{i=1}^{N} x_i \tag{D.3}$$

$$\hat{\sigma} = \sqrt{\sum \frac{(x_i - \hat{\bar{x}})^2}{N - 1}} \tag{D.4}$$

The use of $N - 1$ in the definition of the estimator of the standard deviation stems from the fact that the empirical mean is used and not the real mean, and is called the Bessel correction. For a different quantity $\theta(P)$ we would have to use the appropriate estimator $\hat{\theta}(\boldsymbol{x})$.

What is the error on $\hat{\bar{x}}$ and $\hat{\sigma}$ (or on any other parameter that can be computed from the drawn numbers)?

1. If the probability distribution form is known (gaussian, uniform, exponential…), a formula might exist for some of the quantities we want to compute. In the case of a gaussian distribution whose mean we want to know, we can compute the standard error $\mathrm{SE} = \hat{\sigma}/\sqrt{N}$ from which we can deduce the confidence interval on $\hat{\bar{x}}$. However, such formulas are not always available.

2. If we have the ability to draw several sets of N numbers according to the same probability law, we can compute $\hat{\bar{x}}$, $\hat{\sigma}$ or $\hat{\theta}$ for each draw and look at the dispersion of the results. Let's have a look at the results of such a experiment as presented in figure D.1. Many samples at fixed N

were drawn, the measured $\hat{\bar{x}}$ and $\hat{\sigma}$ are recorded and the reconstructed probability distribution is plotted. From this, the uncertainty on $\hat{\bar{x}}$ and $\hat{\sigma}$ can be assessed. For the mean value, we see that it matches the prediction of the standard error. We also check that increasing N a hundred times decreases the spread of the results by a factor of ten. This method is usually impractical or impossible to use, but it is interesting to understand the bootstrap.

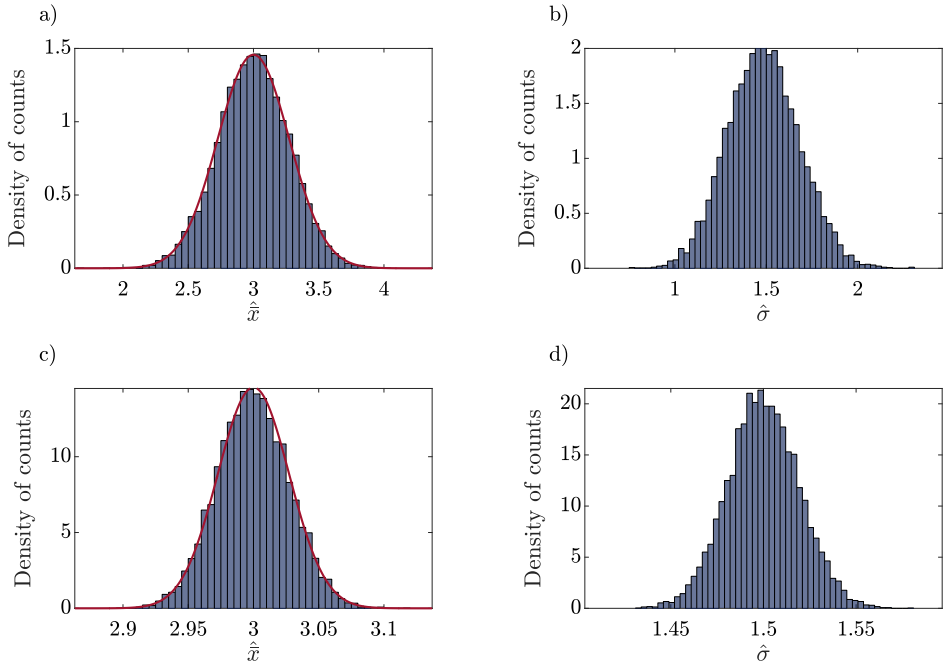

Figure D.1: Drawing several samples from a known probablity distribution and looking at the spread of the results. Initial distribution is a gaussian one with mean $\bar{x} = 3$ and standard deviation $\sigma = 1.5$. In a) and b), 10^4 samples with $N = 30$ were drawn. In c) and d), 10^4 samples with $N = 3000$ were drawn. The expected spread of the results given by the standard error is represented in solid red line. For draws with $N = 30$, the mean value for $\hat{\bar{x}}$ is 3.00 with a standard deviation of 0.27 (the standard error gives 0.27), and the mean value for $\hat{\sigma}$ is 1.5 with a standard deviation of 0.2. For draws with $N = 3000$, the mean value for $\hat{\bar{x}}$ is 3.00 with a standard deviation of 0.028 (the standard error gives 0.027), and the mean value for $\hat{\sigma}$ is 1.50 with a standard deviation of 0.02.

D.2 THE BOOTSTRAP PRINCIPLE

The bootstrap principle consists in computing the confidence interval not by considering the (unknown) probability distribution P but by considering the distribution $\hat{P}$ built from the observed data $(x_1, \ldots, x_N)$:

$$\hat{P}(X = x) = \frac{n_x}{N} \text{ where } n_x = \sum_i \mathbb{1}(x_i = x) \tag{D.5}$$

According to the law of large numbers, $\hat{P}$ converges towards P as $N \to \infty$.

Now we can use one of the two methods of the previous section to compute the error on the parameter we are interested in ($\hat{x}$, $\hat{\sigma}$ or $\hat{\theta}$) using $\hat{P}$ instead of P. This is the bootstrap principle. It might still be difficult to have an exact formula to compute the error associated to a quantity with the probability distribution $\hat{P}$. However, the second technique, consisting in drawing many samples of the same length and looking at the spread of the quantity of interest, is now easy to implement. It is sometimes referred to as the Monte-Carlo bootstrap principle.

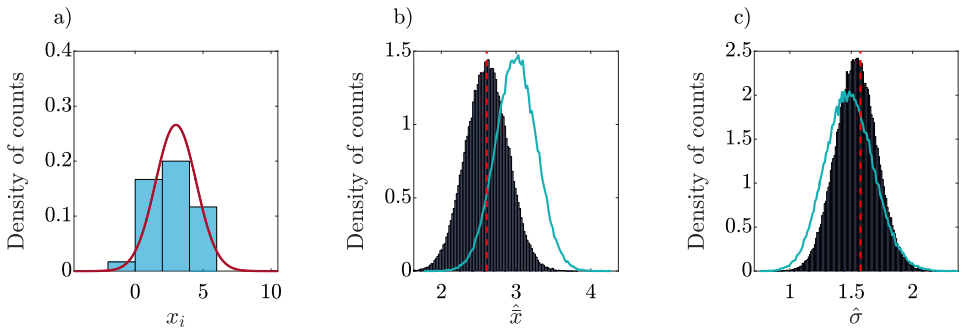

Figure D.2: Implementing the Monte-Carlo bootstrap principle on an example. A sample $\boldsymbol{x} = (x_1, \ldots, x_{30})$ of 30 real numbers were drawn following a Gaussian law P of mean 3 and of standard deviation 1.5. The histogram of the binned drawn numbers is shown in (a) (blue histogram) along with the probability density function of P (red curve). Using the probability distribution $\hat{P}$ as defined in D.5, we perform the same type of sampling as in figure D.1: 100 000 samples of size 30 were drawn according to $\hat{P}$, the histograms of the distribution of measured $\hat{x}$ (resp. $\hat{\sigma}$) are represented in dark blue in (b) (resp. in (c)). The light blue curves represent the distribution obtained with the same procedure using P and not $\hat{P}$ as in figure D.1. The dashed red line in (b) (resp. in (c)) represents the mean (resp. the standard deviation) computed from the original distribution $\boldsymbol{x}$.

Let us illustrate this principle using the example of figure D.2. Here, a set of numbers $\boldsymbol{x} = (x_1, \ldots, x_N)$, $N = 30$ has been drawn with a Gaussian law of mean 3 and standard deviation of 1.5; it has an empirical mean $\hat{\bar{x}}$ and standard deviation $\hat{\sigma}$. We try to estmate the uncertainty on some parameters (mean and standard deviation) using the probability distribution $\hat{P}$ instead of P. This is the Monte-Carlo bootstrap principle. We draw 100 000 samples of size $N = 30$ from the $\{x_i\}$ with replacement (a single x_i can be drawn several times). For each sample, the mean and the standard deviation are computed. The dispersion in the results obtained for $\hat{\bar{x}}_{\text{BS}}$ and $\hat{\sigma}_{\text{BS}}$ gives the errorbar on $\hat{\bar{x}}$ and $\hat{\sigma}$ — the 95 % confidence interval can for example be constructed from distributions such as D.2b) and D.2c).

A variant version of this resampling technique is called the jackknife. There, the samples are not drawn at random. If $\hat{\theta}$ is the statistics to be computed, then we compute for each $1 \leqslant i \leqslant N$ the values $\hat{\theta}_i$ which is the estimator of the parameter computed leaving out the observation x_i. From this set of N values, we can compute the bias of the estimator or the variance of the estimator.

D.3 PRECAUTIONS IN USING THE BOOTSTRAP

D.3.1 *The bootstrap does not provide better estimates of parameters*

The bootstrap technique does not improve the knowledge on $\hat{\bar{x}}$, $\hat{\sigma}$ or $\hat{\theta}$. It only provides an estimate of the confidence interval of that parameter.

D.3.2 *Bootstrap caveats*

D.3.2.1 *Narrowness bias*

It usually happens that the bootstrap distribution is too narrow compared to the original one. This can already be seen on the naive example of the previous section: the bootstrap distribution (dark blue histogram) is not as spread as the equivalent distribution obtained from the true original probability distribution, i. e. the width of the distribution of $\hat{\sigma}_{\text{BS}}$ is smaller than the width of the distribution of $\hat{\sigma}$ computed from the original probability distribution. This can sometimes be solved using several techniques [239]:

- by drawing a large number of samples of size $N - 1$ instead of size N
- by using the bootknife sampling to draw the samples (see [239] for more details)
- by adding a small random noise to the samples that are drawn (also known as the smoothed bootstrap). This is used in particular when the initial probability law is continuous.

D.3.2.2 *Biased estimator*

It sometimes happens that the formula we use to compute the empirical value of the parameter $\hat{\theta}$ does not coincide (or only coincides asymptotically as $N \to \infty$) with the true value of the parameter θ. This is called a biased estimator. It is for example the case for the naive estimator for the standard deviation without the Bessel correction

$$\hat{\sigma}_{\text{bias}} = \sqrt{\sum \frac{(x_i - \hat{\bar{x}})^2}{N}} \tag{D.6}$$

In such a case, it is not good to define the 95 % confindence interval by the two values that leave out 2.5 % of the distribution on each side, because this interval will be off-centered compared to the theoretical central value θ not due to the form of the probability distribution but due to the bias of the estimator.

The effect of a biased estimator is even more important for the bootstrap procedure, since a bias is felt twice. If the bias of the estimate is $C \in \mathbb{R}$, the empirical estimate will then be offset by C, and the bootstrap distribution (i. e. the probability density distribution of $\hat{\theta}_{\text{BS}}$) by $2C$.

This effect can be corrected by comparing the empirical estimate $\hat{\theta}$ to the overall shape of the bootstrap distribution, off-centered compared to $\hat{\theta}$, which leads to the *bias-corrected* bootstrap algorithm. If we have a biased estimator such that $\left(\theta - \hat{\theta}\right)$ follows a Gaussian law centered on z_0, the value of z_0 can be estimated

by comparing $\hat{\theta}$ to the bootstrap cumulated density function $\hat{\theta}_{\text{BS}} \mapsto G\left(\hat{\theta}_{\text{BS}}\right)$. If Φ represents the cumuated density function of the normal distribution, an estimated value of z_0 is [167, 239]

$$z_0 = \Phi^{-1}\left(G\left(\hat{\theta}\right)\right) \tag{D.7}$$

The edges of the confidence interval found by the bootstrap technique can then be offset by $2z_0$.

D.3.2.3 *Asymmetric distributions*

It is not easy to provide reliable confidence interval when the underlying distribution of the parameter θ is asymmetric, or skewed in probabilistic terminology. For example, we usually construct the 95 % confidence interval for a parameter θ by computing the standard error SE associated to it and considering that

$$\theta \in [\hat{\theta} - A\,\text{SE}, \hat{\theta} + A\,\text{SE}] \quad \text{with } 95\,\% \text{ confidence} \tag{D.8}$$

The value of $A = \Phi^{-1}(0.975) \simeq 1.96$ comes from the normal cumulated density function Φ, and can be replaced by another numerical value in case of small samples according to Student's law.

This symmetric interval is very inaccurate in the case where the probability distribution for θ is skewed. The bootstrap accelerated method computes correct confidence intervals using an acceleration constant a [167, 239]. Considering the bootstrap cumulated density function $\hat{\theta}_{\text{BS}} \mapsto G\left(\hat{\theta}_{\text{BS}}\right)$, the acceleration constant a and the bias constant z_0, the bias corrected and accelerated method (BCa) provides according to [167, 239] the $(1-\alpha)$ % confidence interval by computing

$$\left(G^{-1}\left(p(\alpha/2)\right), G^{-1}\left(p(1-\alpha/2)\right)\right) \tag{D.9}$$

with

$$p(\gamma) = \Phi\left(z_0 + \frac{z_0 + \Phi^{-1}(\gamma)}{1 - a\left(z_0 + \Phi^{-1}(\gamma)\right)}\right) \tag{D.10}$$

We already know how to obtain z_0. The proposed procedure in [167, 239] to compute a in the case where we do not make any hypothesis on the underlying probability distribution (the non-parametric case) given the set of observed data $\boldsymbol{x} = (x_1, \ldots, x_N)$ is the following:

- Compute $\hat{\theta}^{(i)}$ the wanted statistics (mean, standard deviation, etc.) which excludes observation number i, x_i.
- Compute the mean of those values $\bar{\hat{\theta}}^{\text{exclude}}$.
- Get a with the following formula [167, 239]

$$a = \frac{-\sum_{i=1}^{N}\left(\hat{\theta}^{(i)} - \bar{\hat{\theta}}^{\text{exclude}}\right)^3}{6\sum_{i=1}^{N}\left(\hat{\theta}^{(i)} - \bar{\hat{\theta}}^{\text{exclude}}\right)^{3/2}} \tag{D.11}$$

The BCa method can require to draw more samples to be accurate (because it might span the edges of the bootstrap distribution).

D.4 CONCLUSION

The bootstrap principle, developed by Efron, enables to estimate the error on a parameter by resampling the original set of data. It does not provide better estimates but confidence intervals for the estimates. These confidence intervals are sensitive to bias and skewness of the distribution, which is accounted for when using the bias corrected and accelerated method. For the data analysis described in chapter 3, the bias-corrected and accelerated method has been used. For the data analysis (result of fit) of chapter 5, an uncorrected bootstrap approach has been used.

BIBLIOGRAPHY

[1] M. H. Anderson, J. R. Ensher, M. R. Matthews, C. E. Wieman, and E. A. Cornell. "Observation of Bose-Einstein Condensation in a Dilute Atomic Vapor." In: *Science* 269.5221 (1995), pp. 198–201 (cit. on pp. 1, 2).

[2] K. B. Davis, M. O. Mewes, M. R. Andrews, N. J. van Druten, D. S. Durfee, D. M. Kurn, and W. Ketterle. "Bose-Einstein Condensation in a Gas of Sodium Atoms." In: *Phys. Rev. Lett.* 75 (22 1995), pp. 3969–3973 (cit. on p. 1).

[3] C. C. Bradley, C. A. Sackett, J. J. Tollett, and R. G. Hulet. "Evidence of Bose-Einstein Condensation in an Atomic Gas with Attractive Interactions." In: *Phys. Rev. Lett.* 75 (9 1995), pp. 1687–1690 (cit. on p. 1).

[4] S. N. Bose. "Plancks gesetz und lichtquantenhypothese." In: *Z. phys* 26.3 (1924), p. 178 (cit. on pp. 1, 9).

[5] A. Einstein. *Quantentheorie des einatomigen idealen Gases*. Preussische Akademie der Wissenschaften, 1924 (cit. on pp. 1, 9).

[6] J. Daunt and R. Smith. "The problem of liquid helium—Some recent aspects." In: *Reviews of Modern Physics* 26.2 (1954), p. 172 (cit. on p. 1).

[7] P Kapitza. "Viscosity of liquid helium below the l-point." In: *Nature* 141.3558 (1938), p. 74 (cit. on p. 1).

[8] V. Sears and E. Svensson. "Pair Correlations and the Condensate Fraction in Superfluid He 4." In: *Physical Review Letters* 43.27 (1979), p. 2009 (cit. on p. 1).

[9] J. Klaers, J. Schmitt, F. Vewinger, and M. Weitz. "Bose-Einstein condensation of photons in an optical microcavity." In: *Nature* 468.7323 (2010), pp. 545–548 (cit. on p. 1).

[10] H. Deng, G. Weihs, C. Santori, J. Bloch, and Y. Yamamoto. "Condensation of semiconductor microcavity exciton polaritons." In: *Science* 298.5591 (2002), pp. 199–202 (cit. on p. 1).

[11] J. Kasprzak, M Richard, S Kundermann, A Baas, P Jeambrun, J. Keeling, F. Marchetti, M. Szymańska, R Andre, J. Staehli, et al. "Bose–Einstein condensation of exciton polaritons." In: *Nature* 443.7110 (2006), pp. 409–414 (cit. on p. 1).

[12] R Balili, V Hartwell, D Snoke, L Pfeiffer, and K West. "Bose-Einstein condensation of microcavity polaritons in a trap." In: *Science* 316.5827 (2007), pp. 1007–1010 (cit. on p. 1).

[13] S. Demokritov, V. Demidov, O Dzyapko, G. Melkov, A. Serga, B Hillebrands, and A. Slavin. "Bose–Einstein condensation of quasi-equilibrium magnons at room temperature under pumping." In: *Nature* 443.7110 (2006), pp. 430–433 (cit. on p. 1).

[14] E. P. Gross. "Structure of a quantized vortex in boson systems." In: *Il Nuovo Cimento (1955-1965)* 20.3 (1961), pp. 454–477 (cit. on p. 1).

[15] L. Pitaevskii. "Vortex linex in an imperfect Bose gas." In: *Sov. Phys. JETP* 13 (1961), p. 451 (cit. on p. 1).

[16] T. D. Lee, K. Huang, and C. N. Yang. "Eigenvalues and eigenfunctions of a Bose system of hard spheres and its low-temperature properties." In: *Physical Review* 106.6 (1957), p. 1135 (cit. on p. 1).

[17] M. Andrews, C. Townsend, H.-J. Miesner, D. Durfee, D. Kurn, and W Ketterle. "Observation of interference between two Bose condensates." In: *Science* 275.5300 (1997), pp. 637–641 (cit. on pp. 1, 51).

[18] I Bloch, T. W. Hänsch, and T Esslinger. "Measurement of the spatial coherence of a trapped Bose gas at the phase transition." In: *Nature* 403.6766 (2000), pp. 166–170 (cit. on p. 1).

[19] M. R. Matthews, B. P. Anderson, P. Haljan, D. Hall, C. Wieman, and E. Cornell. "Vortices in a Bose-Einstein condensate." In: *Physical Review Letters* 83.13 (1999), p. 2498 (cit. on p. 1).

[20] K. Madison, F Chevy, W Wohlleben, and J Dalibard. "Vortex formation in a stirred Bose-Einstein condensate." In: *Physical Review Letters* 84.5 (2000), p. 806 (cit. on p. 1).

[21] J. Abo-Shaeer, C Raman, J. Vogels, and W. Ketterle. "Observation of vortex lattices in Bose-Einstein condensates." In: *Science* 292.5516 (2001), pp. 476–479 (cit. on p. 1).

[22] C Raman, M Köhl, R Onofrio, D. Durfee, C. Kuklewicz, Z Hadzibabic, and W Ketterle. "Evidence for a critical velocity in a Bose-Einstein condensed gas." In: *Physical Review Letters* 83.13 (1999), p. 2502 (cit. on p. 1).

[23] A. J. Leggett. *Quantum liquids: Bose condensation and Cooper pairing in condensed-matter systems*. Oxford University Press, 2006 (cit. on p. 1).

[24] M. W. Zwierlein, J. R. Abo-Shaeer, A. Schirotzek, C. H. Schunck, and W. Ketterle. "Vortices and superfluidity in a strongly interacting Fermi gas." In: *Nature* 435.7045 (2005), pp. 1047–1051 (cit. on pp. 1, 2).

[25] D. Miller, J. Chin, C. Stan, Y Liu, W Setiawan, C Sanner, and W Ketterle. "Critical velocity for superfluid flow across the BEC-BCS crossover." In: *Physical review letters* 99.7 (2007), p. 070402 (cit. on p. 1).

[26] W. Ketterle and M. W. Zwierlein. "Making, probing and understanding ultracold Fermi gases." In: *PROCEEDINGS-INTERNATIONAL SCHOOL OF PHYSICS ENRICO FERMI*. Vol. 164. IOS Press; Ohmsha; 1999. 2007, p. 95 (cit. on p. 1).

[27] I. Bloch, J. Dalibard, and W. Zwerger. "Many-body physics with ultracold gases." In: *Reviews of Modern Physics* 80.3 (2008), p. 885 (cit. on pp. 1, 5).

[28] R. P. Feynman. "Simulating physics with computers." In: *International journal of theoretical physics* 21.6 (1982), pp. 467–488 (cit. on p. 1).

[29] C. J. Pethick and H. Smith. *Bose-Einstein condensation in dilute gases*. Cambridge university press, 2002 (cit. on pp. 1, 5, 19, 20, 28, 31).

[30] A. Griesmaier, J. Werner, S. Hensler, J. Stuhler, and T. Pfau. "Bose-Einstein condensation of chromium." In: *Physical Review Letters* 94.16 (2005), p. 160401 (cit. on p. 1).

[31] M. Lu, N. Q. Burdick, S. H. Youn, and B. L. Lev. "Strongly dipolar Bose-Einstein condensate of dysprosium." In: *Physical review letters* 107.19 (2011), p. 190401 (cit. on pp. 1, 155).

[32] K Aikawa, A Frisch, M Mark, S Baier, A Rietzler, R Grimm, and F Ferlaino. "Bose-Einstein condensation of erbium." In: *Physical review letters* 108.21 (2012), p. 210401 (cit. on p. 1).

[33] K. Baumann, C. Guerlin, F. Brennecke, and T. Esslinger. "Dicke quantum phase transition with a superfluid gas in an optical cavity." In: *Nature* 464.7293 (2010), pp. 1301–1306 (cit. on pp. 1, 99).

[34] P. Courteille, R. Freeland, D. Heinzen, F. Van Abeelen, and B. Verhaar. "Observation of a Feshbach resonance in cold atom scattering." In: *Physical Review Letters* 81.1 (1998), p. 69 (cit. on p. 1).

[35] S Inouye, M. Andrews, J Stenger, H.-J. Miesner, D. Stamper-Kurn, and W Ketterle. "Observation of Feshbach resonances in a Bose–Einstein condensate." In: *Nature* 392.6672 (1998), pp. 151–154 (cit. on p. 1).

[36] M. W. Zwierlein, C. H. Schunck, A. Schirotzek, and W. Ketterle. "Direct observation of the superfluid phase transition in ultracold Fermi gases." In: *nature* 442.7098 (2006), pp. 54–58 (cit. on p. 2).

[37] D. Jacob, L. Shao, V. Corre, T. Zibold, L. De Sarlo, E. Mimoun, J. Dalibard, and F. Gerbier. "Phase diagram of spin-1 antiferromagnetic Bose-Einstein condensates." In: *Physical Review A* 86.6 (2012), p. 061601 (cit. on p. 2).

[38] G. E. Marti, A. MacRae, R. Olf, S. Lourette, F. Fang, and D. M. Stamper-Kurn. "Coherent magnon optics in a ferromagnetic spinor Bose-Einstein condensate." In: *Physical review letters* 113.15 (2014), p. 155302 (cit. on p. 2).

[39] J. Dalibard, F. Gerbier, G. Juzeliūnas, and P. Öhberg. "Colloquium: Artificial gauge potentials for neutral atoms." In: *Reviews of Modern Physics* 83.4 (2011), p. 1523 (cit. on pp. 2, 151–153).

[40] M. Barrett, J. Sauer, and M. Chapman. "All-optical formation of an atomic Bose-Einstein condensate." In: *Physical Review Letters* 87.1 (2001), p. 010404 (cit. on p. 2).

[41] Y. Colombe, E. Knyazchyan, O. Morizot, B. Mercier, V. Lorent, and H. Perrin. "Ultracold atoms confined in rf-induced two-dimensional trapping potentials." In: *EPL (Europhysics Letters)* 67.4 (2004), p. 593 (cit. on p. 2).

[42] B. Paredes, A. Widera, V. Murg, O. Mandel, S. Fölling, I. Cirac, G. V. Shlyapnikov, T. W. Hänsch, and I. Bloch. "Tonks–Girardeau gas of ultracold atoms in an optical lattice." In: *Nature* 429.6989 (2004), pp. 277–281 (cit. on p. 2).

[43] T. Kinoshita, T. Wenger, and D. S. Weiss. "Observation of a one-dimensional Tonks-Girardeau gas." In: *Science* 305.5687 (2004), pp. 1125–1128 (cit. on p. 2).

[44] Z. Hadzibabic, P. Krüger, M. Cheneau, B. Battelier, and J. Dalibard. "Berezinskii–Kosterlitz–Thouless crossover in a trapped atomic gas." In: *Nature* 441.7097 (2006), pp. 1118–1121 (cit. on pp. 2, 10, 19, 49, 51, 57, 91).

[45] S Tung, G Lamporesi, D Lobser, L Xia, and E. A. Cornell. "Observation of the presuperfluid regime in a two-dimensional Bose gas." In: *Physical review letters* 105.23 (2010), p. 230408 (cit. on pp. 2, 5, 10, 19, 49, 55).

[46] N. D. Mermin and H. Wagner. "Absence of ferromagnetism or antiferromagnetism in one-or two-dimensional isotropic Heisenberg models." In: *Physical Review Letters* 17.22 (1966), p. 1133 (cit. on pp. 2, 9).

[47] N. D. Mermin. "Crystalline order in two dimensions." In: *Physical Review* 176.1 (1968), p. 250 (cit. on pp. 2, 9).

[48] P. Hohenberg. "Existence of long-range order in one and two dimensions." In: *Physical Review* 158.2 (1967), p. 383 (cit. on pp. 2, 9).

[49] D. Jaksch, C. Bruder, J. I. Cirac, C. W. Gardiner, and P. Zoller. "Cold bosonic atoms in optical lattices." In: *Physical Review Letters* 81.15 (1998), p. 3108 (cit. on p. 2).

[50] M. Greiner, O. Mandel, T. Esslinger, T. W. Hänsch, and I. Bloch. "Quantum phase transition from a superfluid to a Mott insulator in a gas of ultracold atoms." In: *nature* 415.6867 (2002), pp. 39–44 (cit. on p. 2).

[51] C. Ryu, M. Andersen, P. Clade, V. Natarajan, K. Helmerson, and W. D. Phillips. "Observation of persistent flow of a Bose-Einstein condensate in a toroidal trap." In: *Physical Review Letters* 99.26 (2007), p. 260401 (cit. on pp. 2, 61, 151, 160).

[52] A Ramanathan, K. Wright, S. Muniz, M Zelan, W. Hill III, C. Lobb, K. Helmerson, W. Phillips, and G. Campbell. "Superflow in a toroidal Bose-Einstein condensate: an atom circuit with a tunable weak link." In: *Physical review letters* 106.13 (2011), p. 130401 (cit. on pp. 2, 3).

[53] S. Beattie, S. Moulder, R. J. Fletcher, and Z. Hadzibabic. "Persistent currents in spinor condensates." In: *Physical review letters* 110.2 (2013), p. 025301 (cit. on pp. 2, 61, 151).

[54] T. Meyrath, F Schreck, J. Hanssen, C.-S. Chuu, and M. Raizen. "Bose-Einstein condensate in a box." In: *Physical Review A* 71.4 (2005), p. 041604 (cit. on p. 2).

[55] A. L. Gaunt, T. F. Schmidutz, I. Gotlibovych, R. P. Smith, and Z. Hadzibabic. "Bose-Einstein condensation of atoms in a uniform potential." In: *Physical review letters* 110.20 (2013), p. 200406 (cit. on pp. 2, 45, 47, 51).

[56] J. Billy, V. Josse, Z. Zuo, A. Bernard, B. Hambrecht, P. Lugan, D. Clément, L. Sanchez-Palencia, P. Bouyer, and A. Aspect. "Direct observation of Anderson localization of matter waves in a controlled disorder." In: *Nature* 453.7197 (2008), pp. 891–894 (cit. on p. 2).

[57] Y.-J. Lin, R. L. Compton, K Jiménez-García, J. V. Porto, and I. B. Spielman. "Synthetic magnetic fields for ultracold neutral atoms." In: *Nature* 462.7273 (2009), pp. 628–632 (cit. on pp. 2, 151).

[58] S Jennewein, M Besbes, N. Schilder, S. Jenkins, C Sauvan, J Ruostekoski, J.-J. Greffet, Y. Sortais, and A Browaeys. "Observation of the Failure of Lorentz Local Field Theory in the Optical Response of Dense and Cold Atomic Systems." In: *arXiv preprint arXiv:1510.08041* (2015) (cit. on pp. 2, 95, 98–100).

[59] J Pellegrino, R Bourgain, S Jennewein, Y. R. Sortais, A Browaeys, S. Jenkins, and J Ruostekoski. "Observation of suppression of light scattering induced by dipole-dipole interactions in a cold-atom ensemble." In: *Physical review letters* 113.13 (2014), p. 133602 (cit. on pp. 2, 99, 100, 117).

[60] T. Langen, R. Geiger, and J. Schmiedmayer. "Ultracold Atoms Out of Equilibrium." In: *Annual Review of Condensed Matter Physics* 6.1 (2015), pp. 201–217 (cit. on p. 3).

[61] J.-P. Brantut, J. Meineke, D. Stadler, S. Krinner, and T. Esslinger. "Conduction of ultracold fermions through a mesoscopic channel." In: *Science* 337.6098 (2012), pp. 1069–1071 (cit. on p. 3).

[62] J.-P. Brantut, C. Grenier, J. Meineke, D. Stadler, S. Krinner, C. Kollath, T. Esslinger, and A. Georges. "A thermoelectric heat engine with ultracold atoms." In: *Science* 342.6159 (2013), pp. 713–715 (cit. on p. 3).

[63] S. Krinner, D. Stadler, D. Husmann, J.-P. Brantut, and T. Esslinger. "Observation of quantized conductance in neutral matter." In: *Nature* 517.7532 (2015), pp. 64–67 (cit. on p. 3).

[64] S Eckel, J. G. Lee, F Jendrzejewski, C. Lobb, G. Campbell, and W. Hill III. "Contact resistance and phase slips in mesoscopic superfluid-atom transport." In: *Physical Review A* 93.6 (2016), p. 063619 (cit. on p. 3).

[65] D. Papoular, L. Pitaevskii, and S Stringari. "Quantized conductance with bosonic atoms." In: *arXiv preprint arXiv:1510.02618* (2015) (cit. on p. 3).

[66] A. C. White, B. P. Anderson, and V. S. Bagnato. "Vortices and turbulence in trapped atomic condensates." In: *Proceedings of the National Academy of Sciences* 111.Supplement 1 (2014), pp. 4719–4726 (cit. on p. 3).

[67] G. Lamporesi, S. Donadello, S. Serafini, F. Dalfovo, and G. Ferrari. "Spontaneous creation of Kibble-Zurek solitons in a Bose-Einstein condensate." In: *Nature Physics* 9.10 (2013), pp. 656–660 (cit. on pp. 3, 56, 70).

[68] N. Navon, A. L. Gaunt, R. P. Smith, and Z. Hadzibabic. "Critical dynamics of spontaneous symmetry breaking in a homogeneous Bose gas." In: *Science* 347.6218 (2015), pp. 167–170 (cit. on pp. 3, 36, 38, 56, 70).

[69] E. Akkermans and G. Montambaux. *Mesoscopic physics of electrons and photons*. Cambridge University Press, 2007 (cit. on p. 3).

[70] K. v. Klitzing, G. Dorda, and M. Pepper. "New method for high-accuracy determination of the fine-structure constant based on quantized Hall resistance." In: *Physical Review Letters* 45.6 (1980), p. 494 (cit. on p. 3).

[71] D. C. Tsui, H. L. Stormer, and A. C. Gossard. "Two-dimensional magnetotransport in the extreme quantum limit." In: *Physical Review Letters* 48.22 (1982), p. 1559 (cit. on p. 3).

[72] R. B. Laughlin. "Anomalous quantum Hall effect: an incompressible quantum fluid with fractionally charged excitations." In: *Physical Review Letters* 50.18 (1983), p. 1395 (cit. on p. 3).

[73] B. Van Wees, H Van Houten, C. Beenakker, J. G. Williamson, L. Kouwenhoven, D Van der Marel, and C. Foxon. "Quantized conductance of point contacts in a two-dimensional electron gas." In: *Physical Review Letters* 60.9 (1988), p. 848 (cit. on p. 3).

[74] T. Li, H Kelkar, D Medellin, and M. Raizen. "Real-time control of the periodicity of a standing wave: an optical accordion." In: *Optics express* 16.8 (2008), pp. 5465–5470 (cit. on pp. 4, 91).

[75] M. Glück, A. R. Kolovsky, and H. J. Korsch. "Wannier–Stark resonances in optical and semiconductor superlattices." In: *Physics Reports* 366.3 (2002), pp. 103–182 (cit. on pp. 4, 128, 138).

[76] D. Thouless. "Quantization of particle transport." In: *Physical Review B* 27.10 (1983), p. 6083 (cit. on pp. 4, 169, 172).

[77] M. Lohse, C. Schweizer, O. Zilberberg, M. Aidelsburger, and I. Bloch. "A Thouless quantum pump with ultracold bosonic atoms in an optical superlattice." In: *Nature Physics* (2015) (cit. on pp. 4, 172).

[78] L. Pitaevskii and S. Stringari. *Bose-Einstein Condensation and Superfluidity*. Vol. 164. Oxford University Press, 2016 (cit. on pp. 5, 19, 20, 28, 31).

[79] Z. Hadzibabic and J. Dalibard. "Two-dimensional Bose fluids: An atomic physics perspective." In: *La Rivista del Nuovo Cimento* 6 (2011) (cit. on pp. 5, 15, 20).

[80] T. Yefsah, R. Desbuquois, L. Chomaz, K. J. Günter, and J. Dalibard. "Exploring the thermodynamics of a two-dimensional Bose gas." In: *Physical review letters* 107.13 (2011), p. 130401 (cit. on pp. 5, 10, 19).

[81] C.-L. Hung, X. Zhang, L.-C. Ha, S.-K. Tung, N. Gemelke, and C. Chin. "Extracting density–density correlations from in situ images of atomic quantum gases." In: *New Journal of Physics* 13.7 (2011), p. 075019 (cit. on p. 5).

[82] L. Chomaz, L. Corman, T. Bienaimé, R. Desbuquois, C. Weitenberg, S. Nascimbène, J. Beugnon, and J. Dalibard. "Emergence of coherence via transverse condensation in a uniform quasi-two-dimensional Bose gas." In: *Nature communications* 6 (2015) (cit. on pp. 5, 10, 17, 18, 46, 49, 56).

[83] N. Van Druten and W. Ketterle. "Two-step condensation of the ideal Bose gas in highly anisotropic traps." In: *Physical review letters* 79.4 (1997), p. 549 (cit. on pp. 5, 10, 11, 49).

[84] V. Berezinskii. "Destruction of long-range order in one-dimensional and two-dimensional systems having a continuous symmetry group I. classical systems." In: *Soviet Journal of Experimental and Theoretical Physics* 32 (1971), p. 493 (cit. on pp. 5, 20).

[85] J. M. Kosterlitz and D. J. Thouless. "Ordering, metastability and phase transitions in two-dimensional systems." In: *Journal of Physics C: Solid State Physics* 6.7 (1973), p. 1181 (cit. on pp. 5, 20, 57).

[86] P Cladé, C Ryu, A Ramanathan, K. Helmerson, and W. Phillips. "Observation of a 2D Bose gas: from thermal to quasicondensate to superfluid." In: *Physical review letters* 102.17 (2009), p. 170401 (cit. on pp. 10, 19, 49, 55).

[87] J.-y. Choi, W. J. Kwon, and Y.-i. Shin. "Observation of topologically stable 2D skyrmions in an antiferromagnetic spinor Bose-Einstein condensate." In: *Physical review letters* 108.3 (2012), p. 035301 (cit. on pp. 10, 19).

[88] I. Boettcher, L. Bayha, D. Kedar, P. Murthy, M. Neidig, M. Ries, A. Wenz, G. Zuern, S. Jochim, and T. Enss. "Equation of state of ultracold Fermions in the 2D BEC-BCS crossover region." In: *Physical review letters* 116.4 (2016), p. 045303 (cit. on pp. 10, 19).

[89] W. Weimer, K. Morgener, V. P. Singh, J. Siegl, K. Hueck, N. Luick, L. Mathey, and H. Moritz. "Critical velocity in the BEC-BCS crossover." In: *Physical review letters* 114.9 (2015), p. 095301 (cit. on pp. 10, 19, 21).

[90] L. Chomaz. "Coherence and superfluidity of Bose gases in reduced dimensions: from harmonic traps to uniform fluids." PhD thesis. Ecole normale supérieure-ENS PARIS, 2014 (cit. on pp. 10, 38, 41, 44, 47, 70, 91).

[91] M Naraschewski and R. Glauber. "Spatial coherence and density correlations of trapped Bose gases." In: *Physical Review A* 59.6 (1999), p. 4595 (cit. on p. 14).

[92] O. Penrose and L. Onsager. "Bose-Einstein condensation and liquid helium." In: *Physical Review* 104.3 (1956), p. 576 (cit. on p. 18).

[93] R. Desbuquois. "Thermal and superfluid properties of the two-dimensional Bose gas." PhD thesis. Université Pierre et Marie Curie-Paris VI, 2013 (cit. on pp. 18, 41, 44, 87).

[94] J. Dalibard. "Collisional dynamics of ultra-cold atomic gases." In: *Proceedings of the International School of Physics-Enrico Fermi*. Vol. 321. 1999, p. 14 (cit. on p. 18).

[95] M Egorov, B Opanchuk, P Drummond, B. Hall, P Hannaford, and A. Sidorov. "Measurement of s-wave scattering lengths in a two-component Bose-Einstein condensate." In: *Physical Review A* 87.5 (2013), p. 053614 (cit. on p. 18).

[96] D. Petrov, M. Holzmann, and G. Shlyapnikov. "Bose-Einstein condensation in quasi-2D trapped gases." In: *Physical Review Letters* 84.12 (2000), p. 2551 (cit. on p. 18).

[97] D. Petrov and G. Shlyapnikov. "Interatomic collisions in a tightly confined Bose gas." In: *Physical Review A* 64.1 (2001), p. 012706 (cit. on p. 18).

[98] N. Prokof'ev, O. Ruebenacker, and B. Svistunov. "Critical point of a weakly interacting two-dimensional Bose gas." In: *Physical review letters* 87.27 (2001), p. 270402 (cit. on pp. 19, 20).

[99] N. Prokof'ev and B. Svistunov. "Two-dimensional weakly interacting Bose gas in the fluctuation region." In: *Physical Review A* 66.4 (2002), p. 043608 (cit. on pp. 19, 20, 55).

[100] R. Desbuquois, L. Chomaz, T. Yefsah, J. Léonard, J. Beugnon, C. Weitenberg, and J. Dalibard. "Superfluid behaviour of a two-dimensional Bose gas." In: *Nature Physics* 8.9 (2012), pp. 645–648 (cit. on pp. 21, 49, 62).

[101] H. Nishimori and G. Ortiz. *Elements of phase transitions and critical phenomena*. OUP Oxford, 2010 (cit. on pp. 23, 25–27, 29).

[102] H. E. Stanley. "Scaling, universality, and renormalization: Three pillars of modern critical phenomena." In: *Reviews of modern physics* 71.2 (1999), S358 (cit. on pp. 23, 25).

[103] L. P. Kadanoff, W. Götze, D. Hamblen, R. Hecht, E. Lewis, V. V. Palciauskas, M. Rayl, J Swift, D. Aspnes, and J. Kane. "Static phenomena near critical points: theory and experiment." In: *Reviews of Modern Physics* 39.2 (1967), p. 395 (cit. on pp. 23, 25, 27, 28).

[104] H. L. Swinney and D. L. Henry. "Dynamics of fluids near the critical point: decay rate of order-parameter fluctuations." In: *Physical Review A* 8.5 (1973), p. 2586 (cit. on p. 23).

[105] P. C. Hohenberg and B. I. Halperin. "Theory of dynamic critical phenomena." In: *Reviews of Modern Physics* 49.3 (1977), p. 435 (cit. on pp. 23, 29–32, 60).

[106] T. W. Kibble. "Topology of cosmic domains and strings." In: *Journal of Physics A: Mathematical and General* 9.8 (1976), p. 1387 (cit. on pp. 23, 39, 60, 62, 66).

[107] W. Zurek. "Cosmological experiments in superfluid helium?" In: *Nature* 317.6037 (1985), pp. 505–508 (cit. on pp. 23, 36, 39, 60, 62, 66).

[108] M. Sigrist. *Statistical Physics*. Tech. rep. 2011. 2012, pp. 1–140 (cit. on p. 27).

[109] R. Pathria and P. Beale. *Statistical Mechanics. Butterworh*. Heinemann. Elsevier, 1996 (cit. on pp. 27, 28).

[110] A. Pelissetto and E. Vicari. "Critical phenomena and renormalization-group theory." In: *Physics Reports* 368.6 (2002), pp. 549–727 (cit. on pp. 28, 29).

[111] B. Josephson. "Relation between the superfluid density and order parameter for superfluid He near Tc." In: *Physics Letters* 21.6 (1966), pp. 608–609 (cit. on p. 28).

[112] T. Donner, S. Ritter, T. Bourdel, A. Öttl, M. Köhl, and T. Esslinger. "Critical behavior of a trapped interacting Bose gas." In: *Science* 315.5818 (2007), pp. 1556–1558 (cit. on p. 29).

[113] M. Campostrini, M. Hasenbusch, A. Pelissetto, P. Rossi, and E. Vicari. "Critical behavior of the three-dimensional XY universality class." In: *Physical Review B* 63.21 (2001), p. 214503 (cit. on p. 29).

[114] M. Campostrini, M. Hasenbusch, A. Pelissetto, and E. Vicari. "Theoretical estimates of the critical exponents of the superfluid transition in He 4 by lattice methods." In: *Physical Review B* 74.14 (2006), p. 144506 (cit. on p. 29).

[115] E. Burovski, J. Machta, N. Prokof'ev, and B. Svistunov. "High-precision measurement of the thermal exponent for the three-dimensional X Y universality class." In: *Physical Review B* 74.13 (2006), p. 132502 (cit. on p. 29).

[116] C. Mudry. *Lecture Notes on Field Theory in Condensed Matter Physics*. World Scientific, 2014 (cit. on p. 34).

[117] J. Dziarmaga and W. H. Zurek. "Quench in the 1D Bose-Hubbard model: Topological defects and excitations from the Kosterlitz-Thouless phase transition dynamics." In: *Scientific reports* 4 (2014) (cit. on pp. 34, 38).

[118] A. Del Campo and W. H. Zurek. "Universality of phase transition dynamics: Topological defects from symmetry breaking." In: *International Journal of Modern Physics A* 29.08 (2014), p. 1430018 (cit. on pp. 36–39).

[119] W. H. Zurek. "Topological relics of symmetry breaking: winding numbers and scaling tilts from random vortex–antivortex pairs." In: *Journal of Physics: Condensed Matter* 25.40 (2013), p. 404209 (cit. on p. 37).

[120] P. M. Chesler, A. M. García-García, and H. Liu. "Defect formation beyond Kibble-Zurek mechanism and holography." In: *Physical Review X* 5.2 (2015), p. 021015 (cit. on pp. 37, 38).

[121] G. Biroli, L. F. Cugliandolo, and A. Sicilia. "Kibble-Zurek mechanism and infinitely slow annealing through critical points." In: *Physical Review E* 81.5 (2010), p. 050101 (cit. on p. 38).

[122] F. Corberi, L. F. Cugliandolo, and H. Yoshino. "Growing length scales in aging systems." In: *Dynamical heterogeneities in glasses, colloids, and granular media* 150 (2011), p. 370 (cit. on p. 38).

[123] S. P. Rath. "Production and investigation of quasi-two-dimensional Bose gases." PhD thesis. Université Pierre et Marie Curie-Paris VI, 2010 (cit. on pp. 41, 47, 91, 96).

[124] T. Yefsah. "Thermodynamique du gaz de Bose à deux dimensions." PhD thesis. Université Pierre et Marie Curie-Paris VI, 2011 (cit. on pp. 41, 84).

[125] B. Battelier. "Gaz bidimensionnel de Bosons ultrafroids Nouvelle expérience de condensation de Bose-Einstein." PhD thesis. Université Pierre et Marie Curie-Paris VI, 2007 (cit. on p. 42).

[126] A. Invernizzi. *Characterization of a magnetic quadrupole trap for ultracold atoms via Radiofrequency evaporation*. Tech. rep. October. Department of physics - University of Trento, 2014 (cit. on p. 44).

[127] Y.-J. Lin, A. Perry, R. Compton, I. Spielman, and J. Porto. "Rapid production of R 87 b Bose-Einstein condensates in a combined magnetic and optical potential." In: *Physical Review A* 79.6 (2009), p. 063631 (cit. on p. 44).

[128] L. Chomaz, L. Corman, T. Yefsah, R. Desbuquois, and J. Dalibard. "Absorption imaging of a quasi-two-dimensional gas: a multiple scattering analysis." In: *New Journal of Physics* 14.5 (2012), p. 055001 (cit. on pp. 46, 103, 105, 121, 189, 190).

[129] G Reinaudi, T. Lahaye, Z. Wang, and D. Guéry-Odelin. "Strong saturation absorption imaging of dense clouds of ultracold atoms." In: *Optics letters* 32.21 (2007), pp. 3143–3145 (cit. on p. 46).

[130] I. Gotlibovych, T. F. Schmidutz, A. L. Gaunt, N. Navon, R. P. Smith, and Z. Hadzibabic. "Observing properties of an interacting homogeneous Bose-Einstein condensate: Heisenberg-limited momentum spread, interaction energy, and free-expansion dynamics." In: *Physical Review A* 89.6 (2014), p. 061604 (cit. on p. 47).

[131] C.-L. Hung, X. Zhang, N. Gemelke, and C. Chin. "Observation of scale invariance and universality in two-dimensional Bose gases." In: *Nature* 470.7333 (2011), pp. 236–239 (cit. on p. 49).

[132] L.-C. Ha, C.-L. Hung, X. Zhang, U. Eismann, S.-K. Tung, and C. Chin. "Strongly interacting two-dimensional Bose gases." In: *Physical review letters* 110.14 (2013), p. 145302 (cit. on p. 49).

[133] J.-y. Choi, S. W. Seo, and Y.-i. Shin. "Observation of thermally activated vortex pairs in a quasi-2D Bose gas." In: *Physical review letters* 110.17 (2013), p. 175302 (cit. on pp. 49, 57).

[134] J. Armijo, T. Jacqmin, K. Kheruntsyan, and I. Bouchoule. "Mapping out the quasicondensate transition through the dimensional crossover from one to three dimensions." In: *Physical Review A* 83.2 (2011), p. 021605 (cit. on p. 49).

[135] W. RuGway, A. Manning, S. Hodgman, R. Dall, A. Truscott, T Lamberton, and K. V. Kheruntsyan. "Observation of Transverse Bose-Einstein Condensation via Hanbury Brown–Twiss Correlations." In: *Physical review letters* 111.9 (2013), p. 093601 (cit. on p. 49).

[136] S Hofferberth, I Lesanovsky, B Fischer, T Schumm, and J Schmiedmayer. "Non-equilibrium coherence dynamics in one-dimensional Bose gases." In: *Nature* 449.7160 (2007), pp. 324–327 (cit. on p. 51).

[137] C. Kohstall, S. Riedl, L. Sidorenkov, J. H. Denschlag, R Grimm, et al. "Observation of interference between two molecular Bose? Einstein condensates." In: *New Journal of Physics* 13.6 (2011), p. 065027 (cit. on p. 51).

[138] A. Polkovnikov, E. Altman, and E. Demler. "Interference between independent fluctuating condensates." In: *Proceedings of the National Academy of Sciences* 103.16 (2006), pp. 6125–6129 (cit. on p. 53).

[139] I. Chuang, B. Yurke, R. Durrer, and N. Turok. "Cosmology in the laboratory-Defect dynamics in liquid crystals." In: *Science* 251.4999 (1991), pp. 1336–1342 (cit. on p. 56).

[140] C Bäuerle, Y. M. Bunkov, S. Fisher, H Godfrin, and G. Pickett. "Laboratory simulation of cosmic string formation in the early Universe using superfluid 3 He." In: *Nature* 382.6589 (1996), pp. 332–334 (cit. on p. 56).

[141] V. Ruutu, V. Eltsov, A. Gill, T. Kibble, M Krusius, Y. G. Makhlin, B Placais, G. Volovik, W. Xu, et al. "Vortex formation in neutron-irradiated superfluid He-3 as an analog of cosmological defect formation." In: *Nature* 382.6589 (1996), pp. 334–336 (cit. on p. 56).

[142] S Ulm, J Roßnagel, G Jacob, C Degünther, S. Dawkins, U. Poschinger, R Nigmatullin, A Retzker, M. Plenio, F Schmidt-Kaler, et al. "Observation of the Kibble–Zurek scaling law for defect formation in ion crystals." In: *Nature communications* 4 (2013) (cit. on p. 56).

[143] K Pyka, J Keller, H. Partner, R Nigmatullin, T Burgermeister, D. Meier, K Kuhlmann, A Retzker, M. Plenio, W. Zurek, et al. "Topological defect formation and spontaneous symmetry breaking in ion Coulomb crystals." In: *Nature communications* 4 (2013) (cit. on p. 56).

[144] R Monaco, J. Mygind, R. Rivers, and V. Koshelets. "Spontaneous fluxoid formation in superconducting loops." In: *Physical Review B* 80.18 (2009), p. 180501 (cit. on p. 56).

[145] S Casado, W. González-Viñas, and H Mancini. "Testing the Kibble-Zurek mechanism in Rayleigh-Bénard convection." In: *Physical Review E* 74.4 (2006), p. 047101 (cit. on p. 56).

[146] C. N. Weiler, T. W. Neely, D. R. Scherer, A. S. Bradley, M. J. Davis, and B. P. Anderson. "Spontaneous vortices in the formation of Bose–Einstein condensates." In: *Nature* 455.7215 (2008), pp. 948–951 (cit. on p. 56).

[147] S. Braun, M. Friesdorf, S. S. Hodgman, M. Schreiber, J. P. Ronzheimer, A. Riera, M. del Rey, I. Bloch, J. Eisert, and U. Schneider. "Emergence of coherence and the dynamics of quantum phase transitions." In: *Proceedings of the National Academy of Sciences* 112.12 (2015), pp. 3641–3646 (cit. on p. 56).

[148] A Del Campo, A Retzker, and M. Plenio. "The inhomogeneous Kibble–Zurek mechanism: vortex nucleation during Bose–Einstein condensation." In: *New Journal of Physics* 13.8 (2011), p. 083022 (cit. on p. 56).

[149] A Del Campo, T. Kibble, and W. Zurek. "Causality and non-equilibrium second-order phase transitions in inhomogeneous systems." In: *Journal of Physics: Condensed Matter* 25.40 (2013), p. 404210 (cit. on p. 56).

[150] W. Ketterle and N. Van Druten. "Evaporative cooling of trapped atoms." In: *Advances in atomic, molecular, and optical physics* 37 (1996), pp. 181–236 (cit. on pp. 59, 62).

[151] P. Fedichev and G. Shlyapnikov. "Dissipative dynamics of a vortex state in a trapped Bose-condensed gas." In: *Physical Review A* 60.3 (1999), R1779 (cit. on pp. 59, 61).

[152] L. Giorgetti, I. Carusotto, and Y. Castin. "Semiclassical field method for the equilibrium Bose gas and application to thermal vortices in two dimensions." In: *Physical Review A* 76.1 (2007), p. 013613 (cit. on p. 57).

[153] J. Anglin and W. Zurek. "Vortices in the wake of rapid Bose-Einstein condensation." In: *Physical review letters* 83.9 (1999), p. 1707 (cit. on p. 60).

[154] R. J. Donnelly. *Quantized vortices in helium II*. Vol. 2. Cambridge University Press, 1991 (cit. on p. 61).

[155] R. Bisset, M. Davis, T. Simula, and P. Blakie. "Quasicondensation and coherence in the quasi-two-dimensional trapped Bose gas." In: *Physical Review A* 79.3 (2009), p. 033626 (cit. on p. 61).

[156] L. Mathey and A. Polkovnikov. "Light cone dynamics and reverse Kibble-Zurek mechanism in two-dimensional superfluids following a quantum quench." In: *Physical Review A* 81.3 (2010), p. 033605 (cit. on p. 61).

[157] A. Das, J. Sabbatini, and W. H. Zurek. "Winding up superfluid in a torus via Bose Einstein condensation." In: *Scientific reports* 2 (2012) (cit. on pp. 61, 66, 67).

[158] S. Cockburn and N. Proukakis. "Ab initio methods for finite-temperature two-dimensional Bose gases." In: *Physical Review A* 86.3 (2012), p. 033610 (cit. on p. 61).

[159] L. Corman, L. Chomaz, T. Bienaimé, R. Desbuquois, C. Weitenberg, S. Nascimbene, J. Dalibard, and J. Beugnon. "Quench-induced supercurrents in an annular Bose gas." In: *Physical review letters* 113.13 (2014), p. 135302 (cit. on p. 61).

[160] A. Silver and J. Zimmerman. "Quantum states and transitions in weakly connected superconducting rings." In: *Physical Review* 157.2 (1967), p. 317 (cit. on p. 61).

[161] P. J. Bendt. "Superfluid Helium Critical Velocities in a Rotating Annulus." In: *Physical Review* 127.5 (1962), p. 1441 (cit. on p. 61).

[162] S. Moulder, S. Beattie, R. P. Smith, N. Tammuz, and Z. Hadzibabic. "Quantized supercurrent decay in an annular Bose-Einstein condensate." In: *Physical Review A* 86.1 (2012), p. 013629 (cit. on pp. 61, 151, 160, 161).

[163] J. Clark. *Superconductor Applications: SQUIDs and Machines*. Ed. by B. B. Schwartz and S. Foner. Plenu, New York, 1977 (cit. on p. 61).

[164] R. E. Packard and S. Vitale. "Principles of superfluid-helium gyroscopes." In: *Physical Review B* 46.6 (1992), p. 3540 (cit. on p. 61).

[165] K. Wright, R. Blakestad, C. Lobb, W. Phillips, and G. Campbell. "Driving phase slips in a superfluid atom circuit with a rotating weak link." In: *Physical review letters* 110.2 (2013), p. 025302 (cit. on p. 61).

[166] S Eckel, F Jendrzejewski, A Kumar, C. Lobb, and G. Campbell. "Interferometric measurement of the current-phase relationship of a superfluid weak link." In: *Physical Review X* 4.3 (2014), p. 031052 (cit. on p. 62).

[167] B. Efron. "Better bootstrap confidence intervals." In: *Journal of the American statistical Association* 82.397 (1987), pp. 171–185 (cit. on pp. 65, 197).

[168] A. Jelić and L. F. Cugliandolo. "Quench dynamics of the 2d XY model." In: *Journal of Statistical Mechanics: Theory and Experiment* 2011.02 (2011), P02032 (cit. on p. 68).

[169] *Datasheet MOT2D+* (cit. on p. 76).

[170] K Dieckmann, R. Spreeuw, M Weidemüller, and J. Walraven. "Two-dimensional magneto-optical trap as a source of slow atoms." In: *Physical Review A* 58.5 (1998), p. 3891 (cit. on p. 76).

[171] J Schoser, A Batär, R Löw, V Schweikhard, A Grabowski, Y. B. Ovchinnikov, and T Pfau. "Intense source of cold Rb atoms from a pure two-dimensional magneto-optical trap." In: *Physical Review A* 66.2 (2002), p. 023410 (cit. on p. 76).

[172] S. Chaudhuri, S. Roy, and C. Unnikrishnan. "Realization of an intense cold Rb atomic beam based on a two-dimensional magneto-optical trap: Experiments and comparison with simulations." In: *Physical Review A* 74.2 (2006), p. 023406 (cit. on p. 76).

[173] P. Cheinet. "Conception et réalisation d'un gravimètre à atomes froids." PhD thesis. Université Pierre et Marie Curie-Paris VI, 2006 (cit. on pp. 76, 77).

[174] J.-L. Ville. *Generation of highly tunable light potentials on a two-dimensional degenerate Bose gas*. Tech. rep. 2015 (cit. on p. 87).

[175] V. Dagard. *Caractérisation optique d'une matrice de micro-miroirs*. Tech. rep. 2015 (cit. on p. 89).

[176] D. Rychtarik, B Engeser, H.-C. Nägerl, and R Grimm. "Two-dimensional Bose-Einstein condensate in an optical surface trap." In: *Physical review letters* 92.17 (2004), p. 173003 (cit. on p. 91).

[177] N. Smith, W. Heathcote, G Hechenblaikner, E Nugent, and C. Foot. "Quasi-2D confinement of a BEC in a combined optical and magnetic potential." In: *Journal of Physics B: Atomic, Molecular and Optical Physics* 38.3 (2005), p. 223 (cit. on p. 91).

[178] K. Jimenez-Garcia, R. Compton, Y.-J. Lin, W. Phillips, J. Porto, and I. Spielman. "Phases of a two-dimensional Bose gas in an optical lattice." In: *Physical review letters* 105.11 (2010), p. 110401 (cit. on p. 91).

[179] C Weitenberg. "Single-Atom resolved imaging and manipulation of an atomic Mott insulator." PhD thesis. 2011 (cit. on p. 91).

[180] S Al-Assam, R. Williams, and C. Foot. "Ultracold atoms in an optical lattice with dynamically variable periodicity." In: *Physical Review A* 82.2 (2010), p. 021604 (cit. on p. 91).

[181] M Miranda, A Nakamoto, Y Okuyama, A Noguchi, M Ueda, and M Kozuma. "All-optical transport and compression of ytterbium atoms into the surface of a solid immersion lens." In: *Physical Review A* 86.6 (2012), p. 063615 (cit. on p. 91).

[182] R. Saint-Jalm. *Development of a dynamically tunable, bidimensionally confining optical trap for ultracold rubidium atoms*. Tech. rep. 2015 (cit. on p. 91).

[183] C. Cohen-Tannoudji, J. Dupont-Roc, G. Grynberg, and P. Thickstun. *Atom-photon interactions: basic processes and applications*. Wiley Online Library, 1992 (cit. on p. 95).

[184] J.-M. Raimond and S. Haroche. *Exploring the quantum*. Oxford University Press, Oxford, 2006 (cit. on p. 95).

[185] T. Bienaime, R. Bachelard, N. Piovella, and R. Kaiser. "Cooperativity in light scattering by cold atoms." In: *Fortschritte der Physik* 61.2-3 (2013), pp. 377–392 (cit. on pp. 96, 99, 104).

[186] S. L. Bromley, B. Zhu, M. Bishof, X. Zhang, T. Bothwell, J. Schachenmayer, T. L. Nicholson, R. Kaiser, S. F. Yelin, M. D. Lukin, et al. "Collective atomic scattering and motional effects in a dense coherent medium." In: *Nature communications* 7 (2016) (cit. on pp. 96, 99, 100, 117).

[187] S. Schnatterly and C Tarrio. "Local fields in solids: microscopic aspects for dielectrics." In: *Reviews of modern physics* 64.2 (1992), p. 619 (cit. on pp. 97, 99).

[188] J. D. Jackson. *Classical electrodynamics*. Wiley, 1999 (cit. on p. 97).

[189] O. Morice, Y. Castin, and J. Dalibard. "Refractive index of a dilute Bose gas." In: *Physical Review A* 51.5 (1995), p. 3896 (cit. on pp. 97, 98).

[190] R. Friedberg, S. R. Hartmann, and J. T. Manassah. "Frequency shifts in emission and absorption by resonant systems ot two-level atoms." In: *Physics Reports* 7.3 (1973), pp. 101–179 (cit. on p. 98).

[191] J. Keaveney, A. Sargsyan, U. Krohn, I. G. Hughes, D. Sarkisyan, and C. S. Adams. "Cooperative lamb shift in an atomic vapor layer of nanometer thickness." In: *Physical review letters* 108.17 (2012), p. 173601 (cit. on pp. 98, 99).

[192] J. Javanainen, J. Ruostekoski, Y. Li, and S.-M. Yoo. "Shifts of a resonance line in a dense atomic sample." In: *Physical review letters* 112.11 (2014), p. 113603 (cit. on p. 98).

[193] N. Schilder, C. Sauvan, J.-P. Hugonin, S. Jennewein, Y. Sortais, A. Browaeys, and J.-J. Greffet. "Role of polaritonic modes on light scattering from a dense cloud of atoms." In: *arXiv preprint arXiv:1510.07993* (2015) (cit. on p. 98).

[194] M. Saffman, T. Walker, and K. Mølmer. "Quantum information with Rydberg atoms." In: *Reviews of Modern Physics* 82.3 (2010), p. 2313 (cit. on p. 99).

[195] A. Gaëtan, Y. Miroshnychenko, T. Wilk, A. Chotia, M. Viteau, D. Comparat, P. Pillet, A. Browaeys, P. Grangier, et al. "Observation of collective excitation of two individual atoms in the Rydberg blockade regime." In: *Nature Physics* 5.2 (2009), pp. 115–118 (cit. on p. 99).

[196] E Urban, T. A. Johnson, T Henage, L Isenhower, D. Yavuz, T. Walker, and M Saffman. "Observation of Rydberg blockade between two atoms." In: *Nature Physics* 5.2 (2009), pp. 110–114 (cit. on p. 99).

[197] T. Bienaimé. "Effets coopératifs dans les nuages d'atomes froids." PhD thesis. Université Nice Sophia Antipolis, 2011 (cit. on p. 99).

[198] W. Guerin, M. O. Araújo, and R. Kaiser. "Subradiance in a large cloud of cold atoms." In: *Physical review letters* 116.8 (2016), p. 083601 (cit. on pp. 99, 100).

[199] M. O. Araújo, I. Kresic, R. Kaiser, and W. Guerin. "Superradiance in a Large Cloud of Cold Atoms in the Linear-Optics Regime." In: *arXiv preprint arXiv:1603.07204* (2016) (cit. on pp. 99, 100).

[200] S. Roof, K. Kemp, M. Havey, and I. Sokolov. "Observation of single-photon superradiance and the cooperative Lamb shift in an extended sample of cold atoms." In: *arXiv preprint arXiv:1603.07268* (2016) (cit. on pp. 99, 100).

[201] R. DeVoe and R. Brewer. "Observation of superradiant and subradiant spontaneous emission of two trapped ions." In: *Physical review letters* 76.12 (1996), p. 2049 (cit. on pp. 99, 100).

[202] Y. Takasu, Y. Saito, Y. Takahashi, M. Borkowski, R. Ciuryło, and P. S. Julienne. "Controlled production of subradiant states of a diatomic molecule in an optical lattice." In: *Physical review letters* 108.17 (2012), p. 173002 (cit. on pp. 99, 100).

[203] G. Weinreich. "Coupled piano strings." In: *The Journal of the Acoustical Society of America* 62.6 (1977), pp. 1474–1484 (cit. on p. 99).

[204] R. H. Dicke. "Coherence in spontaneous radiation processes." In: *Physical Review* 93.1 (1954), p. 99 (cit. on pp. 99, 100, 123).

[205] Z Meir, O Schwartz, E Shahmoon, D. Oron, and R Ozeri. "Cooperative lamb shift in a mesoscopic atomic array." In: *Physical review letters* 113.19 (2014), p. 193002 (cit. on p. 99).

[206] S Balik, A. Win, M. Havey, I. Sokolov, and D. Kupriyanov. "Near-resonance light scattering from a high-density ultracold atomic 87 Rb gas." In: *Physical Review A* 87.5 (2013), p. 053817 (cit. on pp. 99, 100).

[207] R. Bourgain. "Diffusion de la lumière dans les nuages denses mésoscopiques d'atomes froids." PhD thesis. Palaiseau, Institut d'optique théorique et appliquée, 2014 (cit. on pp. 101–103).

[208] M Kiffner, M Macovei, J Evers, and C. Keitel. "Vacuum-Induced Processes in Multi-Level Atoms, edited by E. Wolf." In: *Progress in Optics* 55 (2010) (cit. on p. 102).

[209] A Goetschy and S. Skipetrov. "Euclidean matrix theory of random lasing in a cloud of cold atoms." In: *EPL (Europhysics Letters)* 96.3 (2011), p. 34005 (cit. on p. 103).

[210] E Akkermans, A Gero, and R Kaiser. "Photon localization and Dicke superradiance in atomic gases." In: *Physical review letters* 101.10 (2008), p. 103602 (cit. on p. 104).

[211] R. Olf, F. Fang, G. E. Marti, A. MacRae, and D. M. Stamper-Kurn. "Thermometry and cooling of a Bose gas to 0.02 times the condensation temperature." In: *Nature Physics* 11.9 (2015), pp. 720–723 (cit. on p. 112).

[212] Y Castin and R Dum. "Bose-Einstein condensates in time dependent traps." In: *Physical Review Letters* 77.27 (1996), p. 5315 (cit. on p. 115).

[213] W. Ketterle, D. S. Durfee, and D. M. Stamper-kurn. "Making, probing and understanding Bose-Einstein condensates." In: *PROCEEDINGS OF THE INTERNATIONAL SCHOOL OF PHYSICS "ENRICO FERMI", COURSE CXL, EDITED BY M. INGUSCIO, S. STRINGARI AND C.E. WIEMAN (IOS)*. 1999, p. 67 (cit. on p. 127).

[214] T. Plisson. "Propriétés d'équilibre et de transport de gaz de Bose bidimensionnels en présence de désordre." PhD thesis. Ecole Polytechnique X, 2012 (cit. on p. 127).

[215] G. Bird. "Molecular gas dynamics and the direct simulation monte carlo of gas flows." In: *Clarendon, Oxford* 508 (1994) (cit. on p. 128).

[216] C. Monroe, E. A. Cornell, C. Sackett, C. Myatt, and C. Wieman. "Measurement of Cs-Cs elastic scattering at T= 30 μK." In: *Physical review letters* 70.4 (1993), p. 414 (cit. on p. 140).

[217] H. Wu, E. Arimondo, and C. J. Foot. "Dynamics of evaporative cooling for Bose-Einstein condensation." In: *Physical Review A* 56.1 (1997), p. 560 (cit. on p. 143).

[218] E. Mandonnet, A. Minguzzi, R. Dum, I. Carusotto, Y. Castin, and J. Dalibard. "Evaporative cooling of an atomic beam." In: *The European Physical Journal D-Atomic, Molecular, Optical and Plasma Physics* 10.1 (2000), pp. 9–18 (cit. on p. 143).

[219] L. Levy, G Dolan, J Dunsmuir, and H Bouchiat. "Magnetization of mesoscopic copper rings: Evidence for persistent currents." In: *Physical review letters* 64.17 (1990), p. 2074 (cit. on pp. 151, 157, 158).

[220] V Chandrasekhar, R. A. Webb, M. Brady, M. Ketchen, W. Gallagher, and A Kleinsasser. "Magnetic response of a single, isolated gold loop." In: *Physical review letters* 67.25 (1991), p. 3578 (cit. on pp. 151, 157, 158).

[221] D Mailly, C Chapelier, and A Benoit. "Experimental observation of persistent currents in GaAs-AlGaAs single loop." In: *Physical review letters* 70.13 (1993), p. 2020 (cit. on pp. 151, 157, 158).

[222] N. Cooper. "Optical flux lattices for ultracold atomic gases." In: *Physical review letters* 106.17 (2011), p. 175301 (cit. on pp. 151, 167, 180).

[223] N. R. Cooper and J. Dalibard. "Optical flux lattices for two-photon dressed states." In: *EPL (Europhysics Letters)* 95.6 (2011), p. 66004 (cit. on pp. 151, 167).

[224] K. Jimenez-Garcia, L. J. LeBlanc, R. A. Williams, M. C. Beeler, A. R. Perry, and I. B. Spielman. "Peierls substitution in an engineered lattice potential." In: *Physical review letters* 108.22 (2012), p. 225303 (cit. on p. 151).

[225] M. Aidelsburger, M. Atala, S. Nascimbène, S. Trotzky, Y.-A. Chen, and I. Bloch. "Experimental realization of strong effective magnetic fields in an optical lattice." In: *Physical review letters* 107.25 (2011), p. 255301 (cit. on p. 151).

[226] M. Aidelsburger, M. Atala, M. Lohse, J. T. Barreiro, B Paredes, and I. Bloch. "Realization of the Hofstadter Hamiltonian with ultracold atoms in optical lattices." In: *Physical review letters* 111.18 (2013), p. 185301 (cit. on p. 151).

[227] H. Miyake, G. A. Siviloglou, C. J. Kennedy, W. C. Burton, and W. Ketterle. "Realizing the Harper Hamiltonian with laser-assisted tunneling in optical lattices." In: *Physical review letters* 111.18 (2013), p. 185302 (cit. on p. 151).

[228] A. Leanhardt, A Görlitz, A. Chikkatur, D. Kielpinski, Y.-i. Shin, D. Pritchard, and W Ketterle. "Imprinting vortices in a Bose-Einstein condensate using topological phases." In: *Physical review letters* 89.19 (2002), p. 190403 (cit. on pp. 153, 166).

[229] M. Ray, E Ruokokoski, S Kandel, M Möttönen, and D. Hall. "Observation of Dirac monopoles in a synthetic magnetic field." In: *Nature* 505.7485 (2014), pp. 657–660 (cit. on pp. 153, 157).

[230] M. Ray, E Ruokokoski, K Tiurev, M Möttönen, and D. Hall. "Observation of isolated monopoles in a quantum field." In: *Science* 348.6234 (2015), pp. 544–547 (cit. on pp. 153, 157).

[231] J.-y. Choi, S. Kang, S. W. Seo, W. J. Kwon, and Y.-i. Shin. "Observation of a geometric Hall effect in a spinor Bose-Einstein condensate with a skyrmion spin texture." In: *Physical review letters* 111.24 (2013), p. 245301 (cit. on p. 153).

[232] N. Murray, M. Krygier, M. Edwards, K. Wright, G. Campbell, and C. W. Clark. "Probing the circulation of ring-shaped Bose-Einstein condensates." In: *Physical Review A* 88.5 (2013), p. 053615 (cit. on p. 160).

[233] J. Ringot, P. Szriftgiser, and J. C. Garreau. "Subrecoil Raman spectroscopy of cold cesium atoms." In: *Physical Review A* 65.1 (2001), p. 013403 (cit. on p. 164).

[234] M. V. Berry. "Quantal phase factors accompanying adiabatic changes." In: *Proceedings of the Royal Society of London A: Mathematical, Physical and Engineering Sciences*. Vol. 392. 1802. The Royal Society. 1984, pp. 45–57 (cit. on pp. 164, 165).

[235] N. R. Cooper and J. Dalibard. "Reaching fractional quantum Hall states with optical flux lattices." In: *Physical review letters* 110.18 (2013), p. 185301 (cit. on p. 167).

[236] T. Kitagawa, E. Berg, M. Rudner, and E. Demler. "Topological characterization of periodically driven quantum systems." In: *Physical Review B* 82.23 (2010), p. 235114 (cit. on p. 169).

[237] S. Nakajima, T. Tomita, S. Taie, T. Ichinose, H. Ozawa, L. Wang, M. Troyer, and Y. Takahashi. "Topological Thouless pumping of ultracold fermions." In: *Nature Physics* (2016) (cit. on p. 172).

[238] D. Thouless, M. Kohmoto, M. Nightingale, and M Den Nijs. "Quantized Hall conductance in a two-dimensional periodic potential." In: *Physical Review Letters* 49.6 (1982), p. 405 (cit. on p. 172).

[239] T. Hesterberg. "Bootstrap." In: *Wiley Interdisciplinary Reviews: Computational Statistics* 3.6 (2011), pp. 497–526 (cit. on pp. 196, 197).

COLOPHON

This document was typeset using the typographical look-and-feel `classicthesis` developed by André Miede. The style was inspired by Robert Bringhurst's seminal book on typography *"The Elements of Typographic Style"*. `classicthesis` is available for both LaTeX and LyX:

https://bitbucket.org/amiede/classicthesis/

Résumé

Les gaz quantiques atomiques constituent un outil de choix pour étudier la physique à N corps grâce à leurs nombreux paramètres de contrôle. Ils offrent la possibilité d'explorer la physique en basse dimension, modifiée par rapport au cas à trois dimensions (3D) à cause du rôle accru des fluctuations. Dans ce travail, nous étudions le gaz de Bose à deux dimensions (2D) avec un confinement original dans le plan atomique, uniforme et de motif arbitraire. Ces gaz 2D et uniformes, développés sur un montage existant, ont été installés sur un nouveau montage grâce à des potentiels optiques polyvalents.

Nous présentons une série d'expériences exploitant cette géométrie flexible. D'abord, nous étudions le comportement statique et dynamique d'un gaz uniforme lors de la transition d'un état 3D normal vers un état 2D superfluide. Nous observons l'établissement de la cohérence de phase dans un gaz à l'équilibre puis nous montrons l'apparition après une trempe de défauts topologiques dont le nombre est comparé à la prédiction de Kibble-Zurek. Ensuite, nous étudions grâce au nouveau montage les effets collectifs dans l'interaction lumière-matière, où les propriétés de résonance d'un nuage d'atomes dense sont fortement modifiées par rapport à celles d'un atome unique.

Enfin, nous proposons deux protocoles pour le nouveau montage. Le premier permet d'évaporer de manière uniforme un gaz 2D grâce au réseau incliné du confinement à 2D. Le second propose de produire des supercourants de manière déterministe dans des pièges en anneaux, soit par condensation dans un champ de jauge, soit en réalisant une pompe à vortex topologique.

Mots Clés

Condensats de Bose-Einstein, Basse dimension, Interaction lumière-matière, Transition de phase, Mécanisme de Kibble-Zurek, Systèmes hors d'équilibre

Abstract

Degenerate atomic gases are a versatile tool to study many-body physics. They offer the possibility to explore low-dimension physics, which strongly differs from the three dimensional (3D) case due to the enhanced role of fluctuations. In this work, we study degenerate 2D Bose gases whose original in-plane confinement is uniform and of arbitrary shape. These 2D uniform traps, which we first developed on an existing set-up, were subsequently implemented on a new set-up using versatile optical potentials.

We present a series of experiments that take advantage of this flexible geometry. First, we study the static and dynamic behaviours of a uniform gas at the transition between a 3D normal and a 2D superfluid state. We observe the establishement of extended phase coherence, followed, as the gas is quench cooled, by the apparition of topological defects whose scaling is compared to the Kibble-Zurek prediction. Second, we present the first results of the new set-up: we investigate collective effects in light-matter interactions, where the resonance properties of a dense ensemble of atoms are strongly modified with respect to the single atom ones.

Last, we develop two experimental proposals for the new set-up. The first one studies how a 2D gas can be uniformly evaporated using the tilted lattice providing the 2D confinement. In the second one, we propose to produce supercurrents in a deterministic way in ring-shaped traps either by condensing in an artificial gauge field or by implementing a topological vortex pump.

Keywords

Bose-Einstein condensate, low dimensionality, light-matter interaction, phase transition, Kibble-Zurek mechanism, out-of-equilibrium systems

Numéro national de thèse:
xxxxx